Optimal receptivity and the generalization of the One-Way Navier-Stokes (OWNS) Equations to complex high-speed boundary layers and jets

Thesis by

Omar Kamal

In Partial Fulfillment of the Requirements for the
Degree of
Doctor of Philosophy in Mechanical Engineering

CALIFORNIA INSTITUTE OF TECHNOLOGY
Pasadena, California

2023
Defended December 15, 2022

Omar Kamal
ORCID: 0000-0002-3431-2964

ACKNOWLEDGEMENTS

The PhD journey has been an arduous, yet invaluable and unforgettable, experience, largely due to the incredible support I received from so many people. To start, I would like to extend my utmost gratitude to Tim Colonius, my advisor, who provided incredible support and guidance throughout the last four years, and continuously pushed me to a higher level. Although at times I would feel there is no possible solution, you were patient and helped me tackle the problem from a different angle until eventually a solution was found. I will also never forget the skit made with Guillaume Blanquart during the 2022 MCE Banquet as a parody of our Zoom calls during the COVID-19 pandemic. In all, I could not have asked for a better advisor.

I would like to next acknowledge my collaborators from The Boeing Company, Matthew Lakebrink, Ashley Purkey, Kevin Bowcutt, and Abdi Khodadoust. During the summer of 2021, I had the privilege of working as a virtual Boeing Graduate Researcher in the Aerosciences department, where Matthew provided incredible mentorship in learning the computational tools used at Boeing Research & Technology. Ashley and Kevin also provided incredible support if I had any logistical questions with continuous feedback to ensure I was performing optimally. I would like to additionally thank Abdi for planning an amazing visit to the Huntington Beach site and being able to present my doctoral research to a panel of expert aerodynamicists.

Members of the Computational Flow Physics group, whether they be undergraduates, graduates, or postdocs, have undoubtedly contributed to the success of my PhD studies. In fear of forgetting someone, I will refrain from explicitly enumerating the members, but want to emphasize the amazing experience I have had interacting with the past and current members, both socially and academically. I would like to, however, extend a special thanks to Liam Heidt and Wei Hou who have helped me on numerous occasions with Richardson issues at a moment's notice. I also cannot forget the unforgettable experience Liam and I had in spending innumerable hours trying to complete the CDS 131 homework assignments. Lastly, I would like to thank Georgios Rigas for providing excellent mentorship when I first started working with OWNS and for the countless late nights we spent together on Zoom while working on the optimal OWNS paper.

Without a doubt, I am grateful for the amazing friendships made with my first-

year cohort class. I could not have imagined completing first year without the collaborative efforts of everyone. I especially want to thank Vatsa Gandhi and Padmanabha Simha whom I frequently collaborated with in completing assignments. Struggling with countless assignments each week for three terms definitely creates long-lasting bonds.

I am also grateful for my parents and my sister, Tasnia, who provided continuous support not just during my PhD, but all the years leading up to this point. I want to additionally extend my gratitude for all the amazing friends I made at Caltech (in addition to the aforementioned people), but want to highlight one particular individual, Matthew Yao, whom I have known now for almost 9 years. In addition to being my roommate for most of my time at Caltech, we shared many memorable experiences, ranging from taking classes together to TAing to partaking in social events. I also want to extend a special thanks to him for helping me to the hospital when I had my medical emergency back in G2.

I want to now acknowledge my amazing partner, Abira Rajah, whom I have had the privilege of knowing for nearly 2 years. Her unconditional support is ineffable, especially during times of high stress (which were more frequent than not). I cannot express enough gratitude for making the time to talk to me, even if I just am ranting about research, especially considering the time-zone difference and our polar opposite working/sleeping schedules. I especially enjoyed the surprise delivery of desserts whenever I was feeling down from research. I could not have accomplished the said items in this thesis had it not been for her support.

In addition to members of the Caltech community, I would like to thank the external collaborators, including Pedro Paredes for his insightful suggestions in the curvilinear implementation of CSTAT and Daniel Araya and Neal Bitter from APL for an incredible collaborative effort in analyzing the complex 3D finned-cone geometry. I would also like to thank my undergraduate advisor, Jean-Pierre Hickey, for exposing me to the field of hypersonics and helping me kick-start my research career.

Lastly, I would like to thank my committee members, Guillaume Blanquart, Joanna Austin, and Fazle Hussain, for providing insightful feedback regarding my thesis. I would like to extend a special thanks to Fazle for being my research mentor since my undergraduate days at the University of Waterloo, who, similarly to Tim, has always pushed me to understand the fundamentals of my research.

ABSTRACT

Prediction of the linear amplification of disturbances in hypersonic boundary layers is challenging due to the presence and interactions of discrete modes (e.g. Tollmien-Schlichting and Mack) and continuous modes (entropic, vortical, and acoustic). While direct numerical simulations (DNS) and global analysis can be used, the large grids required make the stability calculations expensive, particularly when a large parameter space is required. At the same time, parabolized stability equations are non-convergent and unreliable for problems involving multi-modal and non-modal interactions. We therefore apply the One-Way Navier-Stokes (OWNS) Equations to study transitional hypersonic boundary layers. OWNS is based on a rigorous, approximate parabolization of the equations of motion that removes disturbances with upstream group velocity using a higher-order recursive filter. We extend the original algorithm by considering non-orthogonal curvilinear coordinates and incorporate full compressibility with temperature-dependent fluid properties. The generalized OWNS methodology is validated by comparing to DNS data for flat plates and a sharp cone, and to linear stability theory results for local disturbances on the centerline of the Mach 6 HIFiRE-5 elliptic cone. OWNS provides DNS-quality results for the former flows at a small fraction of the computational expense. We further demonstrate the capability of OWNS to track fully 3D instabilities by applying the algorithm to a complex Mach 6 finned-cone geometry as well as a 3D Mach 1.5 turbulent jet.

It is often desirable, especially for design purposes, to compute worst-case disturbances, i.e. solving the inverse problem, otherwise known as resolvent or input-output analysis. While DNS and global analysis can be used to compute optimal forced responses, their large computational expense render these tools less practical for large design parameter spaces. We address this issue by modifying the original OWNS framework to find the optimal forcing and responses using Lagrangian multipliers via an iterative, adjoint-based, space-marching technique that appreciably reduces the computational burden compared to the global approach that uses singular value decomposition without sacrificing accuracy. The input-output OWNS model is validated against optimal forcings and responses of a Mach 4.5 flat-plate boundary layer from literature and a Mach 1.5 turbulent jet. We then apply these equations to study worst-case disturbances on the centerline of the Mach 6 HIFiRE-5 elliptic cone and on a highly cooled Mach 6 flat-plate boundary layer.

Although the worst-case forcings are theoretically informative, they are not physically realizable. In natural receptivity analysis, disturbances are forced by matching local solutions within the boundary layer to outer solutions consisting of free-stream vortical, entropic, and acoustic disturbances. We pose a scattering formalism to restrict the input forcing to a set of realizable disturbances associated with plane-wave solutions of the outer problem. The formulation is validated by comparing with DNS of a Mach 4.5 flat-plate boundary layer. We show that the method provides insight into transition mechanisms by identifying those linear combinations of plane-wave disturbances that maximize energy amplification over a range of frequencies. We also discuss how the framework can be extended to accommodate scattering from shocks and in shock layers for supersonic flow.

PUBLISHED CONTENT AND CONTRIBUTIONS

Kamal, O., Rigas, G., Lakebrink, M. T., and Colonius, T. (2023). *Generalization of the One-Way Navier-Stokes Equations within the Caltech Stability and Transition Analysis Toolkit*. Submitted to AIAA Journal. 2023.

Araya, D., Bitter, N., Wheaton, B. M., Kamal, O., Colonius, T., Knutson, A., Johnson, H., Nichols, J., Candler, G. V., Russo, V., and Brehm, C. (2022). "Assessment of linear methods for analysis of boundary layer instabilities on a finned cone at Mach 6". In: AIAA AVIATION Forum. 2022. DOI: 10.2514/6.2022-3247.

Kamal, O., Lakebrink, M. T., and Colonius, T. (2022). "Global receptivity analysis: physically realizable input-output analysis". In: *arXiv* (2022). Accepted by the Journal of Fluid Mechanics. DOI: 10.48550/arXiv.2211.10466.

Kamal, O., Rigas, G., Lakebrink, M. T., and Colonius, T. (2022). "Input/output analysis of a Mach-6 cooled-wall hypersonic boundary layer using the One-Way Navier-Stokes (OWNS) Equations". In: AIAA AVIATION Forum. 2022. DOI: 10.2514/6.2022-3556.

Towne, A., Rigas, G., Kamal, O., Pickering, E., and Colonius, T. (2022). "Efficient global resolvent analysis via the one-way Navier-Stokes equations". In: *Journal of Fluid Mechanics* 948 (2022), A9. DOI: 10.1017/jfm.2022.647.

Kamal, O., Rigas, G., Lakebrink, M. T., and Colonius, T. (2021). "Input/output analysis of hypersonic boundary layers using the One-Way Navier-Stokes (OWNS) Equations". In: AIAA AVIATION Forum. 2021. DOI: 10.2514/6.2021-2827.

Kamal, O., Rigas, G., Lakebrink, M. T., and Colonius, T. (2020). "Application of the One-Way Navier-Stokes (OWNS) Equations to hypersonic boundary layers". In: AIAA AVIATION Forum. 2020. DOI: 10.2514/6.2020-2986.

These contributions will be dispersed throughout the thesis. The author was the primary writer and analyst for all contributions except for the second and the third to last, in which components of those papers contributed by the author will be presented. At the time of writing, the second contribution is being submitted to the AIAA Journal and only results for the journal article will be presented.

TABLE OF CONTENTS

LIST OF ILLUSTRATIONS

LIST OF TABLES

NOMENCLATURE

Variables

(ξ, η, ζ)	=	Streamwise, wall-normal/radial, and spanwise coordinates
(x, y, z)	=	Global Cartesian coordinates
(N_ξ, N_η, N_ζ)	=	Streamwise, wall-normal/radial, and spanwise resolution
M	=	Mach number
T	=	Temperature
ν	=	Kinematic viscosity
p	=	Pressure
a	=	Speed of sound
c_Φ	=	Phase speed
ρ	=	Density
k	=	Thermal conductivity
μ	=	Dynamic viscosity
c_v	=	Isochoric specific heat capacity
c_p	=	Isobaric specific heat capacity
$\mathbf{u}$	=	Velocity vector defined as $(u, v, w)^T$
Re^*	=	Unit Reynolds number
α	=	Complex streamwise wavenumber defined as $\alpha_r + i\alpha_i$
β	=	Spanwise wavenumber
κ	=	Bulk viscosity
γ	=	Specific heat ratio
R	=	Gas constant
N_b	=	Order of one-way approximation for OWNS
δ^*_0	=	Inlet Blasius length scale defined as $\sqrt{\frac{\nu^*_\infty x^*_0}{u^*_\infty}}$
D^*	=	Jet diameter
δ	=	Boundary/jet-layer thickness
δ_{ij}	=	Kronecker delta
δ^i_j	=	Mixed Kronecker delta (dot product between co/contravariant basis vectors)
t	=	Time
f^*	=	Disturbance frequency
ω	=	Angular disturbance frequency
F	=	Non-dimensional frequency defined as $\frac{\omega^* \nu^*_\infty}{u^{*2}_\infty}$

St	=	Non-dimensional frequency defined as $\frac{f^* D^*}{u_j^*}$
N	=	Disturbance amplification factor
$\boldsymbol{\mathcal{B}_p}$	=	Primitive input restriction matrix
$\boldsymbol{C_p}$	=	Primitive output restriction matrix
$\boldsymbol{W_f}$	=	Characteristic input weighting matrix
$\boldsymbol{W^{\ddagger}}$	=	Characteristic output weighting matrix

Superscripts

H	=	Hermitian transpose
$*$	=	Dimensional quantities
$\ddagger$	=	Approximate OWNS operators
$\hat{}$	=	Unit vector

Subscripts

∞	=	Free-stream conditions
e	=	Boundary-layer edge conditions
w	=	Wall conditions
j	=	Conditions at the jet nozzle exit
p	=	Primitive variables
ϕ	=	Characteristic variables
$+ - 0$	=	Plus, minus, and zero characteristics
$\mathbb{0}$	=	Inlet plane
$\mathbb{1}$	=	Outlet plane

The nomenclature outlined above holds true for the entirety of the thesis unless otherwise stated for a specific section.

Chapter 1

INTRODUCTION

1.1 Challenges of hypersonic boundary-layer transition

Developing an in-depth understanding of hypersonic laminar-to-turbulent transition will help formulate methods to control aerodynamic and thermal loads. For example, due to the difficulty of predicting the onset of turbulence, the take-off mass of the US National Aerospace Plane (NASP/X-30) was affected by a factor of two or more (Hirschel, 2005). Thus, it is of utmost importance to understand the state of the aerodynamic boundary layer throughout the flight trajectory for optimal vehicular design. We will first review the fundamentals of high-speed boundary-layer transition and thereafter describe the current tools used to predict the onset of transition.

For idealized flow conditions, i.e. slender geometries experiencing minor pressure gradients (if at all) and low free-stream perturbations, at subsonic and low supersonic speeds, natural transition is due to the first mode which is characterized by the amplification of Tollmien-Schlichting (T-S) waves (Fedorov, 2011). This occurs when the boundary layer is receptive to infinitesimal disturbances (e.g. surface roughness). The disturbance waves, which are intrinsically hydrodynamic, amplify as they travel downstream until they reach a finite amplitude of $\approx$1% of the free-stream velocity in which then three-dimensional velocity and pressure fluctuations appear along with hairpin eddies (Zhong and Wang, 2012; Hirschel, 2005). The flow then exhibits nonlinear breakdown where the streamwise stretched vortices cascade energy to smaller structures. Turbulent spots begin to appear after which the flow becomes fully turbulent.

In contrast, at hypersonic speeds (M > 4), natural transition is far more complex due to the presence and interaction of multiple discrete modes including the first, second, and higher-order modes as denoted by Mack (1984) and Mack (1969). Second and higher-order modes are characterized by convectively amplified streamwise-propagating acoustic disturbances usually in the ultrasonic range. Several numerical (Sivasubramanian and Fasel, 2014; Sivasubramanian and Fasel, 2015; Sivasubramanian, Sandberg, et al., 2007) and experimental (Demetriades, 1960; Demetriades, 1974; Fischer and Wagner, 1972; Kendall, 1975; Kimmel, Demetriades, and Don-

aldson, 1996; Stetson and Kimmel, 1992; Stetson, Kimmel, et al., 1991; Stetson, 1983) works have substantiated the existence of such instabilities. These disturbances approximately behave as acoustic waves reflecting between the solid wall and the relative sonic line (Fedorov, 2011). The second Mack mode is usually the dominant instability in zero-pressure-gradient boundary layers at hypersonic speeds with insulated walls. Even with the aforementioned simplified conditions, the second mode becomes unstable due to a complex synchronization of *fast* (Mode F) and *slow* (Mode S) discrete modes that originate from upstream/downstream acoustic branches relative to a supersonic local velocity (Fedorov and Tumin, 2011). Additionally, it has been shown that the first mode along with other instabilities, such as the concave-wall Görtler instability (Saric, 1994), the supersonic mode (Knisely and Zhong, 2019a; Knisely and Zhong, 2019b), and three-dimensional crossflow instability (Arnal and Casalis, 2000; Saric, Reed, and White, 2003) interact with and/or modify the acoustic properties of the second mode (e.g. Görtler-modified azimuthal Mack-modes (Kuehl and Paredes, 2016)). Thus, efficient predictive tools capable of capturing these multi-modal instabilities are critical for engineering design.

Cool surfaces can destabilize the second Mack mode at even lower Mach numbers. Bitter and Shepherd (2015) demonstrated that Mode F (the fast acoustic mode) can become destabilized over a broad range of frequencies. Under high wall-cooling, this mode can synchronize with the slow acoustic branch causing an acoustic emission at a Mach angle corresponding to the relative phase speed. This additional mode, referred to as the supersonic mode (Knisely and Zhong, 2019a; Knisely and Zhong, 2019b), can elongate and modulate the disturbance within the boundary layer (Chuvakhov and Fedorov, 2016). Thus, high-speed transition with the presence of wall-cooling adds an additional layer of complexity with the potential involvement of the supersonic mode.

Current tools to predict boundary-layer transition include direct numerical simulations (DNS) and its linear counterparts such as global stability analysis, local linear stability theory (LST), and parabolized stability equations (PSE). Although global methods are most accurate, they are computationally intensive, especially with complex geometries. LST is more computationally efficient but typically employs the parallel-flow assumption that introduces error as seen in Ma and Zhong (2003a), which studies the stability characteristics of a Mach 4.5 flat-plate boundary layer. PSE may seem to be the optimal method between DNS and LST, but there are intrinsic disadvantages. Instead of formally deriving a one-way operator, PSE

achieves a stable spatial march by numerically damping all upstream-propagating waves, as well as a subset of the downstream-propagating ones, by using an implicit streamwise discretization along with a restriction on the minimum step-size, or by explicitly adding damping terms to the equations (Towne, Rigas, and Colonius, 2019). In either form, the associated damping prevents the upstream waves from destabilizing the spatial march, but also has the unintended consequence of damping and distorting, to differing degrees, all of the downstream waves. This has, in turn, profound negative consequence for non-modal instabilities that are associated with an interacting group of stable modes and for flows with more rapid streamwise evolution (Towne, Rigas, and Colonius, 2019). To clarify, modal instabilities are instabilities associated with a single temporally or spatially amplified discrete mode of the spectrum. Non-modal instabilities, however, can lead to transient amplification due to interaction of stable modes even when there are no unstable modes (Schmid, 2007). In spatial analysis, this phenomena is represented by spatial amplification at a prescribed frequency. Finally, the minimum step size associated with the regularization of the equations leads to non-convergence in many cases of interest. For instance, the synchronization region between Mode F and Mode S, which leads to the second Mack mode instability, can exhibit spectrum singularities (Fedorov, 2011) which may lead to rapid disturbance variation and thus require high spatial resolution to accurately capture the physics. In essence, using PSE and LST as engineering tools for boundary-layer transition prediction is suboptimal due to their inability to accurately model receptivity, non-modal and multi-modal instabilities along with the synchronization and coalescence of discrete modes with continuous branches which is relevant for hypersonic boundary layers (Chuvakhov and Fedorov, 2016; Bitter and Shepherd, 2015).

1.2 One-Way Navier-Stokes (OWNS) Equations

We alleviate the aforementioned deficiencies in PSE by introducing a novel marching technique, the One-Way Navier-Stokes (OWNS) Equations. Originally developed for hyperbolic equations (e.g. Euler), OWNS employs a rigorous parabolization technique to generate well-posed, one-way approximations (Towne, 2016; Towne and Colonius, 2013; Towne and Colonius, 2015; Towne, Rigas, Kamal, et al., 2022). Efficient (fast) approximations of the resulting operator can then be made using recursive filters that were originally developed for non-reflecting boundary conditions (NRBC). Since OWNS tracks the full spectrum of downstream-propagating modes without any damping, it is an efficient tool to study multi-modal and non-modal insta-

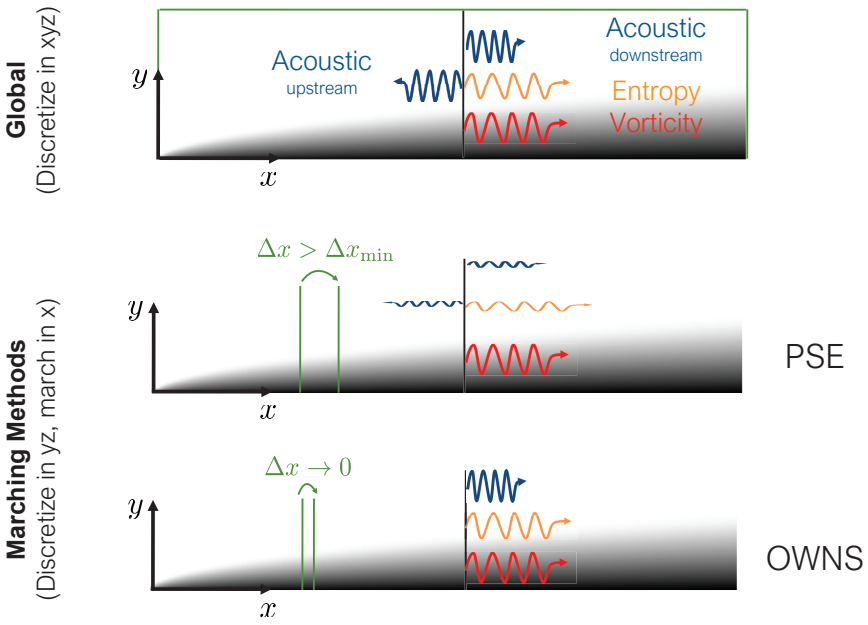

Figure 1.1: Global versus marching methods PSE and OWNS on a flat-plate boundary layer. In PSE, the linearized Navier-Stokes equations are *regularized* to damp the upstream modes, whereas in OWNS the equations are *parabolized* by filtering out modes with upstream group velocity, similar to applying a NRBC. Figure from Towne, Rigas, Kamal, et al. (2022).

bilities at a computational expense comparable to other low-cost stability/transition codes such as LASTRAC (Chang, 2004). The only restriction is the parabolization itself – meaning that OWNS can be applied to flows such as boundary and free-shear layers that are dominated by convective instabilities, i.e. flows lacking feedback (global instability). Finally, and importantly, unlike PSE, the OWNS algorithm is convergent and not restricted to a dominant wavelength. A schematic comparing the global, PSE, and OWNS methods on a flat-plate boundary layer is shown in Fig. 1.1.

From a computational perspective, assuming $N_\xi > N_b$, where N_b is the number of recursion parameters used in OWNS to remove upstream waves, OWNS provides a CPU-cost (FLOPS) and memory speedup by factors of N_ξ^{l-1}/N_b^l and N_ξ^m/N_b^m, respectively, where the factors $1 < l \leq 3$ and $1 < m \leq 2$ depend on the sparsity and structure of the matrix to be inverted, and the efficiency of the algorithm employed (Duff, Erisman, and Reid, 2017). The significant savings in memory, and, for sufficiently large N_ξ, significant savings in FLOPS compared to global methods

allow problems that would normally require high-performance computing resources to be solved on a laptop.

1.3 Input-output analysis

In traditional stability analyses, we analyze how incident disturbances evolve into flow instabilities. However, for design problems, the inverse study is often more useful: what are the worst-case disturbances that lead to the fastest transition from laminar to turbulent flows? Recently, a new technique referred to as *resolvent* or *input-output* analysis has been introduced that combines the linear receptivity and instability problem via optimization techniques, such as singular value decomposition (SVD), to determine surface or volumetric inhomogeneities, i.e. inputs, that lead to maximal amplification of disturbances, i.e. outputs. Trefethen et al. (1993) introduced studying the pseudospectra of the "linearized Navier-Stokes evolution" operator as a tool for understanding non-modal amplification of disturbances in Couette and Poiseuille flows. Monokrousos et al. (2010) used the input-output framework to determine optimal amplification in the spatially evolving flat-plate boundary layer, and it has subsequently been used in a variety of contexts, including extensions to computing optimal disturbances in turbulent mean flows (Schmidt et al., 2018). Owing to their large computational requirements, these global analyses were only tractable for simple geometries at low speeds initially, but with recent advancements in computer architecture, their extension to high-speed flows has now gained traction (Nichols and Lele, 2011; Nichols and Candler, 2019; Cook, Knutson, et al., 2020; Cook and Nichols, 2022; Lugrin et al., 2021; Bugeat et al., 2019; Bae, Dawson, and McKeon, 2020). There have also been contemporary methodological advancements pertaining to the nature of the optimal forcing, such as using sparsity-promoting norms in computing localized forcing structures (Skene et al., 2022).

While promising results have been shown, their routine application to practical, in-flight geometries would involve complex algorithms and large-scale computing. In this thesis, we address this issue by modifying the original OWNS framework to find the optimal forcing and responses using Lagrangian multipliers via an iterative, adjoint-based, space-marching technique that appreciably reduces the computational burden compared to the global approach without sacrificing accuracy.

1.4 Natural boundary-layer receptivity

Natural boundary-layer receptivity analyses determine how free-stream vortical, entropic, and acoustic waves excite instabilities. Several approaches have been developed to accomplish this inner-to-outer matching, such as forcing a flat-plate boundary layer with an induced traveling wave having a frequency of an incident acoustic wave and a wavenumber associated with surface irregularities (Crouch, 1992). However, many studies (Goldstein, 1983; Duck, Ruban, and Zhikharev, 1996; Qin and Wu, 2016; Ruban, Keshari, and Kravtsova, 2021) still rely upon asymptotic expansions, which often require additional approximations such as restrictions to low frequencies (Fedorov, 2003). Although DNS can alleviate these challenges, many (expensive) calculations are needed to characterize the dominant natural receptivity mechanisms. A powerful tool, especially for design problems, would be to determine the worst-case free-stream disturbances that lead to maximal amplification, alluding to the possibility of coupling natural boundary-layer receptivity to the aforementioned input-output analysis. We first highlight that although the inputs for the optimization problem can be readily restricted to subspaces by, for example, forcing only in certain equations (mass, momentum, or energy), and/or in certain flow regions (e.g. Jeun, Nichols, and Jovanović (2016)), the resulting inhomogeneous problem is not *physically realizable*, in the sense that the sources are unconnected to any physical mechanism that produces them. Thus, a new methodology is proposed in this thesis that employs a scattering formalism to restrict input-output analysis to forcings that are associated with free-stream disturbances.

1.5 Outline of thesis

The remainder of the thesis is organized as follows. We begin by generalizing the original OWNS formulation by using a non-orthogonal curvilinear coordinate system and the fully compressible Navier-Stokes equations, including variation of fluid properties, in Sec. 2. We validate the new algorithm to 2D numerical/LST solutions of adiabatic and highly cooled flat-plate boundary layers, an isothermal sharp cone, and the centerline of the Mach 6 HIFiRE-5 elliptic cone (Kimmel, Adamczak, et al., 2010). Thereafter, we demonstrate the capability of OWNS to track fully 3D instabilities in Sec. 3 by applying the algorithm to a complex Mach 6 finned-cone geometry as well as a Mach 1.5 turbulent jet. In Sec. 4, we tackle the inverse problem of determining the worst-case disturbances using the OWNS equations, which considerably reduces the computational burden relative to global techniques using SVD. The methodology is validated to a Mach 4.5 flat-plate

boundary layer from literature and a Mach 1.5 turbulent jet. We then apply this technique to study the optimal forcings and responses along the centerline of the Mach 6 HIFiRE-5 elliptic cone and of a Mach 6 cooled-wall flat-plate boundary layer. In the penultimate section, Sec. 5, we address the issue of the physical realizability of the input forcings in input-output analyses. Specifically, we develop a scattering technique that restricts the forcings to those associated with free-stream disturbances to study natural boundary-layer receptivity. Finally, we conclude and outline future work in Sec. 6. Note that Sec. B provides details of the newly developed stability code, Caltech Stability and Transition Analysis Toolkit (CSTAT), that encompasses the OWNS methodology and is used for all stability calculations in this thesis.

Chapter 2

GENERALIZED OWNS ALGORITHM

This chapter uses the non-orthogonal curvilinear coordinate system and the various grid-related nomenclature from Sec. A. Here we generalize the OWNS methodology for application to complex geometries using the aforementioned coordinate system across all speed regimes with full compressibility effects including temperature-dependent fluid properties. The derivation of the OWNS equations from the generalized Navier-Stokes equations is presented for both the homogeneous and inhomogeneous stability problems, along with the new algorithm used to compute the recursion parameters for jets and boundary layers. We validate this generalized OWNS technique to various hypersonic boundary-layer flows, ranging from flat plates to the Mach 6 HIFiRE-5 elliptic cone.

2.1 Linearized equations of motion

The non-dimensional, compressible Navier-Stokes equations for an ideal gas can be written in tensor form as

$$\frac{\partial \rho}{\partial t} + \nabla \cdot (\rho \boldsymbol{u}) = 0, \tag{2.1a}$$

$$\rho \frac{D\boldsymbol{u}}{Dt} + \boldsymbol{g^{-1}} \nabla p = \frac{1}{Re} \nabla \cdot \boldsymbol{\tau}, \tag{2.1b}$$

$$\rho c_p(T) \frac{DT}{Dt} - \frac{Dp}{Dt} = \frac{1}{PrRe} \nabla \cdot \left(k(T) \boldsymbol{g^{-1}} \nabla T \right) + \frac{1}{Re} \left(\boldsymbol{\tau} : \boldsymbol{g} \nabla \boldsymbol{u} \right), \tag{2.1c}$$

$$\boldsymbol{\tau} = 2\mu(T) \boldsymbol{S} + \kappa(T) (\nabla \cdot \boldsymbol{u}) \boldsymbol{g^{-1}}, \tag{2.1d}$$

$$S = \frac{1}{2} \left(\nabla \boldsymbol{u} \boldsymbol{g^{-1}} + (\nabla \boldsymbol{u} \boldsymbol{g^{-1}})^T - \frac{2}{3} (\nabla \cdot \boldsymbol{u}) \boldsymbol{g^{-1}} \right), \tag{2.1e}$$

$$p = \frac{\gamma_\infty - 1}{\gamma_\infty} \rho T, \tag{2.1f}$$

$$Re = \frac{\rho^*_\infty a^*_\infty \mathrm{L}^*}{\mu^*_\infty}, \tag{2.1g}$$

$$Pr = \frac{\mu^*_\infty c^*_{p\infty}}{k^*_\infty}, \tag{2.1h}$$

where asterisks denote dimensional quantities. All relevant variables have been non-dimensionalized with a characteristic length scale L^* (later chosen as either the inlet Blasius scale δ^*_0 or jet diameter D^*), as well as characterisitc speed, density, and temperature scales, a^*_∞, ρ^*_∞, and $a^{*2}_\infty / c^*_{p\infty}$, respectively. Furthermore, the

fluid properties are normalized with appropriate free-stream quantities such that $c_p(T) = c_p^*(T)/c_{p_\infty}^*$, $k(T) = k^*(T)/k_\infty^*$, $\mu(T) = \mu^*(T)/\mu_\infty^*$, and $\kappa(T) = \kappa^*(T)/\mu_\infty^*$. Note that unless otherwise stated, Stokes' hypothesis is enforced throughout the thesis where bulk viscosity $\kappa \equiv 0$. Finally, the covariant ($\boldsymbol{g}$) and contravariant ($\boldsymbol{g^{-1}}$) metric tensors and the Christoffel symbols and scale factors embodied in the nabla operators in Eq. 2.1 correspond to the *physical* counterparts from Sec. A.1. We then linearize all equations about a time-independent base flow such that

$$\boldsymbol{q}(\xi,\eta,\zeta,t) = \bar{\boldsymbol{q}}(\xi,\eta,\zeta) + \boldsymbol{q'}(\xi,\eta,\zeta,t), \tag{2.2}$$

where $\boldsymbol{q} = [\rho, u, v, w, T]^T$ is the state vector. Due to algebraic complexity, we have automated this transformation using the Mathematica software and present the general matrix form of the resulting forced linear equation

$$\begin{aligned}\boldsymbol{G}\frac{\partial \boldsymbol{q'}}{\partial t} + \boldsymbol{A_{\xi,ivs}}\frac{\partial \boldsymbol{q'}}{\partial \xi} + \boldsymbol{A_{\eta,ivs}}\frac{\partial \boldsymbol{q'}}{\partial \eta} + \boldsymbol{A_{\zeta,ivs}}\frac{\partial \boldsymbol{q'}}{\partial \zeta} + \boldsymbol{A_{ivs}}\boldsymbol{q'} = \boldsymbol{A_{\xi,vis}}\frac{\partial \boldsymbol{q'}}{\partial \xi} + \boldsymbol{A_{\eta,vis}}\frac{\partial \boldsymbol{q'}}{\partial \eta} + \\ \boldsymbol{A_{\zeta,vis}}\frac{\partial \boldsymbol{q'}}{\partial \zeta} + \boldsymbol{A_{vis}}\boldsymbol{q'} + \boldsymbol{B_{\xi\xi}}\frac{\partial^2 \boldsymbol{q'}}{\partial \xi^2} + \boldsymbol{B_{\eta\eta}}\frac{\partial^2 \boldsymbol{q'}}{\partial \eta^2} + \boldsymbol{B_{\zeta\zeta}}\frac{\partial^2 \boldsymbol{q'}}{\partial \zeta^2} + \boldsymbol{B_{\xi\eta}}\frac{\partial^2 \boldsymbol{q'}}{\partial \xi \partial \eta} + \\ \boldsymbol{B_{\xi\zeta}}\frac{\partial^2 \boldsymbol{q'}}{\partial \xi \partial \zeta} + \boldsymbol{B_{\eta\zeta}}\frac{\partial^2 \boldsymbol{q'}}{\partial \eta \partial \zeta} + \boldsymbol{\mathcal{B}_p}\boldsymbol{f_p},\end{aligned} \tag{2.3}$$

where $\boldsymbol{f_p} = [f_\rho, f_\xi, f_\eta, f_\zeta, f_T]^T$ is a general primitive forcing vector that is dimensionally consistent with $\boldsymbol{G}\frac{\partial \boldsymbol{q'}}{\partial t}$ and $\boldsymbol{\mathcal{B}_p}$ is an operator that maps unit inputs into the system's state space for input-output analysis. Note that all of the aforementioned base-flow coefficient matrices are functions of (ξ,η,ζ) and have been normalized with the original coefficient matrix of $\frac{\partial \boldsymbol{q'}}{\partial t}$ and further scaled by the local speed of sound such that $\boldsymbol{G} = \frac{1}{a}\boldsymbol{I}$. The coefficient matrices also contain all the physical covariant/contravariant metric tensors, Christoffel symbols, and the scale factors computed using the methodology outlined in Secs. A.1 and A.2 on the stability grid constructed as per Sec. A.3. Lastly, in the linearization process, the fluid is assumed to be an ideal gas with $c_v = c_v(T)$ and $c_p = c_p(T)$, and fluid properties k, μ, κ, and γ that depend solely on temperature (the functional dependence is user-defined in OWNS). By denoting any of the aforementioned fluid properties as Φ, we can perform a Taylor series expansion about $\overline{T}$ as follows

$$\Phi(T) = \Phi(\overline{T}) + \left.\frac{d\Phi}{dT}\right|_{T=\overline{T}} T' + \text{higher order terms}. \tag{2.4}$$

The linearized fluid-property perturbation is thus

$$\Phi' = \left.\frac{d\Phi}{dT}\right|_{T=\overline{T}} T'. \tag{2.5}$$

After discretizing in the η and ζ directions (if performing 3D analyses, otherwise we invoke spanwise periodicity and consider one wavenumber at a time for 3DF computations), and entering the stationary frequency domain via the Laplace transform with $s = -i\omega$, we have

$$-i\omega \boldsymbol{G}\boldsymbol{q'} + \boldsymbol{A}_{\boldsymbol{\xi},\boldsymbol{ivs}}\frac{d\boldsymbol{q'}}{d\xi} + \boldsymbol{B}\boldsymbol{q'} = \boldsymbol{C}\frac{d\boldsymbol{q'}}{d\xi} + \boldsymbol{B}_{\boldsymbol{\xi\xi}}\frac{d^2\boldsymbol{q'}}{d\xi^2} + \boldsymbol{\mathcal{B}}_{\boldsymbol{p}}\boldsymbol{f}_{\boldsymbol{p}}, \tag{2.6}$$

where the discrete operators $\boldsymbol{B}(\xi)$ and $\boldsymbol{C}(\xi)$ are defined as

$$\boldsymbol{B}(\xi) = \boldsymbol{A}_{\boldsymbol{\eta},\boldsymbol{ivs}}\frac{\partial}{\partial\eta} + \boldsymbol{A}_{\boldsymbol{\zeta},\boldsymbol{ivs}}\frac{\partial}{\partial\zeta} + \boldsymbol{A}_{\boldsymbol{ivs}} - \left(\boldsymbol{A}_{\boldsymbol{\eta},\boldsymbol{vis}}\frac{\partial}{\partial\eta} + \boldsymbol{A}_{\boldsymbol{\zeta},\boldsymbol{vis}}\frac{\partial}{\partial\zeta} + \boldsymbol{A}_{\boldsymbol{vis}} + \boldsymbol{B}_{\boldsymbol{\eta\eta}}\frac{\partial^2}{\partial\eta^2} + \boldsymbol{B}_{\boldsymbol{\zeta\zeta}}\frac{\partial^2}{\partial\zeta^2} + \boldsymbol{B}_{\boldsymbol{\eta\zeta}}\frac{\partial^2}{\partial\eta\partial\zeta}\right), \tag{2.7}$$

$$\boldsymbol{C}(\xi) = \boldsymbol{A}_{\boldsymbol{\xi},\boldsymbol{vis}} + \boldsymbol{B}_{\boldsymbol{\xi\eta}}\frac{\partial}{\partial\eta} + \boldsymbol{B}_{\boldsymbol{\xi\zeta}}\frac{\partial}{\partial\zeta}. \tag{2.8}$$

Refer to Sec. A.2 for the classification of analysis types (2D, 3DF, or 3D). Note that all perturbation quantities hereafter remain in the frequency domain unless otherwise stated.

We now transform the discretized equation to characteristic space via the transformation

$$\boldsymbol{\phi}(\xi,\eta,\zeta,t) = \boldsymbol{T}(\xi,\eta,\zeta)\boldsymbol{q'}(\xi,\eta,\zeta,t), \qquad \widetilde{\boldsymbol{A}}_{\boldsymbol{\xi},\boldsymbol{ivs}} = \boldsymbol{T}\boldsymbol{A}_{\boldsymbol{\xi},\boldsymbol{ivs}}\boldsymbol{T}^{-\boldsymbol{1}}, \tag{2.9}$$

where the rows of $\boldsymbol{T}$ are the left eigenvectors of $\boldsymbol{A}_{\boldsymbol{\xi},\boldsymbol{ivs}}$. The discretized characteristic equation reads

$$-i\omega\widetilde{\boldsymbol{G}}\boldsymbol{\phi} + \widetilde{\boldsymbol{A}}_{\boldsymbol{\xi},\boldsymbol{ivs}}\frac{d\boldsymbol{\phi}}{d\xi} + \widetilde{\boldsymbol{B}}\boldsymbol{\phi} = \widetilde{\boldsymbol{C}}\frac{d\boldsymbol{\phi}}{d\xi} + \widetilde{\boldsymbol{B}}_{\boldsymbol{\xi\xi}}\frac{d^2\boldsymbol{\phi}}{d\xi^2} + \widetilde{\boldsymbol{D}}\boldsymbol{\phi} + \widetilde{\boldsymbol{\mathcal{B}}}_{\boldsymbol{p}}\boldsymbol{f}_{\boldsymbol{\phi}}, \tag{2.10}$$

where

$$\widetilde{\boldsymbol{G}} = \boldsymbol{T}\boldsymbol{G}\boldsymbol{T}^{-\boldsymbol{1}}, \qquad \widetilde{\boldsymbol{B}} = \boldsymbol{T}\boldsymbol{B}\boldsymbol{T}^{-\boldsymbol{1}} + \boldsymbol{T}\boldsymbol{A}_{\boldsymbol{\xi},\boldsymbol{ivs}}\frac{d\boldsymbol{T}^{-\boldsymbol{1}}}{d\xi}, \qquad \widetilde{\boldsymbol{C}} = \boldsymbol{T}\boldsymbol{C}\boldsymbol{T}^{-\boldsymbol{1}} + 2\boldsymbol{T}\boldsymbol{B}_{\boldsymbol{\xi\xi}}\frac{d\boldsymbol{T}^{-\boldsymbol{1}}}{d\xi},$$
$$\widetilde{\boldsymbol{B}}_{\boldsymbol{\xi\xi}} = \boldsymbol{T}\boldsymbol{B}_{\boldsymbol{\xi\xi}}\boldsymbol{T}^{-\boldsymbol{1}}, \qquad \widetilde{\boldsymbol{D}} = \boldsymbol{T}\boldsymbol{C}\frac{d\boldsymbol{T}^{-\boldsymbol{1}}}{d\xi} + \boldsymbol{T}\boldsymbol{B}_{\boldsymbol{\xi\xi}}\frac{d^2\boldsymbol{T}^{-\boldsymbol{1}}}{d\xi^2}, \qquad \widetilde{\boldsymbol{\mathcal{B}}}_{\boldsymbol{p}} = \boldsymbol{T}\boldsymbol{\mathcal{B}}_{\boldsymbol{p}}\boldsymbol{T}^{-\boldsymbol{1}}, \tag{2.11}$$

and $\boldsymbol{f}_{\boldsymbol{\phi}} = \boldsymbol{T}\boldsymbol{f}_{\boldsymbol{p}}$. The right-hand-side of Eq. 2.10 (excluding the forcing) corresponds to streamwise viscous terms which will be discretized explicitly when performing the spatial march and thus we can denote it as a forcing term

$$\boldsymbol{f}_{\boldsymbol{\xi},\boldsymbol{vis}} = \widetilde{\boldsymbol{C}}\frac{d\boldsymbol{\phi}}{d\xi} + \widetilde{\boldsymbol{B}}_{\boldsymbol{\xi\xi}}\frac{d^2\boldsymbol{\phi}}{d\xi^2} + \widetilde{\boldsymbol{D}}\boldsymbol{\phi}. \tag{2.12}$$

We now formally isolate the marching variable, ξ, by writing

$$\frac{\mathrm{d}\boldsymbol{\phi}}{\mathrm{d}\xi} = \boldsymbol{L}\boldsymbol{\phi} + \widetilde{\boldsymbol{A}}^{-1}_{\boldsymbol{\xi},\boldsymbol{ivs}}\widetilde{\boldsymbol{\mathcal{B}}}_{\boldsymbol{p}}\boldsymbol{f}_{\boldsymbol{\phi}} + \widetilde{\boldsymbol{A}}^{-1}_{\boldsymbol{\xi},\boldsymbol{ivs}}\boldsymbol{f}_{\boldsymbol{\xi},\boldsymbol{vis}}, \tag{2.13}$$

where

$$\boldsymbol{L} = -\widetilde{\boldsymbol{A}}^{-1}_{\boldsymbol{\xi},\boldsymbol{ivs}}(-i\omega\widetilde{\boldsymbol{G}} + \widetilde{\boldsymbol{B}}). \tag{2.14}$$

Eq. 2.13 is still exact, but cannot be solved as an initial-value problem in ξ because L has eigenvalues of both signs. In PSE, this equation is *regularized* to damp the upstream modes, whereas in OWNS, described in the next section, the equation is *parabolized* by filtering out the modes with upstream group velocity.

2.2 OWNS equations

The OWNS parabolization, derived in detail in Towne and Colonius (2015) and Towne, Rigas, Kamal, et al. (2022), is now applied to Eq. 2.13. We provide the two variations of the parabolization that can be applied under different scenarios as outlined below.

2.2.1 Variation 1: outflow approach

The outflow approach is appropriate when there is no external forcing ($\boldsymbol{f}_{\boldsymbol{\phi}} = 0$). In addition, streamwise viscous terms must be neglected ($\boldsymbol{f}_{\boldsymbol{\xi},\boldsymbol{vis}} = 0$) in this version as the parabolization is applied to the inviscid portion of the operator, following the original approach in Towne and Colonius (2015). This is consistent with the traditional thin-layer approximation invoked in PSE. In the projection approach, discussed in the next section, the need for this approximation is eliminated though we point out that it is highly accurate for the cases considered in this thesis. Setting $\boldsymbol{f}_{\boldsymbol{\phi}} = \boldsymbol{f}_{\boldsymbol{\xi},\boldsymbol{vis}} = 0$, we have

$$\frac{\mathrm{d}\boldsymbol{\phi}}{\mathrm{d}\xi} = \boldsymbol{L}\boldsymbol{\phi}. \tag{2.15}$$

We can rewrite Eq. 2.15 by partitioning L as follows

$$\frac{\mathrm{d}}{\mathrm{d}\xi}\begin{bmatrix}\boldsymbol{\phi}_+\\ \boldsymbol{\phi}_-\end{bmatrix} = \begin{bmatrix}\boldsymbol{L}_{++} & \boldsymbol{L}_{+-}\\ \boldsymbol{L}_{-+} & \boldsymbol{L}_{--}\end{bmatrix}\begin{bmatrix}\boldsymbol{\phi}_+\\ \boldsymbol{\phi}_-\end{bmatrix}, \tag{2.16}$$

where the $++$, $--$, $+-$, and $-+$ partitioned blocks are associated with the negative and positive characteristic variables. We now perform an eigenvalue decomposition of $\boldsymbol{L} = \boldsymbol{VDU}$ such that

$$\boldsymbol{\phi} = \boldsymbol{V}\boldsymbol{\psi} \quad \leftrightarrow \quad \boldsymbol{\psi} = \boldsymbol{U}\boldsymbol{\phi},$$
$$\frac{\mathrm{d}\boldsymbol{\psi}}{\mathrm{d}\xi} = \boldsymbol{D}\boldsymbol{\psi},$$

where the diagonal matrix $\boldsymbol{D}$ contains the eigenvalues, columns of $\boldsymbol{V}$ are the right eigenvectors and rows of $\boldsymbol{U} = \boldsymbol{V}^{-1}$ are the left eigenvectors, all ordered in the same way as the expansion coefficients $\boldsymbol{\psi}$. We can further partition the matrices as follows

$$\frac{\mathrm{d}}{\mathrm{d}\xi}\begin{bmatrix}\boldsymbol{\psi}_+\\ \boldsymbol{\psi}_-\end{bmatrix} = \begin{bmatrix}\boldsymbol{D}_{++} & \boldsymbol{0}\\ \boldsymbol{0} & \boldsymbol{D}_{--}\end{bmatrix}\begin{bmatrix}\boldsymbol{\psi}_+\\ \boldsymbol{\psi}_-\end{bmatrix}, \tag{2.17}$$

$$\begin{bmatrix}\boldsymbol{\phi}_+\\ \boldsymbol{\phi}_-\end{bmatrix} = \begin{bmatrix}\boldsymbol{V}_{++} & \boldsymbol{V}_{+-}\\ \boldsymbol{V}_{-+} & \boldsymbol{V}_{--}\end{bmatrix}\begin{bmatrix}\boldsymbol{\psi}_+\\ \boldsymbol{\psi}_-\end{bmatrix}, \tag{2.18}$$

$$\begin{bmatrix}\boldsymbol{\psi}_+\\ \boldsymbol{\psi}_-\end{bmatrix} = \begin{bmatrix}\boldsymbol{U}_{++} & \boldsymbol{U}_{+-}\\ \boldsymbol{U}_{-+} & \boldsymbol{U}_{--}\end{bmatrix}\begin{bmatrix}\boldsymbol{\phi}_+\\ \boldsymbol{\phi}_-\end{bmatrix}, \tag{2.19}$$

where $\boldsymbol{\psi}_+$ and $\boldsymbol{\psi}_-$ are the downstream and upstream expansion coefficients, respectively. The exact parabolization is

$$\frac{\mathrm{d}\boldsymbol{\psi}_+}{\mathrm{d}\xi} = \boldsymbol{D}_{++}\boldsymbol{\psi}_+, \tag{2.20a}$$

$$\boldsymbol{\psi}_- = \boldsymbol{0}, \tag{2.20b}$$

or in terms of characteristics with differential-algebraic equation (DAE) system of index 1

$$\frac{\mathrm{d}\boldsymbol{\phi}_+}{\mathrm{d}\xi} = \boldsymbol{L}_{++}\boldsymbol{\phi}_+ + \boldsymbol{L}_{+-}\boldsymbol{\phi}_-, \tag{2.21a}$$

$$\boldsymbol{U}_{-+}\boldsymbol{\phi}_+ + \boldsymbol{U}_{--}\boldsymbol{\phi}_- = \boldsymbol{0}. \tag{2.21b}$$

The parabolization is at this point exact, but requires an eigenvalue decomposition of $\boldsymbol{L}$ at each step in order to determine $\boldsymbol{U}_{-+}$ and $\boldsymbol{U}_{--}$, which is computationally expensive. However, an excellent approximate parabolization is obtained by designing a higher-order recursive filter (Towne and Colonius, 2015; Towne and Colonius, 2013; Towne, 2016) for these matrices, resulting in the OWNS-outflow DAE system

$$\frac{\mathrm{d}\boldsymbol{\phi}_+}{\mathrm{d}\xi} = \boldsymbol{L}_{++}\boldsymbol{\phi}_+ + \boldsymbol{L}_{+-}\boldsymbol{\phi}_-, \tag{2.22a}$$

$$(\boldsymbol{L} - ib_+^j\boldsymbol{I})\boldsymbol{\phi}^{\boldsymbol{j}} = (\boldsymbol{L} - ib_-^j\boldsymbol{I})\boldsymbol{\phi}^{\boldsymbol{j+1}} \qquad j = 0, \ldots, N_b - 1, \tag{2.22b}$$

$$\boldsymbol{\phi}_-^{\boldsymbol{N_b}} = \boldsymbol{0}, \tag{2.22c}$$

where $\{\boldsymbol{\phi}^{\boldsymbol{j}} : j = 0, ..., N_b\}$ and $\{b_+^j, b_-^j : j = 0, ..., N_b - 1\}$ are the auxiliary variables and complex-valued recursion parameters, respectively. Note that N_b is the order of the approximate one-way system such that as $N_b \to \infty$, we recover

the exact parabolization in Eq. 2.20 (Towne, 2016). The physical variable $\boldsymbol{\phi}$ is the zero-indexed quantity $\boldsymbol{\phi^0}$ and the remaining auxiliary variables are defined via the recursions. The DAE system can then be solved using an implicit integration method of choice such as backward differentiation formula (BDF) or implicit Runge-Kutta (RK).

2.2.2 Variation 2: projection approach

The projection approach alleviates the need to neglect the streamwise viscous terms and the inhomogeneous term and is fully described in Towne, Rigas, Kamal, et al. (2022), but we provide a synopsis here. Using the same eigenvalue decomposition as the outflow approach $\boldsymbol{L} = \boldsymbol{VDU}$, we define a projection operator that splits the solution $\boldsymbol{\phi}$ into the right-going ($\boldsymbol{\phi'}$) and left-going ($\boldsymbol{\phi''}$) components

$$\boldsymbol{P} = \begin{bmatrix} \boldsymbol{V_+} & \boldsymbol{V_-} \end{bmatrix} \begin{bmatrix} \boldsymbol{I} & \boldsymbol{0} \\ \boldsymbol{0} & \boldsymbol{0} \end{bmatrix} \begin{bmatrix} \boldsymbol{U_+} \\ \boldsymbol{U_-} \end{bmatrix}, \tag{2.23}$$

such that

$$\boldsymbol{\phi'} = \boldsymbol{P\phi}, \qquad \boldsymbol{\phi''} = \boldsymbol{(I - P)\phi}. \tag{2.24}$$

Applying the projection operator to Eq. 2.13 yields

$$\boldsymbol{P}\frac{\mathrm{d}\boldsymbol{\phi}}{\mathrm{d}\xi} = \boldsymbol{P}\left(\boldsymbol{L\phi} + \widetilde{\boldsymbol{A}}^{\boldsymbol{-1}}_{\boldsymbol{\xi,ivs}}\widetilde{\boldsymbol{\mathcal{B}}}_{\boldsymbol{p}}\boldsymbol{f_\phi} + \widetilde{\boldsymbol{A}}^{\boldsymbol{-1}}_{\boldsymbol{\xi,ivs}}\boldsymbol{f_{\xi,vis}}\right), \tag{2.25}$$

and the fact that $\boldsymbol{P}$ and $\boldsymbol{L}$ commute we write (Towne, 2016)

$$\frac{\mathrm{d}\boldsymbol{\phi'}}{\mathrm{d}\xi} = \boldsymbol{P}\left(\boldsymbol{L\phi} + \widetilde{\boldsymbol{A}}^{\boldsymbol{-1}}_{\boldsymbol{\xi,ivs}}\widetilde{\boldsymbol{\mathcal{B}}}_{\boldsymbol{p}}\boldsymbol{f_\phi} + \widetilde{\boldsymbol{A}}^{\boldsymbol{-1}}_{\boldsymbol{\xi,ivs}}\boldsymbol{f_{\xi,vis}}\right). \tag{2.26}$$

As with the outflow approach, we again use a higher-order recursive filter to generate an approximate projection operator $\boldsymbol{P}^{\ddagger}$ (Towne, 2016). Specifically, the following recursions are used to determine $\boldsymbol{P}^{\ddagger}$ acting on an arbitrary vector $\boldsymbol{\phi}$

$$\boldsymbol{\phi}_+^{-N_b} = \boldsymbol{0}, \tag{2.27a}$$

$$(\boldsymbol{L} - ib_-^j\boldsymbol{I})\boldsymbol{\phi^{-j}} - (\boldsymbol{L} - ib_+^j\boldsymbol{I})\boldsymbol{\phi^{-(j+1)}} = \boldsymbol{0} \qquad j = 1, \ldots, N_b - 1, \tag{2.27b}$$

$$(\boldsymbol{L} - ib_-^0\boldsymbol{I})\boldsymbol{\phi^0} - (\boldsymbol{L} - ib_+^0\boldsymbol{I})\boldsymbol{\phi^{-1}} = (\boldsymbol{L} - ib_-^0\boldsymbol{I})\boldsymbol{\phi}, \tag{2.27c}$$

$$(\boldsymbol{L} - ib_+^j\boldsymbol{I})\boldsymbol{\phi^j} - (\boldsymbol{L} - ib_-^j\boldsymbol{I})\boldsymbol{\phi^{(j+1)}} = \boldsymbol{0} \qquad j = 0, \ldots, N_b - 1, \tag{2.27d}$$

$$\boldsymbol{\phi}_-^{N_b} = \boldsymbol{0}. \tag{2.27e}$$

The above recursion equations defining the approximate projection operator can be rewritten in the following form (Towne, Rigas, Kamal, et al., 2022)

$$\boldsymbol{\phi'_\pm} = \boldsymbol{P_3}\boldsymbol{\phi^{aux}}, \tag{2.28a}$$

$$\boldsymbol{P_2}\boldsymbol{\phi^{aux}} = \boldsymbol{P_1}\boldsymbol{\phi_\pm}, \tag{2.28b}$$

where $\boldsymbol{\phi}^{\mathbf{aux}}$ contains the auxiliary variables, the matrices $\boldsymbol{P_1}$ and $\boldsymbol{P_2}$ are defined by the recursive relations, and $\boldsymbol{P_3}$ is a matrix that extracts the projected state from the auxiliary variables. The approximate form of Eq. 2.26 can therefore be expressed as a DAE input-output system (Towne, Rigas, Kamal, et al., 2022)

$$\boldsymbol{A}^{\ddagger}\frac{d\boldsymbol{\phi}^{\ddagger}}{d\xi} = \boldsymbol{L}^{\ddagger}\boldsymbol{\phi}^{\ddagger} + \boldsymbol{B}^{\ddagger}\left(\widetilde{\mathcal{B}}_{\boldsymbol{p}}\boldsymbol{f}_{\phi} + \boldsymbol{f}_{\xi,vis}\right), \tag{2.29a}$$

$$\boldsymbol{\phi}' = \boldsymbol{C}^{\ddagger}\boldsymbol{\phi}^{\ddagger}. \tag{2.29b}$$

The augmented state vector is

$$\boldsymbol{\phi}^{\ddagger} = \begin{bmatrix} \boldsymbol{\phi}'_{\pm} \\ \boldsymbol{\phi}'_{\mathbf{0}} \\ \boldsymbol{\phi}^{\mathbf{aux}} \end{bmatrix}, \tag{2.30}$$

and the operators in Eq. 2.29 are

$$\boldsymbol{A}^{\ddagger} = \begin{bmatrix} \boldsymbol{I} & & \\ & \mathbf{0} & \\ & & \mathbf{0} \end{bmatrix}, \quad \boldsymbol{B}^{\ddagger} = \begin{bmatrix} \mathbf{0} & \mathbf{0} \\ \boldsymbol{P_1}\widetilde{\boldsymbol{A}}^{-\mathbf{1}}_{\boldsymbol{\xi},\boldsymbol{ivs}_{\pm\pm}} & \mathbf{0} \\ \mathbf{0} & \boldsymbol{I} \end{bmatrix}, \quad \boldsymbol{C}^{\ddagger} = \begin{bmatrix} \boldsymbol{I} & \mathbf{0} & \mathbf{0} \\ \mathbf{0} & \boldsymbol{I} & \mathbf{0} \end{bmatrix}, \tag{2.31}$$

and

$$\boldsymbol{L}^{\ddagger} = \begin{bmatrix} \mathbf{0} & \mathbf{0} & \boldsymbol{P_3} \\ \boldsymbol{P_1}\widetilde{\boldsymbol{A}}^{-\mathbf{1}}_{\boldsymbol{\xi},\boldsymbol{ivs}_{\pm\pm}}\boldsymbol{L}_{\pm\pm} & \boldsymbol{P_1}\widetilde{\boldsymbol{A}}^{-\mathbf{1}}_{\boldsymbol{\xi},\boldsymbol{ivs}_{\pm\pm}}\boldsymbol{L}_{\pm\mathbf{0}} & -\boldsymbol{P_2} \\ \boldsymbol{L}_{\mathbf{0}\pm} & \boldsymbol{L}_{\mathbf{00}} & \mathbf{0} \end{bmatrix}. \tag{2.32}$$

The input to the system is either the forcing $\boldsymbol{f}_{\boldsymbol{\phi}} = \boldsymbol{T}\boldsymbol{f}_{\boldsymbol{p}}$ and/or an inlet boundary condition $\boldsymbol{\phi}_{\mathbf{0}} = \boldsymbol{T}\boldsymbol{q}'_{\mathbf{0}}$, while the output is $\boldsymbol{\phi}'$, the downstream-projected component of the characteristic variable, from which the primitive state vector can be retrieved as $\boldsymbol{q}' = \boldsymbol{T}^{-\mathbf{1}}\boldsymbol{\phi}'$. Eq. 2.29 can thus be efficiently integrated in the positive ξ-direction given an appropriate input.

However, the integration method has an impact on the streamwise viscous terms, which must be treated explicitly and where the streamwise derivatives are approximated with second-order finite differences. The remaining terms, on the other hand, require an implicit integration and thus the stepper must be of a split implicit-explicit (IMEX) type. We have found that an IMEX-BDF scheme (typically second order) is the most efficient choice meeting these requirements. Details of the IMEX-BDF schemes and their numerical stability properties can be found in Frank, Hundsdorfer, and Verwer (1997) and Hu and Shu (2021). Including the streamwise viscous terms, however, can occasionally lead to numerical instability. Specifically, we must have

a sufficiently large local grid Reynolds number $Re_g = \frac{\bar{\rho}^* \bar{u}^* d\xi^*}{\bar{\mu}^*}$, which essentially requires the base flow to be advection dominated. Should numerical instability occur, either the streamwise grid size $d\xi$ can be increased or the streamwise viscous terms can be neglected altogether. In fact, extensive calculations with both boundary layers and jets have demonstrated that these streamwise viscous terms are insignificant compared to the other terms from Eq. 2.13 and thus neglected for the remainder of the thesis.

2.2.3 Recursion parameters

The recursion parameters for both the outflow and projection approaches are based on the original algorithm described in Towne and Colonius (2015), which uses the spatial eigenvalues of the linearized Euler equations about a uniform flow. These eigenvalues provide a basis which can be used to predict the eigenvalues of the semi-discrete operator $\boldsymbol{L}$ for complicated, non-uniform flows. Note that the recursion parameters are different between boundary layers and jets, and the original method from Towne and Colonius (2015) has been adapted to accommodate the curvilinear coordinate system. The complete algorithm (MATLAB script) for computing the recursion parameters for 2D/3DF calculations is presented in Sec. C, where for 3D analyses, the same method is used but the base-flow quantities are cross-stream averaged.

The effectiveness of the OWNS method in accurately filtering the upstream-traveling modes without modifying the downstream ones is demonstrated using the projection approach in Fig. 2.1, where the local spectra (in ξ) of the Navier-Stokes and OWNS equations are shown for the Mach 4.5 flat-plate boundary layer from Sec. 4.2 for three values of N_b. The spectra were calculated by solving a generalized eigenvalue problem obtained from the homogeneous form of Eq. 2.29 by assuming a locally parallel flow, for which $\partial_\xi \rightarrow i\alpha$ and the complex streamwise wavenumber α is the eigenvalue. With sufficient N_b of recursion parameters, the OWNS operator converges to the downstream-traveling waves, thus removing the ellipticity associated with the upstream-propagating acoustic modes and enabling a stable, convergent marching in the slowly varying ξ direction.

2.3 Validation of generalized OWNS algorithm

In this section, we will validate the generalized OWNS methodology to various 2D boundary-layer flows, i.e. $\beta = 0$. Note that computations presented in this section are from Kamal, Rigas, et al. (2020) where the thermodynamic state variables

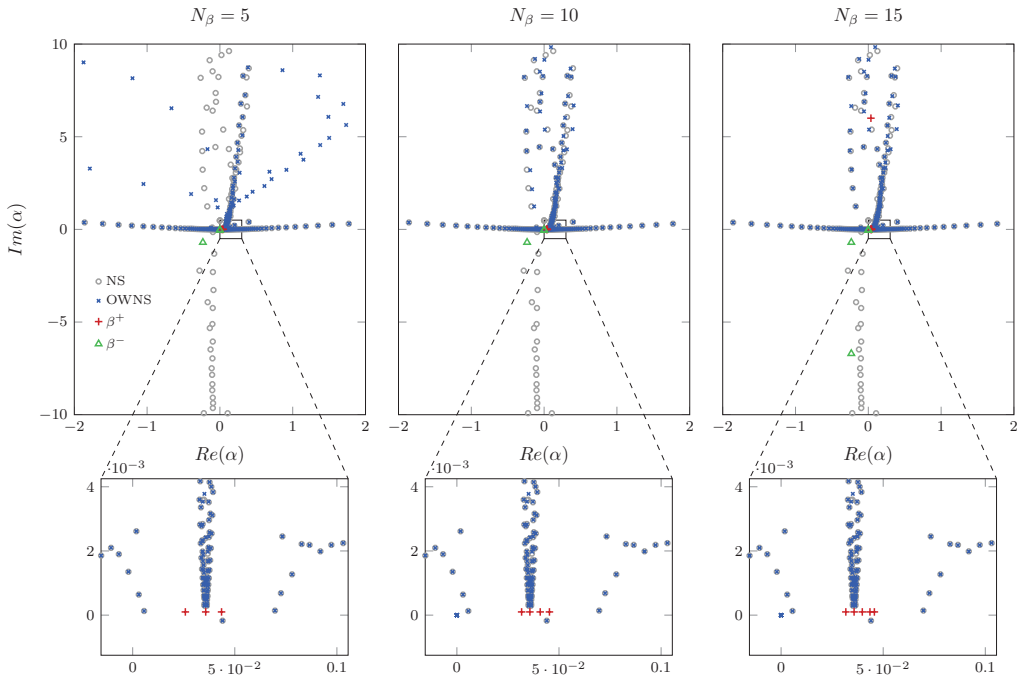

Figure 2.1: Placement of recursion parameters b^+ and b^- for the Mach 4.5 flat-plate boundary layer from Sec. 4.2. The local spectra of the Navier-Stokes and OWNS operators are shown. The b^+ recursion parameters are placed in the vicinity of the downstream-propagating modes, whereas the b^- parameters are placed adjacent to the upstream acoustic modes. Figure from Towne, Rigas, Kamal, et al. (2022) where β denotes the recursion parameters.

were v' (specific volume) and p' rather than ρ' and T' from Eq. 2.1. Additionally, the numerical solutions used for comparison all assume a calorically perfect gas (constant specific heats). Thus, unless otherwise stated, we likewise assume the fluid as calorically perfect air with $\gamma = 1.4$ and $Pr = 0.72$ and, moreover, viscosity and thermal conductivity calculated using Sutherland's law

$$\mu^* = \mu^*_\infty \left(\frac{T^*}{T^*_\infty}\right)^{3/2} \frac{T^*_\infty + S^*}{T^* + S^*}, \tag{2.33}$$

where $S^* = 110.4$ K.

Finally, reference to the η-coordinate in this section and for the remainder of the thesis will correspond to the *physical* wall-normal coordinate (for boundary layers) *except* when defining any wall-normal grid-stretching functions, any association to the grid metrics from Sec. A, or otherwise stated.

2.3.1 Computational setup

To properly resolve the instabilities near the wall and critical layer, we employ a grid stretching technique (Malik, 1990) for all validation cases

$$\begin{aligned} \eta &= \frac{a\lambda}{b-\lambda}, \\ b &= 1 + a/\eta_{max}, \\ a &= \eta_{max}\eta_i/(\eta_{max} - 2\eta_i), \end{aligned} \tag{2.34}$$

where $0 \leq \lambda \leq 1$ (equidistant grid points). Using the above scheme, half the points in the η direction are placed between $\eta = 0$ and $\eta = \eta_i$.

Details of each validation case are outlined below. Note that all validation cases have no external forcing, and thus, the outflow approach is used for all OWNS computations with second-order BDF (BDF2) streamwise integration.

2.3.1.1 Adiabatic flat plate

We first validate OWNS by comparing to DNS of a two-dimensional Mach 4.5 adiabatic-wall, flat-plate boundary layer (Ma and Zhong, 2003a). The parameters are given in Table 2.1. The base flow is computed using the Howarth–Dorodnitsyn transformation of the compressible Blasius equations under the assumption $d\bar{p} = 0$. Note that γ was not explicitly provided in Ma and Zhong (2003a) so a value of 1.4 was assumed. The computational domain is summarized in Table 2.2 where ξ and η coincide with the global x and y axes with its origin placed at the plate leading edge. The grid resolution for this validation, and all subsequent computations in this thesis, is chosen after performing grid-convergence studies to ensure the wavenumber, growth rates, optimal gains, and/or other quantities of interest are grid independent. The initial resolution for the grid-convergence study is usually estimated based on the frequency, Mach number, and size of the domain.

Table 2.1: Adiabatic flat-plate flow parameters from Ma and Zhong (2003a).

M_∞	T^*_∞ [K]	T^*_w [K]	p^*_∞ [Pa]	Re^*_∞ [1/m]
4.5	65.15	T^*_{ad}	728.438	7.2×10^6

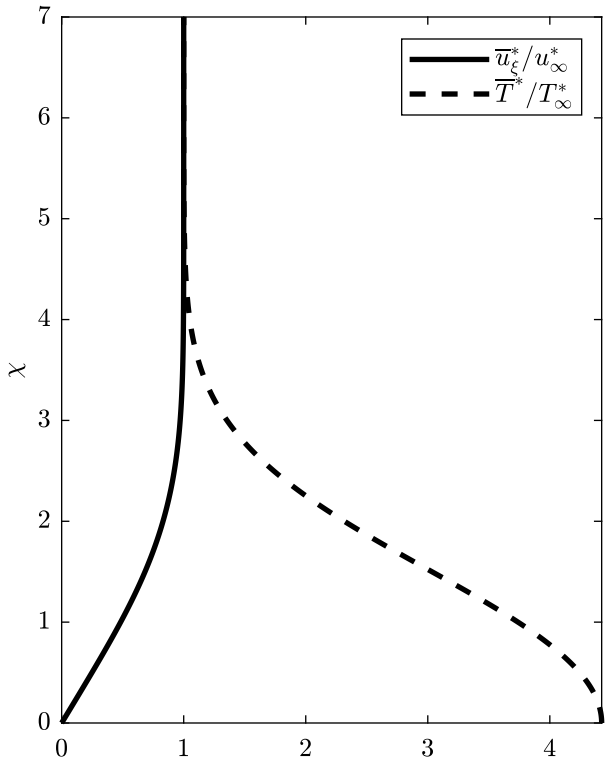

Figure 2.2: Self-similar base flow solutions $\frac{\bar{u}^*_\xi}{u^*_\infty}$ and $\frac{\bar{T}^*}{T^*_\infty}$ for Case 1.

Table 2.2: Computational domain used for adiabatic flat-plate stability analyses.

ξ^*_{min} [m]	ξ^*_{max} [m]	η^*_{min} [m]	η^*_{max} [m]	N_ξ	N_η
0.025	0.63	0.0	0.0118	8000	800

The self-similar base flow solutions for $\frac{\bar{u}^*_\xi}{u^*_\infty}$ and $\frac{\bar{T}^*}{T^*_\infty}$ are presented in Fig. 2.2. The similarity variable χ is defined as

$$\chi = \sqrt{\frac{u^*_\infty \rho^*_\infty}{2\mu^*_\infty \xi^*}} \int_0^{\eta^*} \frac{\rho^*}{\rho^*_\infty} d\eta^*. \tag{2.35}$$

2.3.1.2 Highly cooled (isothermal) flat plate

The second validation case is also a flat-plate configuration but with a cold wall (Chuvakhov and Fedorov, 2016). Parameters are given in Table 2.3. Similar to the adiabatic case, the base flow is computed using the Howarth–Dorodnitsyn transformation of the compressible Blasius equations under the assumption $d\bar{p} = 0$.

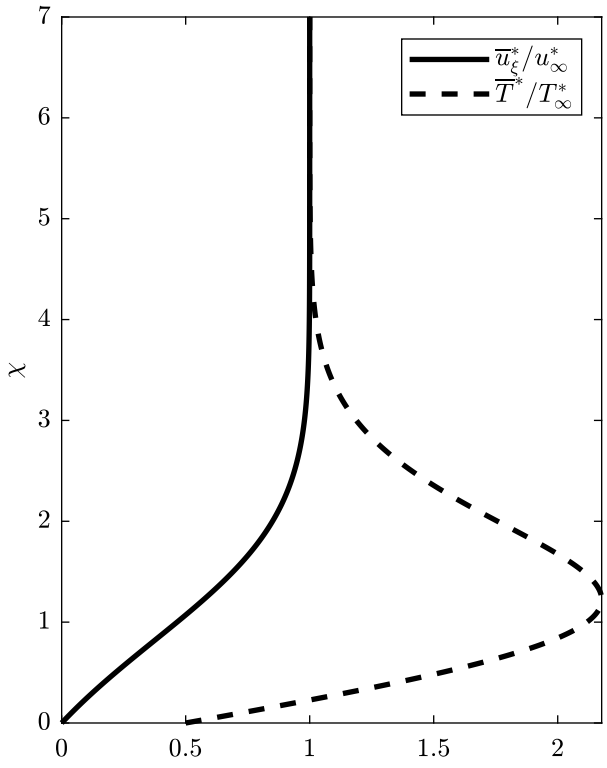

Figure 2.3: Self-similar base flow solutions $\frac{\bar{u}^*_\xi}{u^*_\infty}$ and $\frac{\bar{T}^*}{T^*_\infty}$ for Case 2.

The computational domain is summarized in Table 2.4 where ξ and η coincide with the global x and y axes with its origin placed at the plate leading edge.

Table 2.3: Highly cooled flat-plate flow parameters from Chuvakhov and Fedorov (2016). Note that $L^* = 0.0382$ m.

M_∞	T^*_∞ [K]	T^*_w [K]	p^*_∞ [kPa]	$Re = \frac{\rho^*_\infty u^*_\infty L^*}{\mu^*_\infty}$
6.0	300	150	20	10^6

Table 2.4: Computational domain used for highly cooled flat-plate stability analyses.

F	ξ^*_{min} [m]	ξ^*_{max} [m]	η^*_{min} [m]	η^*_{max} [m]	N_ξ	N_η
$1.3124 \cdot 10^{-4}$	0.0956	0.2677	0.0	0.0574	8000	1000
$2.0590 \cdot 10^{-4}$	0.0388	0.1721	0.0	0.0367	8000	1000

The self-similar base flow solutions for $\frac{\bar{u}^*_\xi}{u^*_\infty}$ and $\frac{\bar{T}^*}{T^*_\infty}$ are presented in Fig. 2.3. The similarity variable χ is the same as the adiabatic flat-plate case.

2.3.1.3 Isothermal sharp cone

The third case we consider is an axisymmetric 7-deg half-angle sharp cone (Sousa et al., 2019) with the flow parameters based on tests performed by Wagner (2014) in the DLR High Enthalpy Shock Tunnel Göttingen (HEG) and given in Table 2.5. An inviscid solution of the base flow was first determined by solving the Taylor-Maccoll ODE (Taylor and Maccoll, 1933) using a modified MATLAB code from Lassaline, J. V. (2009). Thereafter, the compressible Blasius boundary layer was computed by applying the Mangler transformation (Mangler, 1948) for axisymmetric flows (Lees, 1956). Note that $Pr = 0.704$ for this case and although not explicitly mentioned in Sousa et al. (2019), γ was assumed to be 1.4 and the viscosity is chosen by satisfying Sutherland's law (Eq. 2.33) with $Re^*_e = 5.69 \times 10^6$ m^{-1}. The computational domain is summarized in Table 2.6 in which the ξ and η axes originate from the cone nose.

Table 2.5: Sharp-cone flow parameters from Sousa et al. (2019).

M_∞	T^*_∞ [K]	T^*_w [K]	p^*_∞ [Pa]	Re^*_∞ [1/m]	f^* [kHz]
7.4	268	300	2129	4.06×10^6	550

Table 2.6: Computational domain used for sharp-cone stability analyses.

ξ^*_{min} [m]	ξ^*_{max} [m]	η^*_{min} [m]	η^*_{max} [m]	N_ξ	N_η
0.14	0.95	0.0	0.0186	8294	400

The self-similar base flow solutions for $\frac{\bar{u}^*_\xi}{u^*_e}$ and $\frac{\bar{T}^*}{T^*_e}$ are presented in Fig. 2.4. The similarity variable χ is defined as

$$\chi = \sqrt{\frac{3u^*_e\rho^*_e}{2\mu^*_e\xi^*}} \int_0^{\eta^*} \frac{\rho^*}{\rho^*_e} d\eta^*. \tag{2.36}$$

2.3.1.4 HIFiRE-5 elliptic cone

The final validation case is a 38.1% scale model of the HIFiRE-5 elliptic cone with an axial length of 38.1 mm and an aspect ratio of 2:1 at the tip. The cone half-angles are 7.00 and 13.797 degrees along the minor (centerline) and major (attachment line) axes, respectively. The base flow is provided by The Boeing Company with the free-stream parameters summarized in Table 2.7. We focus our study on the centerline,

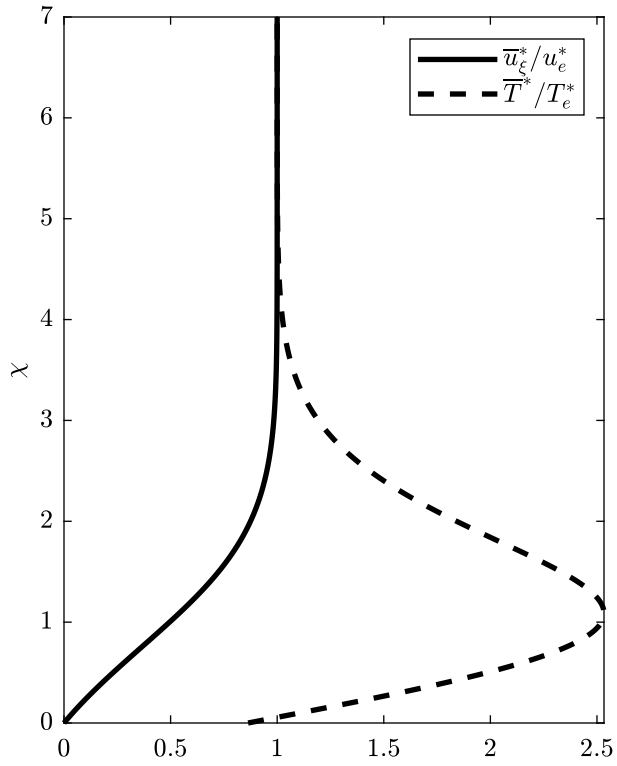

Figure 2.4: Self-similar base flow solutions $\frac{\overline{u}^*_\xi}{u^*_e}$ and $\frac{\overline{T}^*}{T^*_e}$ for Case 3.

and for validation purposes treat the flow and disturbances there as locally two-dimensional and compare with solutions found using LASTRAC (Chang, 2004). The streamwise computational domain varies slightly depending on the frequency analyzed and is summarized in Table 2.8. For all LST computations, we have $N_\xi \times N_\eta = 100 \times 600$ and for the OWNS computations we have $N_\xi \times N_\eta = 5000 \times 600$. The origin of the curvilinear coordinates correspond to $x^* = 8.364 \cdot 10^{-4}$ m and $y^* = 9.454 \cdot 10^{-4}$ m (global x and y axes originate from the cone nose).

Table 2.7: HIFiRE-5 flow parameters.

M_∞	T^*_∞ [K]	T^*_w [K]	p^*_∞ [Pa]	Re^*_∞ [1/m]
6.0	49.45	315	417.315	8.1×10^6

Table 2.8: Computational domain used for HIFiRE-5 stability analyses.

f^* [kHz]	ξ^*_{min} [m]	ξ^*_{max} [m]
60	0.101	0.305
70	0.0807	0.305
80	0.0652	0.305

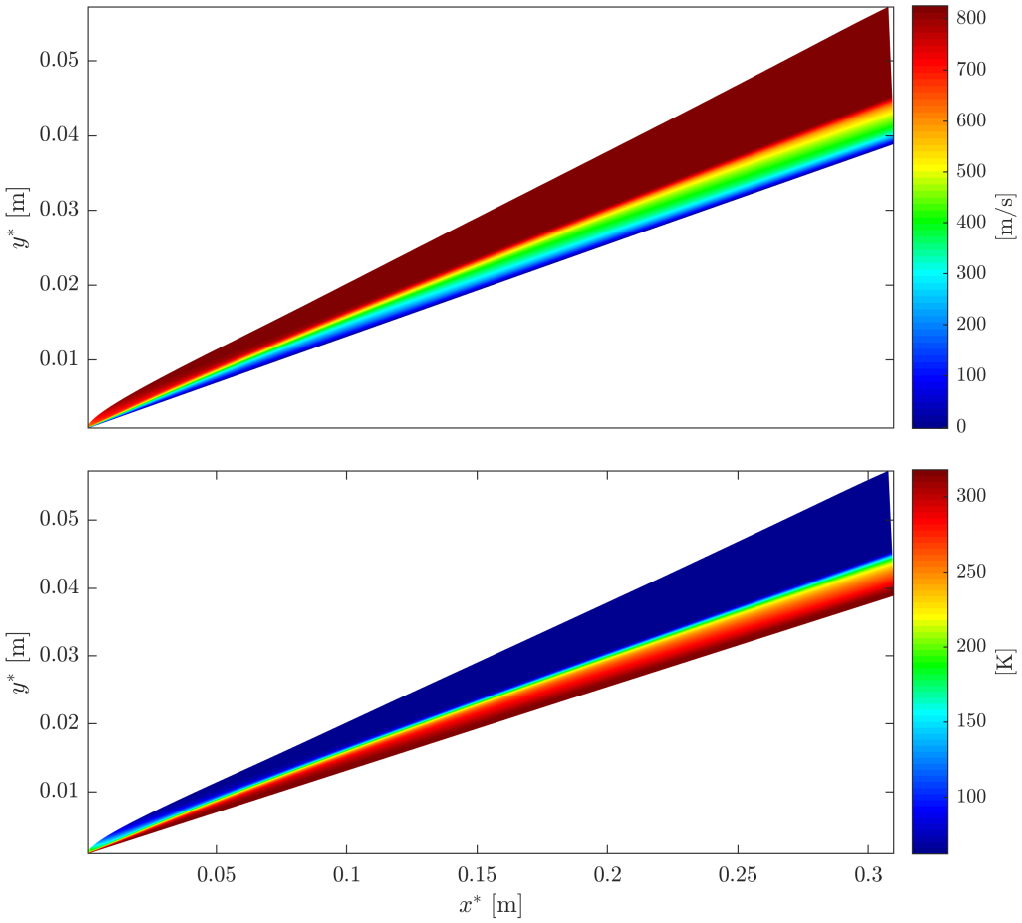

Figure 2.5: DNS-computed centerline base flow solutions $\bar{u}_x^*$ (top) and $\overline{T}^*$ (bottom) from The Boeing Company for Case 4.

Contour plots of $\bar{u}_x^*$ and $\overline{T}^*$ acquired from The Boeing Company along the centerline of the HIFiRE-5 elliptic cone are shown in Fig. 2.5.

2.3.2 Boundary conditions

No-slip boundary conditions ($u' = v' = 0$) are imposed at the wall along with $T' = 0$. The latter condition is enforced because Mack (1984) and Malik (1990) argued that for high-frequency disturbances, the thermal inertia of the body will preclude temperature perturbations from penetrating deep into the solid boundary. Thus, at the wall, we solve the continuity and linearized equation of state for p' and v'. At the upper boundary, we impose 1D inviscid Thompson characteristic boundary conditions (Thompson, 1987) to prevent spurious numerical reflections. The inviscid assumption is valid at the upper boundary since viscous effects from the boundary layer are negligible in this region. The OWNS marches are initialized with

the right-going component of eigenfunctions from quasi-parallel LST corresponding to a specific mode at the inlet.

2.3.3 Results

2.3.3.1 Adiabatic flat plate

We initialize the OWNS march at the inlet with the first mode, i.e. Mode S, with $N_b = 20$. Here, Mode S denotes the discrete mode originating from the slow continuous spectrum, whereas Mode F1, F2, F3, etc. are the sequential discrete modes emanating from the fast acoustic branch (refer to Knisely and Zhong (2019b) for more details regarding the discrete-mode classifications). Figs. 2.6 and 2.7 compare the wavenumber α_r, the disturbance growth rate α_i, and the wall-pressure perturbations $|p'_w|$ from OWNS and DNS at $F = 2.2 \cdot 10^{-4}$. The wavenumber and growth rate are defined as Ma and Zhong (2003a)

$$\alpha_r = \frac{d|p'_{w_\theta}|}{d\xi}, \tag{2.37}$$

$$\alpha_i = -\frac{1}{|p'_w|}\frac{d|p'_w|}{d\xi}, \tag{2.38}$$

where p'_{w_θ} is the phase angle of the wall-pressure perturbation. Note that if multiple modes are present, we will observe the modulated effect of these waves in α_r and α_i.

When the unstable Mode S is initialized at $\xi^* = 0.025$ m, there is also the presence of the stable Mode F1 causing the small oscillation in growth rate. Although it cannot be observed in Figs. 2.6 or 2.7, LST results from Ma and Zhong (2003a) indicate synchronization of these two modes at $\xi^* \approx 0.098$ m, in which then Mode S becomes the canonical second Mack mode due to resonant interactions with the stable Mode F1. This resonance continues until $\xi^* \approx 0.142$ m which is the neutral stability point of the second mode after which the wall-pressure perturbations decay rapidly to zero. The oscillation in growth rate after the neutral stability point is due to the presence of the now stable second mode, Mode F1, and other higher-order fast acoustic modes. Overall, we observe excellent agreement between OWNS and DNS in the wall-pressure distribution and streamwise wavenumber. Although there are small discrepancies in the growth rates, both methods yielded a second-mode neutral stability point of $\xi^* \approx 0.142$ m.

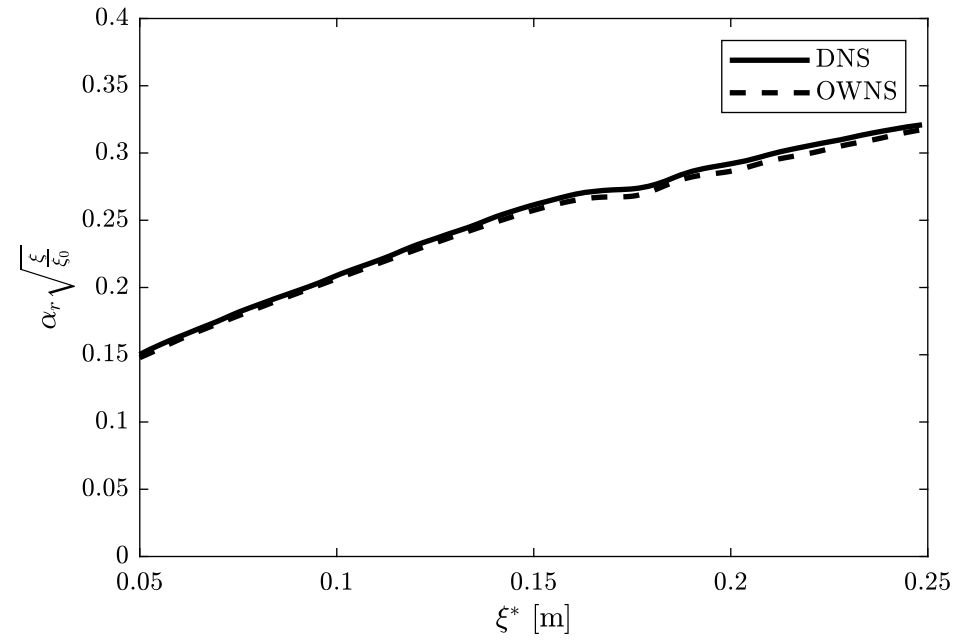

(a) Scaled streamwise wavenumber $\alpha_r\sqrt{\frac{\xi}{\xi_0}}$.

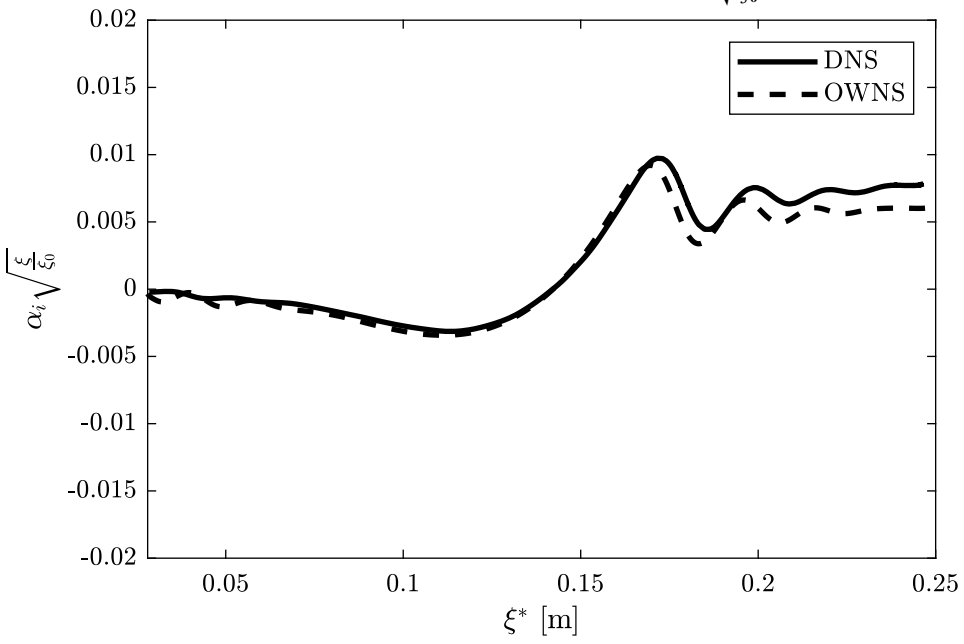

(b) Scaled growth rate $\alpha_i\sqrt{\frac{\xi}{\xi_0}}$.

Figure 2.6: Streamwise wavenumber (a) and growth rate (b) between OWNS and DNS (Ma and Zhong, 2003a) when Mode S is initialized at the inlet.

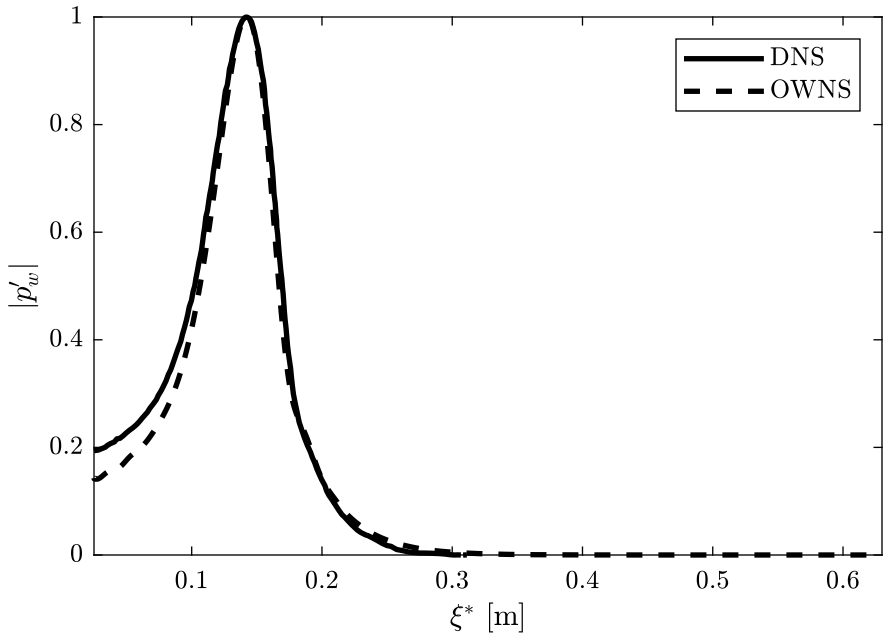

Figure 2.7: Wall-pressure perturbations from DNS (Ma and Zhong, 2003a) and OWNS with arbitrary linear scale applied.

2.3.3.2 Highly cooled (isothermal) flat plate

To compare results with Chuvakhov and Fedorov (2016), we non-dimensionalize ξ^* and η^* with $L^* = 0.0382$ m, i.e. the distance from the plate leading edge. We will first study the low-frequency (LF) wave train at $F = 1.3124 \cdot 10^{-4}$ which corresponds to Mode F1 originating from the branch point $c_F = M_\infty + 1$ of the fast acoustic waves. We thus initialize the OWNS march with this mode at the inlet with $N_b = 20$. Fig. 2.8 shows the wall-pressure distribution and the pressure disturbance field computed with OWNS. In accordance to LST from Chuvakhov and Fedorov (2016), the inlet disturbances grow exponentially in the boundary layer until $\xi_k \approx 4.5$ where the second mode begins to synchronize with the slow acoustic branch. At this point, a new discrete stable mode is also formed. From $4.5 < \xi < 5.6$, the second mode radiates slow acoustic waves and generates the outer acoustic field seen in Fig. 2.8. At $\xi_s \approx 5.6$, the second mode coalesces with the slow acoustic branch. We note that the spontaneous radiation of sound is localized to this region (Chuvakhov and Fedorov, 2016). The complex pattern observed below the main beam is attributed to interactions between monochromatic waves having different amplitudes and front angles (Chuvakhov and Fedorov, 2016). Referring to Fig. 8 from Chuvakhov and Fedorov (2016), there is excellent agreement between DNS and OWNS which demonstrates OWNS' capability of accurately capturing the complete

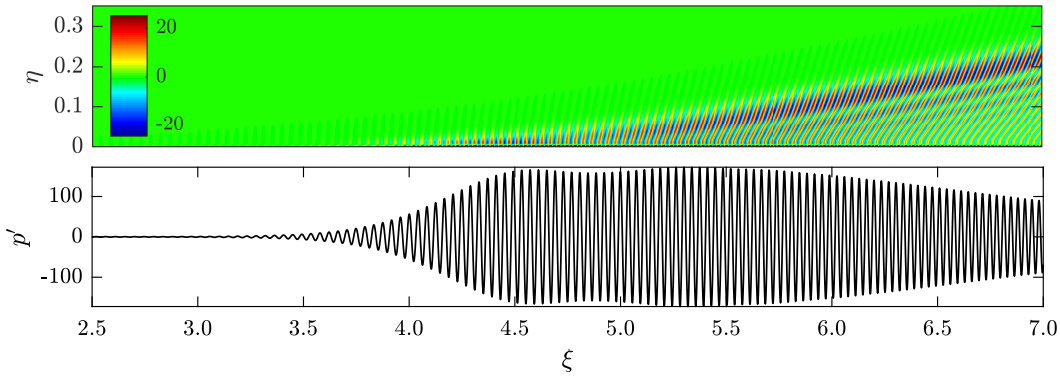

(a) Pressure disturbance field (top) and wall-pressure distribution (bottom).

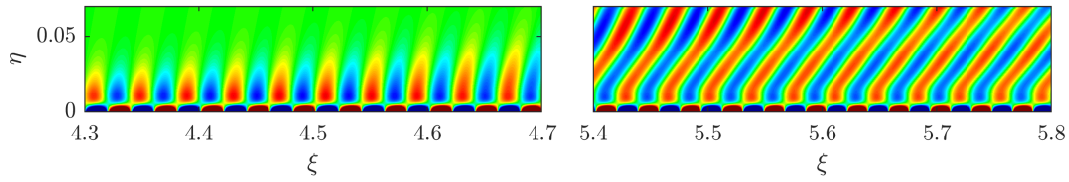

(b) Start of synchronization region at $\xi_k \approx 4.5$ (left) and point of coalescence at $\xi_s \approx 5.6$ (right).

Figure 2.8: OWNS results for LF wave train at $F = 1.3124 \cdot 10^{-4}$ for highly cooled flat plate. Pressure disturbance field and wall-pressure distribution (a) and close-up of start of synchronization region and point of coalescence (b).

disturbance evolution at a fraction of the cost of DNS.

We now study the high-frequency (HF) wave train at $F = 2.0590 \cdot 10^{-4}$ which corresponds to the mode originating near the branch point $c_S = M_\infty - 1$ of the slow acoustic waves. The OWNS march is therefore initialized with this mode at the inlet with $N_b = 20$. Fig. 2.9 shows the wall-pressure distribution and the pressure disturbance field calculated using OWNS. LST results from Chuvakhov and Fedorov (2016) indicate that this mode becomes unstable as it propagates downstream before becoming stable and having its phase speed drop below c_S. In contrast to the LF case, the second mode does not coalesce with the slow acoustic branch but is in close proximity before becoming stable. In the vicinity of c_S, the second mode radiates slow acoustic waves at $\xi_s \approx 1.9$ as observed in Fig. 2.9. However, the outer acoustic field is much narrower and weaker than the LF case which is corroborated with LST and DNS findings of Chuvakhov and Fedorov (2016). Below the main beam, the acoustic pattern is emblematic of slow acoustic waves being radiated by a stationary local harmonic source which is hypothesized to occur due to the spatial inhomogeneity of the region near $\xi_s \approx 1.9$ (Chuvakhov and Fedorov, 2016). Referring to Fig. 11 from Chuvakhov and Fedorov (2016), we again observe excellent

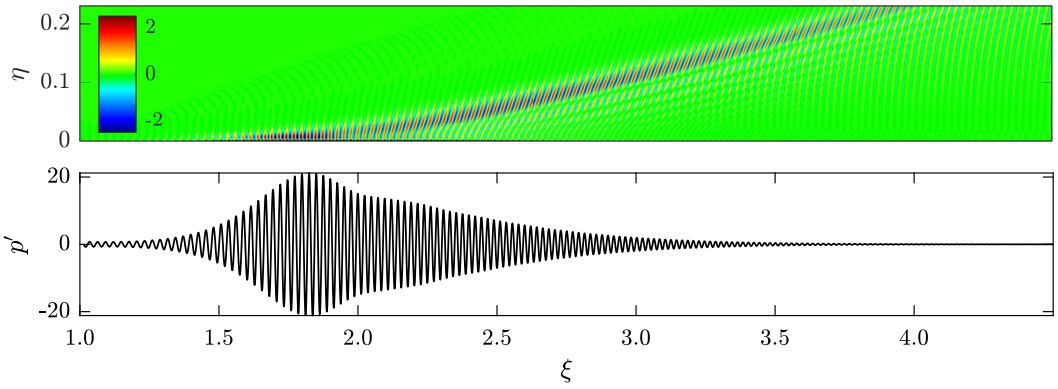

(a) Pressure disturbance field (top) and wall-pressure distribution (bottom).

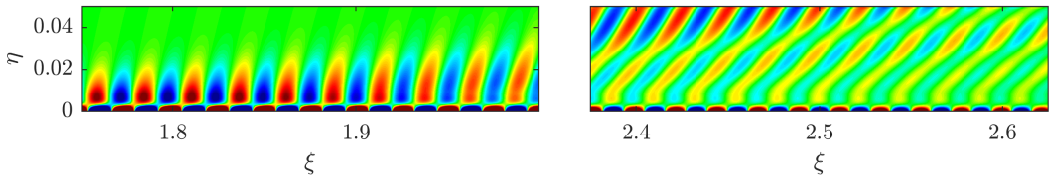

(b) Start of spontaneous acoustic radiation at $\xi_s \approx 1.9$ (left) and downstream region (right).

Figure 2.9: OWNS results for HF wave train at $F = 2.0590 \cdot 10^{-4}$ for highly cooled flat plate. Pressure disturbance field and wall-pressure distribution (a) and close-up of when the second mode begins to radiate slow acoustic waves at $\xi_s \approx 1.9$ and downstream region (b).

agreement between DNS and OWNS.

2.3.3.3 Isothermal sharp cone

We first initialize the OWNS march with Mode S at the inlet with $N_b = 12$. Wall-pressure perturbations from OWNS and DNS (Sousa et al., 2019) at the conditions prescribed in Table 2.5 are compared in Fig. 2.10.

Overall, we see excellent agreement between the OWNS and DNS wall-pressure signal. Although not apparent from Fig. 2.10, LST results indicate that the unstable Mode S (first mode) synchronizes with the stable Mode F1 at $\xi^* \approx 0.323$ m and the former becomes the second Mack mode. At $\xi^* \approx 0.447$ m, the second mode reaches its neutral stability point and the resonant interactions with Mode F1 cease and the wall-pressure disturbances decay rapidly. However, we observe a kink in the wall-pressure profile during the decay. To understand why this occurs, we must gain a better insight into how the modes interact spatially, and thus we plot the specific volume disturbance field in Fig. 2.11.

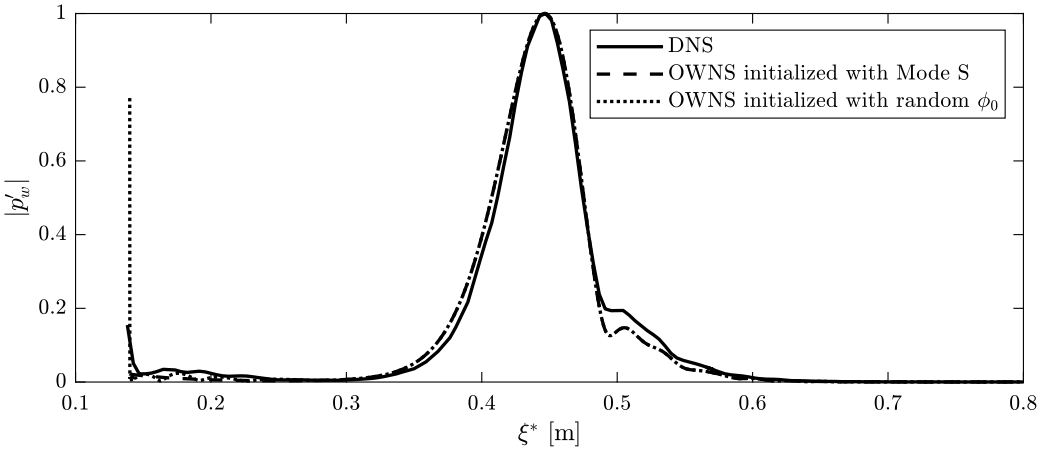

Figure 2.10: Wall-pressure perturbations between OWNS and DNS (Sousa et al., 2019) with different initial conditions at $Re^*_\infty = 4.06\times10^6$ m^{-1} and $f^* = 550$ kHz. Arbitrary linear scale applied.

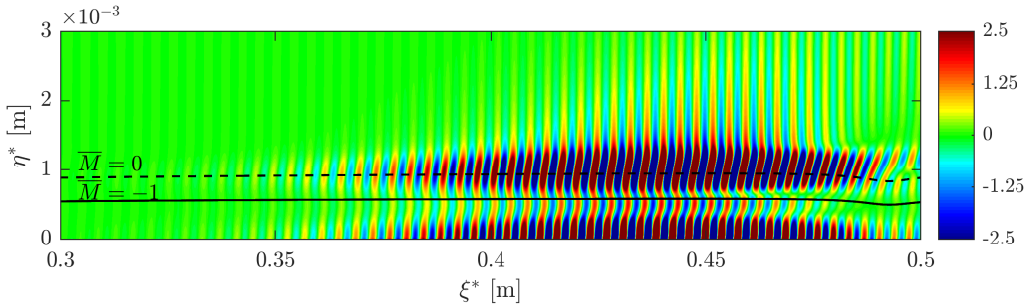

(a) Second mode

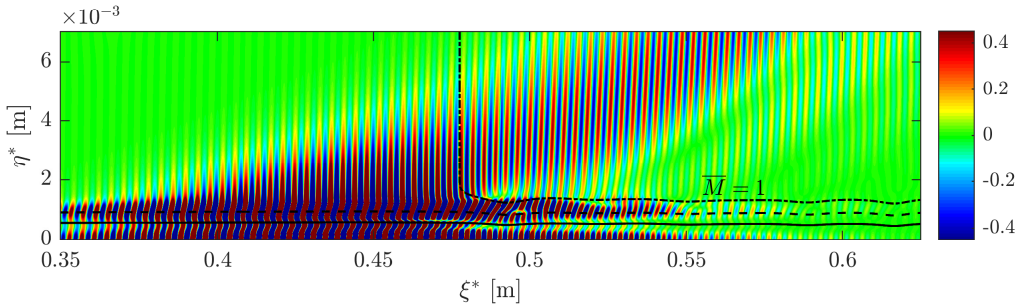

(b) Supersonic mode

Figure 2.11: Specific volume perturbations from OWNS showing the second mode (top) and the supersonic mode appearing further downstream (bottom) at $Re^*_\infty = 4.06\times10^6$ m^{-1} and $f^* = 550$ kHz with Mode S initialized at the inlet.

To understand the instabilities present in Fig. 2.11, we first define the relative Mach number

$$\overline{M}(\eta) = \frac{\bar{u}_\xi(\eta) - c_r}{\bar{a}(\eta)}. \tag{2.39}$$

Note that we use Eq. 2.37 and Eq. 2.38 in determining α_r and α_i, respectively, such that

$$c_r = \mathscr{R}\left(\frac{\omega}{\alpha_r + i\alpha_i}\right). \tag{2.40}$$

Typical of the second Mack mode, we see amplification of acoustic waves trapped between the wall and relative sonic line $\overline{M}(\eta_s) = -1$. In this region, disturbances travel supersonically downstream relative to the local mean flow. Outside this region, for $\overline{M} > -1$, the disturbances travel subsonically relative to the free-stream and thus we observe the subsonic "rope-like" structures centered about the critical layer $\overline{M}(\eta_c) = 0$. However, due to substantial wall-cooling ($T_w/T_e = 0.864$), there is an additional mode—the supersonic mode—which appears at $\xi^* \approx 0.477$ m, causing the modulation of the wall-pressure signal seen in Fig. 2.10, a phenomenon also observed by Chuvakhov and Fedorov (2016). This mode occurs when the phase speed of the disturbances in the free-stream is slow enough such that they travel supersonically *upstream* relative to the free-stream ($\overline{M} > 1$) and creates an acoustic radiation from the boundary layer (Knisely and Zhong, 2019b) (this was also observed for the highly cooled flat-plate case). This acoustic emission eventually decays as Mach waves in the free-stream. This validation case serves to illustrate how OWNS is once again capable of accurately modeling complex multi-modal instabilities.

Following the discussion from Sec. 1, one of the major disadvantages of using PSE is that it is only suited to track a dominant mode of a desired wavenumber. However, it is often desirable to perform unsteady calculations initialized with random perturbations such that the base flow dictates the unstable modes that appear. The normal-mode ansatz that PSE is based upon precludes such analyses. OWNS, however, is capable of tracking downstream-propagating modes that form from arbitrary initial conditions. We illustrate this by initializing the same stability calculation but with a normally distributed random $\boldsymbol{\phi_0}$ within the boundary layer and homogeneous conditions in the free-stream. The wall-pressure signal from this analysis is once again compared to DNS in Fig. 2.10 (note that there is significant overlap to the wall-pressure signal with Mode S initialization). After the initial transients, we observe excellent agreement to the DNS data with the appearance of

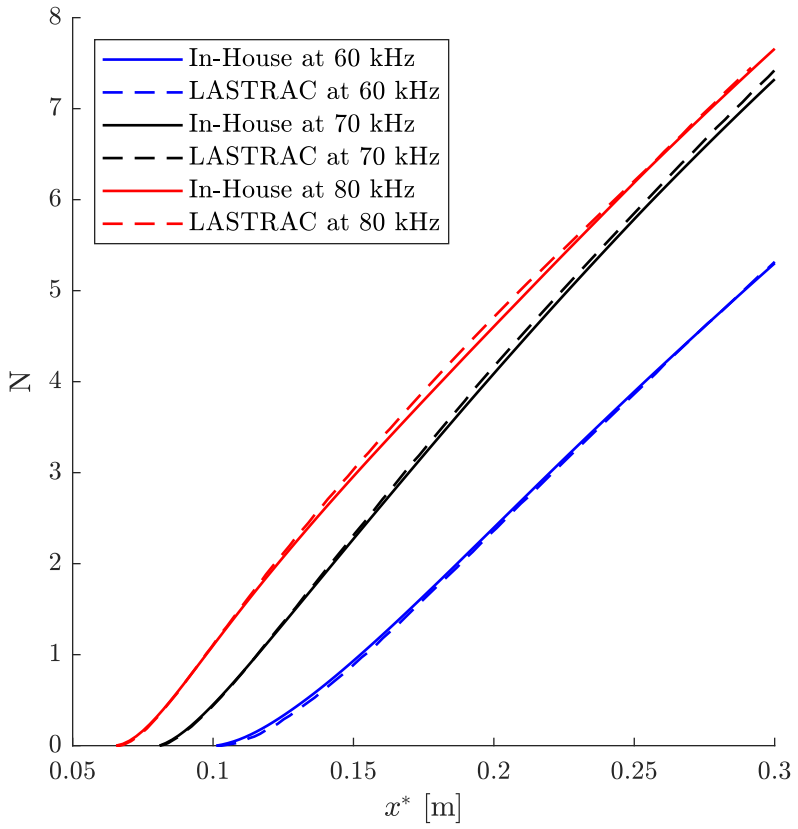

Figure 2.12: N-factors along the HIFiRE-5 centerline computed with our In-House LST code CSTAT versus LASTRAC for $f^* = 60$, 70, and 80 kHz.

the second mode, thus demonstrating the versatility of using OWNS in marching an arbitrary initial condition.

2.3.3.4 HIFiRE-5 elliptic cone

We first validate the linear operator $\boldsymbol{L}$ from Eq. 2.13 (assuming $\boldsymbol{f_\phi} = \boldsymbol{f_{\xi,vis}} = 0$ as usual) by comparing LST N-factors from CSTAT versus those from LASTRAC (Chang, 2004). Fig. 2.12 shows the comparison at $f^* = 60$, 70, and 80 kHz in which the N-factor is defined as

$$N_{LST} = -\int_{\xi_0}^{\xi} \alpha_i(\xi')\, d\xi'. \tag{2.41}$$

We see excellent agreement in the LST N-factors between CSTAT and LASTRAC. Thus, PSE and OWNS computations are performed for the same frequency range in which the second mode is used as the inlet boundary condition with $N_b = 15$ for OWNS. We compare the N-factors from OWNS, PSE, and LST in Fig. 2.13 where

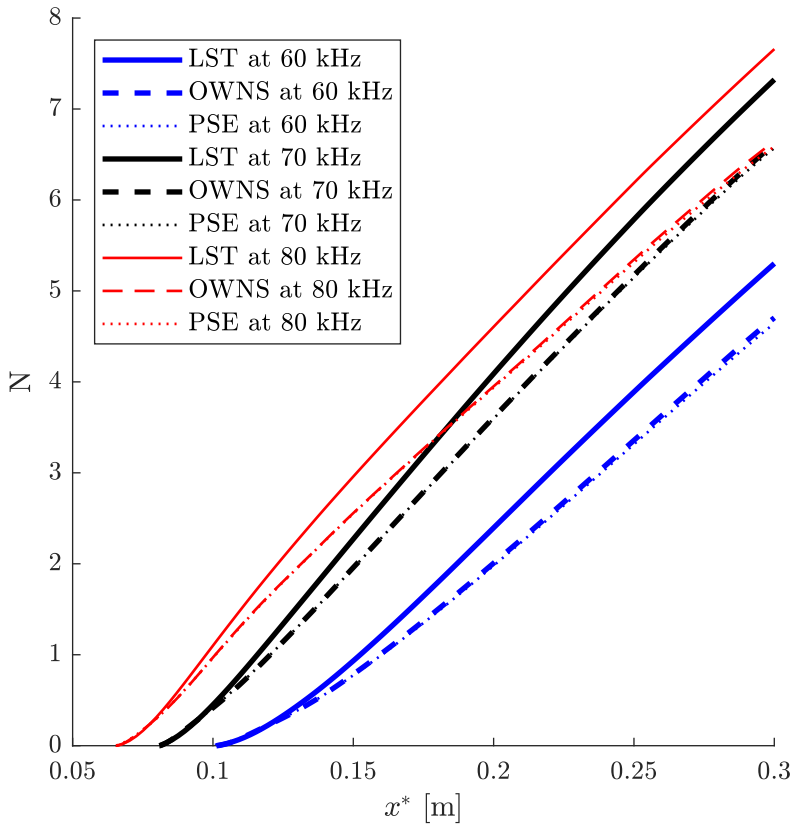

Figure 2.13: Comparing the N-factor along the HIFiRE-5 centerline between LST, OWNS, and PSE for $f^* = 60$, 70, and 80 kHz.

the N-factor for OWNS and PSE is defined as

$$N_{PSE/OWNS} = \ln\left(\frac{|p'_w|}{|p'_{w_0}|}\right). \tag{2.42}$$

From Fig. 2.13, we see that for all frequencies, locally removing the parallel mean-flow assumption that is used in LST but not in OWNS/PSE stabilizes the second mode along the centerline. This is most likely due to the unusually large $\bar{u}_\eta$ from the primary vortex roll-up advecting the perturbation energy upwards and away from the wall. To understand why PSE and OWNS performed almost identically, we visualize the disturbance field by plotting the specific volume perturbations at $f^* = 80$ kHz in Fig. 2.14.

Unlike validation Cases 2 and 3 where we witnessed complex multi-modal interactions, we do not observe any similar physics in Fig. 2.14. The presence of one dominant instability is likely why PSE performed on par with OWNS. However, the peak amplitudes of the perturbations are separated by regions of high shear in the base flow (refer to Fig. 2.5). This is contrary to typical second-mode wave

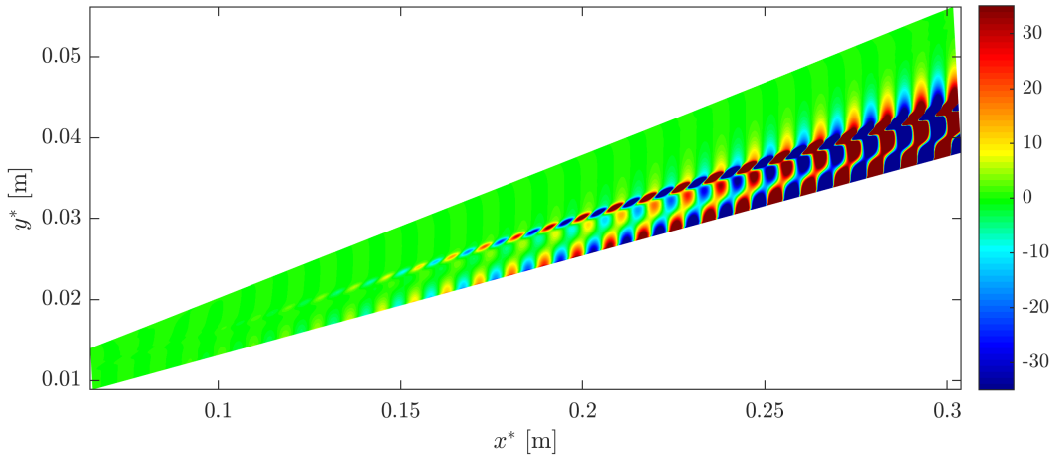

Figure 2.14: Specific volume disturbance field from OWNS along the centerline of the HIFiRE-5 elliptic cone for $f^* = 80$ kHz.

structure as seen in validation Case 3 and alludes to potentially additional unstable modes not revealed under a strictly two-dimensional analysis. In fact, the presence of such complex mode shapes along a plane of symmetry may indicate that a fully three-dimensional stability calculation is required to accurately track the disturbance evolution (this is somewhat expected since the primary vortex roll-up near the leeward line induces strong spanwise variations (Li et al., 2012)).

2.3.4 Summary

To recapitulate, we derived the OWNS DAE for both the outflow and projection approaches corresponding to the homogeneous and inhomogeneous stability problems, respectively, and presented the algorithm for computing the recursion parameters for jets and boundary layers across all speed regimes. We thereafter extended the original methodology by using a non-orthogonal, curvilinear coordinate system with full compressibility effects. We validated the generalization by comparing to DNS data for flat plates and a sharp cone, and to LST results for local disturbances on the centerline of the HIFiRE-5 elliptic cone (all in 2D). OWNS provided DNS-quality results for the former flows at a small fraction of the computational expense. In the next chapter, we extend the application of OWNS to 3D flows, i.e. flows exhibiting inhomogeneity in two or three spatial coordinates, to demonstrate its capability of accurately tracking 3D instabilities.

Chapter 3

APPLICATION OF OWNS TO COMPLEX 3D FLOWS

In this chapter, we use the generalized OWNS technique from Sec. 2 to analyze 3D instabilities on a Mach 6 finned-cone geometry and a Mach 1.5 axisymmetric turbulent jet. For the former flow, we leverage OWNS's ability to march downstream with an arbitrary inlet condition in the form of a spatially randomized inlet forcing to excite all possible instability mechanisms (both modal and non-modal). This obviates the trial-and-error approach needed for PSE, which is also restricted to only modal instabilities. The OWNS results suggest there exists no significant (linear) amplification mechanisms beyond the dominant vortex mode. Finally, the jet case is used to validate the generalized curvilinear implementation of the centerline treatment from Sec. B.1.2.

3.1 Mach 6 finned-cone geometry

We first study the stability characteristics of a complex 3D 7° half-angle finned-cone geometry with a 1 mm nose radius and a fin with 0.125 in leading-edge radius and 75° sweep angle, as depicted in Fig. 3.1. The geometry was designed to experimentally study boundary-layer transition in the Boeing/AFOSR Mach-6 Quiet Tunnel at Purdue University (BAM6QT) with details found in Turbeville and Schneider (2018), Turbeville and Schneider (2019), and Turbeville and Schneider (2021). The addition of the fin provides basic control mechanisms for high-speed flight vehicles, but also a shock-wave-boundary-layer interaction (SWBLI) on the cone surface due to the fin shock in addition to three-dimensional streamwise-aligned corner flow at the fin-cone junction. Previous stability analyses (Knutson, GS, and Candler, 2018b; Knutson, GS, and Candler, 2018a; Knutson, Brock, and Candler, 2021; Mullen, Moyes, et al., 2018; Mullen, Turbeville, et al., 2019; Mullen, Moyes, et al., 2019; McMillan, Mullen, and Reed, 2021; Riha, McMillan, and Reed, 2021) have demonstrated the importance of these streamwise-aligned laminar vortices in predicting transition on the cone surface. This motivates the application of OWNS with its unique attributes in analyzing such a complex flow field. We will also perform similar calculations using PSE for a comparison basis. Note that results in this section correspond to the author's contribution to the AIAA journal article being submitted from the original AIAA AVIATION manuscript (Araya et al., 2022).

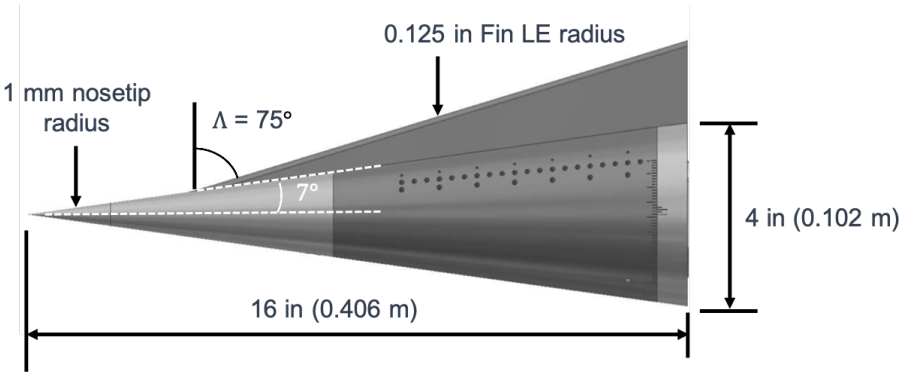

Figure 3.1: Schematic diagram of the Purdue finned-cone wind-tunnel model utillized. Figure from Araya et al. (2022).

3.1.1 Computational setup

The 3D base flow is computed by the Applied Physics Lab (APL) at Johns Hopkins University using the inflow conditions from recent experiments at BAM6QT (Turbeville and Schneider, 2021). These parameters are summarized in Table 3.1. Note that for this section, dimensional quantities are only denoted with their respective dimensions with asterisks omitted for simplicity.

Table 3.1: Base-flow parameters corresponding to inflow conditions from the BAM6QT experiments.

Re_m [m^{-1}]	u_∞ [m/s]	T_∞ [K]	p_∞ [Pa]	T_w [K]
8.4×10^6	865.52	51.78	482.10	309.5

The laminar vortices arising from the SWBLIs situated at the fin and cone surfaces are shown in Fig. 3.2. The goal of the present analyses is to evaluate the importance of the vortex situated on the cone surface for transition, and thus a partitioned domain is used for the stability calculations. The corresponding stability domain acquired from APL is schematically displayed in Fig. 3.3.

All computations are performed at a single frequency at $f = 250$ kHz, which was found to maximally amplify the dominant vortex-mode instability (explained fully in Sec. 3.1.3) by the APL group using PSE calculations. The corresponding stability parameters for the OWNS and PSE marches are summarized in Table 3.2. The cross-stream directions are discretized with fourth-order central finite-difference schemes with summation-by-parts (Mattsson and Nordström, 2004) (SBP) boundary closure. Both the streamwise and spanwise coordinates are uniformly distributed, with grid-

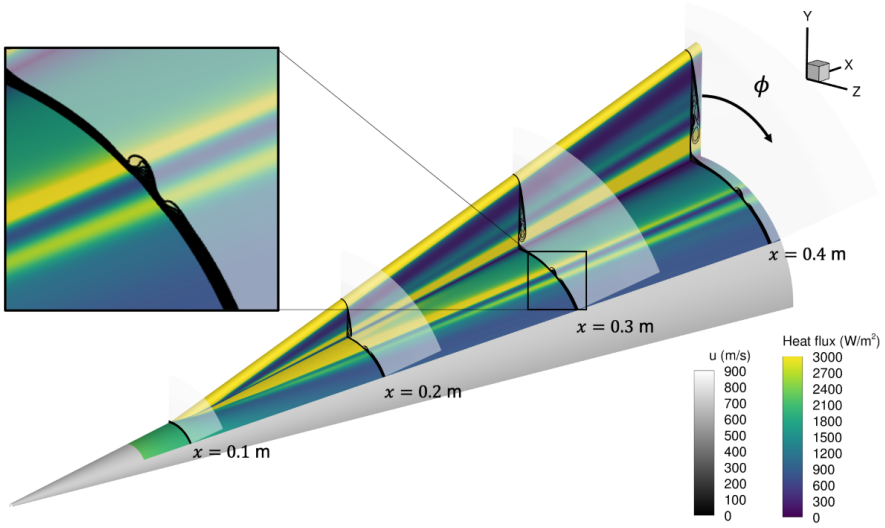

Figure 3.2: Laminar vortices along the fin and cone surfaces due to SWBLIs. The inset in the image corresponds to the domain used for stability calculations. Gray-scale contours correspond to streamwise velocity slices at x = 0.1, 0.2, 0.3, and 0.4 m, whereas colored contours correspond to surface heat flux. Figure from Araya et al. (2022).

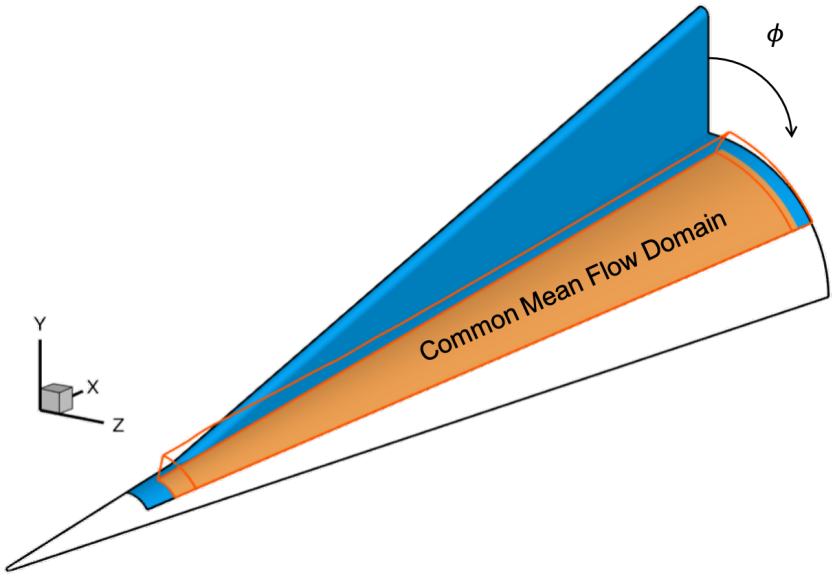

Figure 3.3: Mean-flow domain acquired from APL to be used for stability calculations. Figure from Araya et al. (2022).

stretching in the wall-normal direction (Malik, 1990). The OWNS marches are integrated in the streamwise direction using BDF2.

Due to the increased computational cost of OWNS, the original common base flow from APL is truncated in the spanwise (outboard region) and wall-normal directions to allow the same high cross-stream resolution in both PSE and OWNS. To verify that this has no impact on the dominant vortex-mode growth, the surface N-factors computed using PSE with the original and truncated base flows are shown in Fig. 3.4 where

$$N = \log\left(\frac{|p'_w|}{\max(|p'_w|_{x=0.24\text{ m}})}\right). \tag{3.1}$$

Note that x_{tr} corresponds to the experimental heat-flux based transition onset found to be at $x \approx 0.305$ m. We see that the domain truncation has minimal impact on the overall growth rate, and thus use the truncated domain for all subsequent calculations. However, even with this added efficiency, the OWNS calculations, albeit feasible, still required substantial time and memory (RAM) to invert the DAE matrix at each streamwise station via the lower-upper (LU) decomposition. To circumvent this, we developed a hybrid computational approach in which the LU decomposition was performed on the DAE matrix constructed with second-order cross-stream discretization with reduced-order boundary closure, which significantly increased the sparsity of the matrix and thereby reduced the memory cost. This operation was performed using the Intel® oneAPI Math Kernel Library PARDISO package (Schenk and Gärtner, 2004) to parallelize the LU decomposition. The inverted system and corresponding solution then served as a preconditioner matrix and guess, respectively, for solving the full linear system (see above for the numerics) using the generalized minimum residual (iterative) method from MATLAB. This hybrid approach reduced the total computational time by $\approx 50\%$ at each streamwise station.

Table 3.2: Computational setup of PSE and OWNS marches at f = 250 kHz.

Solver	IC	N_ξ	N_η	N_ζ	N_b	x_{min} [m]	x_{max} [m]
PSE	SBG	627	225	301	-	0.09	0.40
OWNS	SBG	2001	225	301	10	0.09	0.40
OWNS	Random	1232	225	301	10	0.09	0.28

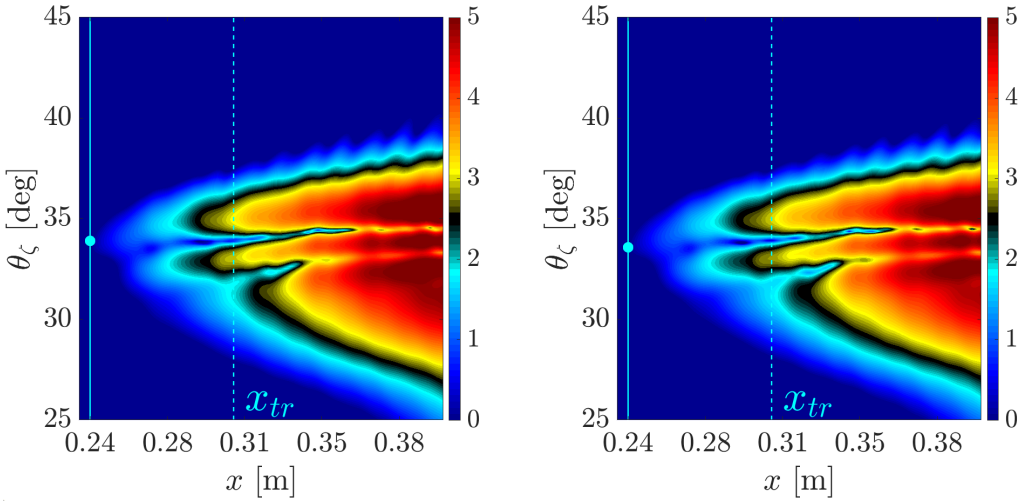

Figure 3.4: Surface N-factors computed with PSE from original (a) and truncated (b) base flows at f = 250 kHz. The cyan circle along the solid vertical line at x = 0.24 m, which was the second location of the experimental PCB sensor, represents the local maximum pressure used for the N-factor normalization. The dashed line is the experimental heat-flux based transition onset x_{tr}.

3.1.2 Boundary conditions

The PSE and one of two separate OWNS calculations are initialized using (the same) spatial BiGlobal (SBG) eigenfunction, whereas the second OWNS computation is initialized using randomized inlet forcing, i.e. forcing of each state variable at every grid point randomly drawn from a normal distribution. This is done to excite all wavenumbers at a given frequency and to trigger the gamut of potential instability mechanisms. No-slip and isothermal boundary conditions are imposed at the wall ($u' = v' = w' = T' = 0$), and thus we solve the linearized continuity equation for ρ'. At the upper boundary, we impose 1D inviscid Thompson characteristic boundary conditions (Thompson, 1987). Lastly, we enforce spanwise symmetry boundary conditions.

3.1.3 Results

3.1.3.1 Randomized forcing vs. SBG initialization at f = 250 kHz

One of the major advantages of OWNS is the ability to initialize the march with an arbitrary initial condition, which allows excitation of all instability mechanisms. This is particularly useful for complex flow configurations, such as the current study, where the dominant mode may not be known apriori or where multi-modal

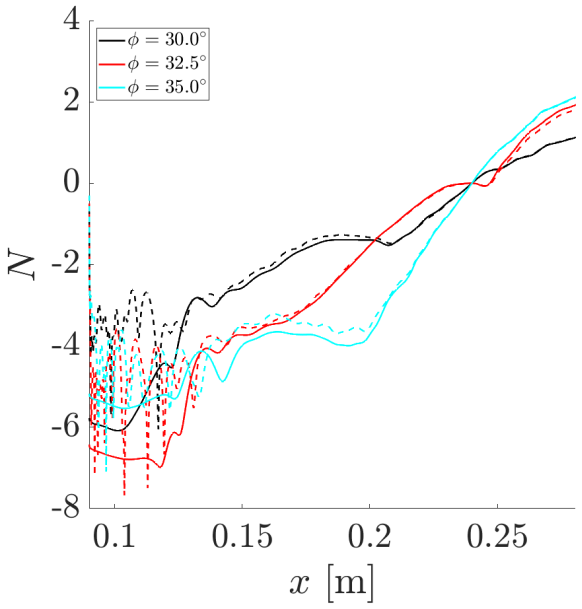

Figure 3.5: Surface N-factors computed using OWNS along prescribed azimuthal rays with randomized inlet forcing (dashed lines) and a SBG inlet boundary condition (solid lines) at f = 250 kHz.

or non-modal effects may be present. Thus, we perform two OWNS computations initialized with a SBG inlet boundary condition and randomized forcing.

We first evaluate the N-factor along azimuthal rays of $\phi = 30.0°$, $32.5°$, and $35.0°$ between the two different initializations in Fig. 3.5. Note that N is computed similarly to Eq. 3.1, but is normalized with the wall-pressure amplitude at $x = 0.24$ m along the selected azimuthal ray. After the initial transients in the upstream region, both computations converge onto the dominant vortex instability with virtually identical growth rates from $x > 0.2$ m along the three selected azimuths. This would suggest the dominant instability is indeed solely the vortex mode. We further substantiate this by comparing the cross-stream pressure amplitudes and $\mathscr{R}(u')$ in Figs. 3.6 and 3.7, respectively, at three axial positions. Even though the cross-stream profiles vastly differ at the inlet ($x = 0.09$ m), both calculations indicate the initial development of the vortex instability by $x = 0.185$ m with similar pressure amplitudes and wavenumber distribution. At $x = 0.28$ m, both computations depict nearly identical pressure amplitude and wave structures corresponding to the lone growth of the vortex mode. Thus, since both OWNS marches track the same instability from $x = 0.2$ m, the calculation with randomized inlet forcing was stopped at $x = 0.28$ m.

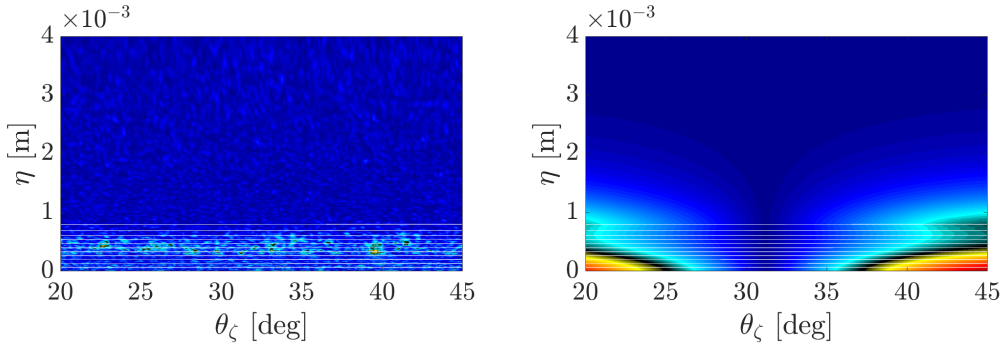

(a) x = 0.09 m

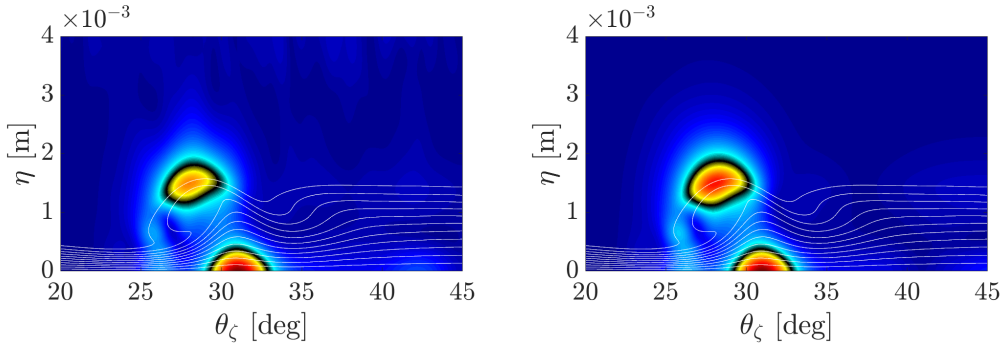

(b) x = 0.185 m

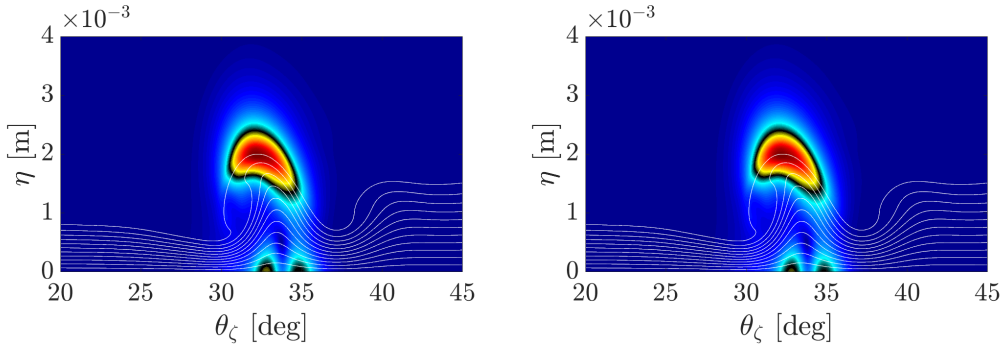

(c) x = 0.28 m

Figure 3.6: Pressure amplitudes computed using OWNS with randomized forcing at the inlet (left) and using a SBG inlet boundary condition (right) at f = 250 kHz. The amplitudes are normalized by the maximum value at each streamwise station such that contour limits blue, black, and red correspond to $0 < |p'| < 1$. The background contour lines correspond to mean streamwise velocity.

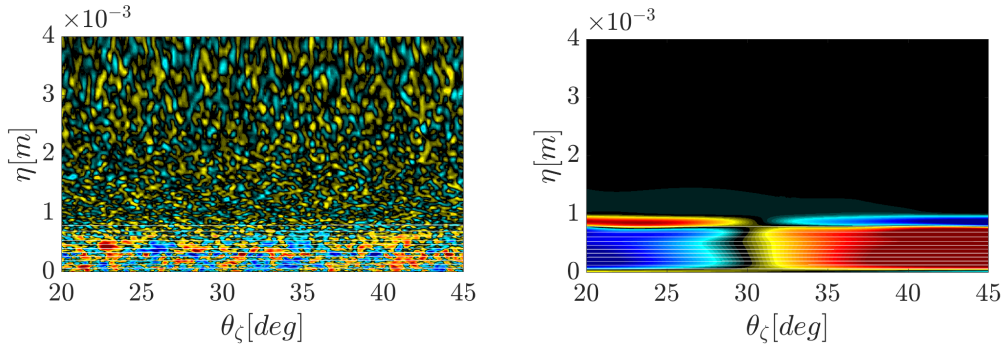

(a) x = 0.09 m

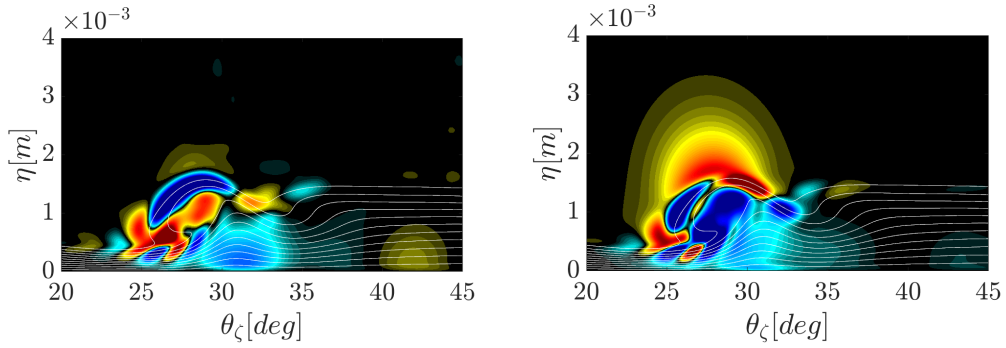

(b) x = 0.185 m

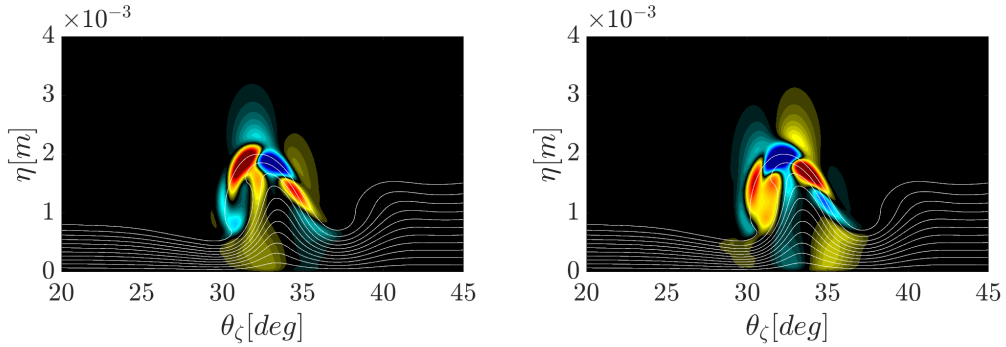

(c) x = 0.28 m

Figure 3.7: $\mathscr{R}(u')$ computed using OWNS with randomized forcing at the inlet (left) and using a SBG inlet boundary condition (right) at f = 250 kHz. All quantities are normalized by the maximum value at each streamwise station such that contour limits blue, black, and red correspond to $-0.5 < \mathscr{R}(u') < 0.5$. The background contour lines correspond to mean streamwise velocity.

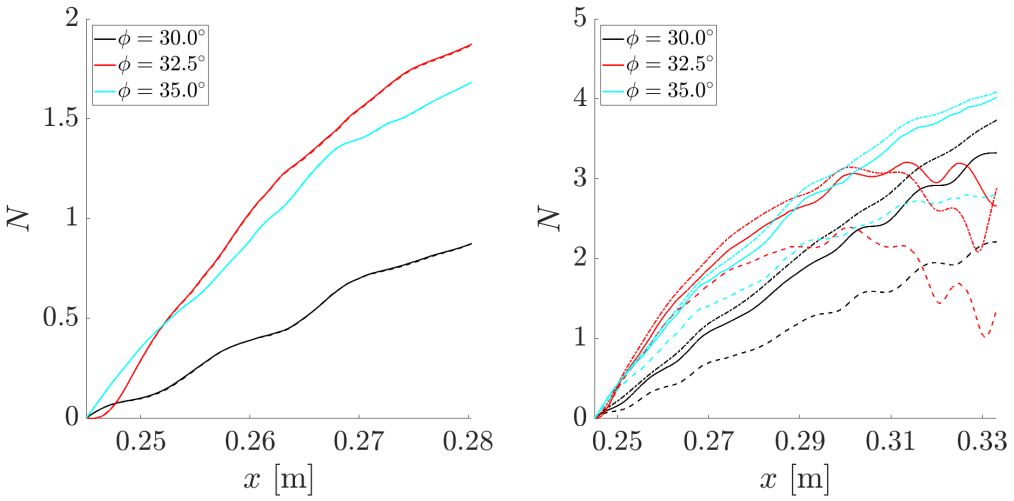

(a) Recursion parameter study where dashed and solid lines correspond to N_b = 10 and N_b = 13, respectively.

(b) Streamwise grid-convergence study where dashed and solid lines correspond to N_ξ = 2001 and N_ξ = 6001, respectively, for the OWNS computations, whereas the dash-dotted line corresponds to the PSE calculation.

Figure 3.8: OWNS recursion parameter and grid-convergence studies using surface N-factors along three azimuthal rays.

3.1.3.2 Comparison with PSE and convergence at f = 250 kHz

At x_{tr}, the maximum N-factor from PSE and OWNS are approximately 3.0 and 2.0, respectively. Although the cross-stream resolution and numerics are identical between OWNS and PSE, two additional factors may explain the lower growth rate from OWNS: the number of recursion parameters, N_b, and the streamwise resolution, N_ξ. Higher N_b allows more accurate filtration of the upstream waves whereas higher N_ξ minimizes numerical dissipation, both of which invariably increases the computational burden. We tested the effect of increasing N_b from 10 to 13 for 0.245 m $< x <$ 0.280 m, but virtually no differences were observed in the surface N-factors along ϕ = 30.0°, 32.5°, and 35.0° azimuths as shown in Fig. 3.8a. Note that the N-factors were computed using Eq. 3.1, but normalized by the wall-pressure amplitude at x = 0.245 m along a given azimuth. Thus, the OWNS computations are recursion-parameter converged.

We then investigated the effect of N_ξ by tripling the streamwise resolution from 0.245 m $< x <$ 0.333 m. The OWNS N-factors along the three azimuthal rays in Fig. 3.8b increases with higher N_ξ, and closely agrees with the PSE values. In fact,

the maximum N-factor at x_{tr} with a slightly downstream neutral point of $x = 0.245$ m is 2.7 and 2.5 for PSE and OWNS, respectively. This suggests that the OWNS calculations are not fully streamwise-grid-converged, but performing the calculation at the refined resolution for the entire domain would be computationally prohibitive. We can thus use the current OWNS calculations to only ascertain the dominant instabilities present with the randomized inlet forcing (see Sec. 3.1.3.1) and general features of the vortex mode as we demonstrate below the qualitative convergence of the OWNS calculations to those using PSE.

The pressure amplitudes and the cross-stream wavenumber distribution from Figs. 3.9 and 3.10, respectively, show qualitative agreement between OWNS and PSE. This suggests that non-modal and/or multi-modal effects are negligible if the flow field is excited strictly at the inlet. The wave structures at $x = 0.2$ m in Fig. 3.10a indicate interaction between the disturbances at the crest of the laminar vortex and those near the wall. However, by $x = 0.3$ m (near x_{tr}), most of the wave structures are situated at the crest with minimal interaction with the wall due to the steepening of the base-flow vortex. This also corroborates the relatively large pressure amplitude observed at the crest in Figs. 3.9b and 3.9c.

3.2 Mach 1.5 turbulent jet

In this section, we apply the planar-marching techniques of OWNS and PSE to a Mach 1.5 turbulent axisymmetric jet (see Fig. 3.11) computed using large-eddy simulation described by Brès et al. (2017), in which the Reynolds number $Re = \rho_j^* u_j^* D^* / \mu_j^* = 1760000$ and temperature ratio $T_j/T_\infty = 1$. In linearizing Eq. 2.1, a turbulent Reynolds number of $Re_T = 1760$ is instead used, which is three orders of magnitude less than the true Reynolds number. This is justified since using an eddy-viscosity model or a reduced effective Reynolds number enhances both the near-field (Pickering, Rigas, Schmidt, et al., 2021) and far-field (Pickering, Towne, et al., 2021) dynamics in free-shear flows.

3.2.1 Computational setup

We use three different azimuthal domains: a 2D-domain (3DF calculation with azimuthal wavenumber $m = 0$), a $\frac{\pi}{4}$-domain, and a full 2π-domain. The latter two domains are enforced with symmetric and periodic spanwise boundary conditions, respectively, with all domains discretized in the cross-stream direction using the fourth-order central finite-difference scheme. The radial grid contains higher concentration of points near the shear layer at $\eta = 0.5$, whereas the azimuthal grid

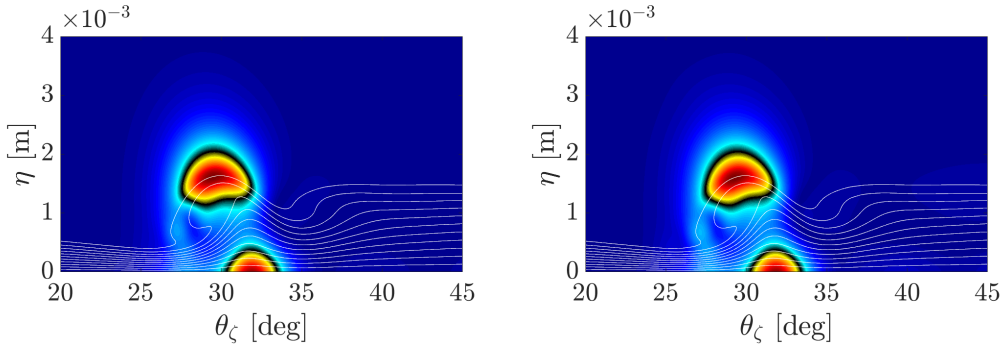

(a) x = 0.2 m

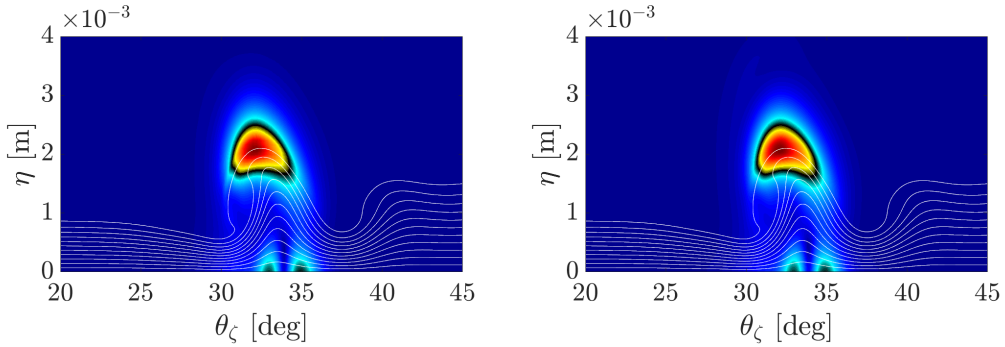

(b) x = 0.3 m

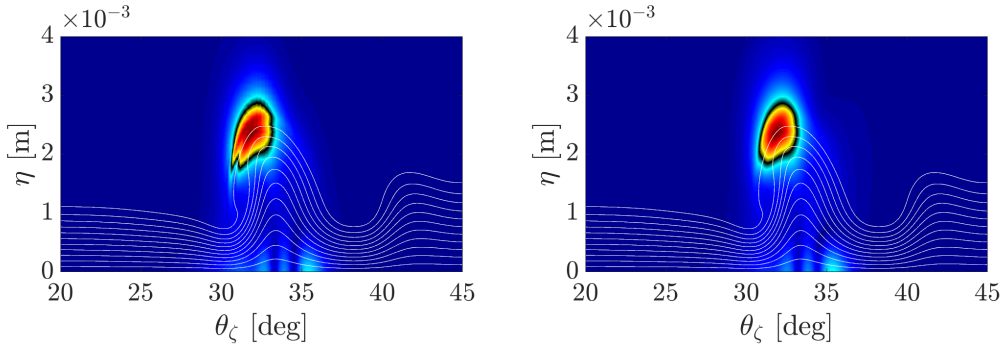

(c) x = 0.4 m

Figure 3.9: Pressure amplitudes computed using PSE (left) and OWNS (right) using a SBG inlet boundary condition at f = 250 kHz. The amplitudes are normalized by the maximum value at each streamwise station such that contour limits blue, black, and red correspond to $0 < |p'| < 1$. The background contour lines correspond to mean streamwise velocity.

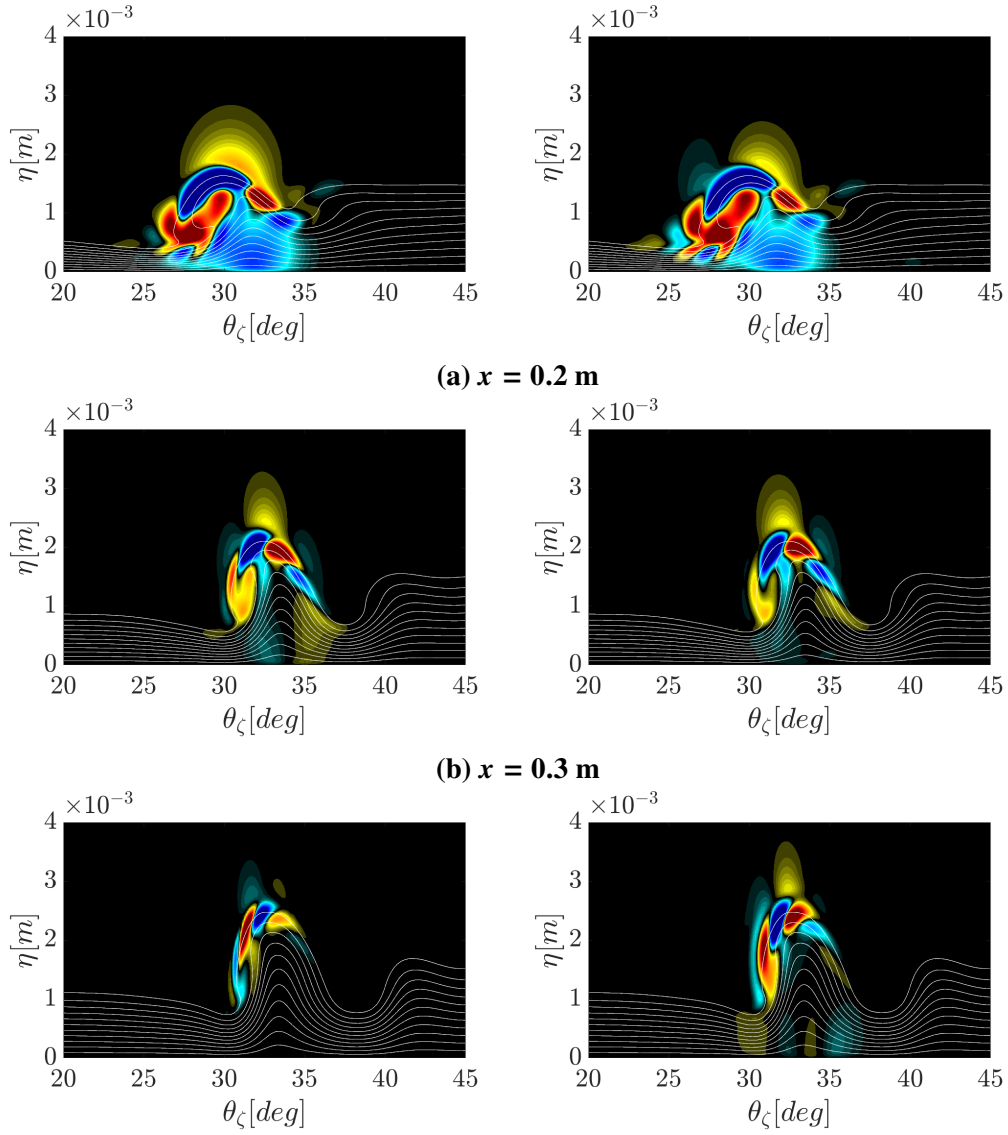

(a) x = 0.2 m

(b) x = 0.3 m

(c) x = 0.4 m

Figure 3.10: $\mathscr{R}(u')$ computed using PSE (left) and OWNS (right) using a SBG inlet boundary condition at f = 250 kHz. All quantities are normalized by the maximum value at each streamwise station such that contour limits blue, black, and red correspond to $-0.5 < \mathscr{R}(u') < 0.5$. The background contour lines correspond to mean streamwise velocity.

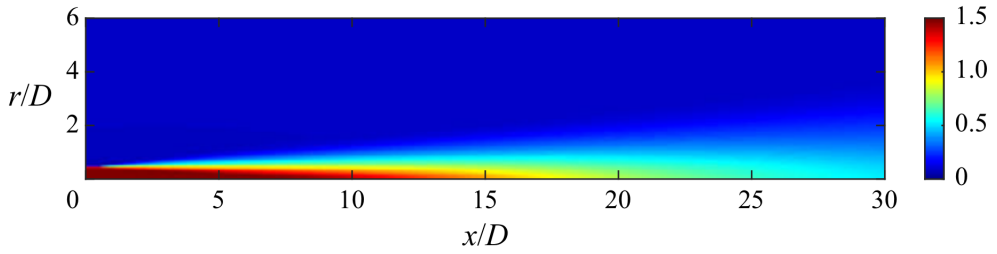

Figure 3.11: Contour plot of the local Mach number for the $M_j = 1.5$ turbulent jet. Figure from Towne, Rigas, Kamal, et al. (2022) where x/D and r/D correspond to ξ and η, respectively.

is uniformly distributed. All marches are initialized with an axisymmetric Kelvin-Helmholtz instability from LST with 1D inviscid Thompson characteristic boundary conditions at the far-field (Thompson, 1987). We chose to focus on the axisymmetric mode since it is generally of most importance in jet aeroacoustics (Cavalieri et al., 2012; Chen and Towne, 2021).

The objective of using the three different azimuthal domains is to validate the generalized curvilinear implementation of the centerline treatment from Sec. B.1.2, and thus we elect to use PSE for these calculations. To more closely analyze the physics, we also perform OWNS marches for the 2D- (3DF) and $\frac{\pi}{4}$-azimuthal domains, along with a 3DF linearized Navier-Stokes (LNS) calculation (see Sec. B.3.3 for details of the LNS solver), and compare the results to PSE. The OWNS calculations are integrated in the streamwise direction using BDF2 with $N_b = 11$, whereas the fourth-order central finite-difference scheme is used for streamwise discretization in the LNS computation along with an outlet sponge to model an open boundary. The flow and computational parameters are summarized in Tables 3.3 and 3.4, respectively.

Finally, all length scales presented in this section are normalized by the jet diameter D^* and (ξ, η, ζ) correspond to the canonical (x, r, θ) cylindrical coordinates.

Table 3.3: Mach 1.5 jet flow parameters.

M_j	$u_j^* = M_j a_j^*$ [m/s]	T_∞^* [K]	p_∞^* [Pa]	Re_T	St
1.5	510.39	288.15	101300	1760	0.52

Table 3.4: Computational parameters used for the Mach 1.5 jet analyses.

ξ_{min}	ξ_{max}	η_{min}	η_{max}	ζ_{min} [rad]	ζ_{max} [rad]	N_ξ	N_η	N_ζ
0.50	30	0.0063	16.17	0	$[0, \pi/4, 2\pi]$	1001	225	[1, 20, 160]

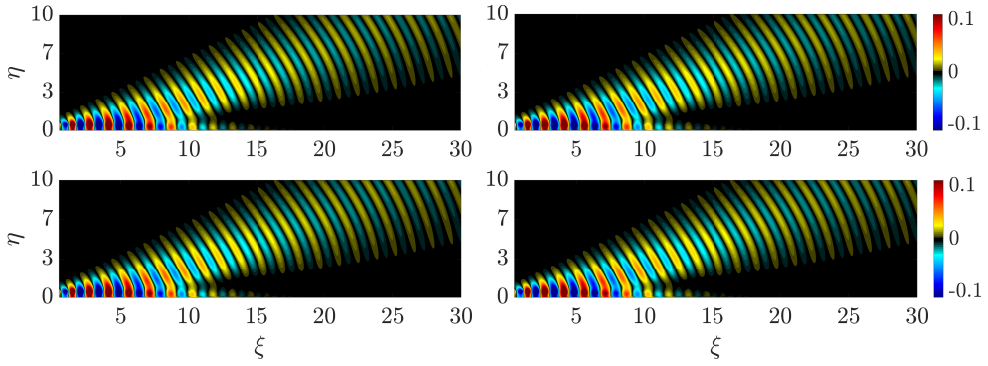

Figure 3.12: $\mathscr{R}(p')$ for the $\frac{\pi}{4}$- (top) and 2π- (bottom) azimuthal domains computed using PSE. Left and right columns correspond to $\zeta = 0$ and $\zeta = \zeta_{max}$, respectively.

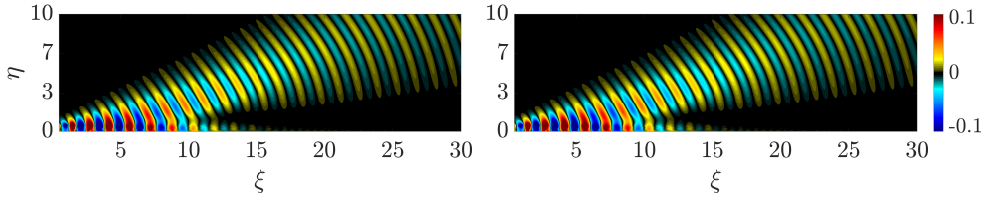

Figure 3.13: $\mathscr{R}(p')$ for the $\frac{\pi}{4}$-azimuthal domain computed using OWNS, where left and right correspond to $\zeta = 0$ and $\zeta = \zeta_{max}$, respectively.

3.2.2 Convergence study with Kelvin-Helmholtz instability initialization

We plot the pressure field along the first and last azimuthal planes for the 3D computations in Fig. 3.12 for PSE and Fig. 3.13 for OWNS and compare to the 3DF calculations in Fig. 3.14. Overall, we see excellent agreement between all three spanwise domains and amongst the azimuthal slices for the 3D calculations, in which the jet dynamics include the near-field Kelvin–Helmholtz instability along with the far-field acoustic radiation. The convergence of the solutions thus validates the generalized curvilinear implementation and the centerline treatment for each type of azimuthal domain.

3.2.3 Comparison of pressure response between OWNS, PSE, and LNS

For a closer quantitative comparison, we plot the pressure amplitude along the jet lip line at $\eta = 0.5$ and at $\zeta = 0$ between PSE, OWNS, and LNS for the 2D- and $\frac{\pi}{4}$-azimuthal domains in Fig. 3.15. Again, all the solutions converge well, but the hydrodynamic Kelvin-Helmholtz instability from the OWNS and LNS computations in the shear layer appears to be modulated by the acoustic radiation in the region $1.5 < \xi < 13$. This coupling is also discussed in Nichols, Lele, and Moin (2009), and further highlights the inability of PSE to resolve multi-modal interactions,

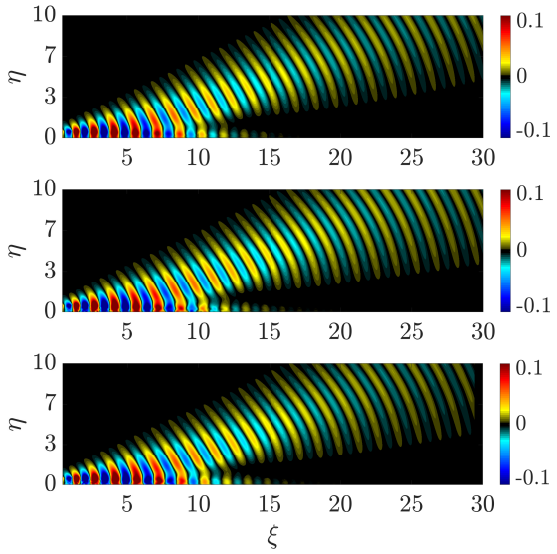

Figure 3.14: Top to bottom corresponds to $\mathscr{R}(p')$ from 3DF computations using PSE, OWNS, and LNS.

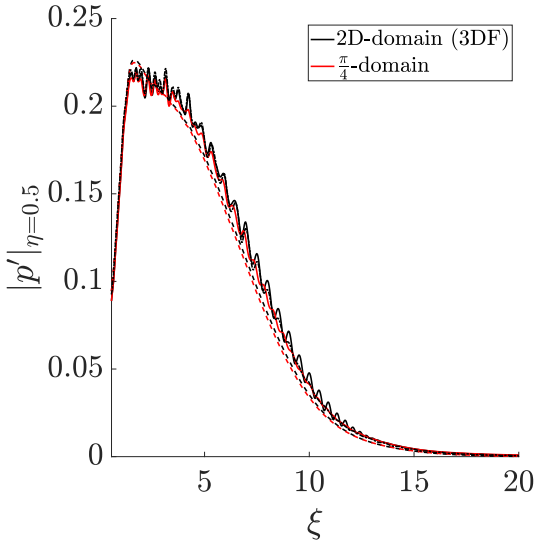

Figure 3.15: Pressure amplitudes along the jet lip line at $\eta = 0.5$ and $\zeta = 0$ for the 2D- and $\frac{\pi}{4}$-azimuthal domains computed using OWNS (solid lines), PSE (dashed lines) and LNS (dash-dotted line). Note that the 3DF OWNS and LNS computations are highly overlapping.

which, in contrast, can be accurately captured using OWNS at a fraction of the cost of LNS.

3.2.4 Summary

We have demonstrated the capability of OWNS to track complex 3D instabilities by studying the evolution of the vortex mode on a Mach 6 finned-cone geometry.

By using both a randomized inlet forcing and a SBG inlet boundary condition, the insensitivity to the initial conditions was established as both calculations converged to the dominant vortex mode. Thereafter, we demonstrated the accurate implementation of the pole conditions for cylindrical coordinates by spatially evolving the Kelvin-Helmholtz instability using various azimuthal domains for a Mach 1.5 axisymmetric turbulent jet. In contrast to PSE, OWNS was able to track the modulated Kelvin-Helmholtz instability due to the acoustic radiation with significantly lower computational burden compared to LNS (global approach).

Up to this point, we have only considered the forward problem, i.e. analyzing how disturbances spatially evolve from a prescribed inlet boundary condition or volumetric forcing. However, the inverse problem of determining the inhomogeneous forcing (inputs) that results in the largest disturbance-energy amplification (outputs) would instead directly illuminate the dominant instability mechanisms present, and is commonly referred to as *input-output* or *resolvent* analysis. This optimization method usually requires solving a system of globally discretized equations, which can become computationally prohibitive for large domains and/or complex flows. In the following chapter, we develop an algorithm using the OWNS projection equations from Sec. 2.2.2 to accurately compute these optimal forcings and responses with considerably reduced computational expense compared to the global approach.

Chapter 4

INPUT-OUTPUT ANALYSIS USING OWNS

Input-output analysis provides a powerful framework for analyzing transitional and turbulent flows, especially for computing coherent flow structures. However, this technique remains computationally expensive for flows exhibiting inhomogeneity in multiple spatial coordinates. In this chapter, we outline how the OWNS projection approach from Sec. 2.2.2 can be reconstructed to *efficiently* compute the optimal (worst-case) forcings and responses using an iterative, adjoint-based method with Lagrangian multipliers. This obviates the need to solve the globally discretized direct and adjoint equations, thereby bypassing the large computational expensive of traditional input-output analysis. We validate this new methodology to a Mach 4.5 transitional zero-pressure-gradient flat-plate boundary layer and a Mach 1.5 turbulent jet against corresponding global calculations. Thereafter, we study worst-case disturbances on the centerline of the Mach 6 HIFiRE-5 elliptic cone and on a highly cooled Mach 6 flat-plate boundary layer.

4.1 Methodology

Although not necessary, the streamwise viscous terms in the derivation of the optimal OWNS framework is omitted for their negligible effects (this will be substantiated in the subsequent validations), i.e. $\boldsymbol{f_{\xi,vis}} = 0$, which allows $\widetilde{\boldsymbol{\mathcal{B}}}_{\boldsymbol{p}}$ to be directly embedded into the $\boldsymbol{B}^{\ddagger}$ operator from Eq. 2.29a. The constrained optimization can then be constructed by defining the Lagrangian function

$$\mathcal{L}(\boldsymbol{\phi}^{\ddagger}, \boldsymbol{\phi}^{\ddagger *}, \boldsymbol{\phi}^{\ddagger}_{\mathbb{0}}, \boldsymbol{\phi}^{\ddagger}_{\mathbb{1}}, \boldsymbol{f_{\phi}}) = \mathcal{J}(\boldsymbol{\phi}^{\ddagger}) - \langle \boldsymbol{\phi}^{\ddagger *}, (\boldsymbol{A}^{\ddagger}\partial_{\xi} - \boldsymbol{L}^{\ddagger})\boldsymbol{\phi}^{\ddagger} - \boldsymbol{B}^{\ddagger}\boldsymbol{f_{\phi}} \rangle, \tag{4.1}$$

where the asterisk denotes adjoint OWNS operators/variables. Here, $\mathcal{J}$ is a generic cost function to be maximized subject to the governing approximate OWNS projection equations, which are enforced via the adjoint variable $\boldsymbol{\phi}^{\ddagger *}$. For succinctness, we have used ∂_{ξ} to indicate ξ-derivatives in this section.

We define an inner product over the cross-stream coordinates

$$(\boldsymbol{a}, \boldsymbol{b})_O = (\boldsymbol{a}, \boldsymbol{W_e}\boldsymbol{b}) = \boldsymbol{a}^{\boldsymbol{H}}(\xi)\boldsymbol{W}_{\eta\zeta}(\xi)\boldsymbol{W_e}(\xi)\boldsymbol{b}(\xi) = \boldsymbol{a}^{\boldsymbol{H}}(\xi)\boldsymbol{W_O}(\xi)\boldsymbol{b}(\xi), \tag{4.2}$$

and over the entire domain

$$\langle \boldsymbol{a}, \boldsymbol{b} \rangle_O = \langle \boldsymbol{a}, \boldsymbol{W_e} \boldsymbol{b} \rangle = \int_\Omega \boldsymbol{a}^{\boldsymbol{H}}(\xi) \boldsymbol{W_{\eta\zeta}}(\xi) \boldsymbol{W_e}(\xi) \boldsymbol{b}(\xi) \, \mathrm{d}\xi = \int_\Omega \boldsymbol{a}^{\boldsymbol{H}}(\xi) \boldsymbol{W_O}(\xi) \boldsymbol{b}(\xi) \, \mathrm{d}\xi$$
$$= \int_\Omega (\boldsymbol{a}, \boldsymbol{b})_O \, \mathrm{d}\xi, \tag{4.3}$$

where $\Omega = [\xi_{\mathbb{0}}, \xi_{\mathbb{1}}]$ is the streamwise extent of the domain, and $\xi_{\mathbb{0}}$ and $\xi_{\mathbb{1}}$ correspond to the streamwise coordinates of the inlet and outlet planes, respectively. The weight matrix is constructed as a composition so that the norm represents a quantity of interest (e.g. energy) and quadrature weights for the cross-stream discretization, i.e. $\boldsymbol{W_O}(\xi) = \boldsymbol{W_{\eta\zeta}}(\xi) \boldsymbol{W_e}(\xi)$. In this way $\langle \boldsymbol{a}, \boldsymbol{b} \rangle_O \approx \langle \boldsymbol{a}, \boldsymbol{b} \rangle_g$, (equal up to a discretization error). The definition of $\langle \boldsymbol{a}, \boldsymbol{b} \rangle_g$ is provided in Sec. B.3.4 and inner products without any subscripts involve only quadrature weights. The diagonal integration-weight matrix $\boldsymbol{W_{\eta\zeta}}(\xi)$ is composed of $h_\xi h_\eta \mathrm{d}\eta$, $h_\xi h_\eta h_\zeta \mathrm{d}\eta$, and $h_\xi h_\eta h_\zeta \mathrm{d}\eta \mathrm{d}\zeta$ for 2D, 3DF, and 3D analyses, respectively. We additionally now define the Chu-energy norm (Chu, 1965)

$$E_{Chu} = \frac{1}{2} \int \int_\Omega \frac{R\overline{T}}{\overline{\rho}} \rho'^2 + \overline{\rho} |\mathbf{u}'|^2 + \frac{R\overline{\rho}}{\overline{T}\left(\gamma(\overline{T}) - 1\right)} T'^2 \, \mathrm{d}\xi \mathrm{d}A \tag{4.4}$$

$$= \int_\Omega \boldsymbol{q'}^{\boldsymbol{H}}(\xi) \boldsymbol{W_{\eta\zeta}}(\xi) \boldsymbol{W_e}(\xi) \boldsymbol{q'}(\xi) \, \mathrm{d}\xi = \langle \boldsymbol{q'}, \boldsymbol{q'} \rangle_O, \tag{4.5}$$

where A represents the streamwise-local cross-stream area and $\boldsymbol{W_e}(\xi)$ from this point onwards is the diagonal Chu-energy weight matrix defined as

$$\boldsymbol{W_e}(\xi) = \frac{1}{2} \begin{bmatrix} \frac{R\overline{T}}{\overline{\rho}} & 0 & 0 & 0 & 0 \\ 0 & \overline{\rho} & 0 & 0 & 0 \\ 0 & 0 & \overline{\rho} & 0 & 0 \\ 0 & 0 & 0 & \overline{\rho} & 0 \\ 0 & 0 & 0 & 0 & \frac{R\overline{\rho}}{\overline{T}\left(\gamma(\overline{T})-1\right)} \end{bmatrix}. \tag{4.6}$$

The inner product in Eq. 4.1 can be expanded through integration by parts, yielding

$$\begin{aligned} &\langle \boldsymbol{\phi}^{\ddagger *}, (\boldsymbol{A}^\ddagger \partial_\xi - \boldsymbol{L}^\ddagger) \boldsymbol{\phi}^\ddagger - \boldsymbol{B}^\ddagger \boldsymbol{f_\phi} \rangle \\ &= \langle (-\boldsymbol{A}^{\ddagger *} \partial_\xi - \boldsymbol{L}^{\ddagger *}) \boldsymbol{\phi}^{\ddagger *}, \boldsymbol{\phi}^\ddagger \rangle + \left[\left(\boldsymbol{A}^{\ddagger *} \boldsymbol{\phi}^{\ddagger *}, \boldsymbol{\phi}^\ddagger \right) \right]_{\xi_{\mathbb{0}}}^{\xi_{\mathbb{1}}} - \langle \boldsymbol{\phi}^{\ddagger *}, \boldsymbol{B}^\ddagger \boldsymbol{f_\phi} \rangle \\ &= \langle (-\boldsymbol{A}^{\ddagger *} \partial_\xi - \boldsymbol{L}^{\ddagger *}) \boldsymbol{\phi}^{\ddagger *}, \boldsymbol{\phi}^\ddagger \rangle + \left(\boldsymbol{A}^{\ddagger *} \boldsymbol{\phi}_{\mathbb{1}}^{\ddagger *}, \boldsymbol{\phi}_{\mathbb{1}}^\ddagger \right) - \left(\boldsymbol{A}^{\ddagger *} \boldsymbol{\phi}_{\mathbb{0}}^{\ddagger *}, \boldsymbol{\phi}_{\mathbb{0}}^\ddagger \right) - \langle \boldsymbol{\phi}^{\ddagger *}, \boldsymbol{B}^\ddagger \boldsymbol{f_\phi} \rangle, \end{aligned} \tag{4.7}$$

where

$$\boldsymbol{A}^{\ddagger *} = \boldsymbol{W}_{\eta\zeta}^{\ddagger\ -1}\boldsymbol{A}^{\ddagger H}\boldsymbol{W}_{\eta\zeta}^{\ddagger}, \quad \boldsymbol{L}^{\ddagger *} = \boldsymbol{W}_{\eta\zeta}^{\ddagger\ -1}\boldsymbol{L}^{\ddagger H}\boldsymbol{W}_{\eta\zeta}^{\ddagger}, \tag{4.8}$$

and $\boldsymbol{W}_{\eta\zeta}^{\ddagger}$ is the augmented diagonal quadrature-weight matrix to accommodate the auxiliary variables. Thus, we can define the adjoint to Eq. 2.29a as

$$(\boldsymbol{A}^{\ddagger *}\partial_\xi - \boldsymbol{L}^{\ddagger *})\boldsymbol{\phi}^{\ddagger *} = \boldsymbol{f}_{\boldsymbol{\phi}}^{*}, \tag{4.9}$$

where $\boldsymbol{f}_{\boldsymbol{\phi}}^{*}$ is the adjoint characteristic forcing determined from evaluating the stationary points of the Lagrangian function. Note that the negative sign in front of $\boldsymbol{A}^{\ddagger *}$ has been dropped since we are marching upstream.

The cost function $\mathcal{J}$ is defined analogously to the global resolvent formulation from Sec. B.3.4 to compute the optimal volumetric forcings, $\boldsymbol{f}_{\boldsymbol{p}}$, that maximize the Chu-energy of the flow. Here, we will express $\mathcal{J}$ in characteristics instead as

$$\begin{aligned}
\mathcal{J}(\boldsymbol{\phi}^{\ddagger}, \boldsymbol{f}_{\boldsymbol{\phi}}) = \sigma_O^2(\omega) =& \frac{\langle \boldsymbol{y}, \boldsymbol{y}\rangle_O}{\langle \boldsymbol{f}_{\boldsymbol{p}}, \boldsymbol{f}_{\boldsymbol{p}}\rangle_O} = \frac{\int_\Omega \boldsymbol{q'}^H \boldsymbol{C}_p^H \boldsymbol{W}_O \boldsymbol{C}_p \boldsymbol{q'}\ \mathrm{d}\xi}{\int_\Omega (\boldsymbol{T}^{-1}\boldsymbol{f}_{\boldsymbol{\phi}})^H \boldsymbol{W}_O (\boldsymbol{T}^{-1}\boldsymbol{f}_{\boldsymbol{\phi}})\ \mathrm{d}\xi} \\
=& \frac{\int_\Omega \boldsymbol{\phi}^{\ddagger H} \boldsymbol{W}_{\eta\zeta}^{\ddagger} \overbrace{\boldsymbol{W}_{\eta\zeta}^{\ddagger\ -1} \boldsymbol{C}^{\ddagger H} \boldsymbol{T}^{-H} \boldsymbol{C}_p^H \boldsymbol{W}_O \boldsymbol{C}_p \boldsymbol{T}^{-1} \boldsymbol{C}^{\ddagger}}^{\boldsymbol{W}^{\ddagger}} \boldsymbol{\phi}^{\ddagger}\ \mathrm{d}\xi}{\int_\Omega \boldsymbol{f}_{\boldsymbol{\phi}}^H \boldsymbol{W}_{\eta\zeta} \underbrace{\boldsymbol{W}_{\eta\zeta}^{-1} \boldsymbol{T}^{-H} \boldsymbol{W}_O \boldsymbol{T}^{-1}}_{\boldsymbol{W}_f} \boldsymbol{f}_{\boldsymbol{\phi}}\ \mathrm{d}\xi} \\
=& \frac{\langle \boldsymbol{\phi}^{\ddagger}, \boldsymbol{W}^{\ddagger}\boldsymbol{\phi}^{\ddagger}\rangle}{\langle \boldsymbol{f}_{\boldsymbol{\phi}}, \boldsymbol{W}_f \boldsymbol{f}_{\boldsymbol{\phi}}\rangle}.
\end{aligned} \tag{4.10}$$

The Lagrangian function from Eq. 4.7, after enforcing $\boldsymbol{\phi}_{\mathbb{0}} = 0$, and after substituting the cost function from Eq. 4.10, is

$$\begin{aligned}
\mathcal{L}(\boldsymbol{\phi}^{\ddagger}, \boldsymbol{\phi}^{\ddagger *}, \boldsymbol{\phi}_{\mathbb{1}}^{\ddagger}, \boldsymbol{f}_{\boldsymbol{\phi}}) =& \frac{\langle \boldsymbol{\phi}^{\ddagger}, \boldsymbol{W}^{\ddagger}\boldsymbol{\phi}^{\ddagger}\rangle}{\langle \boldsymbol{f}_{\boldsymbol{\phi}}, \boldsymbol{W}_f \boldsymbol{f}_{\boldsymbol{\phi}}\rangle} - \langle (\boldsymbol{A}^{\ddagger *}\partial_\xi - \boldsymbol{L}^{\ddagger *})\boldsymbol{\phi}^{\ddagger *}, \boldsymbol{\phi}^{\ddagger}\rangle \\
& - \left(\boldsymbol{A}^{\ddagger *}\boldsymbol{\phi}_{\mathbb{1}}^{\ddagger *}, \boldsymbol{\phi}_{\mathbb{1}}^{\ddagger}\right) + \langle \boldsymbol{\phi}^{\ddagger *}, \boldsymbol{B}^{\ddagger}\boldsymbol{f}_{\boldsymbol{\phi}}\rangle.
\end{aligned} \tag{4.11}$$

The optimal forcing and responses are obtained by finding the stationary points of the Lagrangian function

$$\delta\mathcal{L} = \langle \boldsymbol{\nabla}_{\boldsymbol{\phi}^{\ddagger *}}\mathcal{L}, \delta\boldsymbol{\phi}^{\ddagger *}\rangle + \langle \boldsymbol{\nabla}_{\boldsymbol{\phi}^{\ddagger}}\mathcal{L}, \delta\boldsymbol{\phi}^{\ddagger}\rangle + \langle \boldsymbol{\nabla}_{\boldsymbol{\phi}_{\mathbb{1}}^{\ddagger}}\mathcal{L}, \delta\boldsymbol{\phi}_{\mathbb{1}}^{\ddagger}\rangle + \langle \boldsymbol{\nabla}_{\boldsymbol{f}_{\boldsymbol{\phi}}}\mathcal{L}, \delta\boldsymbol{f}_{\boldsymbol{\phi}}\rangle = 0. \tag{4.12}$$

We now set each inner product of the stationary points individually to zero

$$\langle \boldsymbol{\nabla}_{\boldsymbol{\phi}^{\ddagger *}} \mathcal{L}, \delta\boldsymbol{\phi}^{\ddagger *} \rangle = 0 \rightarrow \langle -(\boldsymbol{A}^{\ddagger}\partial_\xi - \boldsymbol{L}^{\ddagger})\boldsymbol{\phi}^{\ddagger} + \boldsymbol{B}^{\ddagger}\boldsymbol{f}_{\boldsymbol{\phi}}, \delta\boldsymbol{\phi}^{\ddagger *} \rangle = 0, \tag{4.13a}$$

$$\langle \boldsymbol{\nabla}_{\boldsymbol{\phi}^{\ddagger}} \mathcal{L}, \delta\boldsymbol{\phi}^{\ddagger} \rangle = 0 \rightarrow \left\langle \frac{(\boldsymbol{W}^{\ddagger} + \boldsymbol{W}_{\eta\zeta}^{\ddagger\ -1}\boldsymbol{W}^{\ddagger H}\boldsymbol{W}_{\eta\zeta}^{\ddagger})\boldsymbol{\phi}^{\ddagger}}{\langle \boldsymbol{f}_{\boldsymbol{\phi}}, \boldsymbol{W}_f \boldsymbol{f}_{\boldsymbol{\phi}} \rangle} \right.$$

$$\left. - (\boldsymbol{A}^{\ddagger *}\partial_\xi - \boldsymbol{L}^{\ddagger *})\boldsymbol{\phi}^{\ddagger *}, \delta\boldsymbol{\phi}^{\ddagger} \right\rangle = 0, \tag{4.13b}$$

$$\langle \boldsymbol{\nabla}_{\boldsymbol{\phi}_{\mathbb{1}}^{\ddagger}} \mathcal{L}, \delta\boldsymbol{\phi}_{\mathbb{1}}^{\ddagger} \rangle = 0 \rightarrow \langle -\boldsymbol{A}^{\ddagger *}\boldsymbol{\phi}_{\mathbb{1}}^{\ddagger *}, \delta\boldsymbol{\phi}_{\mathbb{1}}^{\ddagger} \rangle = 0, \tag{4.13c}$$

$$\langle \boldsymbol{\nabla}_{f_{\boldsymbol{\phi}}} \mathcal{L}, \delta f_{\boldsymbol{\phi}} \rangle = 0 \rightarrow \left\langle -\frac{\langle \boldsymbol{\phi}^{\ddagger}, \boldsymbol{W}^{\ddagger}\boldsymbol{\phi}^{\ddagger} \rangle}{\langle \boldsymbol{f}_{\boldsymbol{\phi}}, \boldsymbol{W}_f \boldsymbol{f}_{\boldsymbol{\phi}} \rangle^2} (\boldsymbol{W}_f + \boldsymbol{W}_{\eta\zeta}^{-1}\boldsymbol{W}_f^H \boldsymbol{W}_{\eta\zeta})\boldsymbol{f}_{\boldsymbol{\phi}} \right.$$

$$\left. + \boldsymbol{W}_{\eta\zeta}^{-1}\boldsymbol{B}^{\ddagger H}\boldsymbol{W}_{\eta\zeta}^{\ddagger}\boldsymbol{\phi}^{\ddagger *}, \delta f_{\boldsymbol{\phi}} \right\rangle = 0. \tag{4.13d}$$

An iterative procedure for finding the stationary points from Eq. 4.13 is summarized in Algorithm 1 and schematically illustrated in Fig. 4.1. Lastly, N optimal and suboptimal forcings, $\{\boldsymbol{f}_{\boldsymbol{p_1}}, \boldsymbol{f}_{\boldsymbol{p_2}}, \ldots, \boldsymbol{f}_{\boldsymbol{p_N}}\}$, and responses, $\{\boldsymbol{q}'_{\boldsymbol{1}}, \boldsymbol{q}'_{\boldsymbol{2}}, \ldots, \boldsymbol{q}'_{\boldsymbol{N}}\}$, can also be computed by initializing the optimization procedure such that $\langle \boldsymbol{f}_{\boldsymbol{p_i}}, \boldsymbol{f}_{\boldsymbol{p_j}} \rangle = \delta_{ij}$, and orthonormalizing the forcings at each iteration.

Algorithm 1 uses a power iteration scheme, along with Gram-Schmidt orthogonalization, to facilitate the calculation of multiple modes. Other more sophisticated iteration schemes such as the Arnoldi method or RSVD (Halko, Martinsson, and Tropp, 2011) could be used to accelerate convergence. However, for the various validations and applications presented later in this chapter, along with extensive experience using Algorithm 1 for studies beyond the scope of this thesis, the power iteration method was found to converge sufficiently fast in just a few iterations.

4.2 Validation of optimal OWNS to a Mach 4.5 flat-plate boundary layer

We first validate the optimal OWNS framework by considering a Mach 4.5 laminar flat-plate zero-pressure-gradient boundary layer. Optimal forcings and responses are computed using the OWNS and global approach for several frequency and wavenumber combinations corresponding to different linear instability mechanisms. These cases, and the numerical parameters used for each, are summarized in Table 4.1. Results in this section are from Towne, Rigas, Kamal, et al. (2022), in which dimensional quantities are not denoted with asterisks.

Algorithm 1 Optimal forcing and response with OWNS

1: Initialize random $\boldsymbol{f_{p_i}}$ such that $\langle \boldsymbol{f_{p_i}}, \boldsymbol{f_{p_j}} \rangle_O = \delta_{ij}$. Set threshold ϵ (here 10^{-4}).

2: Solve the forced OWNS projection equations to determine the response by spatially marching in $+\xi$

$$(\boldsymbol{A}^{\ddagger}\partial_\xi - \boldsymbol{L}^{\ddagger})\boldsymbol{\phi}_{\boldsymbol{i}}^{\ddagger} = \boldsymbol{B}^{\ddagger}\boldsymbol{f}_{\boldsymbol{\phi_i}}, \quad \boldsymbol{\phi_i}(\xi = \xi_{\mathbb{0}}) = 0.$$

3: Calculate adjoint forcing

$$\boldsymbol{f}^{*}_{\boldsymbol{\phi_i}} = \alpha_i^*(\boldsymbol{W}^{\ddagger} + \boldsymbol{W}^{\ddagger}_{\boldsymbol{\eta\zeta}}{}^{-\mathbf{1}}\boldsymbol{W}^{\ddagger\boldsymbol{H}}\boldsymbol{W}^{\ddagger}_{\boldsymbol{\eta\zeta}})\boldsymbol{\phi}_{\boldsymbol{i}}^{\ddagger},$$

where α_i^* is a normalization coefficient such that $\boldsymbol{f}^{*}_{\boldsymbol{\phi_i}}$ has unit norm.

4: Solve the adjoint OWNS projection equations by spatially marching in $-\xi$

$$(\boldsymbol{A}^{\ddagger *}\partial_\xi - \boldsymbol{L}^{\ddagger *})\boldsymbol{\phi}_{\boldsymbol{i}}^{\ddagger *} = \boldsymbol{f}^{*}_{\boldsymbol{\phi_i}}, \quad \boldsymbol{\phi}^{*}_{\boldsymbol{i}}(\xi = \xi_{\mathbb{1}}) = 0.$$

5: Calculate direct forcing

$$\boldsymbol{f_{p_i}} = \mathcal{G}\left[\boldsymbol{T}^{-\mathbf{1}}(\boldsymbol{W}_f + \boldsymbol{W}^{-\mathbf{1}}_{\boldsymbol{\eta\zeta}}\boldsymbol{W}^{\boldsymbol{H}}_f\boldsymbol{W}_{\boldsymbol{\eta\zeta}})^{-\mathbf{1}}\boldsymbol{W}^{-\mathbf{1}}_{\boldsymbol{\eta\zeta}}\boldsymbol{B}^{\ddagger\boldsymbol{H}}\boldsymbol{W}^{\ddagger}_{\boldsymbol{\eta\zeta}}\boldsymbol{\phi}_{\boldsymbol{i}}^{\ddagger *}\right],$$

where $\mathcal{G}[\ ]$ is the Gram-Schmidt orthonormalization operator such that

$$\langle \boldsymbol{f_{p_i}}, \boldsymbol{f_{p_j}} \rangle_O = \delta_{ij}.$$

6: Calculate the relative change of the cost function

$$\Delta = \left|\frac{\mathcal{J}_{k+1} - \mathcal{J}_k}{\mathcal{J}_k}\right| = \left|\frac{\langle \boldsymbol{y}, \boldsymbol{y}\rangle_{O,k+1} - \langle \boldsymbol{y}, \boldsymbol{y}\rangle_{O,k}}{\langle \boldsymbol{y}, \boldsymbol{y}\rangle_{O,k}}\right|.$$

7: Repeat Steps 2 to 6 until $\Delta < \epsilon$.

4.2.1 Computational setup

For this section only, all boundary-layer quantities are non-dimensionalized using the free-stream velocity u_∞ and the local compressible displacement thickness $\delta^*(x)$ or the displacement thickness at the outlet of the domain δ_0^*. Note that for the present flat-plate geometry, $x = \xi$ and $y = \eta$. The domain inlet is located just downstream of the leading edge at $Re_x^{in} = 105$, corresponding to $Re_{\delta_0^*}^{in} = 871$, to avoid the singularity in the similarity solution used in this validation study. The streamwise domain extends to $Re_x^{out} = \frac{\nu_\infty x}{u_\infty} = 1.74 \times 10^6$ or $Re_{\delta_0^*}^{out} = 11216$. The domain size is similar to the one of Bugeat et al. (2019), where in their calculations the outlet is at $Re_x^{out} = 1.75 \times 10^6$ or $Re_{\delta_0^*}^{out} = 11000$. However, in their analyses, the flat-plate leading edge was also included in the computational domain, resulting in a weak

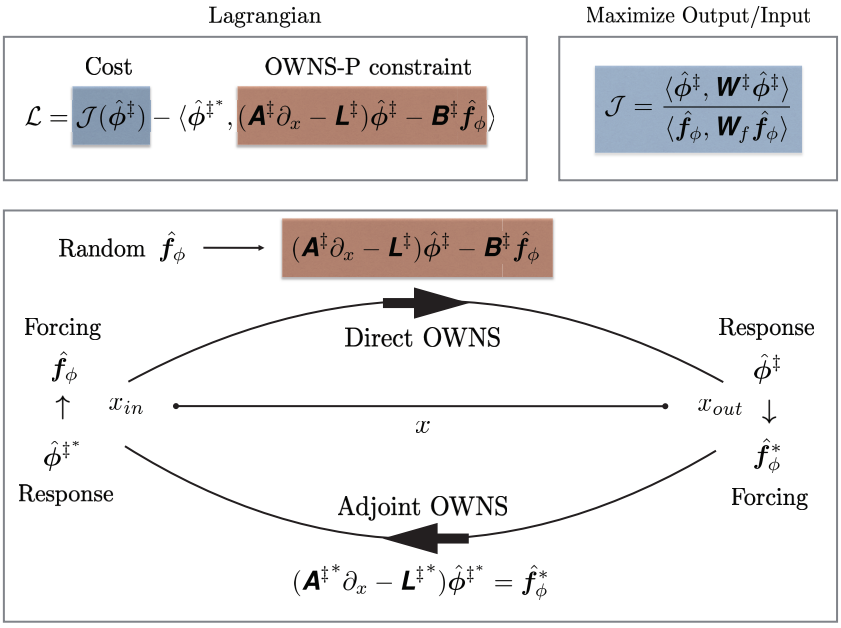

Figure 4.1: Schematic of the iterative, adjoint-based algorithm for computation of the optimal forcings and responses using the OWNS projection approach. Figure from Towne, Rigas, Kamal, et al. (2022), where hats represent frequency-domain variables and x can be replaced with ξ to extend to the present curvilinear coordinates.

shock at the leading edge and small discrepancies in the outlet momentum thickness when compared to the similarity solution.

In order to properly resolve the instabilities near the wall and critical layer, grid stretching in the y-direction is employed clustering half of the points near the wall for $y/\delta_0^* < 0.9$ (Malik, 1990). No-slip and adiabatic boundary conditions ($u' = v' = w' = \partial T'/\partial y = 0$) are enforced at the wall (Poinsot and Lelef, 1992). The OWNS equations are integrated in the streamwise direction using BDF2 with $N_b = 15$, which provided a good approximation for filtering the upstream-propagating waves while accurately tracking the downstream modes. Finally, the streamwise resolution was reduced for the global calculations as indicated in Table 4.1 due to the higher-order discretization and the larger computational memory requirements.

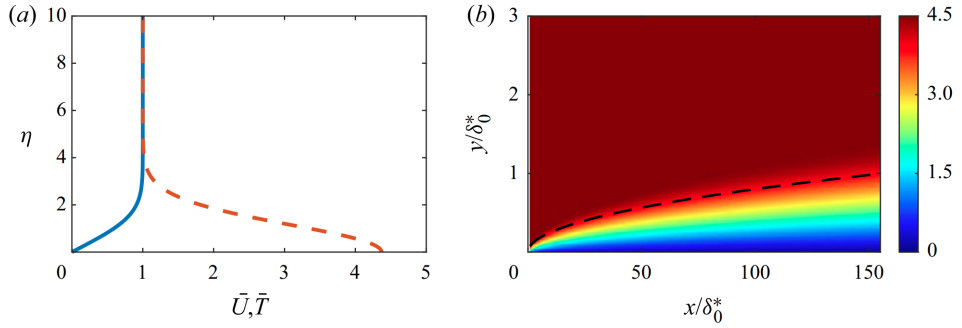

Figure 4.2: Laminar base flow of the $M = 4.5$ adiabatic flat-plate boundary layer calculated using a similarity transformation. Self-similar streamwise velocity and temperature components (left) and local Mach number (right) with the dashed line corresponding to the displacement thickness $\delta^*(x)$. Figure from Towne, Rigas, Kamal, et al. (2022) where η is the self-similar variable.

Table 4.1: Numerical parameters for the $M = 4.5$ flat-plate boundary layer.

Boundary layer	ω	β	$N_x \times N_y$ (OWNS/Global)	x/δ_0^*	y/δ_0^*
Streaks	0.002	2.2	1601×81 / 601×108	$0.01 - 155$	$0 - 9$
Second mode	2.5	0	2401×108 / 1001×180	$0.01 - 155$	$0 - 9$
Oblique mode	0.32	1.2	1601×81 / 651×81	$0.01 - 155$	$0 - 9$

The laminar base flow corresponds to a similarity solution of the compressible boundary-layer equations, where the Howarth-Dorodnitsyn transformation was employed to reduce the governing equations to a set of ODE's. The similarity solution is shown in Fig. 4.2.

Finally, in the optimization, we restrict the forcing only to the momentum components (f_x, f_y, f_z), or equivalently denoted as (f_u, f_v, f_w), using the $\mathcal{B}_p$ operator to match the setup of Bugeat et al. (2019).

4.2.2 Results

4.2.2.1 Optimal gain

Using the optimal OWNS algorithm, we compute the resolvent modes for the adiabatic flat-plate boundary layer across a range of frequencies and spanwise wavenumbers. The optimal input-output gains corresponding to three regions of locally maximum gain in the $\omega - \beta$ plane are shown in Fig. 4.3. Their maxima correspond to the amplification of streaks ($\omega \to 0$), second Mack modes ($\beta = 0$), and oblique first modes. We observe excellent agreement of the optimal ω and/or β when compared

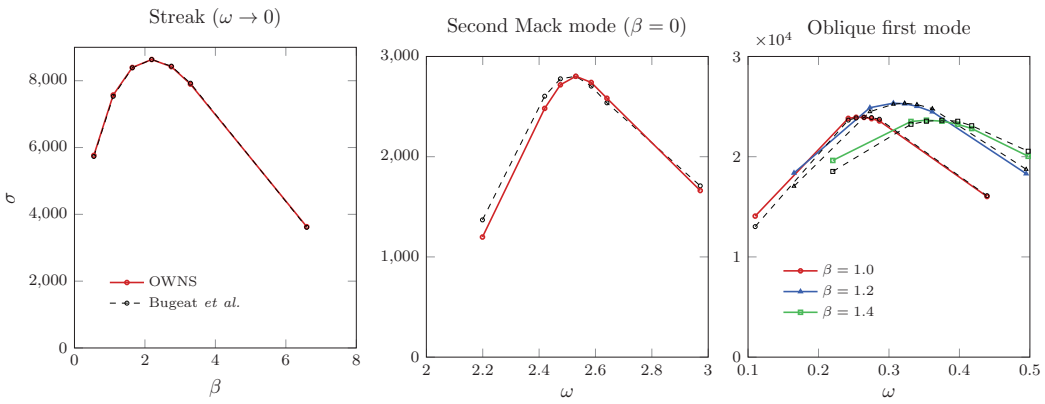

Figure 4.3: Optimal input-output gain for three linear instability mechanisms for the $M = 4.5$ flat-plate adiabatic boundary layer. Validation against normalized results from Bugeat et al. (2019) for a similar configuration. Figure from Towne, Rigas, Kamal, et al. (2022).

to the global resolvent calculations of Bugeat et al., 2019 for all three instability mechanisms.

4.2.2.2 Optimal forcings and responses

For streaks, the optimal forcing consists of streamwise counter-rotating vortices that lift the streamwise base-flow momentum. This is referred to as the *lift-up* mechanism and yields a response that contains primarily streaks of highly amplified streamwise velocity stretching in the streamwise direction. The dominant input (f_v) and output (u') velocity modes from OWNS and global computations are shown in Fig. 4.4. Great agreement is observed between the two methods, with the small differences near the domain inlet/outlet boundaries attributed to the sponges of the global method that attenuate the response to avoid reflections. Based on our experience, the tuning of the sponges is a tedious procedure and problem specific, but is obviated for the OWNS method since upstream-traveling waves are removed at each streamwise station during the parabolization procedure.

In Fig. 4.4, we also plot the OWNS optimal forcing and response profiles for all the perturbed quantities at a given streamwise station near the inlet and outlet, respectively. The OWNS results are compared to our global calculations and the global analyses from Bugeat et al. (2019). Great agreement is observed between OWNS and our global results, confirming the accuracy of the OWNS methodology. Some discrepancies are observed for the forcing away from the wall when compared to Bugeat et al. (2019) (both our global and OWNS). These discrepancies can be

attributed to the differences in the computational domain (inclusion of leading edge and shock) and the different choice of the input norm between the two studies. The forcing amplitudes presented in Bugeat et al. (2019) likely correspond to the conservative form of the momentum equations whereas we perform our analyses using primitive variables (Karban et al., 2020). Essentially, our forcing exists in a different subspace, but we are optimizing the same quantity, i.e. the disturbance-energy amplification with respect to the Chu-energy norm, which explains the agreement observed in the response profiles despite the differences in the forcing modes.

We next analyze the optimal forcing and response for the oblique first mode with contour plots of the dominant components f_w and u' from the OWNS and global calculations shown in Fig. 4.5. The optimal forcing field contains upstream-titled structures that are emblematic of the non-modal Orr mechanism. This generates an oblique wave response with relatively large streamwise velocity. Good agreement is achieved between the global and OWNS results for all perturbed input and output components, although a small error of about 1% in the wavelength can be observed.

Lastly, we compare the results for the second-mode instability in Fig. 4.6, as was done in the two previous cases. We see the classical subsonic second-mode instability in the response field, characterized by the trapped acoustic waves between the wall and relative sonic line as well as thermodynamic amplification near the generalized inflection point (two coexisting mechanisms). For such a response, we require the optimal forcing to be primarily concentrated near the generalized inflection point. Good agreement is again observed between OWNS and our global results.

In comparing the three linear instabilities, the first and second modes exhibit *convective-type* non-normality (Sipp et al., 2010), where there is a streamwise spatial lag between the input and response. In contrast, we observe *component-type* non-normality in the streaks due to the lift-up mechanism, which is local at each streamwise station as the base-flow momentum is advected by the counter-rotating vortices in the cross-stream directions. Consequently, we observe an elongated spatial support in the forcing field when compared to the first or second mode.

The close agreement of the resolvent modes between the global and OWNS calculations also extends to suboptimal modes. To demonstrate this, Fig. 4.7 compares the global and OWNS streamwise velocity response for the first suboptimal mode, i.e. the mode with second highest gain, for each of the three instability mechanisms

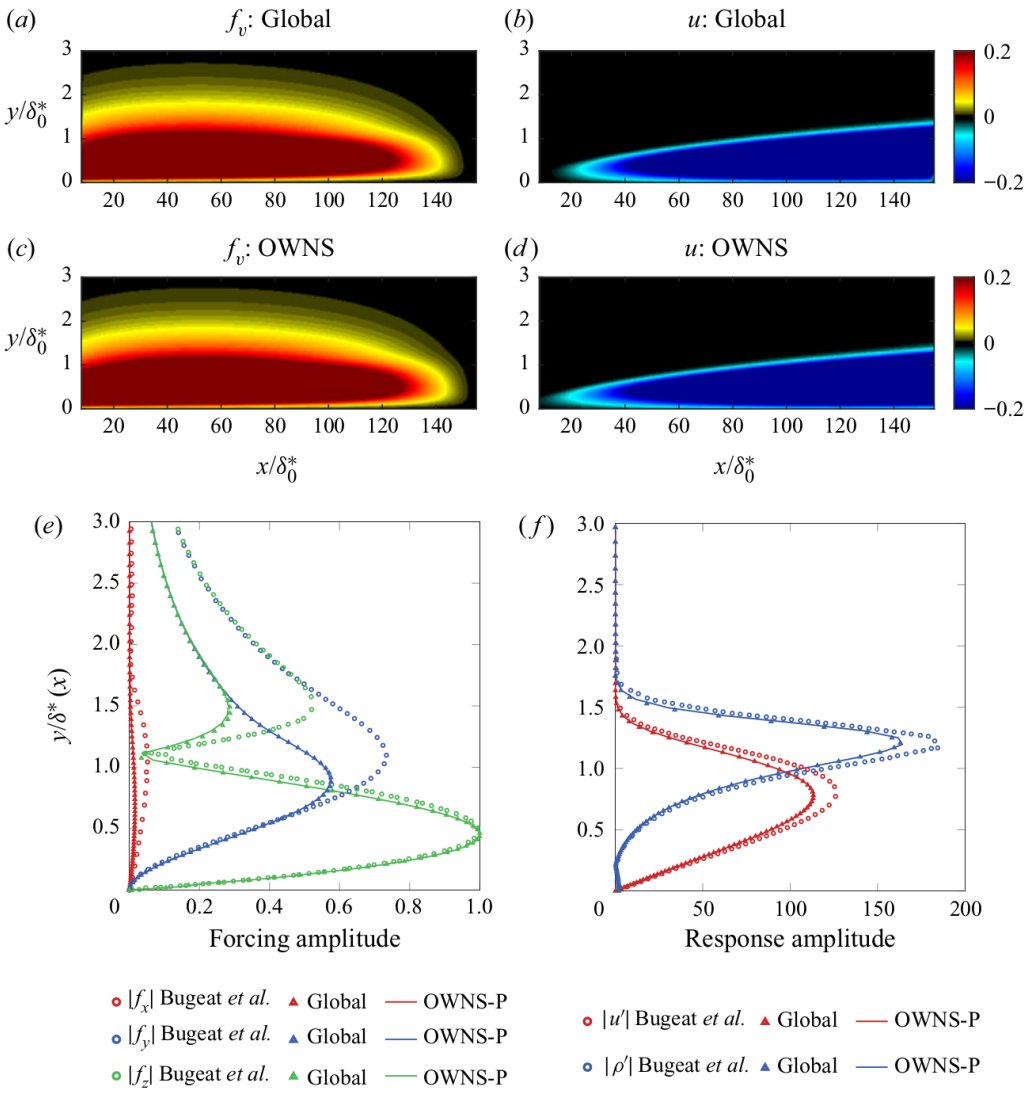

Figure 4.4: Streak (steady 3DF) optimal disturbances at $\omega = 0.002$, $\beta = 2.2$. Forcing and response amplitude components at $x/\delta_0^* = 35$ (left) and $x/\delta_0^* = 159$ (right). Circle symbols: Bugeat et al. (2019); triangle symbols: global using CSTAT; solid lines: OWNS. Figure from Towne, Rigas, Kamal, et al. (2022).

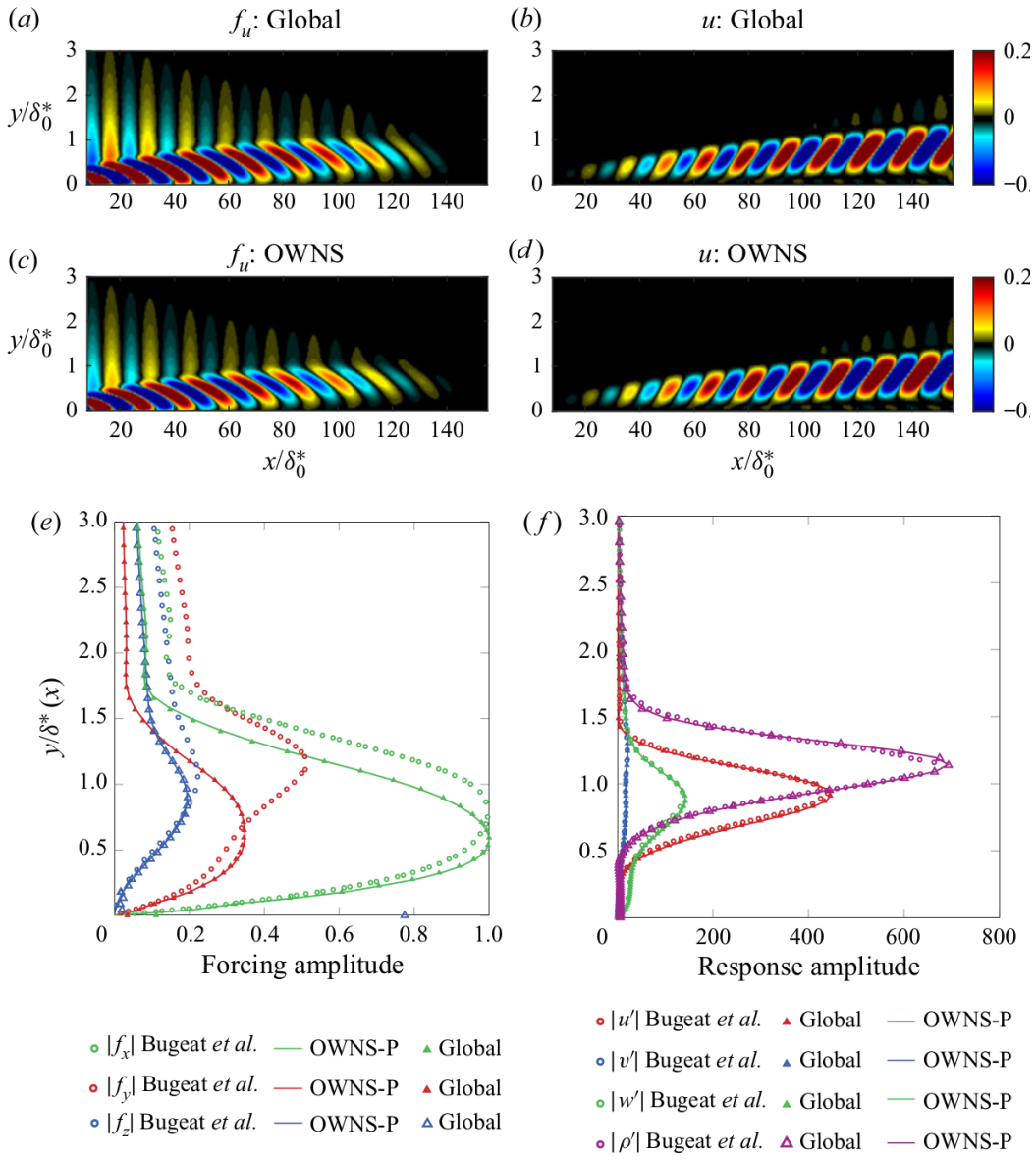

Figure 4.5: Oblique first mode (unsteady 3DF) optimal disturbances at ω = 0.32, β = 1.2. Forcing and response amplitude components at x/δ_0^* = 12 (left) and x/δ_0^* = 159 (right). Circle symbols: Bugeat et al. (2019); triangle symbols: global using CSTAT; solid lines: OWNS. Figure from Towne, Rigas, Kamal, et al. (2022).

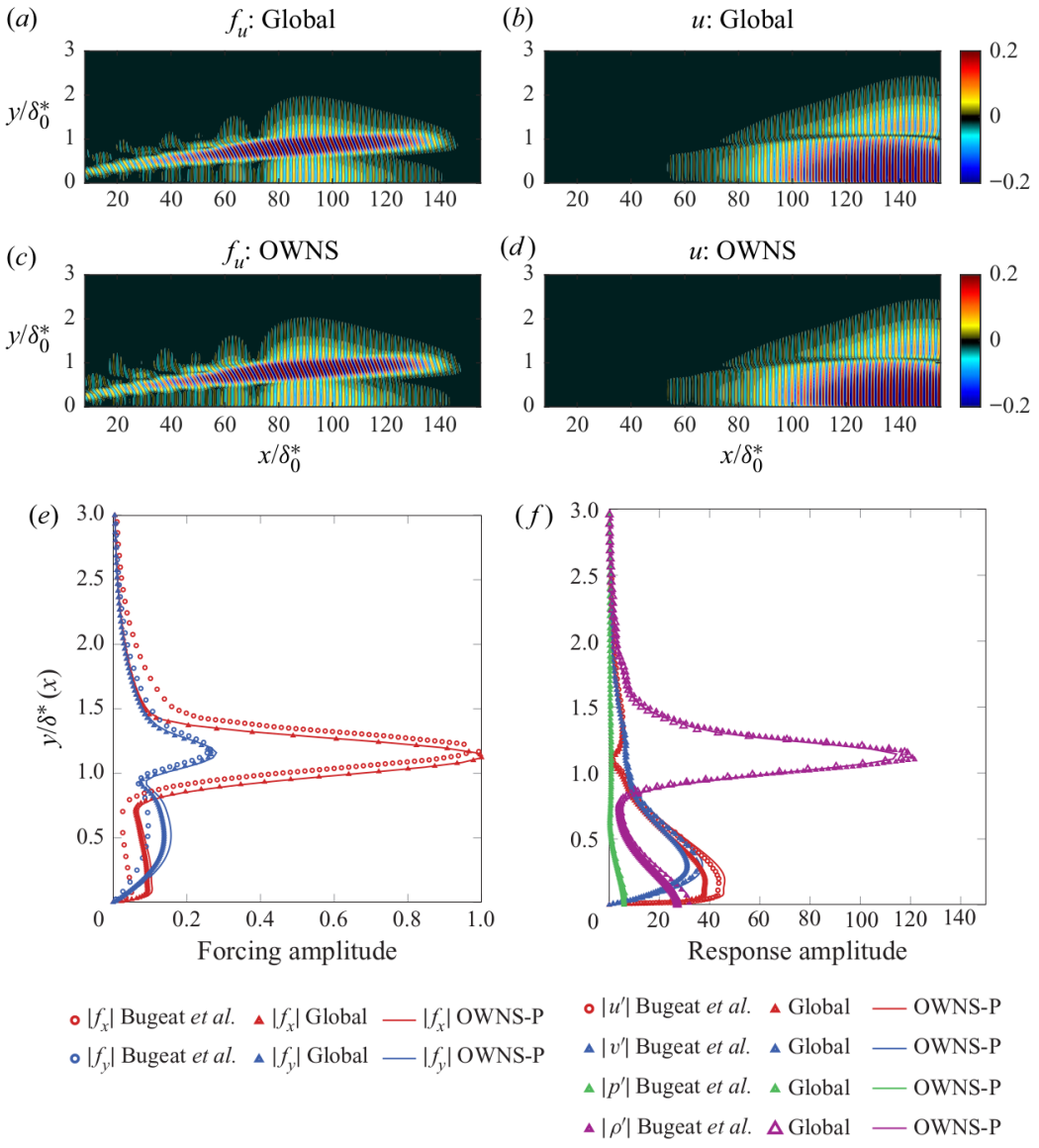

Figure 4.6: Planar second mode (unsteady 2D) optimal disturbances at $\omega = 2.5$, $\beta = 0$. Forcing and response amplitude components at $x/\delta_0^* = 90$ (left) and $x/\delta_0^* = 148$ (right). Circle symbols: Bugeat et al. (2019); triangle symbols: global using CSTAT; solid lines: OWNS. Figure from Towne, Rigas, Kamal, et al. (2022).

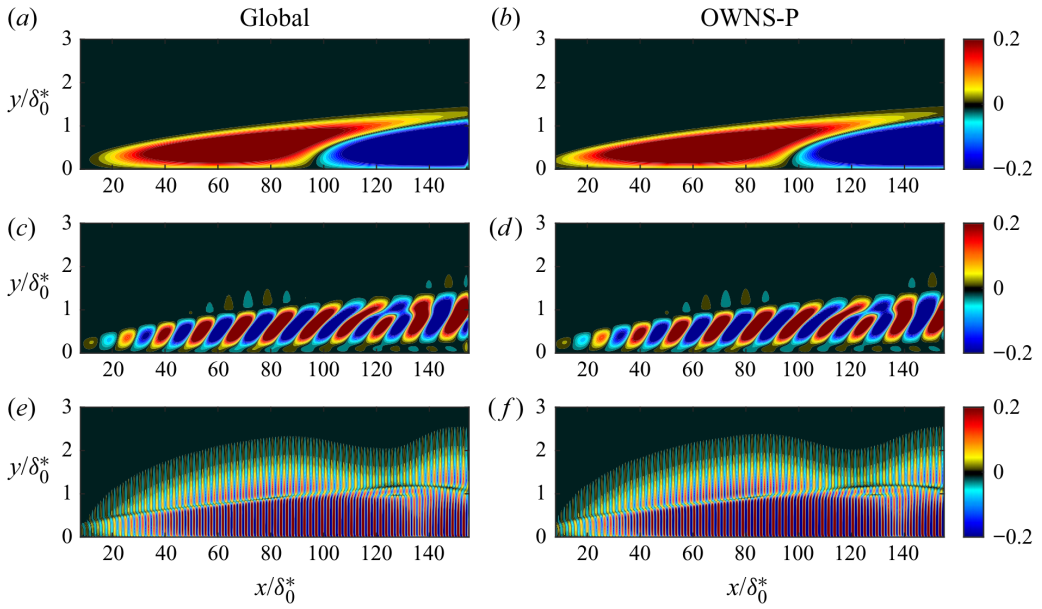

Figure 4.7: Streamwise velocity response for the first suboptimal mode calculated using the global and OWNS methods: (a,b) streaks; (c,d) oblique first mode; (e,f) 2D second mode. Figure from Towne, Rigas, Kamal, et al. (2022).

studied above. As expected, we see an increased number of wavepackets in the responses due to the orthogonality between optimal and suboptimal modes.

4.3 Validation of optimal OWNS to a Mach 1.5 turbulent jet

The last validation of the input-output OWNS framework corresponds to studying the optimal forcings and responses of a turbulent jet. Previous resolvent analyses of jets (Garnaud et al., 2013; Jeun, Nichols, and Jovanović, 2016; Schmidt et al., 2018; Lesshafft et al., 2019) illuminated a diverse set of physical phenomena, such as the Kelvin-Helmholtz instability, which results in large-scale coherent wavepackets (Jordan and Colonius, 2013), the Orr mechanism (Tissot et al., 2017; Schmidt et al., 2018), the lift-up mechanism (Nogueira et al., 2019; Pickering, Rigas, Nogueira, et al., 2020), and acoustic modes within the jet core (Tam and Hu, 1989; Towne, Cavalieri, et al., 2017). The complexity of the physics within the resolvent framework makes it a challenging test case, and thus we apply the optimal OWNS equations to the same Mach 1.5 turbulent jet from Sec. 3.2. The goal is to use OWNS to reproduce the optimal forcings and responses from the global approach at a fraction of the computational expensive. The results presented in this section are from Towne, Rigas, Kamal, et al. (2022).

4.3.1 Computational setup

Since the base flow is axisymmetric, the azimuthal direction is homogeneous and can be decomposed into Fourier modes. We elect to focus on the axisymmetric mode corresponding to azimuthal wavenumber $m = 0$, which is generally of most importance in jet aeroacoustics (Cavalieri et al., 2012; Chen and Towne, 2021), at $St = 0.26$ and 0.52. The computational details for the OWNS and global resolvent analyses are summarized in Table 4.2. The radial direction is discretized using the fourth-order central finite-difference scheme with higher concentration of points near the shear layer at $\eta = 0.5$ and 1D inviscid Thompson characteristic boundary conditions at the far-field (Thompson, 1987). Refer to Sec. B.1.2 for the centerline treatment of 3DF jets. The streamwise grid for the global resolvent computations is also discretized using the fourth-order central finite-difference scheme and is stretched near the inlet using a hyperbolic tangent function. Inlet and outlet sponges are used to model open boundaries for the global calculations, whereas the OWNS marches are streamwise-integrated using BDF2.

Table 4.2: Computational parameters used for the $M_j = 1.5$ optimal jet analyses.

ξ_{min}	ξ_{max}	η_{min}	η_{max}	N_ξ	N_η	N_b (OWNS only)
0.50	30	0.0143	16.97	1001	275	15

Furthermore, the input forcing is radially restricted to $\eta_{min} < \eta < \eta_{max}$ using the $\boldsymbol{\mathcal{B}_p}$ operator. We use $\eta_{min} = 0.0425$ to prevent the forcing from damaging the centerline pole conditions and η_{max} is defined as the radial location where the velocity is greater than 5% of the maximum jet velocity, i.e. the forcing is contained only within the jet layer. No constraints are applied for the output, i.e. $\boldsymbol{C_p} = \boldsymbol{I}$.

4.3.2 Results

The optimal $\mathscr{R}(p')$ from the OWNS and global resolvent analyses at $St = 0.26$ and 0.52 and $m = 0$ are shown in Fig. 4.8. The dominant instability at these frequencies is the Kelvin-Helmholtz instability in the near-field (Schmidt et al., 2018; Pickering, Rigas, Nogueira, et al., 2020) along with the far-field acoustic radiation. We also quantitatively compare the global and OWNS pressure responses at the jet lip-line $\eta = 0.5$ in Fig. 4.9. There is excellent agreement between the two methods, thereby substantiating the assumption of weak influence of the upstream-propagating waves in the OWNS parabolization.

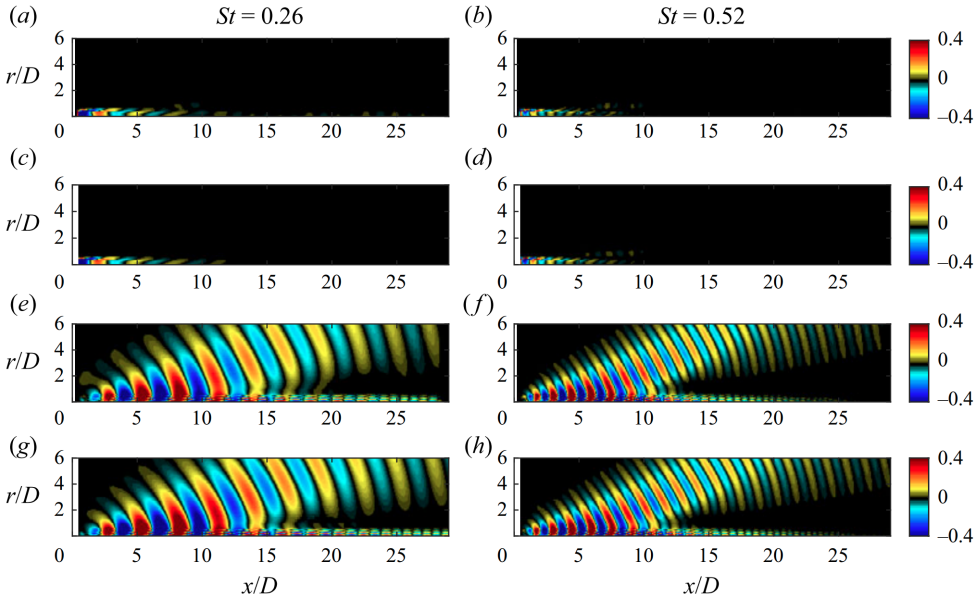

Figure 4.8: Optimal forcing (a-d) and response (e-h) for the $M_j = 1.5$ turbulent jet. Comparison between global (a,b,e,f) and OWNS (c,d,g,h). Contours of $\mathscr{R}(p')$ at $St = 0.26$ and $St = 0.52$ and $m = 0$ are shown. Figure from Towne, Rigas, Kamal, et al. (2022) where x/D and r/D correspond to ξ and η, respectively.

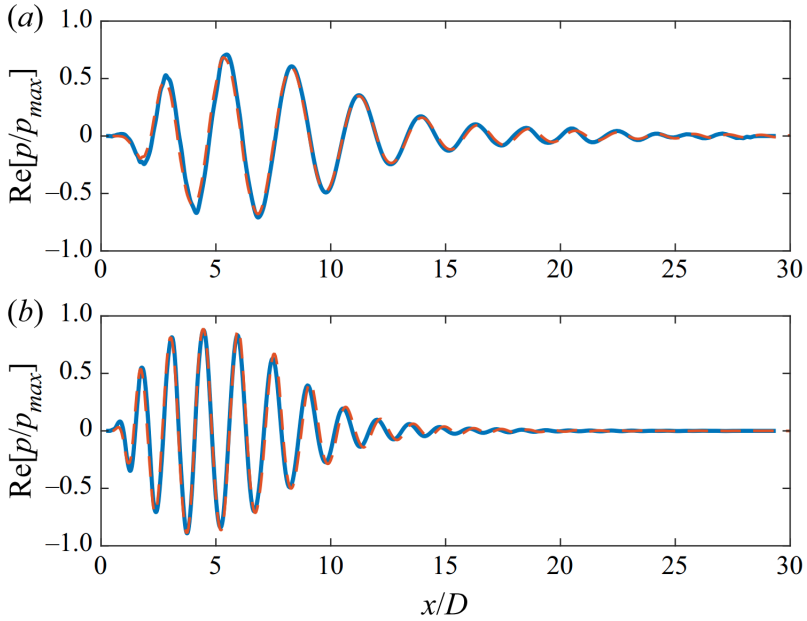

Figure 4.9: Optimal pressure response at the jet lip-line $\eta = 0.5$ for (a) $St = 0.26$; (b) $St = 0.52$ and $m = 0$. Solid and dashed lines correspond to global and OWNS solutions, respectively. Figure from Towne, Rigas, Kamal, et al. (2022) where x/D corresponds to ξ.

4.4 Application of optimal OWNS to the Mach 6 HIFiRE-5 elliptic cone

To assess the optimal OWNS framework for more complex geometries, we perform a 2D optimization ($\beta = 0$) along the centerline of the HIFiRE-5 elliptic cone with streamwise body curvature effects included and full global inputs and outputs ($\boldsymbol{\mathcal{B}_p} = \boldsymbol{C_p} = \boldsymbol{I}$). Results from this section are from Kamal, Rigas, et al. (2021), in which † denotes dimensional quantities rather than asterisks. Stability analyses along the centerline assuming spanwise homogeneity must be performed with caution, however, as the centerline vortices induce strong azimuthal variations in the near vicinity (Kamal, Rigas, et al., 2020; Choudhari et al., 2009).

4.4.1 Computational setup

The HIFiRE-5 elliptic cone in the present study is a 38.1% scale model with an axial length of 38.1 mm and an aspect ratio of 2:1 at the tip. The cone half-angles are 7.00 and 13.797 degrees along the minor (centerline) and major (attachment line) axes, respectively. The base flow is provided by The Boeing Company with the flow parameters summarized in Table 4.3. Note that the wall-normal domain increases in the ξ-direction. We focus our study on the centerline and treat the flow and disturbances there as locally two-dimensional. The origin of the curvilinear and global Cartesian coordinates correspond to the nose tip with a streamwise domain of $\Omega^\dagger = [0.0660, 0.294]$ m with $N_\xi \times N_\eta = 2000 \times 150$. Contour plots of $\bar{u}$ and $\overline{T}$ fields and wall-normal $\bar{u}$ profiles along the centerline are shown in Fig. 4.10.

Table 4.3: HIFiRE-5 flow parameters.

M_∞	$T_\infty^\dagger$ [K]	$T_w^\dagger$ [K]	$p_\infty^\dagger$ [Pa]	$Re_\infty^\dagger$ [1/m]
6.0	49.45	315	417.315	8.1×10^6

To properly resolve the instabilities near the wall and critical layer, we employ a grid stretching technique (Malik, 1990)

$$\eta = \frac{2\eta_i \eta_{max} \lambda}{\eta_{max} - (2\lambda - 1)(\eta_{max} - 2\eta_i)}, \tag{4.14}$$

where $0 \leq \lambda \leq 1$ (equidistant grid points). Using the above scheme, half the points in the η direction are placed between $\eta = 0$ and $\eta = \eta_i$.

No-slip ($u' = v' = 0$) and isothermal ($T' = 0$) boundary conditions are imposed at the wall for all calculations. At the wall, we solve the linearized continuity equation for ρ'. At the upper boundary, we impose 1D inviscid Thompson characteristic boundary conditions (Thompson, 1987) to prevent spurious numerical reflections.

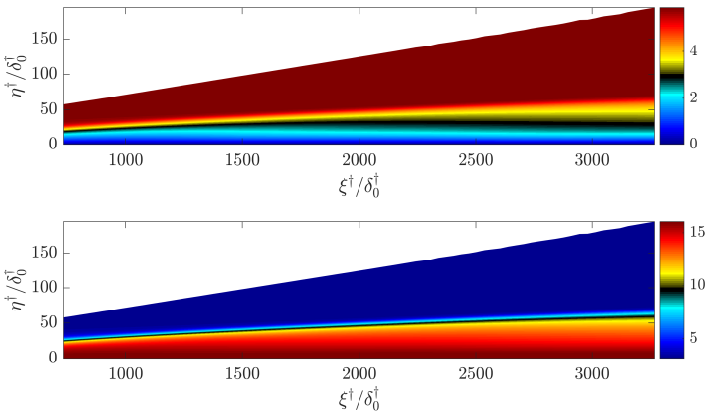

(a) $\bar{u}$ (top) and $\bar{T}$ (bottom) base-flow fields.

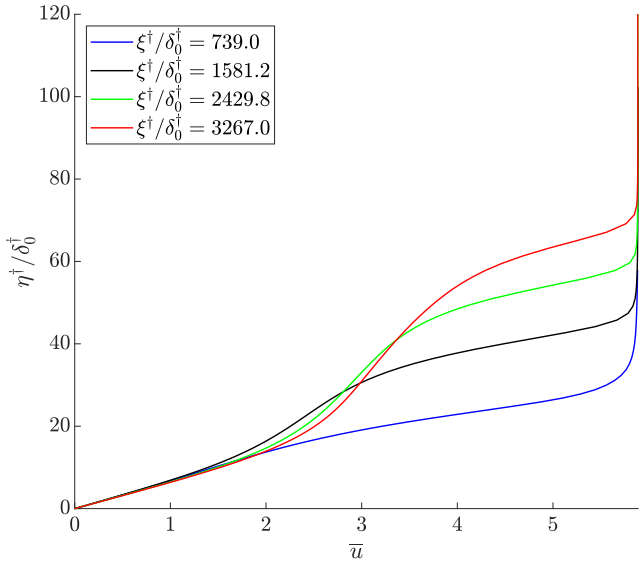

(b) $\bar{u}$ profiles at selected streamwise stations.

Figure 4.10: DNS-computed centerline base-flow solutions from The Boeing Company.

4.4.2 Results

4.4.2.1 Optimal forcings and responses

Although the highest LST N-factor for the centerline was shown to occur at $f^\dagger = 80$ kHz from Kamal, Rigas, et al. (2020), we perform a frequency sweep using OWNS to evaluate the optimal $f^\dagger$ since the parallel-flow assumption in LST introduces error, especially for complex flows. Using the optimal OWNS algorithm, which incorporates all nonparallel and non-modal effects, the optimal $f^\dagger$ is predicted lower at $f^\dagger = 70.0$ kHz as seen in the gain curve of Fig. 4.11. All HIFiRE-5 results hereafter in this section will correspond to this frequency.

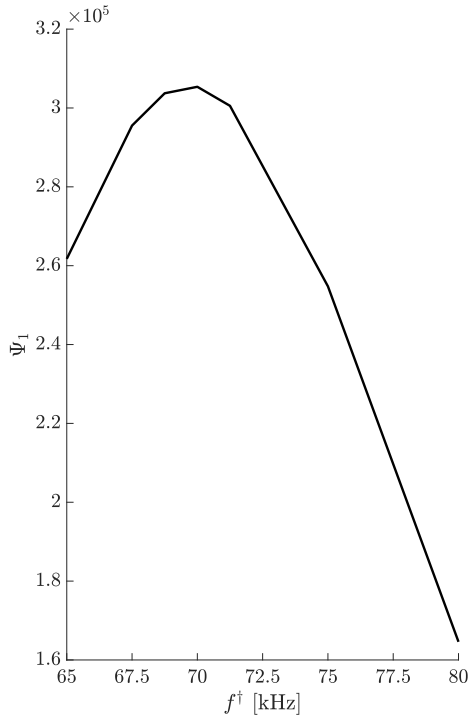

Figure 4.11: Gain curve for Mach 6 HIFiRE-5 elliptic cone with the conditions from Table 4.3 along the centerline at $\beta = 0$. Note the compact range of values on the x-axis as we are zoomed into a small frequency range near the optimal value.

Fig. 4.12 plots the optimal forcing and response fields. The spatial structures exhibit some resemblance to the second mode of the Mach 4.5 flat-plate boundary layer from Sec. 4.2, where the forcing is concentrated near the critical layer and the response contains hydrodynamic and thermodynamic amplification in the relative supersonic region near the wall, with the latter also observed near the critical layer. Furthermore, the response has a wavenumber that is within about 10% of the averaged theoretical second-mode wavenumber (see Fig. 4.13) which is defined as

$$\overline{(\alpha_r)}_{\text{th}} = \pi \left(\frac{1}{(\xi_{\mathbb{1}} - \xi_{\mathbb{0}})} \int_{\xi_{\mathbb{0}}}^{\xi_{\mathbb{1}}} \delta(\xi) \, \mathrm{d}\xi \right)^{-1}, \tag{4.15}$$

where the second-mode wavelength is approximately twice the boundary-layer thickness (Kendall, 1975; Stetson and Kimmel, 1992). However, there are also notable traits that are atypical of the second mode in the optimal forcing and responses.

In the forcing fields, the structures are upstream-tilted (against $\bar{u}$) which is characteristic of the Orr-mechanism but also situated between the relative sonic line and the critical layer (as opposed to centered about the critical layer as seen in the Mach 4.5 flat-plate validation case from Sec. 4.2). To explain this, we first note the relatively

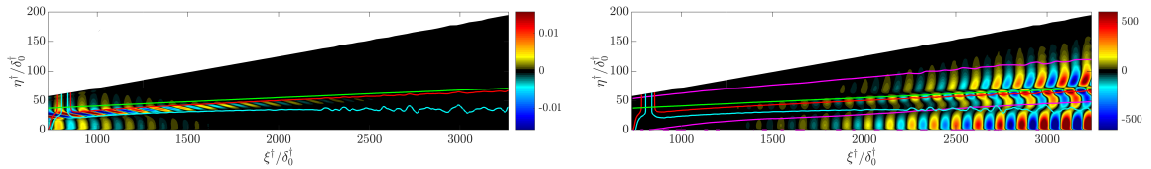

(a) $\mathscr{R}(f_\xi)$ (left) and $\mathscr{R}(u')$ (right).

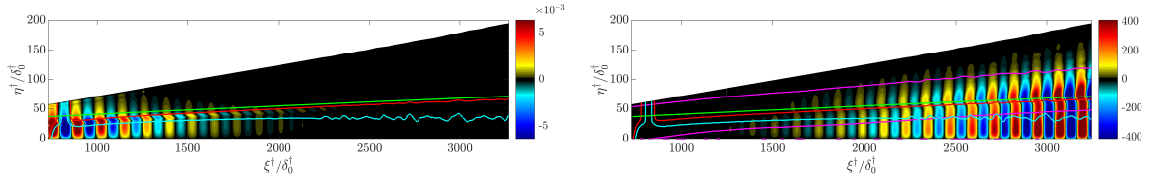

(b) $\mathscr{R}(f_\eta)$ (left) and $\mathscr{R}(v')$ (right).

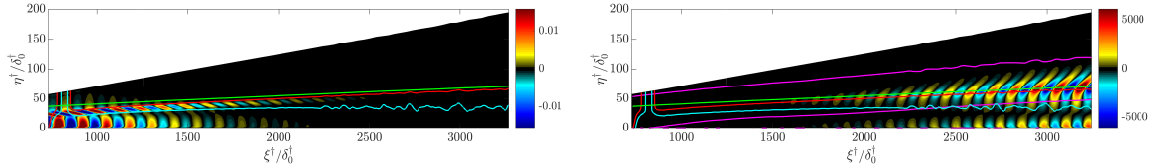

(c) $\mathscr{R}(f_T)$ (left) and $\mathscr{R}(T')$ (right).

Figure 4.12: Optimal OWNS forcing (left) and response (right) fields at $f^\dagger$ = 70.0 kHz for Mach 6 HIFiRE-5 elliptic cone. The red and cyan isocontours represent the critical layer and relative sonic line, i.e. where $\widetilde{M} = \frac{\bar{u}-c_\Phi}{\bar{a}}$ is 0 and -1, and the green and magenta isocontours represent the boundary-layer edge and $\bar{v} = 0$, respectively. Note that undulations of the critical layer and relative sonic line is due to the modulation of the phase speed since the OWNS methodology does not assume any wave-like ansatz (Kamal, Rigas, et al., 2020).

large positive $\bar{v}$ near the critical layer (see Fig. 4.14a) induced by the centerline vortices. Analogous to the upstream-tilting behavior, the Orr-mechanism, which extracts energy from the mean shear through the transport of momentum along the mean momentum gradient via the perturbed Reynolds stresses (Hack and Moin, 2017; Roy and Govindarajan, 2010), places these forcing structures below the critical layer (against $\bar{v}$) so that the mean flow advects them upwards into the region of maximum shear. Below these upstream-tilted structures, we observe forcing in the relative supersonic region to excite trapped acoustic waves that amplify as they propagate downstream.

The response fields also exhibit complex structures that evolve in the boundary layer. Fig. 4.15 provides snapshots of the $|u'|$ and $|T'|$ wall-normal profiles near the beginning, middle, and end of the march. At $\xi = 1144.3$, the $|u'|$ profile contains dual peaks which is emblematic of the second mode. However, as the disturbance evolves along the centerline, the profile transforms to contain three

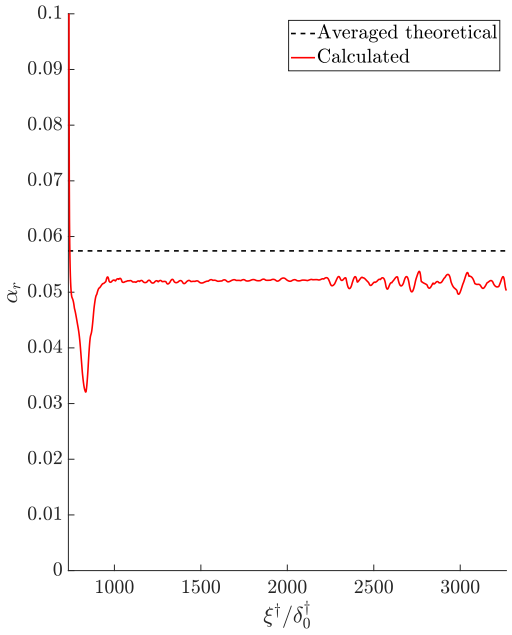

Figure 4.13: Comparison of the calculated and averaged theoretical second-mode wavenumbers for Mach 6 HIFiRE-5 elliptic cone.

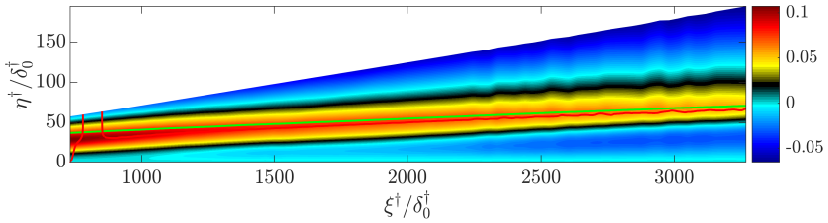

(a) Centerline wall-normal base flow $\bar{v}$.

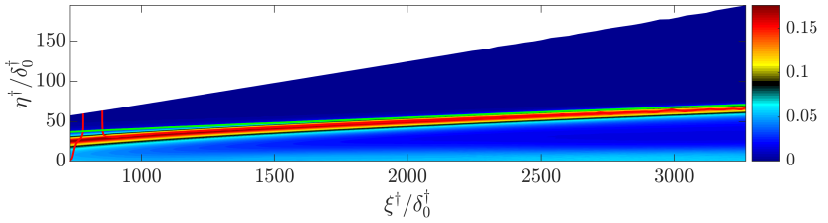

(b) Density-weighted shear $\bar{\rho}\frac{\partial \bar{u}}{\partial \eta}$.

Figure 4.14: Select base-flow quantities for Mach 6 HIFiRE-5 elliptic cone. The red and green isocontours represent the critical layer and boundary-layer edge, respectively.

peaks at $\xi = 1872.5$ and further evolves to contain four peaks by the end of the domain at $\xi = 3267.0$. These peaks are associated with the shear layers in the base flow (see Fig. 4.14b), where local peaks below the critical layer are contained in regions bounded by the wall and the two $\bar{u}$ inflectional points (refer to Fig. 4.10b).

Note that the near-wall $\bar{u}$ inflectional point nearly coincides with the relative sonic line. The common peak throughout the domain occurs at the critical layer where we observe upstream-tilted structures between the second $\bar{u}$ inflectional point and the boundary-layer edge as seen in Fig. 4.12a. Finally, starting from near the middle of the streamwise domain, we observe an additional peak outside the boundary layer which is associated with disturbances near the critical layer being advected upwards due to the large positive $\bar{v}$ and effectively being trapped in a region bounded by where $\bar{v} = 0$ in the freestream. This is further illustrated in Fig. 4.15a in which the peak at the critical layer relative to the freestream disturbances decreases from $\xi = 1872.5$ to $\xi = 3267.0$ due to continual wall-normal advection of energy. In contrast to the topological change in $|u'|$ profiles, the $|T'|$ profiles retain their dual peaks throughout the streamwise domain which is characteristic of the second mode as seen in Fig. 4.15b. However, the subsonic rope-like structures corresponding to the second peak, although initially centered about the critical layer, advect upwards relative to the critical layer while also increasing in magnitude relative to the near-wall structures. The latter observation is most likely due to the Orr-mechanism most efficiently extracting energy from the base flow near the critical layer where the highest shear is observed.

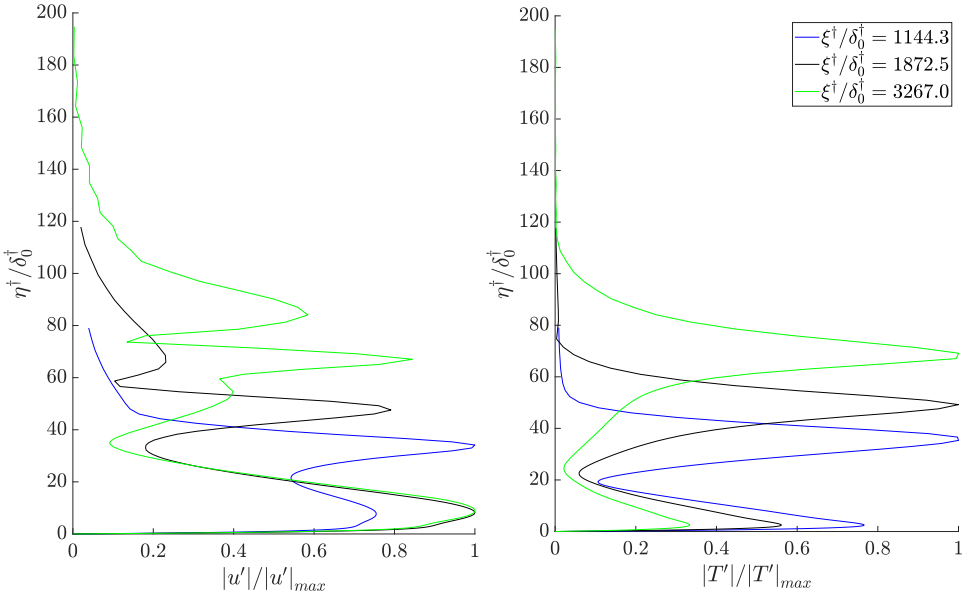

(a) $|u'|$ profiles. **(b) $|T'|$ profiles.**

Figure 4.15: Wall-normal $|u'|$ and $|T'|$ profiles at select streamwise stations for Mach 6 HIFiRE-5 elliptic cone.

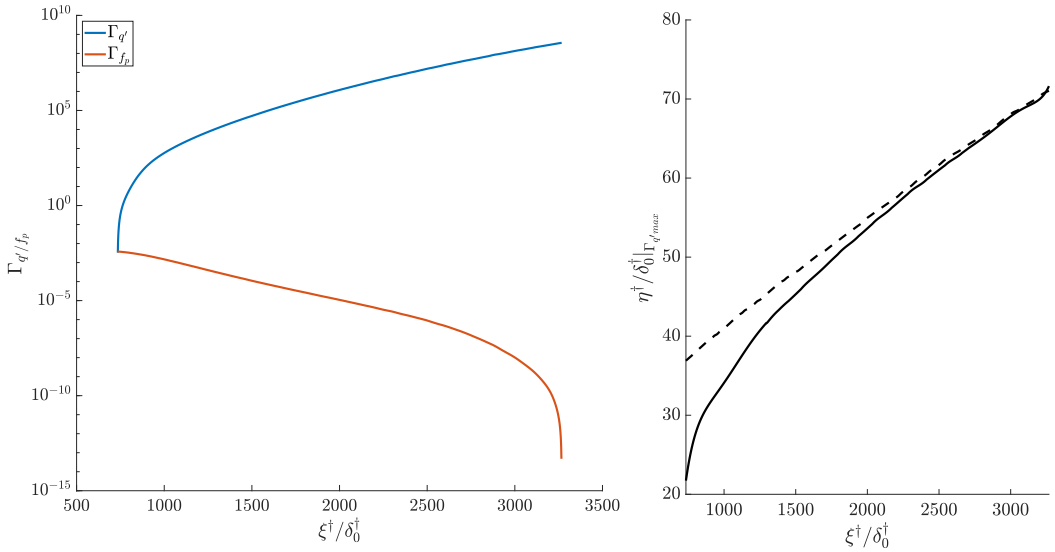

(a) Input forcing Γ_{f_p} and response $\Gamma_{q'}$ energy density functions.

(b) Wall-normal ordinate at which $\Gamma_{q'}|_{max}$ occurs at each streamwise station. The dashed line represents the boundary-layer edge.

Figure 4.16: Streamwise evolution of optimal energy growth for Mach 6 HIFiRE-5 elliptic cone.

4.4.2.2 Energetics

In order to examine the energetics of the responses, we first define the local Chu energy (Chu, 1965)

$$\mathscr{C} = \frac{1}{2}\left(\frac{R\overline{T}}{\overline{\rho}}\rho'^2 + \overline{\rho}|\mathbf{u}'|^2 + \frac{R\overline{\rho}}{\overline{T}\left(\gamma(\overline{T})-1\right)}T'^2\right), \tag{4.16}$$

with corresponding energy density functions Γ_{f_p} and $\Gamma_{q'}$ for the inputs and responses, respectively, as

$$\Gamma_{f_p/q'}(\xi) = \int \mathscr{C}_{f_p/q'}\,\mathrm{d}A. \tag{4.17}$$

The streamwise evolution of these quantities is shown in Fig. 4.16a. Almost all the forcing energy is concentrated near the inlet with relatively little spatial support thereafter as shown by the exponential decay. The response growth rate, however, exhibits faster than exponential growth near the inlet before assuming a near-constant exponential amplification from $\xi \approx 1320$. This is characteristic of convective-type non-normality where there is streamwise separation between the input and response as seen in the forcing and response fields in Fig. 4.12.

To further analyze the cross-stream energy distribution of the response, we compute the wall-normal distance at which $\Gamma_{q'}$ reaches its maximum at each streamwise station. The result is plotted in Fig. 4.16b. From the inlet at $\xi \approx 734$ to $\xi \approx 1320$, the wall-normal ordinate evolves rapidly but monotonically from deep in the boundary layer towards the boundary-layer edge corresponding to the initial ramp-up of $\Gamma_{q'}$ in Fig. 4.16a. Thereafter, the peak-energy location progresses upwards in the η-direction almost linearly, coinciding to where the response disturbance energy undergoes exponential growth. Referring to Fig. 4.14b, this streamwise-progression is likely favorable since the flow exhibits the highest shear near the boundary-layer edge where energy can be most efficiently harvested from the base flow via the Orr-mechanism.

4.5 Application of optimal OWNS to a Mach 6 highly cooled flat-plate boundary layer

In this section, we present results from Kamal, Rigas, et al. (2022), where OWNS is used to conduct a parametric study of the global optimal forcing and responses of a Mach 6 flat-plate boundary layer by varying the frequency and wall temperature. Specifically, we tackle the global forced receptivity problem with highly cooled-wall conditions by parametrically analyzing the unconstrained optimal forcings and corresponding responses with $\boldsymbol{\mathcal{B}_p} = \boldsymbol{C_p} = \boldsymbol{I}$. Here, "forced receptivity" refers to subjecting the boundary layer to input disturbances of the correct frequency-wavelength combination to directly excite instabilities (Saric, Reed, and Kerschen, 2002). Lastly, since the second-mode amplification rates are largest for 2D perturbations (Mack, 1975), we will restrict our analysis to $\beta = 0$.

4.5.1 Computational setup

The base flow is computed using the Howarth–Dorodnitsyn transformation of the compressible Blasius equations under the assumption $d\bar{p} = 0$ at wall-temperature ratios $T_w/T_\infty \in [0.5, 7.02]$. Note that these wall temperatures span high to moderate to no wall-cooling. The fluid is assumed to be calorically perfect air with $\gamma = 1.4$ and $Pr = 0.72$ with viscosity and thermal conductivity calculated using Sutherland's law

$$\mu^* = \frac{1.458 T^{*3/2}}{T^* + S^*} \cdot 10^{-6}, \tag{4.18}$$

where $S^* = 110.4$ K.

The computational domain is summarized in Table 4.4, where the origin of the global x and y Cartesian coordinates is placed at the plate leading edge. Note that $x = \xi$

and $y = \eta$ for the present flat-plate geometry. The grid resolution was determined based on OWNS computations of a similar configuration from Kamal, Rigas, et al. (2020). It is important to recognize that if the global approach, which requires an SVD of the resolvent operator, was instead being used to perform these optimal computations on such a large grid, the computational cost would be considerably higher. For OWNS, the linear dimension of the system of equations at each step is $n_O \approx 2N_bN_qN_yN_z$, whereas in the global approach $n_g = N_qN_xN_yN_z$, where N_q and N_b are the number of state variables and recursion parameters (Towne and Colonius, 2015), respectively. This yields a substantial computational complexity reduction by using OWNS.

Finally, the flow and stability parameters are given in Table 4.5, which were originally derived from Chuvakhov and Fedorov (2016). Note that in addition to OWNS computations, we will perform LST (using CSTAT) at representative streamwise stations to elucidate the underlying modal dynamics from the optimal calculations.

Table 4.4: Computational domain used for flat-plate optimizations.

x^*_{min} [m]	x^*_{max} [m]	y^*_{min} [m]	y^*_{max} [m]	N_x	N_y
0.0388	0.1721	0.0	0.005	8001	200

Table 4.5: Flat-plate flow and stability parameters.

$F \cdot 10^4$	M_∞	T_w/T_∞	T^*_∞ [K]	p^*_∞ [Pa]	Re^*_∞ [1/m]
0.60 – 2.06	6.0	0.5 – 7.02	300	20000	2.61×10^7

To properly resolve the instabilities near the wall and critical layer, we employ a grid stretching technique (Malik, 1990)

$$y = \frac{2y_i y_{max}\lambda}{y_{max} - (2\lambda - 1)(y_{max} - 2y_i)}, \tag{4.19}$$

where $0 \leq \lambda \leq 1$ (equidistant grid points). Using the above scheme, half the points in the y direction are placed between $y = 0$ and $y = y_i$.

No-slip ($u' = v' = 0$) and isothermal ($T' = 0$) boundary conditions are imposed at the wall for all calculations. At the wall, we solve the linearized continuity equation for ρ'. At the upper boundary, we impose 1D inviscid Thompson characteristic boundary conditions (Thompson, 1987) to prevent spurious numerical reflections.

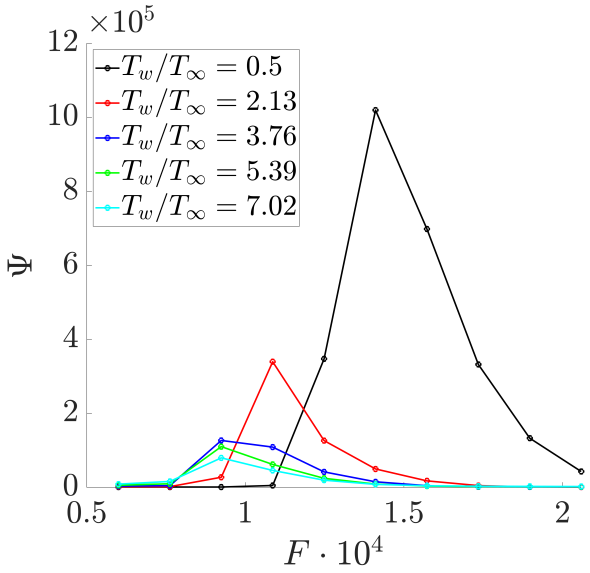

Figure 4.17: Gain from optimal computations versus frequency at various wall-temperature ratios for 2D Mach 6 flat-plate boundary layer.

4.5.2 Results

We analyze the optimal response for different amounts of wall-cooling across a range of frequencies. The overall corresponding gain Ψ of the linearized system is plotted in Fig. 4.17. As is confirmed in more detailed analysis below, the 2D first mode occurring at low frequencies results in comparably small gains, while the Mach 6 boundary layer is more receptive to the 2D second mode for $F > 0.76 \cdot 10^{-4}$. As expected, the second mode is increasingly destabilized with higher wall-cooling, with $F_{\text{opt}} = 0.92 \cdot 10^{-4}$ for moderate to no wall-cooling ($T_w/T_\infty \geq 3.76$). When the wall is cooled even further ($T_w/T_\infty \leq 2.13$), the boundary layer shrinks sufficiently enough to cause F_{opt} to increase due to the inverse relationship between frequency and length scale of the second mode (Parziale, Shepherd, and Hornung, 2015)).

To analyze the amplification mechanisms at play across Fig. 4.17, we examine in the next section the optimal inputs/responses for three characteristic frequencies of $F = 0.60 \cdot 10^{-4}$, $1.09 \cdot 10^{-4}$, and $2.06 \cdot 10^{-4}$ at $T_w/T_\infty = 0.5$ (highly cooled) and 7.02 (adiabatic). We compare the behavior of the global solutions at selected streamwise stations to LST results in order to establish connections between global and local amplification mechanisms. We also analyze the maximally resonant case of $F = 1.41 \cdot 10^{-4}$ and $T_w/T_\infty = 0.5$.

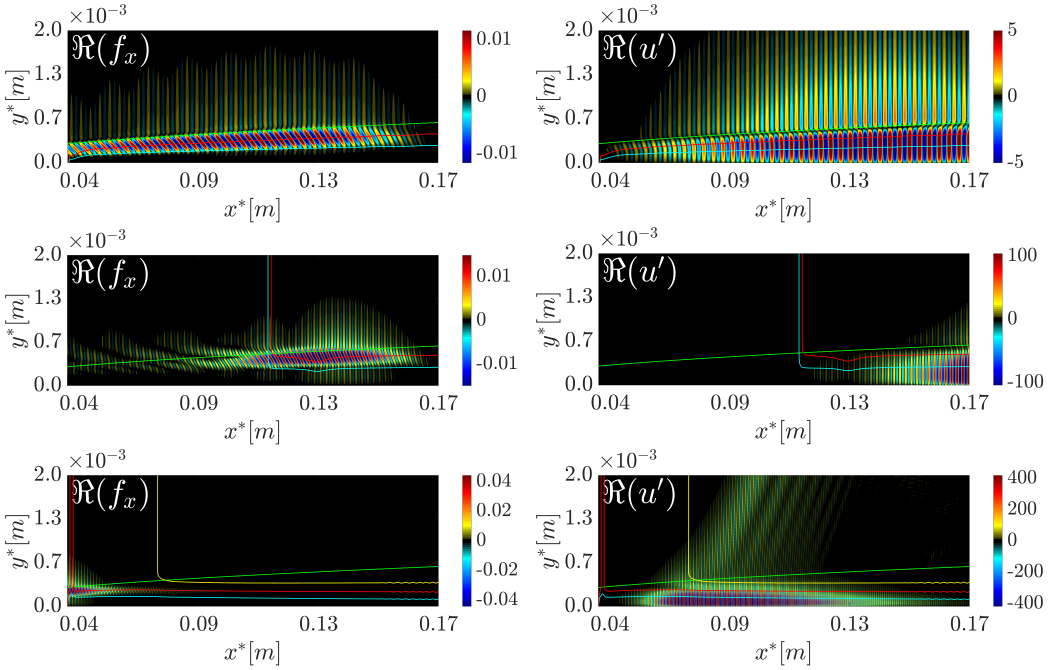

Figure 4.18: Optimal forcings of the x-momentum equation (left) and corresponding u' responses (right) for $F = 0.60 \cdot 10^{-4}$, $1.09 \cdot 10^{-4}$, and $2.06 \cdot 10^{-4}$ from top to bottom at $T_w/T_\infty = 0.5$. The cyan, red, and yellow isocontours represent the lower relative sonic line, critical layer, and the upper relative sonic line, i.e. where $\widehat{M} = \frac{\bar{u}-c_\Phi}{\bar{a}}$ is -1, 0, and 1, and the green isocontours represent the boundary-layer edge, respectively.

4.5.2.1 Optimal input and responses: highly cooled wall ($T_w/T_\infty = 0.5$)

The x-momentum and energy forcings with corresponding responses are plotted in Figs. 4.18 and 4.19 for $T_w/T_\infty = 0.5$. At $F = 0.60 \cdot 10^{-4}$, the input fields contain short-wavelength forcing concentrated between the boundary-layer edge and the relative sonic line with lower amplitude forcing near the wall and in the free-stream. This yields a first-mode/Mode S response that is strongly stabilized due to the wall-cooling (Hirschel, 2005). In fact, our LST results indicate that this mode remains stable throughout the domain, which explains the elongated spatial support in the forcing fields needed to produce the optimal response. The presence of the (damped) first mode is further corroborated by comparing the OWNS wall-normal amplitude profiles to LST eigenfunctions at $x^* = 0.17$ m in Fig. 4.22. Note that to compare OWNS to LST, both state vectors were locally normalized to have unitary L2-norm, i.e. $||\mathbf{q}'_\mathbf{x}||_2 = 1$. Although the LST profiles of Mode S for $F = 0.60 \cdot 10^{-4}$ and $T_w/T_\infty = 0.5$ nearly coincide with those from the OWNS computations, the non-modal growth in the optimal responses could not have been predicted by LST.

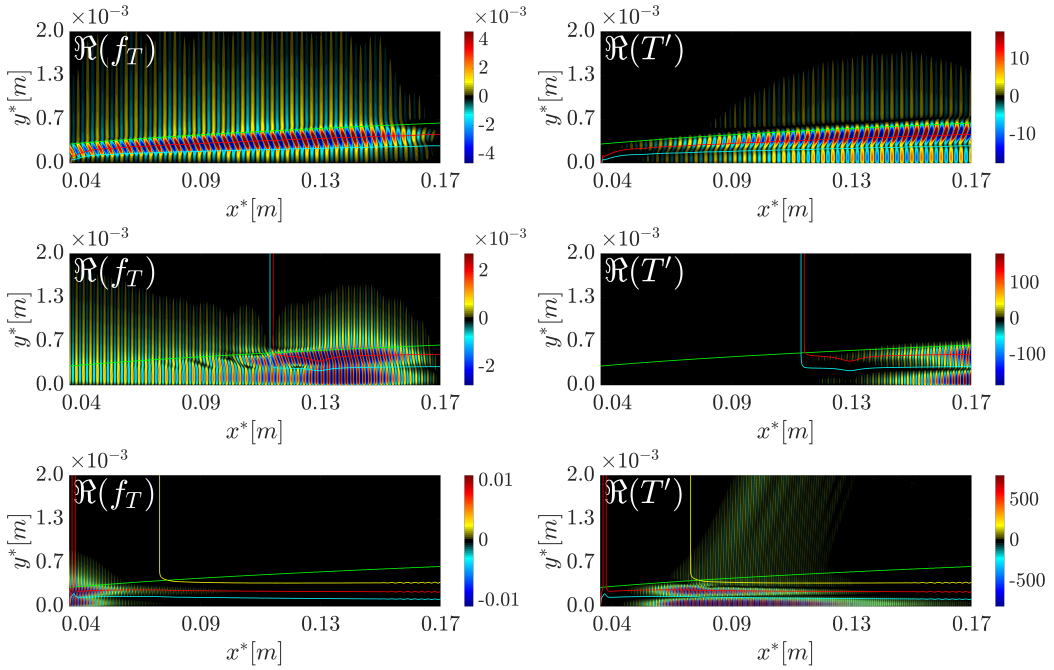

Figure 4.19: Optimal forcings of the energy equation (left) and corresponding T' responses (right) for $F = 0.60 \cdot 10^{-4}$, $1.09 \cdot 10^{-4}$, and $2.06 \cdot 10^{-4}$ from top to bottom at $T_w/T_\infty = 0.5$. The cyan, red, green, and yellow isocontours correspond to those from Fig. 4.18.

When the frequency is increased to $F = 1.09 \cdot 10^{-4}$, the forcing field is more complex and contains upstream-tilted structures before $x^* \approx 0.10$ m, which appears to excite Mode F1 and Mode S waves. From the inlet region, the phase speed of Mode F1 decreases while that of Mode S increases, and at $x^* \approx 0.13$ m, Mode F1 crosses the continuous vorticity/entropy branch. At this point, the phase speeds of Mode F1 and Mode S begin to align, resulting in the disturbance amplification observed in the response fields of Figs. 4.18 and 4.19. At $x^* \gtrapprox 0.15$ m, Modes F1 and S are synchronized, i.e. phase speeds (nearly) coincide, with the former mode being the unstable second mode. The input fields support the second-mode growth from $x^* \approx 0.12$ m via strong forcing near the critical layer and the wall to excite the subsonic rope-like structures and the trapped acoustic waves, respectively. Note that the forcing precedes the response due to *convective-type* non-normality where there is a streamwise spatial lag between the input and response (Sipp et al., 2010). Lastly, comparing the OWNS wall-normal amplitudes to the LST profiles at $x^* = 0.17$ m for $F = 1.09 \cdot 10^{-4}$ and $T_w/T_\infty = 0.5$ in Fig. 4.22 further substantiates the second mode (Mode F1) as the dominant instability in the optimal solutions.

At the highest frequency of $F = 2.06 \cdot 10^{-4}$, the input forcing is concentrated

near the inlet region due to the inverse relationship between frequency and length scale of the second mode (Parziale, Shepherd, and Hornung, 2015)). That is, compared to $F = 1.09 \cdot 10^{-4}$, we expect the second-mode growth to occur further upstream where the boundary layer is thinner and due to convective non-normality, the forcing is pushed even further upstream. Similar to the downstream input region of $F = 1.09 \cdot 10^{-4}$, forcing is predominantly concentrated near the critical layer and the wall to excite the subsonic rope-like structures and the trapped acoustic waves, respectively. From LST, Mode F1's phase speed decreases as it propagates downstream from the inlet and at $x^* \approx 0.04$ m, it synchronizes with Mode S and becomes the unstable second mode as seen by growth of disturbances in the response fields of Figs. 4.18 and 4.19. After de-synchronizing with Mode S, the phase speed of the unstable Mode F1 continues to decrease until it eventually synchronizes with the slow acoustic spectrum at $x^* \approx 0.07$ m. At this point, a new stable discrete mode is generated and the unstable Mode F1 now has a supersonic phase speed and is referred to as the supersonic mode (Knisely and Zhong, 2019a). The appearance of the latter mode corresponds to the emergence of the upper relative sonic line in Figs. 4.18 and 4.19 and the subsequent acoustic radiation from the boundary layer. The supersonic mode remains unstable until $x^* \approx 0.085$ m, but continues to be phase-speed locked to the stable discrete mode until the latter coalesces with the slow acoustic spectrum at $x^* \approx 0.108$ m. Contrasting to $F = 0.60 \cdot 10^{-4}$ or $F = 1.09 \cdot 10^{-4}$, the optimal wall-normal amplitude profiles at $x^* = 0.17$ m in Fig. 4.22 exhibit larger discrepancies to LST eigenfunctions of Mode F1, presumably due to the resonant-like interactions occurring between the supersonic mode and the slow acoustic spectrum and historical effects from interacting with the stable discrete mode further upstream. Discrepancies between DNS and LST when analyzing the supersonic mode excited via modal interactions were similarly reported in Knisely and Zhong (2019b). In essence, LST's inability to resolve inter-modal interactions renders it unreliable for these complex disturbance dynamics. Finally, the oscillations observed in the free-stream for both OWNS and LST further substantiate the presence of the supersonic mode (Knisely and Zhong, 2019a).

4.5.2.2 Optimal input and responses: adiabatic wall ($T_w/T_\infty = 7.02$)

Similar to the $T_w/T_\infty = 0.5$ case, comparisons to LST eigenfunctions at selected streamwise positions is helpful in explaining the observed optimal responses. At the lowest frequency of $F = 0.60 \cdot 10^{-4}$, Mode S is unstable at the inlet and remains

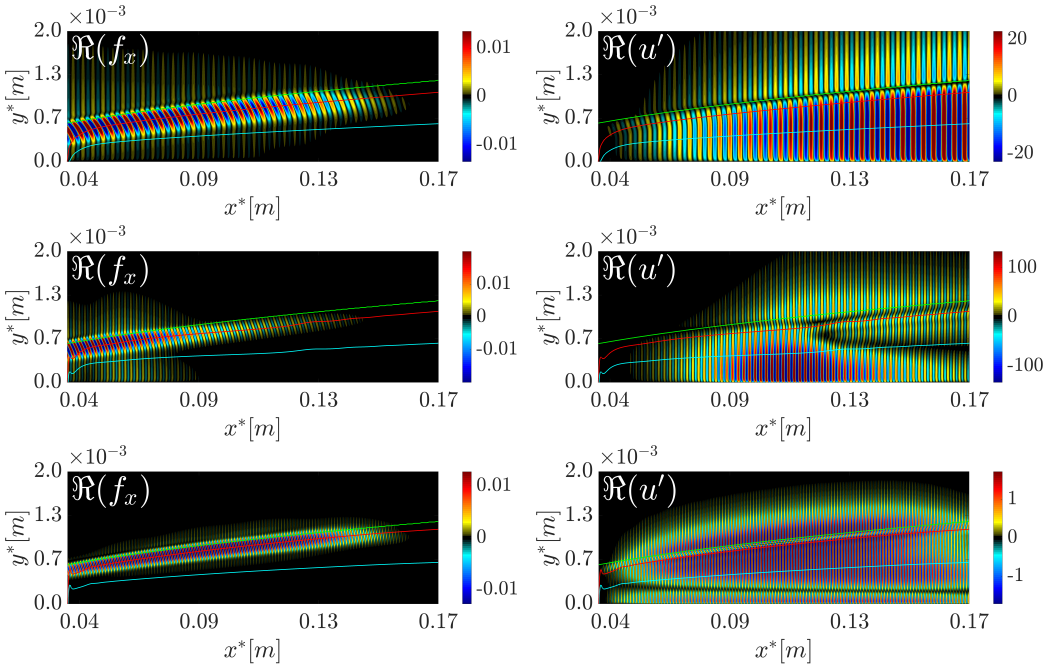

Figure 4.20: Optimal forcings of the x-momentum equation (left) and corresponding u' responses (right) for $F = 0.60 \cdot 10^{-4}$, $1.09 \cdot 10^{-4}$, and $2.06 \cdot 10^{-4}$ from top to bottom at $T_w/T_\infty = 7.02$. The cyan, red, and green isocontours correspond to those from Fig. 4.18.

so until $x^* \approx 0.105$ m. This is reflected in the input fields of Figs. 4.20 and 4.21, where short-wavelength forcing is concentrated near the critical layer with weaker inputs near the wall and free-stream to strictly excite Mode S waves. As expected, the warmer wall *destabilizes* the first mode (recall that Mode S was stable at $F = 0.60 \cdot 10^{-4}$ for $T_w/T_\infty = 0.5$). Thus, the optimal response is obtained with a relatively less extensive spatial forcing field. Although Mode F1 branches off the fast acoustic spectrum, it does not pass through the continuous vorticity/entropy branch by the end of the domain. Therefore, the response fields solely contain Mode S waves, which is further substantiated by the excellent agreement of the LST eigenfunctions of Mode S to the OWNS amplitude profiles in Fig. 4.22.

When F is increased to $1.09 \cdot 10^{-4}$, LST results predict the presence of both Modes F1 and S from the inlet, with Mode S becoming unstable by $x^* \approx 0.062$ m as its phase speed increases prior to synchronizing with Mode F1. Consequently, the input fields in Figs. 4.20 and 4.21 contain the necessary forcing to excite Mode S waves only near the inlet region (until $x^* \approx 0.045$ m). As the phase speed of Mode F1 continues to decrease further downstream, it eventually crosses the continuous vorticity/entropy branch and synchronizes with the (unstable) Mode S at $x^* \approx 0.078$

m in which the latter then becomes the second mode. The input fields support the second-mode growth in a similar fashion to $T_w/T_\infty = 0.5$ with strong forcing near the critical layer and the wall. After the two modes de-synchronize further downstream, the second mode (Mode S) stabilizes at $x^* \approx 0.12$ m, which corresponds to acoustic waves no longer reflecting between the wall and relative sonic line in Fig. 4.21. Finally, we note the excellent agreement of the LST eigenfunctions of Mode S to that of the OWNS amplitude profiles in Fig. 4.22. This illustrates the dominance of modal instabilities in the optimal computations.

At the highest frequency of $F = 2.06 \cdot 10^{-4}$, LST results indicate the presence of both Modes F1 and S by $x^* \approx 0.06$ m, in which the former is characterized by a strong T' peak near the wall and weaker peaks at and below the critical layer. Conversely, Mode S has a strong T' peak at the critical layer and a weaker peak near the wall. Due to the adiabatic-wall boundary condition, the input fields in Figs. 4.20 and 4.21 reflect preferential excitation of Mode S waves with strong forcing near the critical layer. Nevertheless, both modes are excited and as they propagate downstream, the phase speeds of Modes F1 and S decrease and increase, respectively, and by $x^* \approx 0.165$ m, Mode F1 has crossed through the continuous vorticity/entropy branch and synchronized with Mode S. A fundamental distinction from the synchronization of previous cases is that *both* modes are stable. Consequently, the elongated spatial forcing is required to sustain excitation of Modes F1 and S and their inter-modal interactions toward the end of the domain. Moreover, the interaction between the two stable modes causes an additional "zero" to appear in the wall-normal $\mathscr{R}(p')$ profile above the relative sonic line near the outlet (see Fig. 4.21). Although it may be tempting to categorize this as the third mode, Mack (1984) requires the two zeros to be situated *below* the relative sonic line for such a classification. Thus, the increase in nulls is attributed to non-modal effects. Lastly, although the LST eigenfunctions for Mode S in Fig. 4.22 capture the general profile of the OWNS amplitudes, notable differences are still observed. This is once again due to the inability of LST to resolve any inter-modal interactions.

As a final remark, a common observation amongst all frequencies for both $T_w/T_\infty = 0.5$ and 7.02 is the presence of the non-modal Orr mechanism. This manifests itself as upstream-tilted structures in the input fields that are then rotated by the base flow as energy is extracted from the mean shear along the mean momentum gradient via the perturbed Reynolds stresses (Hack and Moin, 2017; Roy and Govindarajan, 2010).

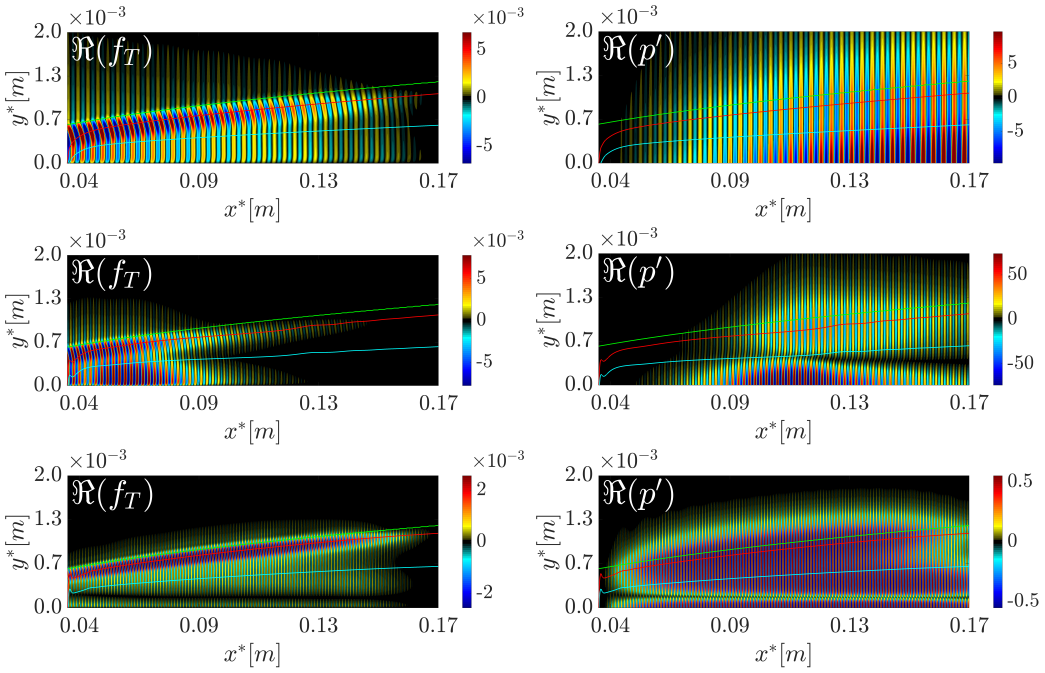

Figure 4.21: Optimal forcings of the energy equation (left) and corresponding p' responses (right) for $F = 0.60 \cdot 10^{-4}$, $1.09 \cdot 10^{-4}$, and $2.06 \cdot 10^{-4}$ from top to bottom at $T_w/T_\infty = 7.02$. The cyan, red, and green isocontours correspond to those from Fig. 4.18.

4.5.2.3 Energetics

As mentioned previously, although LST provides insight into the modal dynamics, it does not predict non-modal growth which occurs due to interaction of stable modes. Thus, to comprehensively analyze the streamwise evolution of the disturbances, the Chu-energy density functions Γ_f and $\Gamma_{q'}$ (as defined in Sec. 4.4.2 where $\Gamma_f = \Gamma_{f_p}$) are plotted in Fig. 4.23 for $T_w/T_\infty = 0.5$ and 7.02 at $F = 0.60 \cdot 10^{-4}$, $1.09 \cdot 10^{-4}$, and $2.06 \cdot 10^{-4}$. After the initial ramp-up of $\Gamma_{q'}$ from introducing the input forcing at $F = 0.60 \cdot 10^{-4}$ and $T_w/T_\infty = 0.5$, the response energy grows and decays in a similar fashion to the input energy. The absence of self-sustaining disturbance-energy growth suggests a strictly non-modal response, which is expected since the first mode is stabilized with wall cooling. In contrast, at $T_w/T_\infty = 7.02$, the input forcing is concentrated near the inlet and decays thereafter, but the response energy continuously grows until the end of the domain. This modal-like behaviour in the response is because the first mode is relatively destabilized under the adiabatic-wall thermal condition.

When the frequency is increased to $F = 1.09 \cdot 10^{-4}$, at $T_w/T_\infty = 0.5$, most of the input energy is concentrated near the end of the domain where the second mode is present.

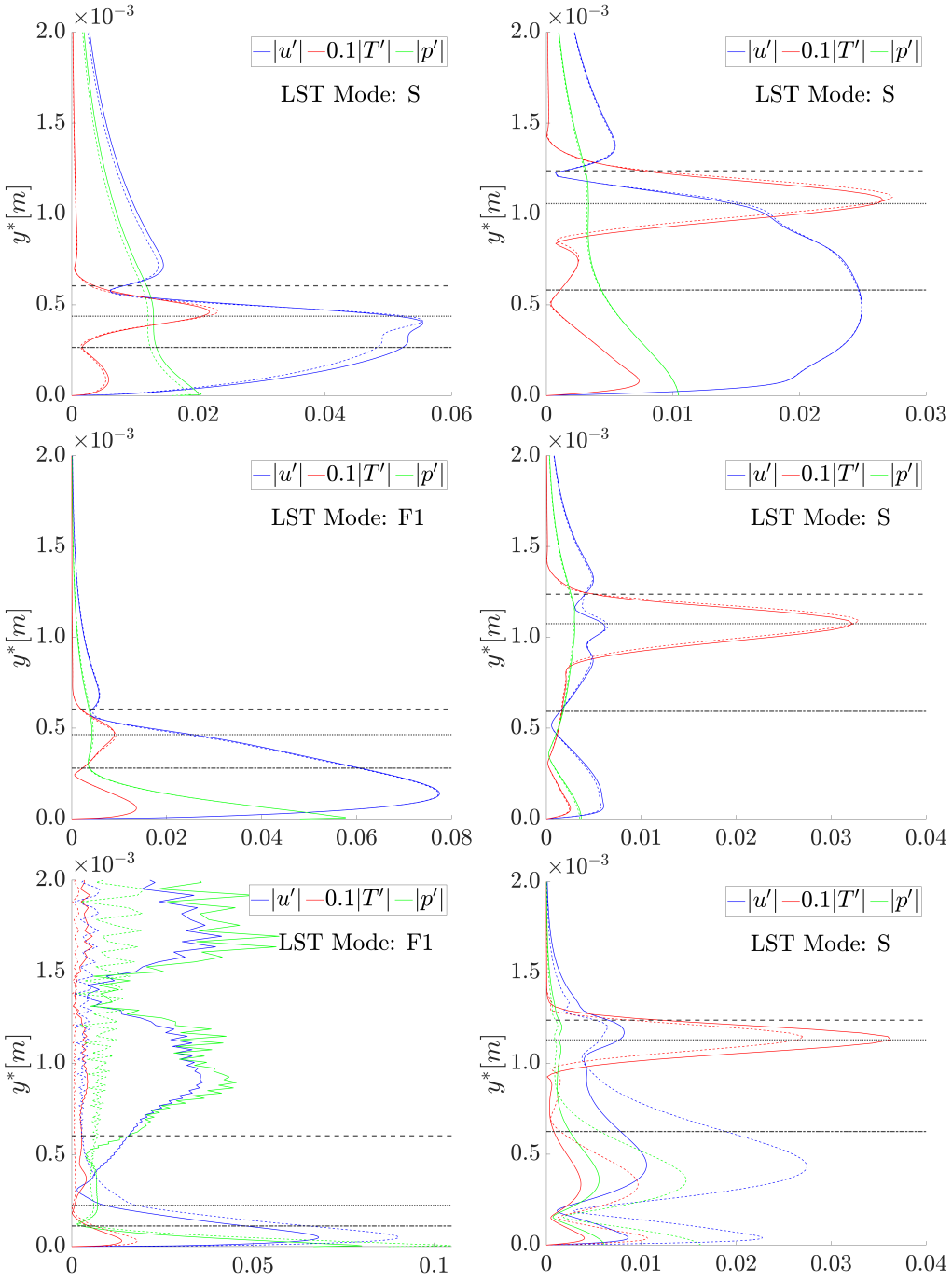

Figure 4.22: Wall-normal amplitude profiles at $x^* = 0.17$ m for $F = 0.60 \cdot 10^{-4}$, $1.09 \cdot 10^{-4}$, and $2.06 \cdot 10^{-4}$ from top to bottom at $T_w/T_\infty = 0.5$ (left) and $T_w/T_\infty = 7.02$ (right). Colored solid and dashed lines correspond to optimal and LST computations, respectively. Boundary-layer edge (- - -), critical layer (·····), and lower relative sonic line (-·-·).

Consequently, the response energy initially exhibits oscillatory behaviour likely due to destructive interference between Modes F1 and S before the former passes through the continuous vorticity/entropy branch at $x^* \approx 0.13$ m and synchronizes with Mode S to become the unstable second mode. Thereafter, $\Gamma_{q'}$ increases sharply due to the second-mode amplification. In the case of $T_w/T_\infty = 7.02$, the input energy is conversely concentrated near the inlet to optimally excite the unstable Mode S (first mode) which becomes the second mode once it synchronizes with Mode F1 at $x^* \approx 0.078$ m. The response energy therefore increases while the first/second modes are unstable until $x^* \approx 0.12$ m, after which the second mode stabilizes and the disturbance energy wanes.

Finally, at the highest frequency of $F = 2.06 \cdot 10^{-4}$ and $T_w/T_\infty = 0.5$, the input energy decreases rapidly from the inlet, but is accompanied with a sharp increase in $\Gamma_{q'}$ due to the second-mode growth. At $x^* \approx 0.07$ m, the response energy begins to decrease due to Mode F1 synchronizing with the slow acoustic spectrum, which initiates the acoustic radiation from the boundary layer. It is interesting to note that while wall-cooling destabilizes the second mode, this acoustic radiation provides a mechanism by which disturbance energy is transferred out of the boundary layer. In the case of adiabatic wall ($T_w/T_\infty = 7.02$), since both Modes F1 and S are stable throughout the domain, the input and response energy profiles are emblematic of the non-modal response at $F = 0.60 \cdot 10^{-4}$ and $T_w/T_\infty = 0.5$, where the response energy mimics the growth and decay of the input energy.

4.5.2.4 Maximal amplification: $\mathbf{F = 1.41 \cdot 10^{-4}}$ and $\mathbf{T_w/T_\infty = 0.5}$

The largest gain from Fig. 4.17 is predicted to occur at $F = 1.41 \cdot 10^{-4}$ and $T_w/T_\infty = 0.5$, which corresponds to conditions where the boundary layer exhibits maximal resonance. The inputs and responses at these optimal conditions are plotted in Fig. 4.24. Near the inlet region, the input fields contain forcing that excite Mode F1 and S waves. Second mode waves are thereafter observed to optimally facilitate the synchronization of Modes F1 and S. The response fields contain both the second mode and the supersonic mode, where the latter emerges downstream of the upper relative sonic line.

The energy density functions Γ_f and $\Gamma_{q'}$ at the optimal conditions are plotted in Fig. 4.23 which show an interesting contrast to the supersonic mode at $F = 2.06 \cdot 10^{-4}$. At the higher frequency, $\Gamma_{q'}$ began decreasing once Mode F1 synchronized with the slow acoustic spectrum and disturbance energy was emitted into the free-

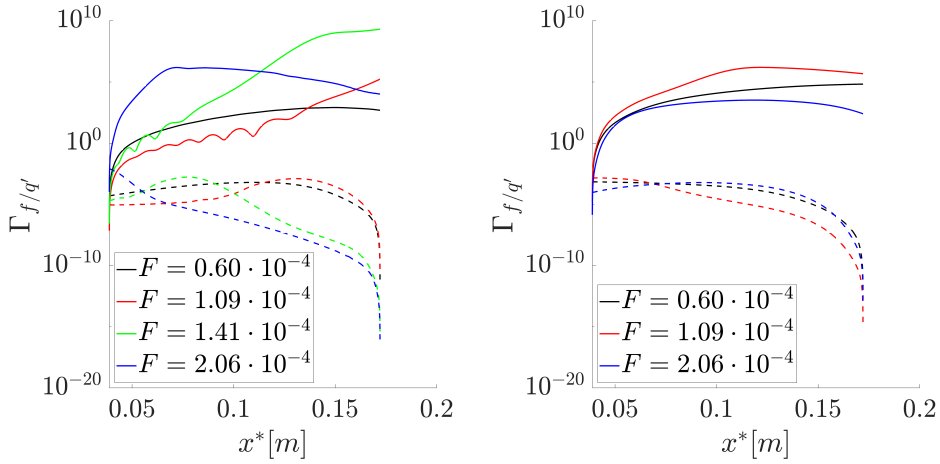

Figure 4.23: Streamwise evolution of the optimal input Γ_f (- - -) and response $\Gamma_{q'}$ (——) Chu-energy density functions at $F = 0.60 \cdot 10^{-4}$, $1.09 \cdot 10^{-4}$, and $2.06 \cdot 10^{-4}$ for $T_w/T_\infty = 0.5$ (left) and $T_w/T_\infty = 7.02$ (right). Note that energy density functions at $F = 1.41 \cdot 10^{-4}$ correspond to the optimal conditions in Fig. 4.17 and thus only shown for $T_w/T_\infty = 0.5$.

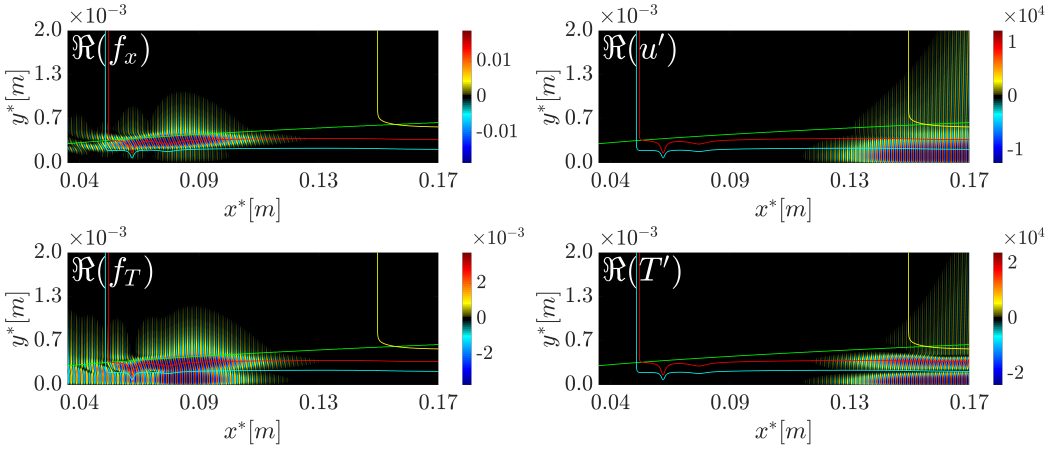

Figure 4.24: Optimal forcings of the x-momentum and energy equations (left) and corresponding u' and T' responses (right) for $F = 1.41 \cdot 10^{-4}$ at $T_w/T_\infty = 0.5$. The cyan, red, green, and yellow isocontours correspond to those from Fig. 4.18.

stream via the acoustic radiation. In contrast, LST results for $F = 1.41 \cdot 10^{-4}$ indicate that Mode F1 synchronizes with the slow acoustic waves at $x^* \approx 0.148$ m, which corresponds to the reduction in the *growth rate* of $\Gamma_{q'}$ in Fig. 4.23, but the quantity itself continues to increase. Essentially, at $F = 1.41 \cdot 10^{-4}$, the amplification of the second-mode supersedes the energy released into the free-stream.

4.5.3 Summary

In this chapter, we developed an efficient, iterative space-marching technique to compute the optimal forcings and responses by reformulating the OWNS projection equations from Sec. 2.2.2. The methodology was first validated against 2D/3DF global input-output analyses of a Mach 4.5 transitional flat-plate boundary layer and a Mach 1.5 turbulent jet. We then applied the optimal OWNS algorithm to analyze the worst-case disturbances along the centerline of the Mach 6 HIFiRE-5 elliptic cone and on a highly cooled Mach 6 flat-plate boundary layer.

For a better understanding of the receptivity mechanisms present, any of the inputs from the aforementioned analyses could have been restricted to, for example, forcing only in certain equations (mass, momentum, or energy), and/or in certain flow regions. However, the resulting inhomogeneous problem would not have been *physically realizable*, in the sense that the sources would be unconnected to any physical mechanism that produced them. Thus, a new technique is proposed in the following chapter that addresses the physical realizablility of the input forcings via a scattering formalism.

Chapter 5

OPTIMAL NATURAL BOUNDARY-LAYER RECEPTIVITY

In the context of transition analysis, linear input-output analysis determines worst-case disturbances to a laminar base flow based on a generic right-hand-side volumetric/boundary forcing term. The worst-case forcing is not physically realizable, and, to our knowledge, a generic framework for posing physically realizable worst-case disturbance problems is lacking. In natural receptivity analysis, disturbances are forced by matching (typically local) solutions within the boundary layer to outer solutions consisting of free-stream vortical, entropic, and acoustic disturbances. In this chapter, we employ a scattering formalism to restrict input-output analysis to forcings that are associated with free-stream disturbances. We decompose the full linear solution into an incident component, representing vortical, entropic, or acoustic disturbances to the free-stream, and a scattered (or residual) component that is forced by the incident wave propagated through the linearized equations. This forcing approaches zero in the free-stream where the incident waves satisfy the governing equations, but is nonzero within the shock- and boundary-layer regions where it can be parameterized and optimized using the standard input-output (SVD) framework. This permits natural receptivity analysis to be performed directly in the global framework without recourse to asymptotic analysis (though with its own challenges as we discuss). The formulation is validated by comparing with DNS of a Mach 4.5 flat-plate boundary layer. We show that the method provides insight into transition mechanisms by identifying those linear combinations of plane-wave disturbances that maximize energy amplification over a range of frequencies. We also discuss how the framework can be extended to accommodate scattering from shocks and in shock layers for supersonic flow. Note that all results in this section are from Kamal, Lakebrink, and Colonius (2022).

5.1 Methodology

5.1.1 Scattering ansatz

After transforming to the stationary frequency domain and taking $\boldsymbol{f_p} = 0$, Eq. 2.3 may be written as

$$\boldsymbol{\mathcal{L}q'} = 0, \tag{5.1}$$

where

$$\boldsymbol{\mathcal{L}} = -i\omega\boldsymbol{G} + \boldsymbol{A_{ivs}} - \boldsymbol{A_{vis}} + \left(\boldsymbol{A_{\xi,ivs}} - \boldsymbol{A_{\xi,vis}}\right)\frac{\partial}{\partial\xi} + \left(\boldsymbol{A_{\eta,ivs}} - \boldsymbol{A_{\eta,vis}}\right)\frac{\partial}{\partial\eta} + \left(\boldsymbol{A_{\zeta,ivs}} - \boldsymbol{A_{\zeta,vis}}\right)\frac{\partial}{\partial\zeta} - \boldsymbol{B_{\xi\xi}}\frac{\partial^2}{\partial\xi^2} - \boldsymbol{B_{\eta\eta}}\frac{\partial^2}{\partial\eta^2} - \boldsymbol{B_{\zeta\zeta}}\frac{\partial^2}{\partial\zeta^2} - \boldsymbol{B_{\xi\eta}}\frac{\partial^2}{\partial\xi\partial\eta} - \boldsymbol{B_{\xi\zeta}}\frac{\partial^2}{\partial\xi\partial\zeta} - \boldsymbol{B_{\eta\zeta}}\frac{\partial^2}{\partial\eta\partial\zeta}. \tag{5.2}$$

We wish to solve these equations subject to inhomogeneous boundary conditions that represent free-stream vortical, acoustic, and entropic waves far from the surface, and homogeneous boundary conditions that represent no-slip and adiabatic/isothermal conditions at the surface. Formally, we write the boundary conditions as

$$\boldsymbol{\mathcal{C}q'} = \boldsymbol{g}, \tag{5.3}$$

where $\boldsymbol{\mathcal{C}}$ is an appropriate differential operator and $\boldsymbol{g}$ represents the incident waves at infinity. Practical implementation of the boundary conditions is discussed later.

Without loss of generality, we can recast this inhomogeneous boundary-value problem as volumetrically forced PDEs with homogeneous boundary conditions by using a scattering ansatz. We decompose the solution into incident and scattered components, $\boldsymbol{q'} = \boldsymbol{q^i} + \boldsymbol{q^s}$, where the incident component satisfies the inhomogeneous boundary conditions, $\boldsymbol{\mathcal{C}q^i} = \boldsymbol{g}$. Then Eq. 5.1 and Eq. 5.3 become

$$\boldsymbol{\mathcal{L}q^s} = -\boldsymbol{\mathcal{L}q^i},\ \boldsymbol{\mathcal{C}q^s} = 0. \tag{5.4}$$

For a known incident-wave solution, these equations can be solved for the scattered component. After discretization (details discussed in Sec. 5.1.4), Eq. 5.4 becomes

$$\boldsymbol{Lq^s} = -\boldsymbol{L'q^i} \equiv \boldsymbol{f}, \tag{5.5}$$

where the inhomogeneous boundary conditions have been imposed in the left-hand-side $\boldsymbol{L}$ matrix but not in the right-hand-side $\boldsymbol{L'}$ matrix. In discretizing, we have also truncated the computational domain to a region incorporating the boundary layer and a portion of the free-stream (shock layer inclusive), and posed far-field artificial (non-reflecting) boundary conditions. We further specify that the incident component takes the form of appropriate linear vortical, entropic, or acoustic waves in a uniform flow (whose analytical solution is known and given in Sec. 5.1.3), such that $\boldsymbol{L'q^i} \approx 0$ towards the free-stream. The support of the forcing term, $\boldsymbol{f}$, is shown in Fig. 5.1, and is confined to the shock- and boundary-layer regions for supersonic flow, depicted by volumetric sources (blue) and surface sources (red). In the discretized case, these are not distinct and are both incorporated directly in $\boldsymbol{L'q^i}$.

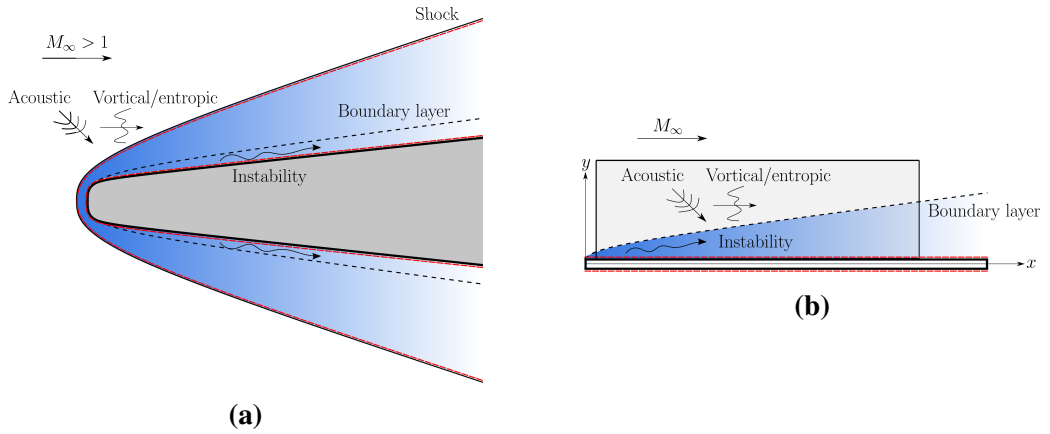

Figure 5.1: A depiction of supp$(\boldsymbol{L'q^i})$; (*a*) supersonic case generally; (*b*) idealized supersonic flat plate without shock layer. Depth of the blue shaded region corresponds to the strength of supp$(\boldsymbol{L'q^i})$, whereas the red dashed lines indicate surface scattering from the body and shock. The grey shaded region in (*b*) corresponds to the computational domain utilized.

The source originating at the shock surface includes the reflection and transmission of incident disturbances of each type to every other. In the linearized framework proposed here, we are implicitly linearizing about a fixed shock position, and this would also neglect effects associated with shock oscillations (Cook and Nichols, 2022).

The shock also gives rise to technical challenges since we are discretizing about a discontinuous solution. As a first step towards establishing the general framework, in what follows, we limit further analysis to the flat-plate scenario shown in Fig. 5.1b, where any shock and shock layer are neglected and $\boldsymbol{L'q^i}$ decays smoothly towards infinity (similar to the scenario in subsonic flow). We choose the computational domain depicted in the sketch, which also neglects scattering sources from any leading-edge geometry, and scattered waves that are generated from below and diffracted around the plate, which are expected to be small compared to direct irradiation. We choose the downstream extent of the computational domain on physical grounds so that dominant instability mechanisms (as a function of Reynolds number) are captured within the domain.

Three potential sources of error may be identified in our framework. The first of these is discretization error, which is controlled by choosing a sufficiently fine grid. However, typical grids that are desirable for the scattered-field solution, i.e. ones that are highly stretched outside the boundary layer, present a challenge for incident waves of sufficiently high frequency, in that a direct computation of $\boldsymbol{L'q^i}$ in this

region is prone to large errors. This is alleviated by computing $\boldsymbol{L'q^i}$ on a much finer grid and then interpolating the results onto the coarser computational mesh used for the solution of the scattered field. The remaining two errors are associated with posing the correct outer solution for $\boldsymbol{q^i}$. It is desirable to use analytical solutions for these free-stream disturbances, but these are only readily available for the inviscid, uniform-flow case. Then, depending on the choice of base flow, an asymptotic error arises in that the base flow may not exactly approach uniform flow (e.g. if a boundary-layer solution is utilized), thus yielding $\boldsymbol{L'q^i} \neq 0$ in the far-field, indicative of an artificial source of scattered waves. For example, if a boundary-layer solution is used for the base flow, then there is a spurious source of $O(Re^{-\frac{1}{2}})$. Moreover, our $\boldsymbol{L'}$ includes viscous terms, and so $\boldsymbol{L'q^i} \rightarrow \frac{1}{Re}$ in the far-field rather than zero, and there are again artificial sources, which we term the viscous error.

In the present work, we control both uniform-flow and viscous errors by choosing a sufficiently high Reynolds number such that the true sources are much larger than the spurious ones. More specifically, the choice of the Reynolds number restricts the maximum cross-stream wavenumbers of the ansatz assumed for $\boldsymbol{q^i}$ as explained next in Secs. 5.1.2 and 5.1.3. We verify this approach by comparing our solutions with ones where the region outside the boundary layer is artificially zeroed in Sec. 5.2. In principle, there are more sophisticated ways of minimizing these errors, such as using a DNS for the base flow or by choosing incident waves that account for viscosity.

5.1.2 Optimization

We may write the incident wave as a sum of fundamental solutions to the (assumed inviscid) exterior (uniform flow) problem

$$\boldsymbol{q^i} = \sum_{j=1}^{N} a_j \boldsymbol{\psi_j} \equiv \boldsymbol{\Psi a}, \tag{5.6}$$

where the $\boldsymbol{\psi_j}$ are each fundamental solution and are placed as columns of the matrix $\boldsymbol{\Psi}$. The specific form (plane waves) is enumerated in Sec. 5.1.3. Now, let $\boldsymbol{B} \equiv -\boldsymbol{L'\Psi}$ so that Eq. 5.5 can be rewritten as

$$\boldsymbol{Lq^s} = \boldsymbol{Ba}, \tag{5.7}$$

where the vector of amplitudes $\boldsymbol{a}$ is the input to the linearized system (analogous to the input forcing fields in the unconstrained problem).

We next define a global inner product

$$\langle \boldsymbol{b}, \boldsymbol{d} \rangle = \boldsymbol{b}^H \boldsymbol{W}_{\xi\eta\zeta} \boldsymbol{W}_e \boldsymbol{d} = \boldsymbol{b}^H \boldsymbol{W} \boldsymbol{d}, \tag{5.8}$$

where H is the Hermitian transpose and $\boldsymbol{W}$ is a positive-definite weight matrix. $\boldsymbol{W}$ is constructed as a product of $\boldsymbol{W}_{\xi\eta\zeta}$, a diagonal positive-definite matrix of quadrature weights, and $\boldsymbol{W}_e$, an energy-weight matrix, so that $<\cdot,\cdot>$ represents the volume-integrated quantity (up to a discretization error). The gain can thus be defined as a Rayleigh quotient

$$G^2 = \frac{\langle \boldsymbol{q}^s, \boldsymbol{q}^s \rangle}{\boldsymbol{a}^H \boldsymbol{a}} = \frac{\boldsymbol{q}^{sH} \boldsymbol{W} \boldsymbol{q}^s}{\boldsymbol{a}^H \boldsymbol{a}} = \frac{\boldsymbol{a}^H \boldsymbol{B}^H \boldsymbol{R}^H \boldsymbol{W} \boldsymbol{R} \boldsymbol{B} \boldsymbol{a}}{\boldsymbol{a}^H \boldsymbol{a}}, \tag{5.9}$$

with optimal solution

$$\{\boldsymbol{q'}^{opt}, \boldsymbol{a}^{opt}\} = \text{argmax } G, \tag{5.10}$$

where $\boldsymbol{R} = \boldsymbol{L}^{-1}$ is the global resolvent operator. In the optimization, we restrict $||\boldsymbol{a}||_2 = 1$ and scale each column of $\boldsymbol{B}$ so that $\left\langle \boldsymbol{b}_j, \boldsymbol{b}_j \right\rangle = 1$, which nullifies the arbitrary norm associated with $-\boldsymbol{L'}\boldsymbol{\psi}_j$. Lastly, comparison to the unconstrained problem can be made by defining the following gains

$$G^c = \left(\langle \boldsymbol{q}^s, \boldsymbol{q}^s \rangle \,/\, \langle \boldsymbol{f}, \boldsymbol{f} \rangle \right)^{\frac{1}{2}}, \quad G^{uc} = \langle \boldsymbol{q}^s, \boldsymbol{q}^s \rangle^{\frac{1}{2}}, \tag{5.11}$$

where $\boldsymbol{f} = \boldsymbol{B}\boldsymbol{a}$ for the constrained problem and where $\langle \boldsymbol{f}, \boldsymbol{f} \rangle = 1$ for the unconstrained optimization, thereby enforcing $G^c \leq G^{uc}$.

To summarize, the scattered-wave ansatz allows us to constrain the optimization to realistic input forcings given by solutions to the outer problem in the form of plane acoustic, vortical, and entropic waves. We will find linear combinations of such waves that maximize the amplification (according to the chosen norm) of the response. The solutions can be directly compared with the worst-case disturbances for right-hand-side forcings that are not restricted to realizable disturbances to the outer problem.

5.1.3 Incident waves

Plane acoustic waves in the uniform (assumed inviscid) free-stream take the form

$$\boldsymbol{\psi}^{\boldsymbol{a}} = \boldsymbol{q}^{\boldsymbol{a}} e^{\mathrm{i}(-\omega t + \alpha_a x + \kappa_a y + \beta_a z)}, \tag{5.12}$$

where $\alpha_a, \kappa_a, \beta_a \in \mathbb{R}$ are the acoustic wavenumbers in the x, y, and z directions, respectively, and where $\omega'^2 = a_\infty^2 \left(\alpha_a^2 + \kappa_a^2 + \beta_a^2 \right)$ and the amplitude $\boldsymbol{q}^{\boldsymbol{a}} =$

Table 5.1: Wavenumber ranges for acoustic waves.

M_∞	Range
< 1	$-\dfrac{1}{1-M_\infty} \leq \dfrac{\alpha_a a_\infty}{\omega} \leq \dfrac{1}{1+M_\infty}$
$= 1$	$\dfrac{\alpha_a a_\infty}{\omega} \leq \dfrac{1}{2}$
> 1	$\dfrac{\alpha_a a_\infty}{\omega} \leq \dfrac{1}{M_\infty+1}$ & $\dfrac{\alpha_a a_\infty}{\omega} \geq \dfrac{1}{M_\infty-1}$

$\begin{bmatrix} 1 & \frac{a_\infty \alpha_a}{\omega'} & \frac{a_\infty \kappa_a}{\omega'} & \frac{a_\infty \beta_a}{\omega'} & (\gamma-1)T_\infty \end{bmatrix}^T$, both with $\omega' = \omega - \alpha_a U_\infty$. These waves satisfy the Euler equations linearized about a uniform flow (taken in the x-direction with speed U_∞).

In the 2D case considered here, $\beta_a = 0$, and the waves are parameterized with α_a (or a wave angle) at a specified real frequency, ω. The ranges of permitted values of α_a are based on the aforementioned dispersion relation for the different Mach-number regimes and are given in Table 5.1. For those cases where $|\alpha_a|$ is unbounded, we limit it to the highest wavenumber that can be resolved over 10 grid points, so that we take $|\alpha_a| \leq \frac{2\pi}{10\Delta x}$.

Planar vortical and entropic wave solutions in the uniform free-stream are of the form

$$\boldsymbol{\psi}^{\boldsymbol{v,e}} = \boldsymbol{q}^{\boldsymbol{v,e}} e^{\mathrm{i}(-\omega t + \alpha_{v,e} x + \kappa_{v,e} y + \beta_{v,e} z)}, \tag{5.13}$$

where the amplitudes are $\boldsymbol{q}^{\boldsymbol{v}} = \begin{bmatrix} 0 & -\frac{\kappa_v+\beta_v}{\alpha_v} & 1 & 1 & 0 \end{bmatrix}^T$ and $\boldsymbol{q}^{\boldsymbol{e}} = \begin{bmatrix} -1 & 0 & 0 & 0 & T_\infty \end{bmatrix}^T$, respectively. The wavenumbers $\alpha_{v,e} = \omega/M_\infty$, $\kappa_{v,e}$, and $\beta_{v,e}$ correspond to the Cartesian x, y, and z directions, respectively, in which the latter two quantities are real but otherwise unconstrained. Realistic vortical and entropic disturbances will be compact and thus an infinite superposition of the plane waves. However, decomposing the disturbances in Fourier modes has the advantage of identifying those wavelengths of disturbances to which the boundary layer is most receptive.

As in the acoustic waves, we limit our attention to the 2D case ($\beta_{v,e} = 0$) and set $\max(\kappa_{v,e})$ to the minimum of either those supported by at least 15 grid points within the boundary layer or satisfy $Re_{\lambda_{v,e}} \geq 2000$. The latter constraint is set to minimize the free-stream viscous error, while still retaining a broad spectrum for $\kappa_{v,e}$.

5.1.4 Computational details

From now, we restrict our attention to strictly 2D, flat-plate boundary layers where $x = \xi$ and $y = \eta$. The LNS equations are discretized with fourth-order central finite-difference schemes and closed with no-slip boundary conditions ($u' = v' = 0$) and 1D inviscid Thompson characteristic boundary conditions (Thompson, 1987) at the wall-normal boundaries. Isothermal conditions ($T' = 0$) are enforced at the wall for the parametric study and those validating to Ma and Zhong (2005), whereas adiabatic conditions ($\partial T'/\partial y = 0$) are used for all other analyses. We employ inlet and outlet sponges to model open boundaries. All computations are performed using the CSTAT code (see Sec. B for full details).

The computational domain contains wall-normal grid clustering in the boundary layer (Malik, 1990) and extends from $x^* \in [0.006, 0.4]$ m and $y^* \in [0, 0.01]$ m with $N_x \times N_y = 3001 \times 250$. The base flow is computed using the Howarth–Dorodnitsyn transformation of the compressible Blasius equations. Finally, each forcing vector $-\boldsymbol{L'\psi_j}$ is computed with a wall-normal resolution of $5N_y$ and interpolated back onto the stability grid to minimize free-stream discretization error.

Different inner products (and associated norm) can be used to measure the strength of the response. Hereafter, we exclusively employ the Chu energy (Chu, 1965) for both the forcing and response norms, which follows previous compressible input-output analyses of Towne, Rigas, Kamal, et al. (2022), Schmidt et al. (2018), and Cook and Nichols (2022). The columns of the $\boldsymbol{B}$ matrix, which correspond to the scattered forcing fields, are therefore also normalized similarly.

5.1.5 Validation

We validate our methodology by comparing to DNS of a 2D Mach 4.5 adiabatic-wall, flat-plate boundary layer from Ma and Zhong (2003a), Ma and Zhong (2003b), and Ma and Zhong (2005), which we subsequently refer to as MZ1, MZ2, and MZ3, respectively, in this chapter. A summary of the relevant computations from each paper is provided in Table 5.2. For validation purposes, we focus on the case where the boundary layer is excited by free-stream slow and fast acoustic waves at incident angles of $\theta^*_\infty = 0°$ and $\theta^*_\infty = 22.5°$, respectively, processed through an oblique shock using DNS. Although the shock is neglected in our computations, the linear theoretical formulation of McKenzie and Westphal (1968) predicts the maximum deflection of fast acoustic waves with $\theta^*_\infty \in [0, 90]°$ to be just $\approx 1.24°$. This is computed with a constant shock angle of $\theta^*_s \approx 13.69°$ from Fig. 4 of MZ1.

Table 5.2: Summary of relevant DNS performed by MZ1, MZ2, and MZ3 of a 2D Mach 4.5 adiabatic-wall, flat-plate boundary layer.

Paper	Relevant DNS
MZ1	Steady-state base flow characterizing the oblique shock.
MZ2	Wall-pressure response from an incident fast acoustic wave at $\theta^*_\infty = 22.5°$; quantification of the response of boundary-layer modes (Mode F1/F2 and second mode) to free-stream fast acoustic waves for $\theta^*_\infty \in [0, 90]°$.
MZ3	Wall-pressure response from an incident slow acoustic wave at $\theta^*_\infty = 0°$.

Furthermore, MZ2 found that for incident fast acoustic waves, the transmitted waves of the same type are responsible for synchronizing with the boundary-layer modes (explained further later), and thus the other wave-modes generated downstream of the shock are unimportant. Lastly, slow acoustic waves at $\theta^*_\infty = 0°$ impinging on the shock generates predominantly the same type of waves propagating nearly parallel to the wall (MZ3). We can thus neglect the shock in comparing our results to MZ2 and MZ3.

In our computations, we force the LNS equations with $-\boldsymbol{L'\psi}_j$ corresponding to fast and slow acoustic waves at the aforementioned incident angles and compare the total solution $\boldsymbol{q'} = \boldsymbol{q}^i + \boldsymbol{q}^s$ to the DNS. In comparing results, we adopt the following nomenclature from LST: Modes F1 and F2 are the sequential discrete modes emanating from the fast acoustic branch, whereas Mode S originates from the slow continuous spectrum, such that the second mode corresponds to Mode S during and post-synchronization with Mode F1. Fig. 5.2a compares the wall-pressure amplitudes between the DNS and the present solution at $F = 2.2 \times 10^{-4}$. The pressure amplitude has been normalized to agree at the peak of each curve since both sets of computations are linear. For the DNS, linearity implies the non-dimensional amplitudes of the disturbances were at least one order of magnitude larger than the maximum numerical noise while also sufficiently small to remain in the linear regime (MZ1). Great agreement is observed for the slow acoustic wave and the agreement is satisfactory for the fast acoustic wave, especially in the region $0.1 < x^* < 0.2$ m, which corresponds to the location where the second Mack mode is dominant. We speculate the discrepancy in the leading-edge region is due to the shock in the DNS being locally oriented at $\theta^*_s \approx 15.8°$, which contrasts the global shock angle of $\theta^*_s \approx 13.69°$ used to estimate the maximum deflection of incident

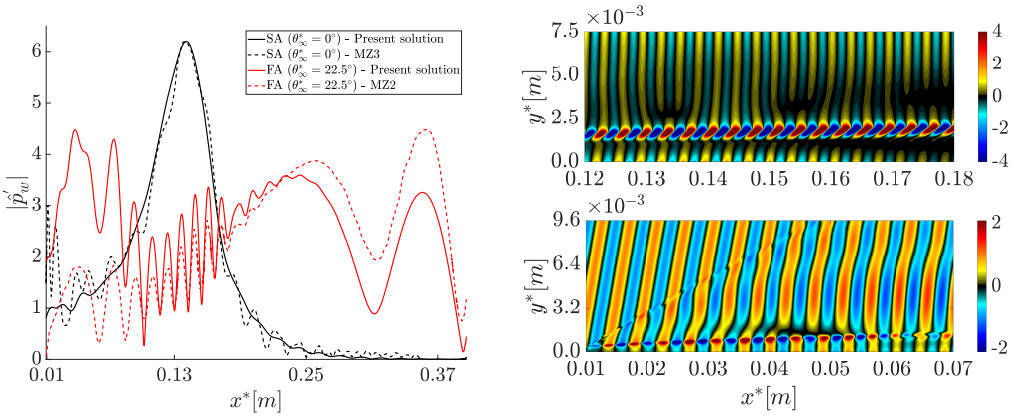

(a) **(b)**

Figure 5.2: (*a*) Wall-pressure amplitudes for the present q' solution compared to those of MZ2 and MZ3 with free-stream slow (SA) and fast (FA) acoustic waves at $M_\infty = 4.5$ and $F = 2.2\times10^{-4}$; (*b*) the corresponding density responses for SA (top) and FA (bottom).

fast acoustic waves, resulting in larger local refraction when compared to further downstream. This likely effects the resonance with Mode F1 (the dominant mode near the inlet) since it exhibits higher sensitivity to incident-disturbance angles compared to the second mode (see Fig. 5.3a). Finally, the density response for slow acoustic waves at $\theta^*_\infty = 0°$ in Fig. 5.2b matches well with the corresponding Fig. 11 of MZ3.

5.2 Optimal global receptivity analysis

We now investigate the inverse problem of determining the linear combination of free-stream disturbances that lead to the maximal flow response. We use the same base flow and parameters from Sec. 5.1.5.

To allow comparison with the results of MZ2 for the forward problem, we initially restrict our attention to downstream-propagating fast acoustic waves from above the plate, i.e. $\alpha_a \geq 0$ and $\kappa_a \leq 0$, with $F = 2.2\times10^{-4}$. We discretize the corresponding incident wave angles $0 \leq \theta^*_\infty \leq 90°$ using $N = 1000$ points. The corresponding distribution of waves with amplitude a is plotted against θ^*_∞ in Fig. 5.3a with prominent peaks observed at incident wave angles of 25° and 35°, and a less significant peak at 44°. We compare this curve to response coefficients computed by MZ2 for the forward problem computed over the range of angles. They measured approximate response coefficients for Modes F1 and F2 by using the maximum wave amplitudes in their respective dominant regions, according to LST, whereas the second-mode response coefficients were calculated by Fourier-transforming the

pressure from the global DNS (at the specified frequency) and selecting the second-mode amplitude with its wavelength again inferred from LST.

The comparison allows us to interpret the optimal solution as one that directly excites the second mode by selecting the fast acoustic waves at $\theta_\infty^* = 25°$, but also one that excites Mode F1 over a range of angles where its response coefficient is largest (and larger than the second mode). The higher response coefficient for Mode F1 is due to the synchronization between its wavenumber/wave speed and those of the free-stream fast acoustic waves at these angles, and largest near the leading edge due to the strongest base-flow non-parallelism, as is evident in Fig. 5.3b. Downstream of the leading edge, the phase speeds of Modes F1 and S approach one another, and by $x^* \approx 0.11$ m, these two modes fully synchronize, which incites the second mode. The second mode remains unstable until it passes through the Branch II neutral point at $x^* \approx 0.155$ m (MZ2) and decays thereafter as Modes F1 and S de-synchronize, the latter of which is now the second mode. For $x^* > 0.3$ m, the small growth and subsequent decay in Fig. 5.3b is due to the emergence of Mode F2 caused by the wavenumber/wave speed synchronization with the fast acoustic waves.

This importance of Mode F1 to second-mode amplification corroborates the finding of MZ2, and is further highlighted by comparing the respective gains from this optimal linear combination of fast acoustic waves, $G^c \approx 40$, with the gain obtained by limiting the input to only fast acoustic waves at $\theta_\infty^* = 25°$, which we computed as $G^c \approx 21$, a reduction of about 48%.

Lastly, we demonstrate how the true scattering sources in our framework are significantly larger than the spurious ones induced by the three sources of error mentioned in Sec. 5.1.1 by repeating the above computation and artificially removing any sources outside the boundary layer. The corresponding amplitude profile is shown in Fig. 5.3a which is quantitatively similar to the original solution with G^c only decreasing by $\approx 2\%$.

We next analyze the case where the free-stream is restricted to vortical waves, again at $F = 2.2 \times 10^{-4}$. As investigated by Schrader, Brandt, and Henningson (2009), there are two competing mechanisms for optimally perturbing the boundary layer using free-stream vortical disturbances: smaller wavelengths (large κ_y) are able to *penetrate* deeper into the boundary layer, but suffer faster viscous decay, whereas the opposite is true for larger wavelengths. The optimal distribution of vortical waves, shown in Fig. 5.4a, shows two maxima corresponding to $\kappa_y \approx 0.014$ and $\kappa_y \approx 0.31$. Maximal excitation of disturbances is achieved by simultaneously subjecting the

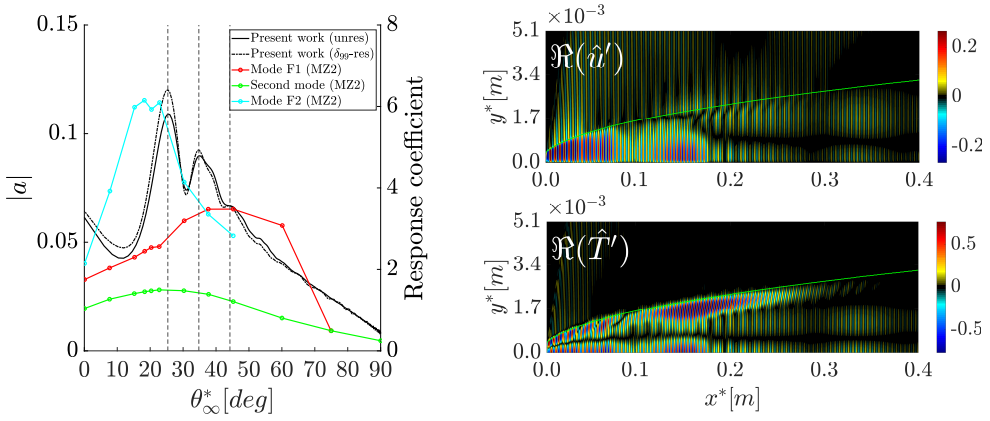

(a) **(b)**

Figure 5.3: (*a*) Optimal amplitude profile with free-stream fast acoustic waves at $M_\infty = 4.5$ and $F = 2.2 \times 10^{-4}$; (*b*) the corresponding q^s responses (green isocontour is δ_{99}). Colored lines in (*a*) are the response coefficients from MZ2, the dashed lines are along the optimal angles from the scattering framework, and the dash-dotted line is the optimal amplitude profile with scattering sources restricted to δ_{99}.

boundary layer to highly penetrating free-stream vortical modes and those that exhibit minimal viscous decay. Near the leading edge, free-stream vorticity penetrates the boundary layer and elicits a non-modal response characterized by large-scale streamwise jets emanating from the wall in the u' response field of Fig. 5.4b. These jets are also seen to be modulated by Modes F1 and S.

Downstream of the leading edge, the phase speed of Mode F1 decreases, and by $x^* \approx 0.11$ m, Mode F1 synchronizes with Mode S to incite the second mode. During the second-mode growth however, the streamwise jets remain as seen in Fig. 5.4b. Once the second mode has decayed appreciably by $x^* \approx 0.18$ m, the jets are once again visible, but only weakly and for a short length as they suffer viscous decay. This is because free-stream vortical disturbances with $\kappa_v \approx 0.31$, which corresponds to $\lambda_v \approx 1.5\delta_{99}$ at the inlet, optimally excite the jets, but also experience relatively large viscous decay.

Similar calculations were performed for slow acoustic waves, entropic waves, and for the gamut of all free-stream waves. The respective gains are summarized in Table 5.3. Firstly, the slow acoustic waves yielded a gain ≈ 1.9 times greater than the fast acoustic waves, which corroborates the general understanding that slow waves dominate acoustically induced transition onset in adiabatic-wall high-speed boundary layers (MZ3, Balakumar (2015)). Vortical waves yielded a gain nearly identical to G^c_{all}, suggesting that the transient streamwise jets excited by vortical

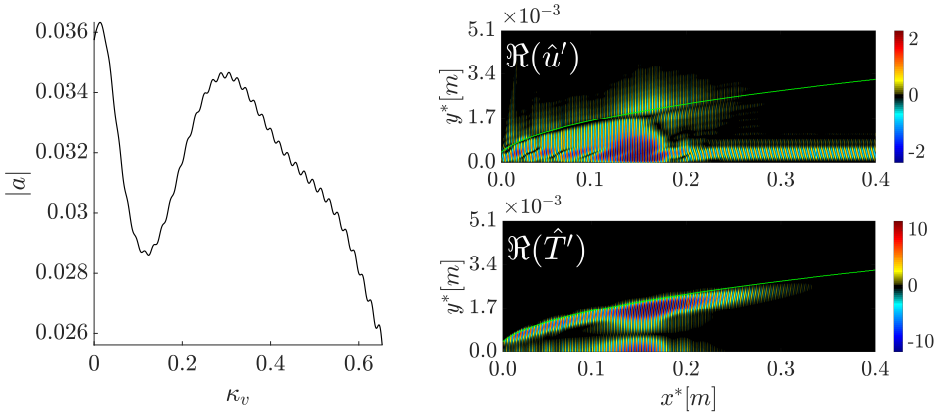

Figure 5.4: (*a*) Optimal amplitude profile with free-stream vortical waves at $M_\infty = 4.5$ and $F = 2.2 \times 10^{-4}$; (*b*) the corresponding q^s responses (green isocontour is δ_{99}).

Table 5.3: Gains from (un)constrained optimizations at $M_\infty = 4.5$ and $F = 2.2 \times 10^{-4}$.

Case	G^c or G^{uc}
Fast acoustic ($\alpha_a \geq 0$ and $\kappa_a \leq 0$)	40
Slow acoustic ($\kappa_a \leq 0$)	76
Vortical	95
Entropic	11
All	96
Unconstrained	3.0×10^4

disturbances is the dominant receptivity mechanism for the current configuration. Entropy waves, on the other hand, play no significant role at these conditions. Lastly, the unconstrained optimization (standard input-output) problem yielded a gain nearly 300 times greater than G^c_{all}, suggesting that the physically realizable inputs have a small projection onto the unconstrained (non-physically realizable) inputs. Conversely, a large number of unconstrained forcing modes would be required to represent the physical forcing.

5.3 Optimal parametric study

We now compute G^c for the gamut of free-stream disturbances across a range of frequencies. Here, each wave-mode (fast/slow acoustic, vortical, and entropic) is discretized with $N = 1000$ points, but in contrast to Sec. 5.1.5, half the acoustic waves radiate above ($\kappa_a \leq 0$) while the other half radiate below ($\kappa_a \geq 0$) the plate. Additionally, $\alpha_a < 0$ is included in the ansatz for fast acoustic waves. The

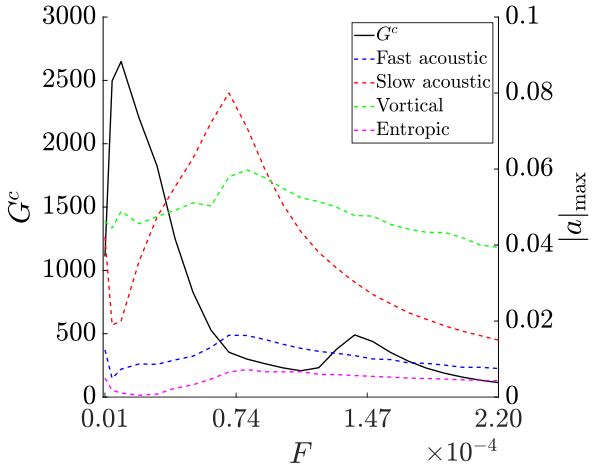

Figure 5.5: G^c vs F at $M_\infty = 4.5$ with gamut of free-stream waves with the corresponding maximum amplitude from each wave-mode (fast/slow acoustic, vortical, and entropic).

gain profile and the maximum amplitude from each wave-mode, which reveals the dominant free-stream disturbance type, are shown in Fig. 5.5. The first mode is optimally excited at $F_{opt} \approx 0.1\times10^{-4}$, but the gain rapidly decreases with increasing frequency up until $F \approx 0.7 \times 10^{-4}$. Then for $F > 1.1 \times 10^{-4}$, the second mode becomes the dominant instability and peaks at $F_{opt} \approx 1.4 \times 10^{-4}$.

Across all frequencies, $|a|_{\max}$ for entropic waves is the lowest, closely followed by fast acoustic waves. Although $|a|_{\max}$ is attributed to a vortical wave at the lowest frequencies, the relative importance of slow acoustic waves steeply increases from $F \approx 0.05 \times 10^{-4}$ and eventually overtakes vortical waves at $F \approx 0.3 \times 10^{-4}$, before becoming subdominant again by $F \approx 0.9 \times 10^{-4}$. The dominance of the vortical wave at high frequencies is likely attributed to the "swallowing" effect (Fedorov and Khokhlov, 2001) where Mode F1 synchronizes with the continuous vorticity branch. The resulting Mode F1 waves, as discussed above, maximize the amplification of the second mode. While the fast acoustic waves are closer in wavenumber to Mode F1, the vortical waves are apparently more effective because they can simultaneously excite Mode F1 ("swallowing" effect) and Mode S (similar wavenumber).

5.3.1 Summary

We have developed a scattered-wave ansatz which can be understood as a generalization of receptivity theory to compute the linear superposition of free-stream disturbances resulting in the maximum disturbance-energy amplification. This global approach circumvents the need for asymptotic expansions which is commonly used

for receptivity analyses based on local methods. Alternatively, the ansatz can be considered as restricting the forcing field in input-output analysis to physically realizable quantities associated with the free-stream disturbances. We validated and applied this novel technique to a 2D Mach 4.5 flat-plate boundary layer for which the forward receptivity problem was previously solved using DNS (MZ2, MZ3).

Chapter 6

CONCLUSIONS AND FUTURE WORK

6.1 Conclusions

In this thesis, we covered a variety of topics ranging from generalizing the One-Way Navier-Stokes (OWNS) Equations to developing a novel framework in restricting input-output analyses to physically realizable free-stream disturbances. We will outline some of the key conclusions from each chapter.

We began by embedding the non-orthogonal curvilinear coordinate system from Sec. A into the OWNS algorithm, along with full compressibility effects with user-defined fluid properties in Sec. 2. The generalization was validated by comparing to DNS results (in the linear regime) of an adiabatic flat plate (Ma and Zhong, 2003a), a highly cooled flat plate (Chuvakhov and Fedorov, 2016), and a 7-deg half-angle sharp cone (Sousa et al., 2019). In all cases, we observe that OWNS gives DNS-quality results at a fraction of the computational expense. Essentially, OWNS was able to fully track the downstream-propagating modes even when initialized with random perturbations since the formulation does not assume any wave-like ansatz. Additionally, we validated the non-orthogonal curvilinear coordinate system by comparing LST results from CSTAT with LST data of the HIFiRE-5 elliptic cone computed using LASTRAC (Chang, 2004).

We then applied OWNS to a complex 3D boundary layer, specifically a Mach 6 finned-cone geometry in Sec. 3. By initializing the march at $f = 250$ kHz with both randomized inlet forcing and a SBG inlet boundary condition, the insensitivity to the initial conditions was established and both computations converged to the dominant vortex mode well upstream of transition. Thus, while more expensive than PSE, OWNS obviates the need for a trial-and-error approach to select the appropriate wavelength for the SBG initial condition, yielding DNS-like confidence that all wavelengths (and instability mechanisms) are accounted for in the solution. In the present flow, the OWNS computations, at least up to the transition location, suggest that there exists no significant amplification mechanisms beyond the dominant vortex mode. Finally, we validated the curvilinear implementation and centerline treatment for 3D jets in cylindrical coordinates for various azimuthal domains using a 3D Mach 1.5 axisymmetric turbulent jet.

We next addressed the inverse problem of reconstructing the OWNS algorithm to determine the worst-case disturbances leading to the fastest transition to turbulence in Sec. 4. Specifically, the optimal input and output modes were computed using Lagrangian multipliers via an iterative, adjoint-based, space-marching technique that appreciably reduced the computational burden compared to the global approach that uses SVD without sacrificing accuracy. The input-output OWNS model was validated against optimal forcings and responses of a Mach 4.5 flat-plate boundary layer from Bugeat et al. (2019) and a Mach 1.5 turbulent jet. We then applied these equations to study worst-case disturbances on the centerline of the Mach 6 HIFiRE-5 elliptic cone and on a highly cooled Mach 6 flat-plate boundary layer. The former study demonstrated the capability of the optimal OWNS method in efficiently computing worst-case disturbances for complex flows. For the latter study, the deficiencies of LST in analyzing flows exhibiting inter-modal interactions and/or non-modal effects (e.g. supersonic mode) were highlighted, while simultaneously exemplifying OWNS's ability to tackle such complex flows with high accuracy.

Finally, in Sec. 5, we developed a scattering ansatz to study global, optimal natural boundary-layer receptivity. The technique can be understood as a generalization of receptivity theory to determine the linear combinations of free-stream disturbances that give rise to the maximal disturbance amplification in the boundary layer. At the same time, it can be considered as a restriction of the forcing field in input-output analysis to a subspace associated with excitation by free-stream disturbances, which addresses a long-standing and contentious issue regarding the realizability of input-output analyses. As compared to many receptivity studies based on local methods, the global approach circumvents the need for asymptotic expansions. As a first application of the approach, we consider 2D disturbances to a Mach 4.5 flat-plate boundary layer for which the forward receptivity problem was previously solved using DNS (Ma and Zhong, 2003b; Ma and Zhong, 2005). The results validate the approach and revealed optimal disturbance amplification scenarios. When the free-stream is restricted to fast acoustic waves, maximal response is achieved by subjecting the boundary layer to acoustic waves with incident angles that optimally excite the second mode, but also, to a lesser extent, Mode F1. The receptivity mechanism vastly changes, however, in the case of incident vortical waves, where an optimal combination of highly penetrating and minimally decaying incident waves produce a transient response characterized by large-scale streamwise jets emanating from the wall and modulated by Modes F1 and S in the u' response field. Finally, the efficiency of our approach was demonstrated by computing

the optimal receptivity for the same Mach 4.5 flat-plate boundary layer over a range of frequencies, highlighting where first- (low-frequency) and second-mode (high-frequency) instabilities are most receptive to different types of free-stream disturbances.

6.2 Future work

The input-output framework of OWNS will be applied to a variety of other flows, including extending the study in Sec. 4.5 to 3DF disturbances. Furthermore, we will apply optimal OWNS along various inviscid streamlines and vortex paths on the HIFiRE-5 elliptic cone and the BOLT geometry (Thome et al., 2018) to parametrically investigate the various instabilities present. The BOLT geometry was specifically designed to excite a multitude of instabilities (Thome et al., 2018), making OWNS a highly attractive stability solver for such a complex flow field. Similarly, while the configurations considered for the optimal global receptivity analyses in Sec. 5 were restricted to 2D flows, the methodology can be readily applied to 3D disturbances and more complex geometries, and the scattering ansatz can include sources associated with the shock and shock layer. We also plan to embed the scattering framework within the optimal OWNS algorithm to compute the physically realizable worst-case disturbances in an efficient manner (in lieu of the global approach used in Sec. 5).

Although the OWNS approach significantly reduces the computational burden compared to global methods, further advancements are required to enable OWNS to be used routinely as an engineering tool for complex 3D stability calculations. Specifically, the OWNS algorithm may be reconstructed in a manner similar to Zhu and Towne (2023), in which the action of the approximate projection operator is performed by sequentially satisfying the recursive relations rather than in parallel as is done in the current formulation. From a computational perspective, additional efficiency can also be achieved by using the Clusters Interface of PARDISO which includes Message Passing Interface (MPI) technology to facilitate communication between multiple nodes (the current PARDISO solver in CSTAT is restricted to only one node), and OpenMP* for parallelizing tasks amongst the processors in a given node. Although this technology exists, the wrapper to synchronize the MATLAB platform with the Clusters Interface needs to be developed. Embedding this new PARDISO feature within CSTAT would also enable efficient computations if chemical non-equilibrium effects are included in the future since a larger linear system of equations would need to be inverted. With these advancements, we plan to conduct

stability analyses, including input-output analyses, on the BOLT geometry. We will also investigate the optimal disturbances of 3D chevron jets (Gudmundsson and Colonius, 2007).

Finally, all of the current solvers within CSTAT are linear, but insight into the nonlinear regime for transition analysis is important to understand the breakdown mechanisms (Rigas, Sipp, and Colonius, 2021). Additionally, the linear regime may altogether be bypassed in the presence of sufficiently large amplitude forcing. Thus, work is underway to incorporate nonlinear PSE and OWNS solvers to study nonlinear transition mechanisms and characterize the breakdown of disturbances just prior to turbulence.

BIBLIOGRAPHY

Araya, D., Bitter, N., Wheaton, B. M., Kamal, O., Colonius, T., Knutson, A., Johnson, H., Nichols, J., Candler, G. V., Russo, V., and Brehm, C. (2022). "Assessment of linear methods for analysis of boundary layer instabilities on a finned cone at Mach 6". In: AIAA AVIATION Forum. 2022.

Arnal, D. and Casalis, G. (2000). "Laminar-turbulent transition prediction in three-dimensional flows". In: *Progress in Aerospace Sciences* 36.2 (2000), pp. 173–191.

Bae, H. J., Dawson, S. T. M., and McKeon, B. J. (2020). "Resolvent-based study of compressibility effects on supersonic turbulent boundary layers". In: *Journal of Fluid Mechanics* 883 (2020), A29.

Balakumar, P. (2015). "Receptivity of hypersonic boundary layers to acoustic and vortical disturbances (Invited)". In: 45th AIAA Fluid Dynamics Conference. 2015.

Bitter, N. P. and Shepherd, J. E. (2015). "Stability of highly cooled hypervelocity boundary layers". In: *Journal of Fluid Mechanics* 778 (2015), pp. 586–620.

Brès, G. A., Ham, F. E., Nichols, J. W., and Lele, S. K. (2017). "Unstructured large-eddy simulations of supersonic jets". In: *AIAA Journal* 55.4 (2017), pp. 1164–1184.

Bugeat, B., Chassaing, J.-C., Robinet, J.-C., and Sagaut, P. (2019). "3D global optimal forcing and response of the supersonic boundary layer". In: *Journal of Computational Physics* 398 (2019), p. 108888.

Cavalieri, A. V. G., Jordan, P., Colonius, T., and Gervais, Y. (2012). "Axisymmetric superdirectivity in subsonic jets". In: *Journal of Fluid Mechanics* 704 (2012), pp. 388–420.

Chang, C.-L. (2004). "Lastrac.3d: transition prediction in 3D boundary layers". In: 34th AIAA Fluid Dynamics Conference and Exhibit. 2004.

Chen, Z. and Towne, A. (2021). "An azimuthal Fourier domain formulation of the Ffowcs Williams and Hawkings equation". In: *The Journal of the Acoustical Society of America* 150.3 (2021), pp. 1967–1978.

Choudhari, M., Chang, C.-L., Jentink, T., Li, F., Berger, K., Candler, G., and Kimmel, R. (2009). "Transition analysis for the HIFiRE-5 vehicle". In: 39th AIAA Fluid Dynamics Conference. 2009.

Chu, B.-T. (1965). "On the energy transfer to small disturbances in fluid flow (Part I)". In: *Acta Mechanica* 1.3 (1965), pp. 215–234.

Chuvakhov, P. V. and Fedorov, A. V. (2016). "Spontaneous radiation of sound by instability of a highly cooled hypersonic boundary layer". In: *Journal of Fluid Mechanics* 805 (2016), pp. 188–206.

Cook, D. A., Knutson, A., Nichols, J. W., and Candler, G. V. (2020). "Matrix methods for input-output analysis of 2D and 3D hypersonic flows". In: AIAA SciTech Forum. 2020.

Cook, D. A. and Nichols, J. W. (2022). "Free-stream receptivity of a hypersonic blunt cone using input–output analysis and a shock-kinematic boundary condition". In: *Theoretical and Computational Fluid Dynamics* 36.1 (2022), pp. 155–180.

Crouch, J. D. (1992). "Non-localized receptivity of boundary layers". In: *Journal of Fluid Mechanics* 244 (1992), pp. 567–581.

Demetriades, A. (1974). "Hypersonic viscous flow over a slender cone. III - Laminar instability and transition". In: 7th Fluid and PlasmaDynamics Conference. 1974.

Demetriades, A. (1960). "An experiment on the stability of hypersonic laminar boundary layers". In: *Journal of Fluid Mechanics* 7.3 (1960), pp. 385–396.

Demirdzic, I., Gosman, A. D., Issa, R. I., and Peric, M. (1987). "A calculation procedure for turbulent flow in complex geometries". In: *Computers & Fluids* 15.3 (1987), pp. 251–273.

Demirdzic, I. A. (1982). "A finite volume method for computation of fluid flow in complex geometries". PhD thesis. University of London, 1982.

Duck, P. W., Ruban, A. I., and Zhikharev, C. N. (1996). "The generation of Tollmien-Schlichting waves by free-stream turbulence". In: *Journal of Fluid Mechanics* 312 (1996), pp. 341–371.

Duff, I. S., Erisman, A. M., and Reid, J. K. (2017). *Direct Methods for Sparse Matrices*. Oxford University Press, 2017.

Fedorov, A., Shiplyuk, A., Maslov, A., Burov, E., and Malmuth, N. (2003). "Stabilization of a hypersonic boundary layer using an ultrasonically absorptive coating". In: *Journal of Fluid Mechanics* 479 (2003), pp. 99–124.

Fedorov, A. (2011). "Transition and stability of high-speed boundary layers". In: *Annual Review of Fluid Mechanics* 43.1 (2011), pp. 79–95.

Fedorov, A. and Tumin, A. (2011). "High-speed boundary-layer instability: old terminology and a new framework". In: *AIAA Journal* 49.8 (2011), pp. 1647–1657.

Fedorov, A. V., Malmuth, N. D., Rasheed, A., and Hornung, H. G. (2001). "Stabilization of hypersonic boundary layers by porous coatings". In: *AIAA journal* 39.4 (2001), pp. 605–610.

Fedorov, A. V. (2003). "Receptivity of a high-speed boundary layer to acoustic disturbances". In: *Journal of Fluid Mechanics* 491 (2003), pp. 101–129.

Fedorov, A. V. and Khokhlov, A. P. (2001). "Prehistory of instability in a hypersonic boundary layer". In: *Theoretical and Computational Fluid Dynamics* 14.6 (2001), pp. 359–375.

Fischer, M. C. and Wagner, R. D. (1972). "Transition and hot-wire measurements in hypersonic helium flow". In: *AIAA Journal* 10.10 (1972), pp. 1326–1332.

Frank, J., Hundsdorfer, W., and Verwer, J. (1997). "On the stability of implicit-explicit linear multistep methods". In: *Applied Numerical Mathematics* 25.2 (1997), pp. 193–205.

Gaponov, S. A. and Smorodskii, B. V. (2008). "Linear stability of three-dimensional boundary layers". In: *Journal of Applied Mechanics and Technical Physics* 49.2 (2008), pp. 157–166.

Garnaud, X., Lesshafft, L., Schmid, P. J., and Huerre, P. (2013). "The preferred mode of incompressible jets: linear frequency response analysis". In: *Journal of Fluid Mechanics* 716 (2013), pp. 189–202.

Goldstein, M. E. (1983). "The evolution of Tollmien–Sclichting waves near a leading edge". In: *Journal of Fluid Mechanics* 127 (1983), pp. 59–81.

Groot, K. J. (2018). "BiGlobal stability of shear flows: spanwise & streamwise analyses". PhD thesis. Delft University of Technology, 2018.

Gudmundsson, K. and Colonius, T. (2007). "Spatial stability analysis of chevron jet profiles". In: 13th AIAA/CEAS Aeroacoustics Conference (28th AIAA Aeroacoustics Conference). 2007.

Hack, M. J. P. and Moin, P. (2017). "Algebraic disturbance growth by interaction of Orr and lift-up mechanisms". In: *Journal of Fluid Mechanics* 829 (2017), pp. 112–126.

Halko, N., Martinsson, P. G., and Tropp, J. A. (2011). "Finding structure with randomness: probabilistic algorithms for constructing approximate matrix decompositions". In: *SIAM Review* 53.2 (2011), pp. 217–288.

Hirschel, E. H. (2005). "Laminar-turbulent transition and turbulence in high-speed viscous flow". In: *Basics of Aerothermodynamics*. Berlin, Heidelberg: Springer Berlin Heidelberg, 2005, pp. 263–310.

Hu, J. and Shu, R. (2021). "On the uniform accuracy of implicit-explicit backward differentiation formulas (IMEX-BDF) for stiff hyperbolic relaxation systems and kinetic equations". In: *Mathematics of Computation* 90.328 (2021), pp. 641–670.

Jeun, J., Nichols, J. W., and Jovanović, M. R. (2016). "Input-output analysis of high-speed axisymmetric isothermal jet noise". In: *Physics of Fluids* 28.4 (2016), p. 047101.

Jordan, P. and Colonius, T. (2013). "Wave packets and turbulent jet noise". In: *Annual Review of Fluid Mechanics* 45.1 (2013), pp. 173–195.

Kamal, O., Lakebrink, M. T., and Colonius, T. (2022). "Global receptivity analysis: physically realizable input-output analysis". In: *arXiv* (2022). Accepted by the Journal of Fluid Mechanics.

Kamal, O., Rigas, G., Lakebrink, M. T., and Colonius, T. (2020). "Application of the One-Way Navier-Stokes (OWNS) Equations to hypersonic boundary layers". In: AIAA AVIATION Forum. 2020.

Kamal, O., Rigas, G., Lakebrink, M. T., and Colonius, T. (2021). "Input/output analysis of hypersonic boundary layers using the One-Way Navier-Stokes (OWNS) Equations". In: AIAA AVIATION Forum. 2021.

Kamal, O., Rigas, G., Lakebrink, M. T., and Colonius, T. (2022). "Input/output analysis of a Mach-6 cooled-wall hypersonic boundary layer using the One-Way Navier-Stokes (OWNS) Equations". In: AIAA AVIATION Forum. 2022.

Karban, U., Bugeat, B., Martini, E., Towne, A., Cavalieri, A. V. G., Lesshafft, L., Agarwal, A., Jordan, P., and Colonius, T. (2020). "Ambiguity in mean-flow-based linear analysis". In: *Journal of Fluid Mechanics* 900 (2020), R5.

Kendall, J. M. (1975). "Wind tunnel experiments relating to supersonic and hypersonic boundary-layer transition". In: *AIAA Journal* 13.3 (1975), pp. 290–299.

Kimmel, R., Adamczak, D., Berger, K., and Choudhari, M. (2010). "HIFiRE-5 flight vehicle design". In: 40th Fluid Dynamics Conference and Exhibit. 2010.

Kimmel, R. L., Demetriades, A., and Donaldson, J. C. (1996). "Space-time correlation measurements in a hypersonic transitional boundary layer". In: *AIAA Journal* 34.12 (1996), pp. 2484–2489.

Knisely, C. P. and Zhong, X. (2019a). "Sound radiation by supersonic unstable modes in hypersonic blunt cone boundary layers. I. Linear stability theory". In: *Physics of Fluids* 31.2 (2019), p. 024103.

Knisely, C. P. and Zhong, X. (2019b). "Sound radiation by supersonic unstable modes in hypersonic blunt cone boundary layers. II. Direct numerical simulation". In: *Physics of Fluids* 31.2 (2019), p. 024104.

Knutson, A., Brock, J., and Candler, G. V. (2021). "Adaptive mesh refinement in US3D". In: AIAA SciTech Forum. 2021.

Knutson, A., GS, S., and Candler, G. V. (2018a). "Direct numerical simulation of Mach 6 flow over a cone with a highly swept fin". In: AIAA SciTech Forum — Aerospace Sciences Meeting. 2018.

Knutson, A., GS, S., and Candler, G. V. (2018b). "Instabilities in Mach 6 flow over a cone with a swept fin". In: AIAA AVIATION Forum — Fluid Dynamics Conference. 2018.

Kocian, T. S., Moyes, A. J., Reed, H. L., Craig, S. A., Saric, W. S., Schneider, S. P., and Edelman, J. B. (2019). "Hypersonic crossflow instability". In: *Journal of Spacecraft and Rockets* 56.2 (2019), pp. 432–446.

Kuehl, J. and Paredes, P. (2016). "Görtler modified Mack-modes on a hypersonic flared cone". In: 54th AIAA Aerospace Sciences Meeting. 2016.

Lassaline, J. V. (2009). *Supersonic right circular cone at zero angle of attack*. `http://e.roohi.profcms.um.ac.ir/imagesm/1019/stories/PDFs/Supersonic/conenotes.pdf`. Online; Accessed: 1 May 2020. 2009.

Lees, L. (1956). "Laminar heat transfer over blunt-nosed bodies at hypersonic flight speeds". In: *Journal of Jet Propulsion* 26.4 (1956), pp. 259–269.

Lesshafft, L., Semeraro, O., Jaunet, V., Cavalieri, A. V. G., and Jordan, P. (2019). "Resolvent-based modeling of coherent wave packets in a turbulent jet". In: *Physical Review Fluids* 4 (6 2019), p. 063901.

Li, F., Choudhari, M., Chang, C.-L., White, J., Kimmel, R., Adamczak, D., Borg, M., Stanfield, S., and Smith, M. (2012). "Stability analysis for HIFiRE experiments". In: 42nd AIAA Fluid Dynamics Conference and Exhibit. 2012.

Lugrin, M., Beneddine, S., Leclercq, C., Garnier, E., and Bur, R. (2021). "Transition scenario in hypersonic axisymmetrical compression ramp flow". In: *Journal of Fluid Mechanics* 907 (2021), A6.

Ma, Y. and Zhong, X. (2003a). "Receptivity of a supersonic boundary layer over a flat plate. Part 1. Wave structures and interactions". In: *Journal of Fluid Mechanics* 488 (2003), pp. 31–78.

Ma, Y. and Zhong, X. (2003b). "Receptivity of a supersonic boundary layer over a flat plate. Part 2. Receptivity to free-stream sound". In: *Journal of Fluid Mechanics* 488 (2003), pp. 79–121.

Ma, Y. and Zhong, X. (2005). "Receptivity of a supersonic boundary layer over a flat plate. Part 3. Effects of different types of free-stream disturbances". In: *Journal of Fluid Mechanics* 532 (2005), pp. 63–109.

Mack, L. M. (1969). *Boundary-layer stability theory*. Document No. 900-277 (Rev. A), Jet Propulsion Laboratory, Pasadena, CA. 1969.

Mack, L. M. (1975). "Linear stability theory and the problem of supersonic boundary-layer transition". In: *AIAA journal* 13.3 (1975), pp. 278–289.

Mack, L. M. (1984). "Special course on stability and transition of laminar flow: boundary-layer linear stability theory". In: *AGARD Report No. 709* (1984).

Malik, M. R. (1990). "Numerical methods for hypersonic boundary layer stability". In: *Journal of Computational Physics* 86.2 (1990), pp. 376–413.

Mangler, W. (1948). "Zusammenhang zwischen ebenen und rotationssymmetrischen grenzschichten in kompressiblen flüssigkeiten". In: *Zeitschrift für Angewandte Mathematik und Mechanik* 28.4 (1948), pp. 97–103.

Mattsson, K. and Nordström, J. (2004). "Summation by parts operators for finite difference approximations of second derivatives". In: *Journal of Computational Physics* 199.2 (2004), pp. 503–540.

McKenzie, J. F. and Westphal, K. O. (1968). "Interaction of linear waves with oblique shock waves". In: *The Physics of Fluids* 11.11 (1968), pp. 2350–2362.

McMillan, M., Mullen, C. D., and Reed, H. L. (2021). "Spatial BiGlobal stability analysis of spanwise vortex rollup on a hypersonic finned cone". In: AIAA AVIATION Forum. 2021.

Mohseni, K. and Colonius, T. (2000). "Numerical treatment of polar coordinate singularities". In: *Journal of Computational Physics* 157.2 (2000), pp. 787–795.

Monokrousos, A., Åkervik, E., Brandt, L., and Henningson, D. S. (2010). "Global three-dimensional optimal disturbances in the Blasius boundary-layer flow using time-steppers". In: *Journal of Fluid Mechanics* 650 (2010), pp. 181–214.

Mullen, C. D., Moyes, A., Kocian, T. S., and Reed, H. L. (2018). "Parametric boundary-layer stability analysis on a hypersonic finned circular cone". In: AIAA AVIATION Forum — Fluid Dynamics Conference. 2018.

Mullen, C. D., Moyes, A., Kocian, T. S., and Reed, H. L. (2019). "Heat transfer and boundary-layer stability analysis of subscale BOLT and the fin cone". In: AIAA AVIATION Forum. 2019.

Mullen, C. D., Turbeville, F. D., Reed, H. L., and Schneider, S. P. (2019). "Computational and experimental boundary-layer stability analysis on a hypersonic finned cone". In: AIAA SciTech Forum. 2019.

Nichols, J. W., Lele, S. K., and Moin, P. (2009). "Global mode decomposition of supersonic jet noise". In: *Center for Turbulence Research — Annual Research Briefs* (2009).

Nichols, J. W. and Candler, G. V. (2019). "Input-output analysis of complex hypersonic boundary layers". In: AIAA SciTech Forum. 2019.

Nichols, J. W. and Lele, S. K. (2011). "Global modes and transient response of a cold supersonic jet". In: *Journal of Fluid Mechanics* 669 (2011), pp. 225–241.

Nogueira, P. A. S., Cavalieri, A. V. G., Jordan, P., and Jaunet, V. (2019). "Large-scale streaky structures in turbulent jets". In: *Journal of Fluid Mechanics* 873 (2019), pp. 211–237.

Parziale, N. J., Shepherd, J. E., and Hornung, H. G. (2015). "Observations of hypervelocity boundary-layer instability". In: *Journal of Fluid Mechanics* 781 (2015), pp. 87–112.

Petrov, G. V. (1985). "Stability of thin viscous shock layer on a wedge in hypersonic flow of a perfect gas". In: *Laminar-Turbulent Transition* (1985), pp. 487–493.

Pickering, E., Rigas, G., Schmidt, O. T., Sipp, D., and Colonius, T. (2021). "Optimal eddy viscosity for resolvent-based models of coherent structures in turbulent jets". In: *Journal of Fluid Mechanics* 917 (2021), A29.

Pickering, E., Towne, A., Jordan, P., and Colonius, T. (2021). "Resolvent-based modeling of turbulent jet noise". In: *The Journal of the Acoustical Society of America* 150.4 (2021), pp. 2421–2433.

Pickering, E., Rigas, G., Nogueira, P. A. S., Cavalieri, A. V. G., Schmidt, O. T., and Colonius, T. (2020). "Lift-up, Kelvin–Helmholtz and Orr mechanisms in turbulent jets". In: *Journal of Fluid Mechanics* 896 (2020), A2.

Poinsot, T. J. and Lelef, S. K. (1992). "Boundary conditions for direct simulations of compressible viscous flows". In: *Journal of Computational Physics* 101.1 (1992), pp. 104–129.

Qin, F. and Wu, X. (2016). "Response and receptivity of the hypersonic boundary layer past a wedge to free-stream acoustic, vortical and entropy disturbances". In: *Journal of Fluid Mechanics* 797 (2016), pp. 874–915.

Rigas, G., Sipp, D., and Colonius, T. (2021). "Nonlinear input/output analysis: application to boundary layer transition". In: *Journal of Fluid Mechanics* 911 (2021), A15.

Riha, A. K., McMillan, M., and Reed, H. L. (2021). "Linear stability of a boundary-layer vortex on a hypersonic finned cone". In: AIAA AVIATION Forum. 2021.

Roy, A. and Govindarajan, R. (2010). "An introduction to hydrodynamic stability". In: *Rheology of Complex Fluids*. 2010, pp. 131–147.

Ruban, A. I., Keshari, S. K., and Kravtsova, M. A. (2021). "On boundary-layer receptivity to entropy waves". In: *Journal of Fluid Mechanics* 929 (2021), A17.

Saric, W. S. (1994). "Görtler vortices". In: *Annual Review of Fluid Mechanics* 26.1 (1994), pp. 379–409.

Saric, W. S., Reed, H. L., and Kerschen, E. J. (2002). "Boundary-layer receptivity to freestream disturbances". In: *Annual review of fluid mechanics* 34.1 (2002), pp. 291–319.

Saric, W. S., Reed, H. L., and White, E. B. (2003). "Stability and transition of three-dimensional boundary layers". In: *Annual Review of Fluid Mechanics* 35.1 (2003), pp. 413–440.

Schenk, O. and Gärtner, K. (2004). "Solving unsymmetric sparse systems of linear equations with PARDISO". In: *Future Generation Computer Systems* 20.3 (2004), pp. 475–487.

Schmid, P. J. (2007). "Nonmodal stability theory". In: *Annual Review of Fluid Mechanics* 39.1 (2007), pp. 129–162.

Schmidt, O. T., Towne, A., Rigas, G., Colonius, T., and Brès, G. A. (2018). "Spectral analysis of jet turbulence". In: *Journal of Fluid Mechanics* 855 (2018), pp. 953–982.

Schrader, L.-U., Brandt, L., and Henningson, D. S. (2009). "Receptivity mechanisms in three-dimensional boundary-layer flows". In: *Journal of Fluid Mechanics* 618 (2009), pp. 209–241.

Sipp, D., Marquet, O., Meliga, P., and Barbagallo, A. (2010). "Dynamics and control of global instabilities in open-flows: a linearized approach". In: *Applied Mechanics Reviews* 63.3 (2010).

Sivasubramanian, J. and Fasel, H. F. (2014). "Numerical investigation of the development of three-dimensional wavepackets in a sharp cone boundary layer at Mach 6". In: *Journal of Fluid Mechanics* 756 (2014), pp. 600–649.

Sivasubramanian, J. and Fasel, H. F. (2015). "Direct numerical simulation of transition in a sharp cone boundary layer at Mach 6: fundamental breakdown". In: *Journal of Fluid Mechanics* 768 (2015), pp. 175–218.

Sivasubramanian, J., Sandberg, R. D., Terzi, D. A. V., and Fasel, H. F. (2007). "Numerical investigation of transitional supersonic base flows with flow control". In: *Journal of Spacecraft and Rockets* 44.5 (2007), pp. 1021–1028.

Skene, C. S., Yeh, C.-A., Schmid, P. J., and Taira, K. (2022). "Sparsifying the resolvent forcing mode via gradient-based optimisation". In: *Journal of Fluid Mechanics* 944 (2022), A52.

Sousa, V. C. B., Patel, D., Chapelier, J.-B., Wartemann, V., Wagner, A., and Scalo, C. (2019). "Numerical investigation of second-mode attenuation over carbon/carbon porous surfaces". In: *Journal of Spacecraft and Rockets* 56.2 (2019), pp. 319–332.

Stetson, K. (1983). "Nosetip bluntness effects on cone frustum boundary layer transition in hypersonic flow". In: 16th Fluid and Plasmadynamics Conference. 1983.

Stetson, K. and Kimmel, R. (1992). "On hypersonic boundary-layer stability". In: 30th Aerospace Sciences Meeting and Exhibit. 1992.

Stetson, K., Kimmel, R., Donaldson, J., and Siler, L. (1991). "A comparison of planar and conical boundary layer stability and transition at a Mach number of 8". In: 22nd Fluid Dynamics, Plasma Dynamics and Lasers Conference. 1991.

Tam, C. K. W. and Hu, F. Q. (1989). "On the three families of instability waves of high-speed jets". In: *Journal of Fluid Mechanics* 201 (1989), pp. 447–483.

Taylor, G. I. and Maccoll, J. W. (1933). "The air pressure on a cone moving at high speeds.—I". In: *Proceedings of the Royal Society of London. Series A* 139.838 (1933), pp. 278–297.

Thome, J., Dwivedi, A., Nichols, J. W., and Candler, G. V. (2018). "Direct numerical simulation of BOLT hypersonic flight vehicle". In: AIAA AVIATION Forum — Fluid Dynamics Conference. 2018.

Thompson, K. W. (1987). "Time dependent boundary conditions for hyperbolic systems". In: *Journal of Computational Physics* 68.1 (1987), pp. 1–24.

Tissot, G., Zhang, M., Lajús, F. C., Cavalieri, A. V. G., and Jordan, P. (2017). "Sensitivity of wavepackets in jets to nonlinear effects: the role of the critical layer". In: *Journal of Fluid Mechanics* 811 (2017), pp. 95–137.

Towne, A. (2016). "Advancements in jet turbulence and noise modeling: accurate one-way solutions and empirical evaluation of the nonlinear forcing of wavepackets". PhD thesis. California Institute of Technology, 2016.

Towne, A., Cavalieri, A. V. G., Jordan, P., Colonius, T., Schmidt, O., Jaunet, V., and Brès, G. A. (2017). "Acoustic resonance in the potential core of subsonic jets". In: *Journal of Fluid Mechanics* 825 (2017), pp. 1113–1152.

Towne, A. and Colonius, T. (2013). "Improved parabolization of the Euler equations". In: 19th AIAA/CEAS Aeroacoustics Conference. 2013.

Towne, A. and Colonius, T. (2015). "One-way spatial integration of hyperbolic equations". In: *Journal of Computational Physics* 300 (2015), pp. 844–861.

Towne, A., Rigas, G., and Colonius, T. (2019). "A critical assessment of the parabolized stability equations". In: *Theoretical and Computational Fluid Dynamics* 33.3 (2019), pp. 359–382.

Towne, A., Rigas, G., Kamal, O., Pickering, E., and Colonius, T. (2022). "Efficient global resolvent analysis via the one-way Navier-Stokes equations". In: *Journal of Fluid Mechanics* 948 (2022), A9.

Trefethen, L. N., Trefethen, A. E., Reddy, S. C., and Driscoll, T. A. (1993). "Hydrodynamic stability without eigenvalues". In: *Science* 261.5121 (1993), pp. 578–584.

Turbeville, F. D. and Schneider, S. P. (2018). "Boundary-layer instability on a slender cone with highly swept fins". In: AIAA AVIATION Forum — Fluid Dynamics Conference. 2018.

Turbeville, F. D. and Schneider, S. P. (2019). "Transition on a cone with a highly-swept fin at Mach 6". In: AIAA AVIATION Forum. 2019.

Turbeville, F. D. and Schneider, S. P. (2021). "Effect of nose bluntness on fin-cone transition at Mach 6". In: AIAA AVIATION Forum. 2021.

Wagner, A. (2014). "Passive hypersonic boundary layer transition control using ultrasonically absorptive carbon-carbon ceramic with random microstructure". PhD thesis. Katholieke Universiteit Leuven, 2014.

Zhong, X. and Wang, X. (2012). "Direct numerical simulation on the receptivity, instability, and transition of hypersonic boundary layers". In: *Annual Review of Fluid Mechanics* 44.1 (2012), pp. 527–561.

Zhu, M. and Towne, A. (2023). "Recursive one-way Navier-Stokes equations with PSE-like cost". In: *Journal of Computational Physics* 473 (2023), p. 111744.

Appendix A

NON-ORTHOGONAL CURVILINEAR COORDINATES

The OWNS algorithm is written in the *physical*, non-orthogonal coordinate system, allowing versatility in performing boundary-layer stability calculations of complex geometries while simultaneously satisfying the cylindrical coordinate system used for jet calculations. This appendix delineates the tensor properties used to write the LNS equations from Sec. 2.1 in the generalized coordinate system and how the fundamental grid metrics are computed for each type of analysis. We also outline how the stability grid is generated for both jets and boundary layers.

A.1 Tensor calculus

We begin by defining (x, y, z) or x^i as the global Cartesian coordinate system and (ξ, η, ζ) or ξ^i as the streamwise, wall-normal, and spanwise curvilinear coordinate system, respectively. The natural or covariant basis vectors can be defined as

$$\boldsymbol{g_1} = \left(\frac{\partial x}{\partial \xi}, \frac{\partial y}{\partial \xi}, \frac{\partial z}{\partial \xi}\right)^T, \quad \boldsymbol{g_2} = \left(\frac{\partial x}{\partial \eta}, \frac{\partial y}{\partial \eta}, \frac{\partial z}{\partial \eta}\right)^T, \quad \boldsymbol{g_3} = \left(\frac{\partial x}{\partial \zeta}, \frac{\partial y}{\partial \zeta}, \frac{\partial z}{\partial \zeta}\right)^T, \tag{A.1}$$

and the corresponding dual or contravariant basis vectors as

$$\boldsymbol{g^1} = \left(\frac{\partial \xi}{\partial x}, \frac{\partial \xi}{\partial y}, \frac{\partial \xi}{\partial z}\right)^T, \quad \boldsymbol{g^2} = \left(\frac{\partial \eta}{\partial x}, \frac{\partial \eta}{\partial y}, \frac{\partial \eta}{\partial z}\right)^T, \quad \boldsymbol{g^3} = \left(\frac{\partial \zeta}{\partial x}, \frac{\partial \zeta}{\partial y}, \frac{\partial \zeta}{\partial z}\right)^T. \tag{A.2}$$

The covariant g_{ij} and contravariant g^{ij} metric tensor components, along with the Jacobian J can therefore be defined as

$$g_{ij} = \boldsymbol{g_i} \cdot \boldsymbol{g_j}, \quad g^{ij} = \boldsymbol{g^i} \cdot \boldsymbol{g^j}, \quad J = \begin{vmatrix} \frac{\partial x}{\partial \xi} & \frac{\partial x}{\partial \eta} & \frac{\partial x}{\partial \zeta} \\ \frac{\partial y}{\partial \xi} & \frac{\partial y}{\partial \eta} & \frac{\partial y}{\partial \zeta} \\ \frac{\partial z}{\partial \xi} & \frac{\partial z}{\partial \eta} & \frac{\partial z}{\partial \zeta} \end{vmatrix}, \tag{A.3}$$

where upon closer examination, the contravariant metric tensor is simply the inverse of the covariant metric tensor $\boldsymbol{g}$. We can now define the Christoffel symbols of the second kind

$$\begin{Bmatrix} l \\ ij \end{Bmatrix} = \frac{1}{2} g^{ls} \left(\frac{\partial g_{is}}{\partial x^j} + \frac{\partial g_{js}}{\partial x^i} - \frac{\partial g_{ij}}{\partial x^s}\right). \tag{A.4}$$

We now transform all of the aforementioned grid metrics onto the *physical* coordinate system as outlined in Demirdzic et al. (1987) and Demirdzic (1982). In this

section, the physical counterparts will be denoted with tildes, except for the physical Christoffel symbols which will be denoted with square brackets

$$\widetilde{g}_{ij} = \frac{g_{ij}}{\sqrt{g_{ii}g_{jj}}}, \tag{A.5}$$

$$\begin{bmatrix} i \\ jk \end{bmatrix} = \sqrt{\frac{g_{ii}}{g_{jj}g_{kk}}} \left(\begin{Bmatrix} i \\ jk \end{Bmatrix} - \delta^i_j \frac{g_{jm}}{g_{jj}} \begin{Bmatrix} m \\ jk \end{Bmatrix} \right), \tag{A.6}$$

$$\widetilde{d\xi}^i = h_i d\xi^i, \quad h_i = ||g_i||, \tag{A.7}$$

where h_i are the scale factors in the respective direction. Similar to the nonphysical case, the physical contravariant metric tensor can be computed by inverting the physical covariant metric tensor $\widetilde{\boldsymbol{g}}$. With the physical quantities now defined, we outline several important tensor-calculus properties used in Sec. 2.1, where, for this example, we assume u, $\boldsymbol{v}$, and $\boldsymbol{w}$ as general zeroth-, first-, and second-order tensors defined in the physical curvilinear coordinates, respectively,

$$\nabla_j u = \frac{1}{h_j}\frac{\partial u}{\partial \xi^j}, \tag{A.8}$$

$$\nabla \cdot \boldsymbol{v} = \frac{1}{h_j}\frac{\partial v^j}{\partial \xi^j} + v^m \begin{bmatrix} j \\ mj \end{bmatrix}, \tag{A.9}$$

$$\nabla_j v^i = \frac{1}{h_j}\frac{\partial v^i}{\partial \xi^j} + v^m \begin{bmatrix} i \\ mj \end{bmatrix}, \tag{A.10}$$

$$\nabla_j w^{ij} = \frac{1}{h_j}\frac{\partial w^{ij}}{\partial \xi^j} + w^{mj} \begin{bmatrix} i \\ mj \end{bmatrix} + w^{im} \begin{bmatrix} j \\ mj \end{bmatrix}. \tag{A.11}$$

A.2 Grid metric generation

In this section, we will outline how the fundamental grid metrics are generated to compute the physical covariant/contravariant metric tensors, Christoffel symbols, and the scale factors from Sec. A.1 for the three different types of OWNS analyses: 2D, 3D-Fourier (3DF), and 3D. 2D calculations have no spanwise coordinate, wavenumber, or velocity, and thus the total state vector reduces to $\boldsymbol{q} = [\rho, u, v, T]^T$. For 3DF analyses, the base flow is assumed to exhibit spanwise homogeneity along the streamwise direction and thus the 3D perturbations are Fourier-transformed with a spanwise wavenumber. Note that the computational domain is still 2D (no spanwise coordinate), but a locally homogeneous spanwise velocity exists, and thus we refer to the 3DF domain hereafter as "quasi 3D." Lastly, 3D calculations have coordinates in all three spatial directions, but only applicable for the local solvers (see Sec. B.3). Note that for all analysis types, the fundamental grid metrics, and

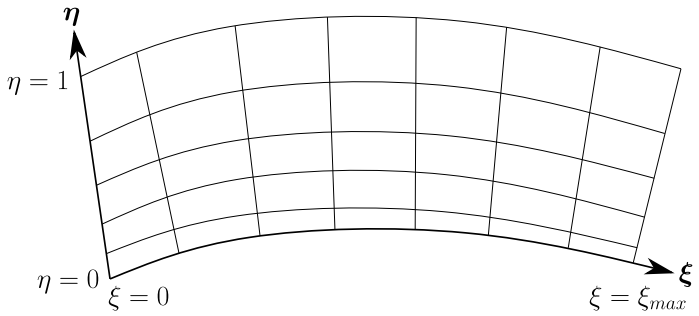

Figure A.1: Schematic of a curvilinear grid for 2D boundary-layer computations.

thereby the quantities from Sec. A.1, are computed on the base-flow grid and then interpolated onto the stability grid via the modified Akima cubic Hermite method from MATLAB.

A.2.1 2D implementation

For 2D calculations of boundary layers, the ξ-coordinate corresponds to the streamwise arclength along the geometry, i.e. at $\eta = 0$, in which the η-coordinate is defined as

$$\eta = \left.\frac{\eta_{wn}}{\eta_{wn,max}}\right|_{\xi=0}, \quad \eta \in [0, 1], \tag{A.12}$$

where η_{wn} is the non-dimensional, physical wall-normal coordinate. A schematic of this coordinate system is presented in Fig. A.1. The wall-normal grid metrics $\frac{\partial x}{\partial \eta}$, $\frac{\partial^2 x}{\partial \eta^2}$, etc. are then computed via second-order numerical differentiation.

In contrast to the wall-normal direction, we wish to ensure any streamwise contraction/expansion of the grid is strictly due to the surface curvature. Thus, we first define the signed curvature of the geometry as

$$\kappa_1(\xi) = -h_1^{-3}\left(\frac{\partial x}{\partial \xi}\frac{\partial^2 y}{\partial \xi^2} - \frac{\partial y}{\partial \xi}\frac{\partial^2 x}{\partial \xi^2}\right), \tag{A.13}$$

where $\kappa_1 < 0$ and $\kappa_1 > 0$ for concave and convex surface curvatures, respectively. Note that all quantities in Eq. A.13 are computed at the wall ($\eta = 0$) with second-order numerical differentiation. The streamwise scale factor at each grid point can therefore be computed as

$$h_1(\xi, \eta) = 1 + \kappa_1 \eta_{wn}(\xi, \eta). \tag{A.14}$$

Thus, the first-order streamwise grid metrics are calculated using Eq. A.1 by constructing $\boldsymbol{g_1}$ as

$$\boldsymbol{g_1}(\xi, \eta) = h_1 \hat{\boldsymbol{g}}_{\boldsymbol{1}}(\xi), \tag{A.15}$$

where $\hat{\boldsymbol{g}}_{\mathbf{1}}$ is the streamwise unit covariant basis vector at the surface (the hat will denote surface unit vectors in this section). Higher-order streamwise grid metrics are then computed with second-order numerical differentiation with any cross-derivatives, e.g. $\frac{\partial^2 x}{\partial \xi \eta}$, calculated by numerically differentiating the streamwise grid metrics from Eq. A.15 along the η-coordinate.

In summary, at each grid point, $\boldsymbol{g}_{\mathbf{1}}$ is oriented along the surface basis vector at $\eta = 0$ with its magnitude corresponding to the contraction/expansion of the grid due to the local streamwise surface curvature. However, analyses neglecting curvature effects can also be performed by enforcing

$$\begin{bmatrix} k \\ i1 \end{bmatrix} = 0, \quad h_1 = 1. \tag{A.16}$$

Essentially, since the Christoffel quantity $\begin{bmatrix} k \\ ij \end{bmatrix}$ represents the k^{th} component of how the i^{th} unit covariant basis vector changes in the j^{th} direction, the effect of κ_1 can be negated by zeroing any variations of the covariant basis vectors in the ξ-direction, while also constraining the streamwise scale factor to unity.

Lastly, the fundamental grid metrics for planar jets are computed analytically knowing that the local coordinate system coincides with the Cartesian coordinates, i.e. $x = \xi$ and $y = \eta$.

A.2.2 3DF implementation

Although 3DF calculations have no "physical" spanwise coordinate due to the Fourier transformation, the fundamental grid metrics are derived using the 3D base-flow grid and subsequently mapped onto a corresponding quasi 3D grid. Similar to Sec. A.2.1, the ξ-coordinate for boundary layers is the streamwise arclength, which is parametrically defined with the 3D surface coordinates (x_s, y_s, z_s) inputted by the user. The wall-normal η-coordinate is defined as

$$\eta = \frac{\bar{\eta}_{wn}}{\bar{\eta}_{wn,max}}, \quad \eta \in [0, 1], \tag{A.17}$$

where $\bar{\eta}_{wn}$ is the streamwise and spanwise averaged non-dimensional, physical wall-normal coordinate. This choice of coordinate system (see Fig. A.2) ensures any variations in the wall-normal stretching within the full 3D domain are encapsulated in the quasi 3D base-flow grid. Furthermore, we will define a spanwise coordinate ζ as follows

$$\zeta = \left. \frac{\zeta_{sa}}{\zeta_{sa,max}} \right|_{\xi=0,\eta=0}, \quad \zeta \in [0, 1], \tag{A.18}$$

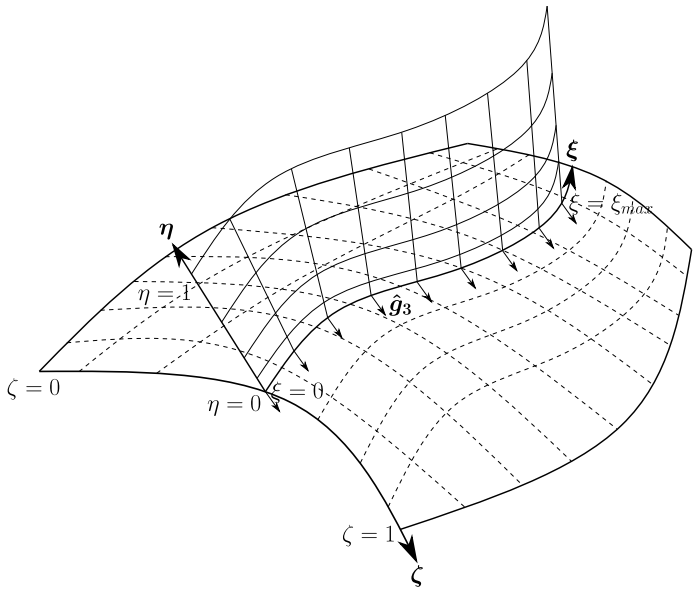

Figure A.2: Schematic of a curvilinear grid for 3DF boundary-layer computations. Arrows projecting from the ξ-coordinate at $\eta = 0$ demonstrate how $\hat{g}_3$ may be oriented. Dashed lines correspond to the discretized 2D base-flow surface used to compute the grid metrics for the quasi 3D grid.

where ζ_{sa} is the non-dimensional, physical spanwise arclength. Although ζ is not used in the stability analysis, we require this coordinate to construct the spanwise grid metrics along the quasi 3D base-flow grid. With (ξ, η, ζ) defined, we can now determine the coordinates (x_b, y_b, z_b) upon which all grid metrics are computed on as follows

$$\begin{pmatrix} x_b(\xi,\eta) \\ y_b(\xi,\eta) \\ z_b(\xi,\eta) \end{pmatrix} = \begin{pmatrix} x_s(\xi) \\ y_s(\xi) \\ z_s(\xi) \end{pmatrix} + \eta\eta_{wn,s}(\xi)\hat{\boldsymbol{g}}_{\boldsymbol{2}}(\xi), \tag{A.19}$$

where $\eta_{wn,s}$ and $\hat{\boldsymbol{g}}_{\boldsymbol{2}}$ are the wall-normal distance and unit wall-normal vector along the streamwise arclength ξ, respectively. Note that we assume the 3D base-flow grid already contains wall-normal grid distribution. The grid metrics $\frac{\partial x_b}{\partial \eta}$, $\frac{\partial^2 x_b}{\partial \eta^2}$, etc. in the wall-normal direction are then computed via second-order numerical differentiation.

Similar to the 2D case, we require any streamwise and spanwise grid contraction/-expansion to be solely due to the streamwise (κ_1) and spanwise (κ_3) *normal* surface curvatures, respectively. However, unlike the 2D case where the surface is parameterized with the ξ-coordinate, we will use the first and second fundamental forms from differential geometry to compute κ_1 and κ_3, in which the coefficients are

defined as follows

$$E^1 = \boldsymbol{g_1} \cdot \boldsymbol{g_1},\ F^1 = \boldsymbol{g_1} \cdot \boldsymbol{g_3},\ G^1 = \boldsymbol{g_3} \cdot \boldsymbol{g_3}, \tag{A.20a}$$

$$E^2 = \frac{\partial \boldsymbol{g_1}}{\partial \xi} \cdot \hat{\boldsymbol{g}}_{\boldsymbol{2}},\ F^2 = \frac{\partial \boldsymbol{g_3}}{\partial \xi} \cdot \hat{\boldsymbol{g}}_{\boldsymbol{2}},\ G^2 = \frac{\partial \boldsymbol{g_3}}{\partial \zeta} \cdot \hat{\boldsymbol{g}}_{\boldsymbol{2}}, \tag{A.20b}$$

where superscripts 1 and 2 denote the first and second fundamental coefficients, respectively. Note that all surface covariant basis vectors in Eq. A.20 are computed on the 3D base-flow grid via second-order numerical differentiation and then interpolated along ξ. With this, κ_1 and κ_3 can be computed as follows

$$\kappa_{1,3}(\xi) = -(E^2\dot{\xi}^2 + 2F^2\dot{\xi}\dot{\zeta} + G^2\dot{\zeta}^2), \tag{A.21a}$$

$$\begin{pmatrix} \dot{\xi} \\ \dot{\zeta} \end{pmatrix} = \begin{pmatrix} E & F \\ F & G \end{pmatrix}^{-1} \begin{pmatrix} \hat{\boldsymbol{g}}_{\boldsymbol{1,3}} \cdot \boldsymbol{g_1} \\ \hat{\boldsymbol{g}}_{\boldsymbol{1,3}} \cdot \boldsymbol{g_3} \end{pmatrix}, \tag{A.21b}$$

where $\hat{\boldsymbol{g}}_{\boldsymbol{1,3}}$ corresponds to the unit streamwise/spanwise surface covariant basis vectors along ξ. Note that the subscript $(1, 3)$ compactly represents either the streamwise (1) or spanwise (3) component. Similar to the 2D case, $\kappa_{1,3}$ is positive and negative for convex and concave normal surface curvatures, respectively. Although $\hat{\boldsymbol{g}}_{\boldsymbol{1}}$ is known since (x_s, y_s, z_s) is supplied into OWNS as an input, $\hat{\boldsymbol{g}}_{\boldsymbol{3}}$ can be oriented in three ways:

1. Locally orthogonal to $\hat{\boldsymbol{g}}_{\boldsymbol{1}}$ and $\hat{\boldsymbol{g}}_{\boldsymbol{2}}$, i.e. $\hat{\boldsymbol{g}}_{\boldsymbol{3}}(\xi) = \frac{\boldsymbol{g_1} \times \boldsymbol{g_2}}{||\boldsymbol{g_1} \times \boldsymbol{g_2}||}$.

2. Along the 3D base-flow grid, i.e. computing $\hat{\boldsymbol{g}}_{\boldsymbol{3}}$ based on the surface spanwise grid lines and interpolating onto ξ.

3. Along a user-prescribed direction projected onto the local surface tangent plane, i.e. $\boldsymbol{g_3}(\xi) = \boldsymbol{g_{3,u}} - \frac{\boldsymbol{g_{3,u}} \cdot \boldsymbol{g_2}}{\boldsymbol{g_2} \cdot \boldsymbol{g_2}} \boldsymbol{g_2}$, where $\boldsymbol{g_{3,u}}$ is the user-defined direction and $\boldsymbol{g_2}$ is the wall-normal surface covariant basis vector along ξ ($\hat{\boldsymbol{g}}_{\boldsymbol{3}}$ can thereafter be computed by normalizing $\boldsymbol{g_3}$).

Note that the non-orthogonal implementation permits $\hat{\boldsymbol{g}}_{\boldsymbol{3}}$ to be oriented in any arbitrary direction along the local surface tangent plane, allowing the user to perform more versatile stability calculations.

With $\kappa_{1,3}$ computed, the streamwise and spanwise scale factors at each grid point of the quasi 3D grid can be calculated as follows

$$h_{1,3}(\xi, \eta) = 1 + \kappa_{1,3}\eta_{wn,b}(\xi, \eta), \tag{A.22}$$

where $\eta_{wn,b}$ is the non-dimensional, physical wall-normal coordinate of the quasi 3D grid. Note that if the user elects to prescribe a streamwise-varying spanwise wavelength, i.e. $\lambda_\zeta = \lambda_\zeta(\xi)$, then h_3 is modified to

$$h_3(\xi,\eta) = \frac{\lambda_\zeta}{\lambda_{\zeta,\mathbb{0}}}\left(1 + \kappa_3\eta_{wn,b}(\xi,\eta)\right), \tag{A.23}$$

where $\lambda_{\zeta,\mathbb{0}}$ is the inlet spanwise wavelength. Finally, the first-order streamwise and spanwise grid metrics are calculated using Eq. A.1 by constructing $\boldsymbol{g_{1,3}}$ as follows

$$\boldsymbol{g_{1,3}}(\xi,\eta) = h_{1,3}\hat{\boldsymbol{g}}_{\boldsymbol{1,3}}(\xi). \tag{A.24}$$

Higher-order streamwise grid metrics and any cross-derivatives involving η are computed in a similar manner to Sec. A.2.1. For the spanwise grid metrics, any cross-derivatives involving ξ or η, e.g. $\frac{\partial^2 x_b}{\partial\xi\zeta}$, are calculated by numerically differentiating the spanwise grid metrics along the ξ- and/or η-coordinate. Finally, to be consistent with the base-flow homogeneity assumption of 3DF calculations, the spanwise covariant basis vectors along ξ are assumed to be invariant in ζ, i.e. $\frac{\partial \boldsymbol{g_3}}{\partial\zeta} = \frac{\partial^2 \boldsymbol{g_3}}{\partial\zeta^2} = 0$, which also implies any derivatives involving $\frac{\partial^2}{\partial\zeta^2} = 0$.

To summarize, at each point of the quasi 3D grid, $\boldsymbol{g_1}$ is oriented along the prescribed pathway corresponding to (x_s, y_s, z_s), whereas $\boldsymbol{g_3}$ is oriented either locally orthogonal, along the 3D base-flow grid, or a user-defined direction projected onto the local surface tangent plane. The magnitudes of $\boldsymbol{g_{1,3}}$, i.e. $h_{1,3}$, dictate the grid contraction/expansion and are computed based on the local streamwise/spanwise normal surface curvatures. The user can also choose to perform stability analyses excluding streamwise and/or spanwise curvature effects by correspondingly setting

$$\left(\begin{bmatrix} k \\ i1 \end{bmatrix} = 0, \quad h_1 = 1\right) \text{ and/or } \left(\begin{bmatrix} k \\ i3 \end{bmatrix} = 0, \quad h_3 = 1\right). \tag{A.25}$$

Similar to Sec. A.2.1, enforcing Eq. A.25 neglects the effect of $\kappa_{1,3}$ by removing any variations of the unit covariant basis vectors in the ξ- and/or ζ-directions, while also constraining the corresponding scale factor(s) to unity.

In contrast to boundary layers, 3DF jet computations are performed in cylindrical coordinates, and thus the fundamental grid metrics can be computed analytically with the following coordinate transformation

$$x = \xi, \quad y = \eta\cos\zeta, \quad z = \eta\sin\zeta, \tag{A.26}$$

where (ξ,η,ζ) correspond to the canonical axial, radial, and tangential coordinates, respectively. Note that stability analyses of 3DF jets are performed only along the

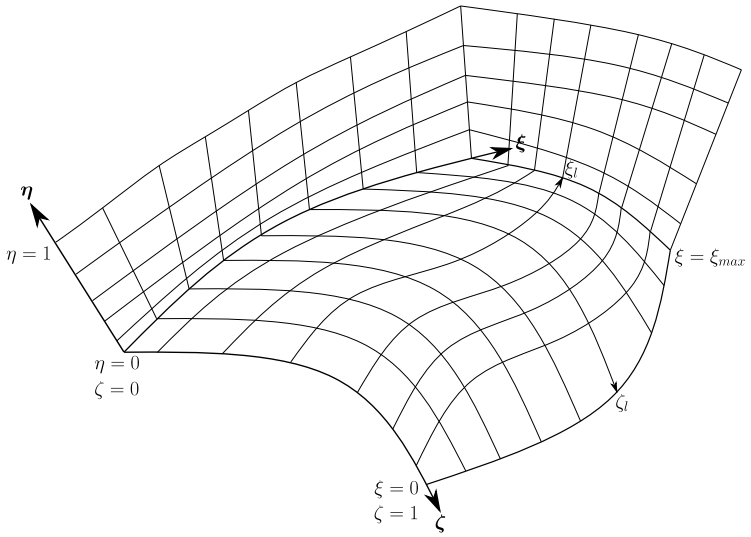

Figure A.3: Schematic of a curvilinear grid for 3D boundary-layer computations. Example of ξ_l and ζ_l, i.e. surface grid lines (arclengths) used to compute local, first-order grid metrics, are also depicted.

$\zeta = 0$ azimuthal plane. Lastly, the singularity at the pole is mitigated by starting the radial grid slightly offset from the centerline with the corresponding pole conditions explained in Sec. B.1.2.

A.2.3 3D implementation

Unlike 2D and 3DF analyses, 3D stability calculations require discretization in all three spatial directions, where the ξ-coordinate for boundary layers corresponds to the streamwise arclength at $\eta = \zeta = 0$, i.e. along the surface geometry at the first spanwise plane. The cross-stream coordinates η and ζ are defined as

$$\eta = \left.\frac{\eta_{wn}}{\eta_{wn,max}}\right|_{\xi=0,\zeta=0}, \quad \eta \in [0,1], \tag{A.27a}$$

$$\zeta = \left.\frac{\zeta_{sa}}{\zeta_{sa,max}}\right|_{\xi=0,\eta=0}, \quad \zeta \in [0,1], \tag{A.27b}$$

where η_{wn} and ζ_{sa} are defined the same as Secs. A.2.1 and A.2.2, respectively. The 3D coordinate system is exemplified in Fig. A.3. The wall-normal grid metrics $\frac{\partial x}{\partial \eta}$, $\frac{\partial^2 x}{\partial \eta^2}$, etc. are then computed via second-order numerical differentiation.

Similar to the 2D and 3DF cases, we wish for any streamwise and spanwise grid contraction/expansion to correspond to the local normal surface curvatures, thus requiring computation of $\kappa_{1,3}(\xi, \zeta)$, at each point on the surface. This is done identically to Sec. A.2.2 by using the first and second fundamental coefficients, and aligning the unit surface covariant basis vectors $\hat{\boldsymbol{g}}_{\mathbf{1,3}}$ along the streamwise and

spanwise surface grid lines. Note that an advantage of the non-orthogonal system is that surface grid points can be distributed arbitrarily to efficiently resolve any rapidly evolving geometric features.

With $\kappa_{1,3}$ computed, the streamwise and spanwise scale factors at each grid point of the 3D grid can be calculated as follows

$$h_{1,3}(\xi, \eta, \zeta) = 1 + \kappa_{1,3}\eta_{wn}(\xi, \eta, \zeta), \tag{A.28}$$

where, similar to Sec. A.2.1, η_{wn} is the non-dimensional, physical wall-normal coordinate. Finally, the first-order streamwise and spanwise grid metrics are calculated using Eq. A.1 by constructing $\boldsymbol{g_{1,3}}$ as follows

$$\boldsymbol{g_{1,3}}(\xi, \eta, \zeta) = h_{1,3}\hat{\boldsymbol{g}}_{\boldsymbol{1,3}}(\xi, \zeta). \tag{A.29}$$

However, the grid metrics computed from Eq. A.29 correspond to the *local* streamwise and spanwise surface grid lines (arclengths), which we will denote as ξ_l and ζ_l (see Fig. A.3), respectively, and are not defined with respect to the ξ-coordinate or ζ-coordinate from Eq. A.27. Thus, the following mappings are required to have consistent first-order grid metrics

$$\frac{\partial}{\partial \xi} = \frac{\partial \xi_l}{\partial \xi}\frac{\partial}{\partial \xi_l}, \quad \frac{\partial}{\partial \zeta} = \frac{\partial \zeta_l}{\partial \zeta}\frac{\partial}{\partial \zeta_l}, \tag{A.30}$$

where the mapping functions $\frac{\partial \xi_l}{\partial \xi}(\xi, \zeta)$ and $\frac{\partial \zeta_l}{\partial \zeta}(\xi, \zeta)$ are computed via second-order numerical differentiation. Higher-order streamwise and spanwise grid metrics and any cross-derivatives are then calculated numerically.

To recapitulate, the local, first-order streamwise and spanwise grid metrics within the 3D domain are determined by first orienting $\boldsymbol{g_{1,3}}$ along the surface covariant basis vectors. The magnitudes of $\boldsymbol{g_{1,3}}$, i.e. $h_{1,3}$, are then computed based on the local streamwise/spanwise normal surface curvatures, which then allows computation of $\frac{\partial x}{\partial \xi_l}$, $\frac{\partial x}{\partial \zeta_l}$, etc. We then map these local grid metrics to be defined with respect to ξ and ζ, upon which higher-order grid metrics can be calculated numerically thereafter. If the user wishes to neglect curvature effects, only the streamwise component can be excluded since 3D stability analyses are streamwise-local but fully discretized in the cross-stream plane. However, extra care must be taken when applying Eq. A.16, such that the streamwise scale factor with respect to ξ_l must be set to unity, which

we will denote as $h_{1,l}$. We can then compute h_1 as follows

$$\begin{aligned} h_1 =& \sqrt{\left(\frac{\partial x}{\partial \xi_l}\frac{\partial \xi_l}{\partial \xi}\right)^2 + \left(\frac{\partial y}{\partial \xi_l}\frac{\partial \xi_l}{\partial \xi}\right)^2 + \left(\frac{\partial z}{\partial \xi_l}\frac{\partial \xi_l}{\partial \xi}\right)^2} \\ =& \frac{\partial \xi_l}{\partial \xi}\sqrt{\left(\frac{\partial x}{\partial \xi_l}\right)^2 + \left(\frac{\partial y}{\partial \xi_l}\right)^2 + \left(\frac{\partial z}{\partial \xi_l}\right)^2} \\ =& \frac{\partial \xi_l}{\partial \xi} h_{1,l} \\ =& \frac{\partial \xi_l}{\partial \xi}. \end{aligned} \tag{A.31}$$

Similar to 3DF jet computations, 3D calculations are performed in cylindrical coordinates with the fundamental grid metrics computed analytically using the coordinate transformation of Eq. A.26. The singularity at the pole is avoided by starting the radial grid slightly offset from the centerline, but the imposition of pole conditions depends on the extent of the azimuthal domain, i.e. whether $\zeta_{max} = 2\pi$ or $\zeta_{max} < \pi$. If the latter, the azimuthal domain must be an integer fraction of π (e.g. π, $\pi/2$, $\pi/3$, etc.) to ensure radially symmetric conditions across the centerline, in which practical implementation of the π-domain would correspond to $\zeta_{max} = \pi - \epsilon$, where ϵ is the machine precision. The two possible azimuthal domains are schematically shown in Fig. A.4 and the corresponding pole conditions are explained in Sec. B.1.2.

A.3 Stability grid generation

After computing the fundamental grid metrics and corresponding physical covariant/contravariant metric tensors, Christoffel symbols, and scale factors on the base-flow grid, the stability grid is subsequently generated. Points along the ξ-coordinate are uniformly distributed, except for global methods (see Sec. B.3), in which a hyperbolic tangent function may be used cluster points near the inlet to improve computational efficiency. This is particularly useful when resolving leading-edge effects for boundary layers or the Kelvin-Helmholtz mode near the nozzle exit for jets. For boundary layers, the stretched η-coordinate can be constructed by one of the following three ways:

1. Malik stretching—half the nodes are clustered below a user-defined η-coordinate denoted as η_h (Malik, 1990).

2. Biquadratic stretching—nodes are distributed into three regions to facilitate interior clustering (in addition to the boundaries) (Groot, 2018). Nodes

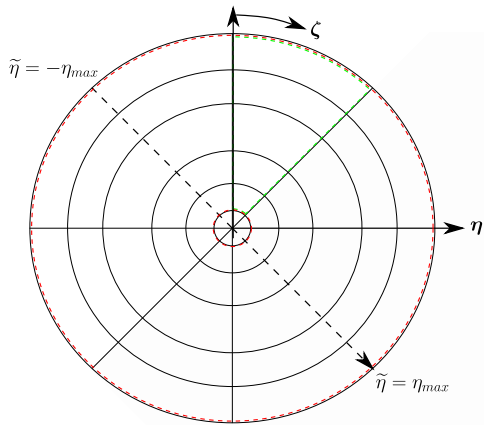

Figure A.4: Schematic of a curvilinear grid for 3D jet computations. The red dashed lines correspond to a full 2π-azimuthal domain, whereas the green dashed lines correspond to an example of an azimuthal slice, i.e. a $\frac{\pi}{4}$-azimuthal domain. The η- and ζ-coordinates correspond to the radial and tangential directions from cylindrical coordinates, respectively. The black dashed line is the transformed radial coordinate $\widetilde{\eta}$ from Mohseni and Colonius (2000).

are clustered in the regions $[0, \frac{3}{4}\eta_h]$,$[\frac{3}{4}\eta_h, \frac{5}{2}\eta_h]$, and $[\frac{5}{2}\eta_h, 1]$, where $\eta_h < 32/87$ is a user-defined η-coordinate (this constraint ensures a monotonic η-distribution without discontinuities). Smaller values of η_h (typically $\eta_h \leq 0.1$) will increase the stretching within the boundary-layer region and near-field free-stream/shock layer, but yield coarse grid resolution near the far-field boundary (this may be suitable for stability analyses where the disturbances decay slowly into the free-stream/shock layer).

3. Base-flow stretching—wall-normal stretching of the stability grid mimics the stretched η-coordinate from Sec. A.2.

For jets, the radial domain of the stability grid is constructed either with a stretched mixing-layer region using a hyperbolic tangent function or replicates the grid distribution from the base-flow grid. Finally, the spanwise grid for 3D computations is generated with a uniformly distributed ζ-coordinate for both jets and boundary layers.

Appendix B

CALTECH STABILITY AND TRANSITION ANALYSIS TOOLKIT (CSTAT)

CSTAT is a comprehensive stability package designed to perform a variety of analyses from subsonic to hypersonic regimes for boundary and free-shear layers in generalized, non-orthogonal, curvilinear coordinates with user-defined fluid properties (these features were delineated in Secs. A and 2). The motivation behind CSTAT was to develop a package containing the modern stability tools, and thereby provide a means to perform exhaustive computations, both for fundamental understanding and engineering design. Note that the current version of the code, CSTAT V2.0, does not support calculation of nonlinear effects.

The code is written predominantly in MATLAB (R2019a) and requires external libraries if the Intel® oneAPI Math Kernel Library PARDISO package (Schenk and Gärtner, 2004) is to be used as the sparse linear solver. The overall structure of CSTAT can be decomposed into two categories: symbolic and numerical computation. The symbolic portion is written in Wolfram Mathematica, which performs the linearization of the fully compressible Navier-Stokes equations and outputs the operators and generalized curvilinear grid metrics in functional form which are then read into MATLAB when performing the desired stability calculation.

This appendix outlines the various boundary conditions, the base-flow processing prior to stability computations, and the wide range of solvers and utilities within CSTAT for both boundary layers and jets.

B.1 Boundary conditions

B.1.1 Boundary layers

For LST and SBG, no streamwise boundary conditions are required, whereas for local marching methods (PSE and OWNS), only the inlet boundary condition in the form of the perturbed state vector $\boldsymbol{q}'_{\mathbf{0}}$ is prescribed. In contrast, for global methods (see Sec. B.3), inlet and outlet sponges of streamwise thickness Δ_{in} and Δ_{out}, respectively, are employed to model open boundaries (these sponges are augmented exterior to the stability domain of interest). We solve the inviscid form of Eq. 5.1 at the outer sponge boundaries (corresponding to the first and last streamwise grid

points), and couple the 1D inviscid Thompson characteristic boundary conditions (Thompson, 1987) to eliminate any incoming waves into the domain. Note that the sponge regions are excluded in the computation of the inputs and/or responses for all the global methods via the input and output screening matrices $\boldsymbol{\mathcal{B}_p}$ and $\boldsymbol{C_p}$, respectively. Lastly, the sponge can be constructed using a power, exponential, or polynomial function, but the polynomial method (default) has demonstrated the best performance from extensive prior applications in damping the waves originating from the stability domain.

At the wall, the usual boundary conditions include no-slip, i.e. $u' = v' = w' = 0$, coupled with either isothermal ($T' = 0$) or adiabatic ($\partial T'/\partial \eta = 0$) thermal conditions. The user may also elect to choose impedance boundary conditions (IBCs) at the wall of either structured or random porosity where additional input parameters such as porosity, depth of pore, pore radius, tortuosity, fiber diameter, and felt-metal flow resistivity are required. The acoustic model for structured- and random-porosity IBCs corresponds to the work of Fedorov, Malmuth, et al. (2001) and Fedorov, Shiplyuk, et al. (2003), respectively.

The far-field boundary conditions include either 1D inviscid Thompson characteristic boundary conditions (Thompson, 1987) to permit waves leaving the domain only, homogeneous Dirichlet conditions for all perturbed state variables, or a shock condition if the wall-normal domain extends to just below the shock (Petrov, 1985). The last option replaces the η-momentum equation at the far-field with the steady, linearized Rankine-Hugoniot condition assuming no disturbances upstream of the shock, which reads (Cook and Nichols, 2022)

$$p_2' = -2\bar{\rho}_2 \bar{v}_{2,s} v_{2,s}' - \rho_2' \bar{v}_{2,s}^2, \tag{B.1}$$

where the subscript 2 corresponds to conditions just downstream of the shock and $v_{2,s}'$ and $\bar{v}_{2,s}$ are the un/steady shock-normal velocities, respectively. When using the shock boundary condition, the streamwise and spanwise fundamental grid metrics at the far-field boundary must be computed directly with numerical differentiation rather than using the surface normal curvatures from Sec. A.2. This is because the far-field $h_{1,3}$ must reflect the shock curvature (since the shock is a physical far-field boundary) with u and w velocities oriented along the shock surface. Furthermore, we require the shock-normal un/steady velocities rather than the wall-normal quantities to satisfy Eq. B.1. Thus, we first calculate the shock normal $\hat{\boldsymbol{g}}_{\boldsymbol{2,s}}$ as follows

$$\hat{\boldsymbol{g}}_{\boldsymbol{2,s}}(\xi, \zeta) = \frac{\hat{\boldsymbol{g}}_{\boldsymbol{3,s}} \times \hat{\boldsymbol{g}}_{\boldsymbol{1,s}}}{||\hat{\boldsymbol{g}}_{\boldsymbol{3,s}} \times \hat{\boldsymbol{g}}_{\boldsymbol{1,s}}||}, \tag{B.2}$$

where $\hat{\boldsymbol{g}}_{\mathbf{1},s}$ and $\hat{\boldsymbol{g}}_{\mathbf{3},s}$ are the unit streamwise and spanwise covariant basis vectors along the shock surface, respectively. For 3DF calculations, $\hat{\boldsymbol{g}}_{\mathbf{3},s}$ is first computed in the 3D base-flow grid and then interpolated along ξ, whereas 2D analyses in which $\hat{\boldsymbol{g}}_{\mathbf{3},s}$ does not exist, $\hat{\boldsymbol{g}}_{\mathbf{2},s}(\xi)$ is simply orthogonal to $\hat{\boldsymbol{g}}_{\mathbf{1},s}$, which can be computed as

$$\hat{\boldsymbol{g}}_{\mathbf{2},s}(\xi) = \begin{pmatrix} 0 & -1 \\ 1 & 0 \end{pmatrix} \hat{\boldsymbol{g}}_{\mathbf{1},s}. \tag{B.3}$$

Using $\hat{\boldsymbol{g}}_{\mathbf{2}}$ from Sec. A.2, we can write the shock-normal velocity as a function of the wall-normal velocity as follows

$$v_{2,s} = v_2 \cos\theta, \quad \cos\theta = \hat{\boldsymbol{g}}_{\mathbf{2}} \cdot \hat{\boldsymbol{g}}_{\mathbf{2},s}. \tag{B.4}$$

We can thus rewrite Eq. B.1 as

$$p_2' = -\bar{v}_2 \cos^2\theta (2\bar{\rho}_2 v_2' + \rho_2' \bar{v}_2), \tag{B.5}$$

which is used in lieu of the wall-normal momentum equation. The remaining governing equations (continuity, streamwise and spanwise momentum, and energy) remain invariant at the far-field boundary.

The spanwise boundary conditions for 3D computations include periodic, symmetric, and antisymmetric. The penultimate condition enforces $\partial/\partial\zeta = 0$ for ρ', u', v', and T' with $w' = 0$ at the spanwise boundaries, whereas the conditions are reversed for the antisymmetric conditions.

B.1.2 Jets

Streamwise boundary conditions (or their absence) for jets are identical to the boundary-layer case from Sec. B.1.1, with far-field conditions being either the 1D inviscid Thompson characteristic boundary conditions or homogeneous Dirichlet conditions.

Symmetric conditions are employed at the centerline for planar (2D) jets, i.e. $\partial/\partial\eta = 0$ for ρ', u', and T' with $v' = 0$. For 3DF or 3D calculations, which are performed in cylindrical coordinates, the singularity at the pole is mitigated by removing the grid point at $\eta = 0$ and using the transformed radial coordinate $\widetilde{\eta}$ (see Fig. A.4) from Mohseni and Colonius (2000). In the case of 3DF computations, i.e. analyses along the $\zeta = 0$ plane, the radial derivative operators near the centerline are modified with symmetric (even azimuthal mode) or antisymmetric (odd azimuthal mode) finite-difference closure schemes. If performing 3D calculations with $\zeta_{max} < \pi$, only the

symmetric conditions are enforced since the azimuthal domain, which is an integer fraction of π, is assumed to be radially symmetric across the centerline. For the case of the full azimuthal domain, i.e. $\zeta_{max} = 2\pi$, the radial transformation is adapted for the present generalized curvilinear coordinates, such that there is a 1-1 mapping between the η- and $\widetilde{\eta}$-coordinates for $\zeta < \pi$, but $\frac{\partial}{\partial\eta} = -\frac{\partial}{\partial\widetilde{\eta}}$ and $\frac{\partial^2}{\partial\eta^2} = \frac{\partial^2}{\partial\widetilde{\eta}^2}$ for $\zeta \geq \pi$. Furthermore, at any given azimuthal position, v' and w' remain defined with respect to the η-coordinate, but the sign of these variables is reversed if the stencil near the centerline includes grid points through $\eta = 0$.

The spanwise boundary condition for 3D analyses is restricted to the symmetric or antisymmetric constraint from Sec. B.1.1 if $\zeta_{max} < \pi$. Otherwise, the ζ-domain must contain the full 2π revolution with the enforcement of spanwise periodic conditions.

B.2 Base-flow processing

The two inputs into CSTAT are the base flow consisting of the Cartesian velocity components, density, and temperature and the corresponding structured grid. However, since the velocity vector $\boldsymbol{u}$ in Eq. 2.1 is composed of the physical curvilinear velocity components, we need to map the input base-flow velocity onto the local coordinate system as follows

$$\text{2D}: \quad u = \frac{h_1}{J}\left(-v_y\frac{\partial x}{\partial \eta} + u_x\frac{\partial y}{\partial \eta}\right), \tag{B.6a}$$

$$v = \frac{h_2}{J}\left(v_y\frac{\partial x}{\partial \xi} - u_x\frac{\partial y}{\partial \xi}\right), \tag{B.6b}$$

$$\text{3DF/3D}: \quad u = \frac{h_1}{J}\left[\frac{\partial z}{\partial \zeta}\left(-v_y\frac{\partial x}{\partial \eta} + u_x\frac{\partial y}{\partial \eta}\right) + \frac{\partial y}{\partial \zeta}\left(w_z\frac{\partial x}{\partial \eta} - u_x\frac{\partial z}{\partial \eta}\right) + \right. \tag{B.6c}$$

$$\left. \frac{\partial x}{\partial \zeta}\left(-w_z\frac{\partial y}{\partial \eta} + v_y\frac{\partial z}{\partial \eta}\right)\right], \tag{B.6d}$$

$$v = -\frac{h_2}{J}\left[\frac{\partial z}{\partial \zeta}\left(-v_y\frac{\partial x}{\partial \xi} + u_x\frac{\partial y}{\partial \xi}\right) + \frac{\partial y}{\partial \zeta}\left(w_z\frac{\partial x}{\partial \xi} - u_x\frac{\partial z}{\partial \xi}\right) + \right. \tag{B.6e}$$

$$\left. \frac{\partial x}{\partial \zeta}\left(-w_z\frac{\partial y}{\partial \xi} + v_y\frac{\partial z}{\partial \xi}\right)\right], \tag{B.6f}$$

$$w = \frac{h_3}{J}\left[\frac{\partial z}{\partial \eta}\left(-v_y\frac{\partial x}{\partial \xi} + u_x\frac{\partial y}{\partial \xi}\right) + \frac{\partial y}{\partial \eta}\left(w_z\frac{\partial x}{\partial \xi} - u_x\frac{\partial z}{\partial \xi}\right) + \right. \tag{B.6g}$$

$$\left. \frac{\partial x}{\partial \eta}\left(-w_z\frac{\partial y}{\partial \xi} + v_y\frac{\partial z}{\partial \xi}\right)\right], \tag{B.6h}$$

where (u, v, w) are the velocity components along the local covariant basis vectors and (u_x, v_y, w_z) are the global Cartesian velocities.

The gradients of all base-flow variables are then computed with finite-difference schemes consistent with the stability analysis (usually fourth-order) with SBP boundary closure (Mattsson and Nordström, 2004). Note that for 3DF or 3D jet calculations with $\zeta_{max} < \pi$, the base flow is taken just offset of the centerline with adjacent radial gradients computed using the pole conditions from Mohseni and Colonius (2000) coupled with symmetric finite-difference closure conditions. The symmetry enforcement is required since the base flow is assumed to be axisymmetric for 3DF or radially symmetric across the centerline for 3D with $\zeta_{max} < \pi$. Finally, for 3D jets with $\zeta_{max} = 2\pi$, the radial derivatives are computed in the same manner as the perturbed state vector $\boldsymbol{q'}$ from Sec. B.1.2.

B.3 Stability solvers

Each type of solver within CSTAT is succinctly described in this section. The reader is encouraged to review the associated references for detailed descriptions. For this section only, the $\hat{}$ will denote the shape function of the ansatz assumed for a given type of solver.

B.3.1 Local marching methods for 2D/3DF/3D analyses

B.3.1.1 One-Way Navier-Stokes (OWNS)

See Sec. 2 for details of the OWNS methodology.

B.3.1.2 Parabolized stability equations (PSE)

Similar to OWNS, PSE tracks the downstream evolution of an initial disturbance specified at a streamwise station with non-parallel base-flow effects included, which contrasts LST or SBG. A key assumption in the PSE algorithm is that the flow is dominated by a single instability characterized by a complex streamwise wavenumber that varies slowly in ξ. For this solver, we substitute the ansatz $\boldsymbol{q'}(\xi,\eta,\zeta,t) = \hat{\boldsymbol{q}}(\xi,\eta)e^{i\left(\int_{\xi_0}^{\xi}\alpha(\xi')\,d\xi'+\beta\zeta-\omega t\right)}$ for 2D/3DF or $\boldsymbol{q'}(\xi,\eta,\zeta,t) = \hat{\boldsymbol{q}}(\xi,\eta,\zeta)e^{i\left(\int_{\xi_0}^{\xi}\alpha(\xi')\,d\xi'-\omega t\right)}$ for 3D into Eq. 2.3 with the streamwise viscous and forcing terms neglected, i.e. $\boldsymbol{C} = \boldsymbol{B_{\xi\xi}} = \boldsymbol{f_p} = 0$ from Eq. 5.1. This method, although computationally efficient, has several intrinsic disadvantages which are detailed in Towne, Rigas, and Colonius (2019).

B.3.2 Local linear stability theory (LST/SBG) for 2D/3DF/3D analyses

In classical linear theory, the base flow is assumed to evolve slowly with ξ and ζ relative to the wavelengths of the associated disturbance, i.e. the base flow is locally

homogeneous in ξ and ζ. By introducing the normal-mode ansatz $\boldsymbol{q'}(\xi,\eta,\zeta,t) = \hat{\boldsymbol{q}}(\eta)e^{i(\alpha\xi+\beta\zeta-\omega t)}$ into Eq. 2.3 with $\boldsymbol{f_p} = 0$, a nonlinear spatial eigenvalue problem can be solved to determine the unstable modes at a given streamwise station, i.e. the complex streamwise wavenumbers α and their corresponding eigenfunctions. The method, however, may yield inaccurate results for complex flows exhibiting multi-modal and/or non-modal (transient) instabilities.

Following similar assumptions to LST, if the base flow also exhibits strong spanwise variations, an SBG analysis can be performed via full cross-stream discretization, thereby only assuming local streamwise homogeneity such that the normal-mode ansatz takes the form $\boldsymbol{q'}(\xi,\eta,\zeta,t) = \hat{\boldsymbol{q}}(\eta,\zeta)e^{i(\alpha\xi-\omega t)}$. Similar to LST, SBG calculations should be qualified for complex flows containing multi-modal instabilities and/or transient growth.

B.3.3 Global methods for 2D/3DF analyses

Note that all global methods outlined below, including global optimal, are restricted to 2D/3DF due to their large computational expense.

B.3.3.1 Global stability analysis (GSA)

In GSA, all viscous terms are retained with no streamwise base-flow homogeneity assumptions. A linear, temporal eigenvalue analysis is conducted to solve for the global modes (the complex frequencies ω and their corresponding eigenfunctions) by globally discretizing Eq. 2.3 in the ξ- and η-directions with $\boldsymbol{f_p} = 0$ and using the ansatz $\boldsymbol{q'}(\xi,\eta,\zeta,t) = \hat{\boldsymbol{q}}(\xi,\eta)e^{i(\beta\zeta-\omega t)}$. Given the large computational expense of this global eigenvalue problem, the user is prompted for the guess of the most unstable complex frequency, in which then CSTAT computes eigenvalues within the vicinity of the guessed value using the Krylov-Schur algorithm from MATLAB. If the adjacent modes calculated are not of relevance, the user is prompted for a new guess and the process continues until the desired modes have been determined.

B.3.3.2 Linearized Navier-Stokes (LNS)

Using the same global discretization and ansatz as GSA, no streamwise assumptions are made regarding the base flow and all terms from Eq. 2.3 are retained. However, instead of determining global eigenmodes, the streamwise evolution of perturbations of a prescribed inlet disturbance profile (usually the eigenfunction from LST corresponding to the most unstable mode) is calculated at a given real

frequency ω. This is accomplished by lifting the inlet boundary condition into an equivalent right-hand-side forcing $\boldsymbol{f_p}$ and setting $\boldsymbol{\mathcal{B}_p} = \boldsymbol{I}$. LNS essentially is the global analogue of the local marching methods OWNS and PSE.

B.3.4 Optimization methods

B.3.4.1 Global optimal for 2D/3DF analyses

In the global approach, Eq. 5.1 is discretized in the streamwise direction with all viscous terms retained, and after incorporating appropriate boundary conditions, can be written in an input-output format as

$$\boldsymbol{L}\boldsymbol{q'} = \boldsymbol{\mathcal{B}_p}\boldsymbol{f_p}, \quad \boldsymbol{y} = \boldsymbol{C_p}\boldsymbol{q'}, \tag{B.7}$$

where $\boldsymbol{L}$ is the LNS operator. We can therefore express the observable in terms of the input forcing as

$$\boldsymbol{y} = \boldsymbol{C_p}\boldsymbol{\mathcal{R}}\boldsymbol{\mathcal{B}_p}\boldsymbol{f_p}, \tag{B.8}$$

where $\boldsymbol{\mathcal{R}} = \boldsymbol{L^{-1}}$ is the global resolvent operator.

Input-output analysis determines the forcing and response pairs that yield the largest gain. We thus need to define a global inner product

$$\langle \boldsymbol{a}, \boldsymbol{b} \rangle_g = \langle \boldsymbol{a}, \boldsymbol{W_e}\boldsymbol{b} \rangle = \boldsymbol{a}^H \boldsymbol{W_{\xi\eta\zeta}} \boldsymbol{W_e} \boldsymbol{b} = \boldsymbol{a}^H \boldsymbol{W_g} \boldsymbol{b}, \tag{B.9}$$

where $\boldsymbol{W_g}$ is a positive-definite weight matrix constructed as $\boldsymbol{W_g} = \boldsymbol{W_{\xi\eta\zeta}}\boldsymbol{W_e}$. Here $\boldsymbol{W_e}$ represents a physical quantity of interest, i.e. the Chu-energy weight matrix (Chu, 1965) from Sec. 4.1, and $\boldsymbol{W_{\xi\eta\zeta}}$ is a diagonal positive-definite matrix of quadrature weights composed of $h_\xi h_\eta \mathrm{d}\xi\mathrm{d}\eta$ and $h_\xi h_\eta h_\zeta \mathrm{d}\xi\mathrm{d}\eta$ for 2D and 3DF analyses, respectively. Thus, the inner product represents the volume-integrated quantity (up to a discretization error). Inner products without any subscripts involve only quadrature weights.

The global optimal forcing and responses can now be calculated via the following Rayleigh quotient

$$\sigma_g^2(\omega) = \frac{\langle \boldsymbol{y}, \boldsymbol{y} \rangle_g}{\langle \boldsymbol{f_p}, \boldsymbol{f_p} \rangle_g} = \frac{\boldsymbol{f_p^H} \boldsymbol{\mathcal{B}_p^H} \boldsymbol{\mathcal{R}^H} \boldsymbol{C_p^H} \boldsymbol{W_g} \boldsymbol{C_p} \boldsymbol{\mathcal{R}} \boldsymbol{\mathcal{B}_p} \boldsymbol{f_p}}{\boldsymbol{f_p^H} \boldsymbol{W_g} \boldsymbol{f_p}}. \tag{B.10}$$

The maximum global gain σ_g can be obtained with either the generalized SVD method or transforming to the standard one by defining $\boldsymbol{k_p} = \boldsymbol{W_g^{1/2}} \boldsymbol{f_p}$ and maximizing

$$\sigma_g^2(\omega) = \frac{\boldsymbol{k_p^H} \boldsymbol{\mathcal{R}_g^H} \boldsymbol{\mathcal{R}_g} \boldsymbol{k_p}}{\boldsymbol{k_p^H} \boldsymbol{k_p}}, \tag{B.11}$$

where $\mathcal{R}_g = \boldsymbol{W}_g^{1/2} \boldsymbol{C}_p \mathcal{R} \mathcal{B}_p \boldsymbol{W}_g^{-1/2}$ is a weighted form of the resolvent operator. The optimal gains and corresponding forcings can now be computed via the eigenvalue decomposition of $\mathcal{R}_g^H \mathcal{R}_g$ or, equivalently, the following SVD

$$\mathcal{R}_g = \boldsymbol{U}_g \boldsymbol{\Sigma}_g \boldsymbol{V}_g^H. \tag{B.12}$$

The singular values contained within the diagonal positive-semi-definite matrix $\boldsymbol{\Sigma}_g$ correspond to σ_g, whereas the input and output modes are contained in the columns of the matrices $\boldsymbol{V} = \boldsymbol{W}_g^{-1/2} \boldsymbol{V}_g$ and $\boldsymbol{U} = \boldsymbol{W}_g^{-1/2} \boldsymbol{U}_g$, respectively.

B.3.4.2 OWNS optimal for 2D/3DF/3D analyses

See Sec. 4 for details of the optimal OWNS methodology.

B.4 Auxiliary utilities

The various auxiliary utilities contained within CSTAT are discussed in this section. These functions allow the user to easily generate the necessary input files (e.g. flat-plate boundary-layer base flows) and/or maximize the efficiency in conducting stability analyses using CSTAT.

B.4.1 Self-similar boundary-layer solutions

CSTAT includes a base-flow generator for zero-pressure-gradient flat-plate and sharp-cone Blasius profiles, the former of which is computed using the Howarth-Dorodnitsyn transformation. For sharp-cone profiles, the Taylor-Maccoll ODE (Taylor and Maccoll, 1933) is solved initially to determine the inviscid, boundary-layer edge properties along the ray emanating from the nose at the cone half-angle using a modified MATLAB code from Lassaline, J. V. (2009). Thereafter, following the work of Lees (1956), the Blasius profile is computed by applying the Mangler transformation (Mangler, 1948) for axisymmetric flows to the self-similar solution. While the calorically perfect gas assumption is used, i.e. c_p is constant, the fluid properties μ and k are both functions of temperature and can vary via Sutherland's Law or with polynomial functions. The similarity solution (Blasius profile) is then numerically computed by solving the boundary-value problem using the fourth-order method from MATLAB (bvp4c).

In addition to the classical Blasius profiles, the more general class of Falkner–Skan (FS) and Falkner–Skan-Cooke (FSC) profiles can also be generated to include pressure gradient and/or sweep angles, which can model infinitely spanning swept wings. Note that the pressure gradient is encapsulated in the Hartree parameter β_H.

Excluding the sharp-cone feature, all important points made regarding the Blasius profiles apply to FS/FSC solutions with the exception that these profiles are *locally* self-similar to accommodate the change in edge Mach number. Essentially, the FS/FSC ODE's are solved at each streamwise station to determine the local profile (this is valid if the edge properties do not experience rapid streamwise variation (Gaponov and Smorodskii, 2008)).

B.4.2 Inviscid-streamline and vortex-path generator

In 3DF boundary-layer computations, an integration pathway must be supplied into CSTAT in the form of surface coordinates (x_s, y_s, z_s). One common pathway is the inviscid streamline, i.e. streamlines based on the boundary-layer edge velocities. CSTAT includes a utility that takes the 3D base flow and corresponding grid as inputs, and computes the inviscid streamlines along the surface of the body. The user can then extract (x_s, y_s, z_s) corresponding to a desired streamline and perform stability analyses thereafter.

Similar to the inviscid-streamline generator, CSTAT also includes a vortex-path generator. This utility calculates vortex paths for stationary crossflow based on the inflection-point method, where the marching direction is locally oriented such that spanwise generalized inflection point (GIP), $\frac{\partial}{\partial\eta}\left(\overline{\rho}\frac{\partial\overline{w}}{\partial\eta}\right) = 0$, occurs at $\overline{\rho}\overline{w} = 0$ (Kocian et al., 2019). The spanwise base-flow velocity $\overline{w}$ here is oriented orthogonal to the marching direction. The user can then extract the surface coordinates corresponding to one vortex path for subsequent stability calculations. However, depending on the resolution of the base flow, certain streamwise stations may not satisfy the GIP and $\overline{\rho}\overline{w} = 0$ requirement within the specified tolerance due to sensitivity of the streamwise basis vectors, especially when near planes of spanwise symmetry. Specifically, the user-input tolerance governs the wall-normal distance between the GIP and where $\overline{\rho}\overline{w} = 0$ (theoretically these two quantities should coincide but numerically a small distance is tolerated). If erroneous pathways are observed, the tolerance is increased incrementally until smooth pathways are computed. There is also an additional input parameter that represents the angular resolution used to iterate through the spanwise velocities until the vortex-path criterion is satisfied, after which the spanwise location at the next streamwise station is determined.

B.4.3 MEX-operator generator

The linear operators used for all the solvers in CSTAT can be constructed using the default MATLAB function handles or pre-compiled MEX files. Given the complex-

ity and generality of the operators, the former method is computationally inefficient, especially for complex geometries, due to MATLAB's interpreted language type. The MEX-operator utility will generate the MEX files that can be used to compute the operators considerably faster. Note that the default MEX files present in CSTAT should be functional for most Linux 64-bit architecture. However, these files can be recompiled if need be with the included script, which is a one-time process and once completed, these operators can be used for any arbitrary geometry and base flow.

B.4.4 Numerical solvers

The default numerical solver in MATLAB for matrix inversion is UMFPACK. Although robust, this algorithm can be memory-intensive especially for 3D computations. A new solver, the Intel® oneAPI Math Kernel Library PARDISO package (Schenk and Gärtner, 2004), has been recently added for the PSE, OWNS, and LNS solvers. PARDISO is a memory-efficient algorithm that can solve large sparse linear systems of equations on multiprocessor computer architecture. The user should review how to compile the solver and all the iparm PARDISO parameters that control the efficiency and accuracy of the linear solver from the Intel® website. The default parameters in CSTAT have been tested for a wide variety of cases (both jets and boundary layers in 2D, 3DF, and 3D) for maximal efficiency and robustness of the matrix inversion, but the user may need to further tune the iparm parameters for complex cases to maximize performance.

The aforementioned two solvers are implemented in CSTAT as "direct" solvers in that they perform the LU decomposition of the desired linear system of equations. However, even with PARDISO, this operation can become computationally expensive, especially for 3D OWNS. Thus, two types of hybrid computational approaches have been implemented for OWNS. The first method involves performing the LU decomposition on the DAE matrix constructed with second-order cross-stream discretization with reduced-order boundary closure, which significantly increases the sparsity of the matrix and thereby reduces the memory cost. The inverted system and corresponding solution then serves as a preconditioner matrix and guess, respectively, for solving the desired linear system using the restarted generalized minimum residual (iterative) method from MATLAB. This hybrid approach was found to reduce the total computational time by $\approx$ 50% when applied to the 3D OWNS equations on the Mach 6 finned-cone geometry from Araya et al. (2022). The second hybrid computational approach is specifically designed for the OWNS

projection method and exploits the slowly varying nature of the base flow in the streamwise direction. Here, the preconditioner matrix and guess corresponds to the DAE matrix and solution from the previous streamwise station, respectively. Note that this algorithm may become inefficient if the base flow exhibits relatively strong streamwise variations (e.g. the Mach 6 HIFiRE-5 elliptic cone or the Mach 6 finned-cone geometry (Araya et al., 2022)), and therefore more suited for simpler flows such as jets.

Appendix C

OWNS RECURSION PARAMETERS

The algorithm for computing the OWNS recursion parameters for both jets and boundary layers is presented in the following MATLAB script. Although the algorithm is for 2D/3DF calculations, the same method is used for 3D analyses, but the base-flow quantities are cross-stream averaged.

```
function [b_plus,b_minus] = ...
    OWNS2D3DF_parameters(xi,equation,baseflow,Nb)


%%%%%%%%%%%%%%%%%%%%%%%%%%%%%%%%%%%%%%%%%%%%%%%%%%%%%%%%%%%%%%%%%%%%%%%%%%%%
% ---------------------------- Unpack Variables ...
    ---------------------------- %

% Frequency
w = equation.w;

% Evaluate required baseflow quantities
[baseflow.Q,¬,¬,¬,¬,¬,¬,¬,¬,¬,baseflow.fp,¬,¬] =  ...
    baseflow.fcn(xi,equation.grid.eta);

% Create scaled baseflow quantities
c   = sqrt(baseflow.fp.ga.*baseflow.Q.p./baseflow.Q.rho); ...
        % Speed of sound
Mxi = baseflow.Q.u./c; ...
                                                % Streamwise ...
    Mach number
k   = w./c; ...
                                                        % ...
    Wavenumber

% Grid parameters
dz   = equation.grid.dz; ...
                                              % Uniform ...
    wall-normal grid spacing
if max(Mxi) < 1 && ...
    strcmp(equation.analysistype,'BoundaryLayer')
```

```
21     Leta = equation.grid.wallnorm_avg; ...
                                    % Average wall-normal domain ...
       length
22 else
23     Leta = equation.grid.Leta;
24 end
25
26 % Allocate storage for b's
27 b_plus  = zeros(1,Nb);
28 b_minus = zeros(1,Nb);
29
30 if strcmp(equation.analysistype,'BoundaryLayer')
31
32     % Distribution is based on the freestream/wall values
33     Mxi1 = Mxi(end);            % Fast-stream Mach number
34     Mxi2 = Mxi(1);              % Slow-stream Mach number
35     k1   = k(end);              % Fast-stream wavenumber
36     k2   = k(1);                % Slow-stream wavenumber
37
38     % Error message if Mxi1 = 1
39     if Mxi1 == 1 error('Recursion Parameters are Inf for ...
       Mxi = 1'); end
40
41     % Ajust minimum Mach number if Mxi1 or Mxi2 very small ...
       or zero
42     epsilon = 10e-12;
43     if abs(Mxi1) < abs(epsilon); Mxi1 = epsilon; end
44     if abs(Mxi2) < abs(epsilon); Mxi2 = epsilon; end
45
46     % Division of parameters among modes
47     Nb1 = ceil(Nb/3);           % Total ...
       fast-stream/propagating acoustic parameters
48     Nb2 = ceil(Nb/3);           % Total ...
       slow-stream/evanescent acoustic parameters
49     Nb0 = Nb - Nb1 - Nb2;       % Vorticity parameters
50
51     Nb1p = floor(Nb1/2);        % Fast-stream propagating ...
       acoustic parameters
52     Nb1e = Nb1 - Nb1p;          % Fast-stream evanescent ...
       acoustic parameters
53     Nb2p = floor(Nb2/2);        % Slow-stream propagating ...
       acoustic parameters
54     Nb2e = Nb2 - Nb2p;          % Slow-stream evanescent ...
```

```
          acoustic parameters
55
56      % ------------------------------------------------------
57      % Make parameters for propogating modes
58
59      if Mxi1 < 1
60
61          % Fast-stream propagating acoustic waves
62          ind = (1:Nb1p);
63          [b_plus(ind),b_minus(ind)] = ...
                AcousticModesPropagating(k1,Mxi1,Nb1p);
64
65          % Slow-stream propagating acoustic waves
66          ind = (1:Nb2p) + Nb1p;
67          [b_plus(ind),b_minus(ind)] = ...
                AcousticModesPropagating(k2,Mxi2,Nb2p);
68
69      else
70
71          % Supersonic propagating acoustic modes
72          ind    = (1:Nb1);
73          [a1,¬] = ...
                AcousticModesPropagating(k1,Mxi1,floor(Nb1/2));
74          [¬,a2] = ...
                AcousticModesPropagating(k1,Mxi1,Nb1-floor(Nb1/2));
75
76          b_plus(ind)  = [a1,a2];
77          b_minus(ind) =  -1i*b_plus(ind);
78
79      end
80
81      % ------------------------------------------------------
82      % Make parameters for evanescent modes
83
84      if Mxi1 < 1
85
86          % Fast-stream evanescent acoustic waves
87          ind = (1:Nb1e) + Nb1p + Nb2p;
88          [b_plus(ind),b_minus(ind)] = ...
                AcousticModesEvanescent(k1,Mxi1,Nb1e,Leta,dz);
89
90          % Slow-stream evanescent acoustic waves
91          ind = (1:Nb2e) + Nb1 + Nb2p;
```

```
92          [b_plus(ind),b_minus(ind)] = ...
               AcousticModesEvanescent(k2,Mxi2,Nb2e,Leta,dz);
93
94      else
95
96          % Supersonic evanescent acoustic modes
97          ind    = (1:Nb2)+Nb1;
98          [a1,¬] = ...
               AcousticModesEvanescent(k1,Mxi1,floor(Nb2/2),Leta,dz);
99          [¬,a2] = ...
               AcousticModesEvanescent(k1,Mxi1,Nb2-floor(Nb2/2),Leta,dz);
100
101         b_plus(ind) = [a1,a2];
102         b_minus(ind)= [-1i*abs(a1),-1i*abs(a2)];
103
104     end
105
106
107     % ------------------------------------------------------
108     % Make parameters for convective modes (vorticity+entropy)
109     ind = (1:Nb0)+Nb1+Nb2;
110
111     [b_plus(ind),b_minus(ind)] = ...
           ConvectiveModes(k1,k2,Mxi1,Mxi2,Nb0,dz);
112
113     % ------------------------------------------------------
114     % Move plus modes from real axis
115     b_plus  = b_plus  + ( abs(imag(b_plus))<1e-9 )*1e-4*1i;
116     b_minus = b_minus + ( abs(imag(b_minus))<1e-9 )*1e-4*1i;
117
118 elseif strcmp(equation.analysistype,'Jets')
119
120     % Define uniform flow parameters
121     Mxi1 = Mxi(1);              % Fast-stream Mach number
122     Mxi2 = Mxi(end);            % Slow-stream Mach number
123     k1   = k(1);                % Fast-stream wavenumber
124     k2   = k(end);              % Slow-stream wavenumber
125
126     % Ajust minimum Mach number if Mxi1 or Mxi2 very small ...
           or zero
127     epsilon = 10e-12;
128     if abs(Mxi1) < abs(epsilon); Mxi1 = epsilon; end
129     if abs(Mxi2) < abs(epsilon); Mxi2 = epsilon; end
```

```
130
131     if Mxi1 < 1.05 % Subsonic jet parameters
132
133         % Division of parameters amoung modes
134         Nb_kh = 3;                                % Total KH ...
                parameters
135         Nb2   = ceil((Nb - Nb_kh)/2);             % Total ...
                free stream acoustic parameters
136         Nb_w  = Nb - Nb_kh - Nb2;                 % Vorticity ...
                parameters
137         Nb_a2 = floor(Nb2/2);                     % Free ...
                stream propagating acoustic parameters
138         Nb_e2 = Nb2 - Nb_a2;                      % Free ...
                stream evanescent acoustic parameters
139
140         % Make parameters for vorticity modes
141         b_w = linspace(k1/Mxi1,k2/Mxi2,Nb_w);
142
143         theta  = 3*pi/4;
144         l(1,1) = cos(theta);
145         l(2,1) = sin(theta);
146
147         for j = 1:Nb_w
148
149             v(1,1) = real(b_w(j));
150             v(2,1) = imag(b_w(j));
151             r      = ...
                    (2*(transpose(v)*l)/(transpose(l)*l))*l - v;
152
153             b_plus(j+Nb-Nb_w)  = b_w(j);
154             b_minus(j+Nb-Nb_w) = r(1) + 1i*r(2);
155
156         end
157
158         % Make parameters for KH mode
159         b_w = linspace(k2/(0.8*Mxi1),k2/(0.6*Mxi1),Nb_kh);
160
161         for j = 1:Nb_kh
162
163             v(1,1) = real(b_w(j));
164             v(2,1) = imag(b_w(j));
165             r      = ...
                    (2*(transpose(v)*l)/(transpose(l)*l))*l - v;
```

```
166
167             b_plus(j)  =  b_w(j);
168             b_minus(j) = r(1) + 1i*r(2);
169
170         end
171
172         % Wave numbers for acoustic modes
173         eta_c = k2/sqrt(1-Mxi2^2);
174         eta_m = 2/(Leta*dz);
175         if Nb_e2 > 1; deta_e = 0.1*(eta_m-eta_c)/(Nb_e2-1); ...
               else deta_e = 0.2*eta_m/2; end
176         if Nb_a2 > 1; deta_a = 0.1*(eta_c-0)/(Nb_e2-1); ...
               else deta_a = 0.2*eta_c/2; end
177         eta_a2 = fliplr(linspace(eta_c-deta_a,0,Nb_a2+1)); ...
               eta_a2 = eta_a2(2:end);
178         eta_e2 = ...
               fliplr(linspace(eta_m,eta_c+deta_e,Nb_e2)); % ...
               eta_e2 = eta_e2(2:end);
179         eta2 = [eta_a2- 0.00i,eta_e2]; ...
                                    % Slow stream wave numbers
180
181         % Make parameters for free stream acoustic modes
182         for j = 1:Nb2
183
184             muj = sqrt(k2^2 - (1-Mxi2^2)*(eta2(j))^2);
185
186             b_plus(j+Nb_kh) = (-Mxi2*k2 + muj)/(1-Mxi2^2) + 0i;
187             b_minus(j+Nb_kh) = (-Mxi2*k2 - muj)/(1-Mxi2^2) ...
                   - 0i;
188
189         end
190
191     else % Supersonic jet parameters
192
193         % Division of parameters among modes
194         N1 = ceil(Nb/10);                          % ...
               Vorticity modes
195         N2 = ceil(Nb/10);                          % ...
               Propagating acoustic modes
196         N3 = ceil(Nb/10);                          % ...
               Evanescent acoustic modes
197         N4 = ceil((Nb - N1 - N2 - N3)/2);          % Core ...
               acoustic modes (negative phase speeds)
```

```
198         N5 = Nb - N1 - N2 - N3 - N4;              % Core ...
                acoustic modes (positive phase speeds)
199
200         % Make parameters for vorticity modes : N1
201         b_w = linspace(k1/Mxi1,k2/Mxi2,N1);
202
203         % Constants for rotation of negative parameters
204         theta  = 3*pi/4;
205         l(1,1) = cos(theta);
206         l(2,1) = sin(theta);
207         zero   = -k2*(-Mxi2)/(1-Mxi2^2)*cos(theta);
208
209         for j = 1:N1
210
211             % Rotate negative parameters by an angle theta ...
                   around zero
212             v(1,1) = real(b_w(j));
213             v(2,1) = imag(b_w(j));
214             r      = (2*(transpose(v)*l - ...
                    zero)/(transpose(l)*l))*l - v;
215
216             % Set parameters
217             b_plus(j)  = b_w(j);
218             b_minus(j) = r(1) + 1i*r(2)-50i;
219
220             % Save parameters
221             b_all.N1(1,j) = b_plus(j);
222             b_all.N1(2,j) = b_minus(j);
223
224         end
225
226         % Define critical wave numbers
227         eta_c = k2/sqrt(1-Mxi2^2);
228         eta_m = 2.7/(Leta*dz);
229         if N2 > 1; deta_a = 0.1*(eta_c-0)/(N2-1); else ...
                deta_a = 0.2*eta_c/2; end
230         if N3 > 1; deta_e = 0.1*(eta_m-eta_c)/(N3-1); else ...
                deta_e = 0.2*eta_m/2; end
231         %if N4 > 1; deta_z = 0.2*(eta_m-0)/(N4-1); else ...
                deta_e = 0.2*eta_m/2; end
232         deta4 = k1*sqrt( (1 - (Mxi1 - ...
                (1-Mxi1^2)*3)^2)/(1-Mxi1^2));
233         deta5 = k1*sqrt( (1 - (Mxi1 + ...
```

```
            (1-Mxi1^2)*3)^2)/(1-Mxi1^2));
234
235         % Define wave numbers for acoustic modes
236         eta2 = fliplr(linspace(eta_c-deta_a,0,N2+1)); eta2 ...
               = eta2(2:end);
237         eta3 = fliplr(linspace(eta_m,eta_c+deta_e,N3));
238         eta4 = fliplr(linspace(eta_m,deta4,N4+0)); % eta4 = ...
               eta4(2:end);
239         eta5 = fliplr(linspace(eta_m,deta5,N5+0)); % eta5 = ...
               eta5(2:end);
240         eta  = [eta2,eta3];                        % Slow ...
               stream wave numbers
241
242         % Make parameters for free-stream acoustic modes: N2,N3
243         for j = 1:N2+N3
244
245             % mu
246             muj = sqrt(k2^2 - (1-Mxi2^2)*(eta(j))^2);
247
248             % Set parameters
249             b_plus(j+N1)   = (-Mxi2*k2 + muj)/(1-Mxi2^2);
250             b_minus(j+N1)  = (-Mxi2*k2 - muj)/(1-Mxi2^2);
251
252             % Save parameters
253             b_all.N23(1,j) = b_plus(j+N1);
254             b_all.N23(2,j) = b_minus(j+N1);
255
256         end
257
258         % ----------------- Core modes ...
               ---------------------------------------
259
260         % Make parameters for core acoustic modes (negative ...
               phase speeds) : N4
261
262         % Constants for rotation of negative parameters
263         theta  = 5*pi/4; % 5
264
265         l(1,1) = cos(theta);
266         l(2,1) = sin(theta);
267         zero   = -k2*(-Mxi2)/(1-Mxi2^2)*cos(theta);
268
269         for j = 1:N4
```

```
270
271             % mu
272             muj    = sqrt(k1^2 - (1-Mxi1^2)*(eta4(j))^2);
273
274             % Positive parameters
275             lam_p  = (-Mxi1*k1 + muj)/(1-Mxi1^2);
276
277             % Rotate negative parameters by an angle theta ...
                    around sonic point
278             v(1,1) = real(lam_p);
279             v(2,1) = imag(lam_p);
280             r      = (2*(transpose(v)*l - ...
                    zero)/(transpose(l)*l))*l - v;
281
282             % Set parameters
283             b_plus(j+N1+N2+N3)  = lam_p;
284             b_minus(j+N1+N2+N3) = r(1) + 1i*r(2);
285
286             % Save parameters
287             b_all.N4(1,j)  = b_plus(j+N1+N2+N3);
288             b_all.N4(2,j)  = b_minus(j+N1+N2+N3);
289
290         end
291
292         % Make parameters for core acoustic modes (positive ...
                phase speeds): N5
293
294         % Constants for rotation of negative parameters
295         theta  = 3*pi/4; % 3
296         l(1,1) = cos(theta);
297         l(2,1) = sin(theta);
298         zero   = -k2*(-Mxi2)/(1-Mxi2^2)*cos(theta);
299
300         for j = 1:N5
301
302             % mu
303             muj    = sqrt(k1^2 - (1-Mxi1^2)*(eta5(j))^2);
304
305             % Positive parameters
306             lam_p  = (-Mxi1*k1 - muj)/(1-Mxi1^2);
307
308             % Rotate negative parameters by an angle theta ...
                    around sonic point
```

```
309             v(1,1) = real(lam_p);
310             v(2,1) = imag(lam_p);
311             r      = (2*(transpose(v)*l - ...
                    zero)/(transpose(l)*l))*l - v;
312
313             % Set parameters
314             b_plus(j+N1+N2+N3+N4)  = lam_p;
315             b_minus(j+N1+N2+N3+N4) = r(1) + 1i*r(2);
316
317
318             % Save parameters
319             b_all.N5(1,j)  = b_plus(j+N1+N2+N3+N4);
320             b_all.N5(2,j)  = b_minus(j+N1+N2+N3+N4);
321
322         end
323
324                 %%%% Alternative supersonic jet parameters %%%%
325 %%%%%%% ...
    ------------------------------------------------------%%%%%%%
326 %
327 %       % Division of parameters among modes
328 %       N1 = ceil(Nb/5);                                % ...
    Vorticity modes
329 %       N2 = ceil((Nb - N1)/4);                         % ...
    Propagating acoustic modes
330 %       N3 = ceil((Nb - N1 - N2)/3);                    % ...
    Evanescent acoustic modes
331 %       N4 = ceil((Nb - N1 - N2 - N3)/2);               % Core ...
    acoustic modes (negative phase speeds)
332 %       N5 = Nb - N1 - N2 - N3 - N4;                    % Core ...
    acoustic modes (positive phase speeds)
333 %
334 %       % Make parameters for vorticity modes : N1
335 %       b_w    = linspace(k1/Mxi1,k2/Mxi2,N1);
336 %
337 %       % Constants for rotation of negative parameters
338 %       theta  = 3*pi/4;
339 %       l(1,1) = cos(theta);
340 %       l(2,1) = sin(theta);
341 %       zero   = -k2*(-Mxi2)/(1-Mxi2^2)*cos(theta);
342 %
343 %       for j = 1:N1
344 %
```

```
345 %         % Rotate negative parameters by an angle theta ...
    around zero
346 %         v(1,1) = real(b_w(j));
347 %         v(2,1) = imag(b_w(j));
348 %         r      = (2*(transpose(v)*l - ...
    zero)/(transpose(l)*l))*l - v;
349 %
350 %         % Set parameters
351 %         b_plus(j)  = b_w(j);
352 %         b_minus(j) = r(1) + 1i*r(2);
353 %
354 %      end
355 %
356 %
357 %      % Define critical wave numbers
358 %      eta_c = k2/sqrt(1-Mxi2^2);
359 %      eta_m = 2.7/(Leta*dz);
360 %      if N2 > 1; deta_a = 0.1*(eta_c-0)/(N2-1); else ...
    deta_a = 0.2*eta_c/2; end
361 %      if N3 > 1; deta_e = 0.1*(eta_m-eta_c)/(N3-1); else ...
    deta_e = 0.2*eta_m/2; end
362 %      %if N4 > 1; deta_z = 0.2*(eta_m-0)/(N4-1); else ...
    deta_e = 0.2*eta_m/2; end
363 %      deta4 = k1*sqrt( (1 - (Mxi1 - ...
    (1-Mxi1^2)*3)^2)/(1-Mxi1^2));
364 %      deta5 = k1*sqrt( (1 - (Mxi1 + ...
    (1-Mxi1^2)*3)^2)/(1-Mxi1^2));
365 %
366 %      % Define wave numbers for acoustic modes
367 %      eta2 = fliplr(linspace(eta_c-deta_a,0,N2+1)); eta2 = ...
    eta2(2:end);
368 %      eta3 = fliplr(linspace(eta_m,eta_c+deta_e,N3));
369 %      eta4 = fliplr(linspace(eta_m,deta4,N4+0)); % eta4 = ...
    eta4(2:end);
370 %      eta5 = fliplr(linspace(eta_m,deta5,N5+0)); % eta5 = ...
    eta5(2:end);
371 %      eta  = [eta2,eta3];                        % Slow ...
    stream wave numbers
372 %
373 %      % Make parameters for free-stream acoustic modes: N2,N3
374 %      for j = 1:N2+N3
375 %
376 %         % mu
```

```
377 %         muj = sqrt(k2^2 - (1-Mxi2^2)*(eta(j))^2);
378 %
379 %         % Set parameters
380 %         b_plus(j+N1)  = (-Mxi2*k2 + muj)/(1-Mxi2^2);
381 %         b_minus(j+N1) = (-Mxi2*k2 - muj)/(1-Mxi2^2);
382 %
383 %     end
384 %
385 %     % Make parameters for core acoustic modes (negative ...
    phase speeds) : N4
386 %
387 %     % Constants for rotation of negative parameters
388 %     theta  = 5*pi/4;
389 %
390 %     l(1,1) = cos(theta);
391 %     l(2,1) = sin(theta);
392 %     zero   = -k2*(-Mxi2)/(1-Mxi2^2)*cos(theta);
393 %
394 %     for j = 1:N4
395 %
396 %         % mu
397 %         muj    = sqrt(k1^2 - (1-Mxi1^2)*(eta4(j))^2);
398 %
399 %         % Positive parameters
400 %         lam_p  = (-Mxi1*k1 + muj)/(1-Mxi1^2)+0i;
401 %
402 %         % Rotate negative parameters by an angle theta ...
    around sonic point
403 %         v(1,1) = real(lam_p);
404 %         v(2,1) = imag(lam_p);
405 %         r      = (2*(transpose(v)*l - ...
    zero)/(transpose(l)*l))*l - v;
406 %
407 %         % Set parameters
408 %         b_plus(j+N1+N2+N3)  = lam_p;
409 %         b_minus(j+N1+N2+N3) = r(1) + 1i*r(2);
410 %
411 %     end
412 %
413 %     % Make parameters for core acoustic modes (positive ...
    phase speeds): N5
414 %
415 %     % Constants for rotation of negative parameters
```

```
416 %       theta  = 3*pi/4;
417 %       l(1,1) = cos(theta);
418 %       l(2,1) = sin(theta);
419 %       zero   = -k2*(-Mxi2)/(1-Mxi2^2)*cos(theta);
420 %
421 %       for j = 1:N5
422 %
423 %          % mu
424 %          muj    = sqrt(k1^2 - (1-Mxi1^2)*(eta5(j))^2);
425 %
426 %          % Positive parameters
427 %          lam_p  = (-Mxi1*k1 - muj)/(1-Mxi1^2);
428 %
429 %          % Rotate negative parameters by an angle theta ...
        around sonic point
430 %          v(1,1) = real(lam_p);
431 %          v(2,1) = imag(lam_p);
432 %          r      = (2*(transpose(v)*l - ...
        zero)/(transpose(l)*l))*l - v;
433 %
434 %          % Set parameters
435 %          b_plus(j+N1+N2+N3+N4)  = lam_p;
436 %          b_minus(j+N1+N2+N3+N4) = r(1) + 1i*r(2);
437 %
438 %
439 %       end
440
441
442     end
443
444
445 end
446
447 end
448
449
450 % ac,a1,a2: convective,acoustic branches
451 % Inviscid parallel flow: Towne,Colonius JCP 2015
452
453 % Offset plus and minus, see page 854, Towne & Colonius JCP ...
        2015
454
455 function [a1,a2] = AcousticModesPropagating(k,Mxi,Nb)
```

```
456
457 % Make parameters for propogating modes
458
459 offset = 1;
460
461 if offset == 0
462
463     th = linspace(0,pi/2,Nb+1); th = th(1:end-1);
464
465     a1 = k*(-Mxi + cos(th))/(1-Mxi^2);
466     a2 = k*(-Mxi - cos(th))/(1-Mxi^2);
467
468 else
469
470     % Distribute twice the number of points
471     th = linspace(0,pi/2,2*Nb+1); th = th(1:end-1);
472
473     % Offset by one point
474     a1 = k*(-Mxi + cos(th(1:2:end-1)))/(1-Mxi^2);
475     a2 = k*(-Mxi - cos(th(2:2:end-0)))/(1-Mxi^2);
476
477 end
478
479
480 end
481
482
483 function [a1,a2] = AcousticModesEvanescent(k,Mxi,Nb,Leta,dz)
484
485 % Define wave numbers for evanescent modes
486 eta_c   = k/sqrt( abs(1-Mxi^2));
487 eta_m   = 1.5/(Leta*dz);
488 if Mxi < 1 deta_e  = 0.1*(eta_m-eta_c)/(Nb-1); else deta_e ...
       = 1.0*(eta_m-eta_c)/(Nb-1); end
489 if Nb == 1, deta_e = 0; end
490
491 offset = 1;
492
493 if offset == 0
494
495     eta = fliplr(linspace(eta_m,eta_c+deta_e,Nb));
496     muj = sqrt(k^2 - (1-Mxi^2)*(eta).^2);
497
```

```
498      % Make parameters for evanescent modes
499      a1 = (-Mxi*k + muj)/(1-Mxi^2);
500      a2 = (-Mxi*k - muj)/(1-Mxi^2);
501
502  else
503
504      eta = fliplr(linspace(eta_m,eta_c+0.5*deta_e,2*Nb));
505      muj = sqrt(k^2 - (1-Mxi^2)*(eta).^2);
506
507      % Make parameters for evanescent modes
508      a1  = (-Mxi*k + muj(1:2:end-1))/(1-Mxi^2);
509      a2  = (-Mxi*k - muj(2:2:end-0))/(1-Mxi^2);
510
511  end
512
513  end
514
515
516  function [ac,ac_minus] = ConvectiveModes(k1,k2,Mxi1,Mxi2,Nb,dz)
517
518  % Make parameters for convective modes (vorticity+entropy)
519  if Mxi1 < 1
520
521      ac = linspace(k1/(0.4*Mxi1),k1/Mxi1,Nb);
522      if abs(k2) < 1e-10
523         ac_minus = -1i*ac + (1+1i)*(-Mxi1/abs(1-Mxi1^2));
524      else
525         ac_minus = (1+1i)*(-2*k2*(Mxi2)/(1-Mxi2^2) - 1i*ac);
526      end
527
528  else
529
530      eta_m    = 1.5/dz; if Nb == 1, eta_m  = 0; end
531      ac       = k1/Mxi1 + 1i*linspace(0,0.2*eta_m,Nb);
532      ac_minus = -1i*imag(ac) +(min((1.8889*Mxi1-1.8333),1)+ ...
            min((6.4444*Mxi1-6.6667),3)*1i)*(-Mxi1/abs(1-Mxi1^2));
533
534  end
535
536  end
```